CALSPAN UB RESEARCH CENTER

(2)

A PRELIMINARY STUDY ASSOCIATED WITH THE EXPERIMENTAL MEASUREMENT OF THE AERO-OPTIC CHARACTERISTICS OF HYPERSONIC CONFIGURATIONS

JUNE 1992

CONTRACT NO. F49620-91-C-0026

Prepared By:

Dr. Michael S. Holden
Calspan-UB Research Center
P. O. Box 400
Buffalo, NY 14225

Prepared For:

Dr. Leonidas Sakell
Air Force Office of Scientific Research
Bolling Air Force Base
Washington, DC 20332-6448

06/26/92 14:54 CALSPAN ATC CONTRACTS DEPT. 002
06/26/92 08:38 202 767 4988 AFOSR/NA 003/003

REPORT DOCUMENTATION PAGE

Form Approved
OMB No. 0704-0188

1. AGENCY USE ONLY (Leave Blank)	2. REPORT DATE	3. REPORT TYPE AND DATES COVERED
	June 1992	Final Report 2/10/91 - 2/9/92

4. TITLE AND SUBTITLE
A Preliminary Study Associated with the Experimental Measurement of the Aero-Optic Characteristics of Hypersonic Configurations

5. FUNDING NUMBERS
PE 61102F
2307/AS

6. AUTHOR(S)
Dr. Michael S. Holden

7. PERFORMING ORGANIZATION NAME(S) AND ADDRESS(ES)
Calspan-UB Research Center
P.O. Box 400
Buffalo, NY 14225

8. PERFORMING ORGANIZATION REPORT NUMBER
AFOSR-TR- 92 0692

9. SPONSORING/MONITORING AGENCY NAME(S) AND ADDRESS(ES)
Air Force Office of Scientific Research
Directorate of Aerospace Sciences
Bolling AFB, DC 20332-6448

NA

10. SPONSORING/MONITORING AGENCY REPORT NUMBER
F49620-91-C-0026

11. SUPPLEMENTARY NOTES

12a. DISTRIBUTION/AVAILABILITY STATEMENT
Unlimited

12b. DISTRIBUTION CODE

13. ABSTRACT *(Maximum 200 words)*

A program of fundamental, experimental research and analysis has been conducted to design additional components necessary to modify, assemble and develop a ground-based facility (LENS) to duplicate flowfield environment around a hypersonic endo-atmospheric interceptor to evaluate optical seeker performance. Aero-optic instrumentation, used to measure the aero-optical characteristics of the viscous and shock layer over transpiration-and-filmed cooled nosetips at hypersonic speeds were also investigated. In the design of the facility, particular care was taken in designing the systems for a contamination-free hypersonic flow and in isolating the loads associated with the operation of the shock tunnel from the model support system and the aero-optic instrumentation. Five instrumentation systems, including holography, imagery, boresight/jitter, radiometry and spectrometry were evaluated to provide consistent evaluation in ENDO-LEAP mission environments. State-of-the-art CFD codes with capabilities for determining the inherent salient flowfield features such as turbulence and reacting chemistry were investigated and the GASP code was selected as the basic computational method. The stress levels and motion of shock tunnels were studied and analyzed using two approaches, a numeric marching code and a numeric solution to the wave equation. A flight test program based on existing sounding rocket technology was examined in order to design a high confidence flight test to validate the LENS ground test results.

14. SUBJECT TERMS
Hypersonic Vehicles, Endo-Atmospheric Interceptor, Optical Seeker, Aero-Optics Instrumentation, GASP

15. NUMBER OF PAGES
150

16. PRICE CODE

17. SECURITY CLASSIFICATION OF REPORT	18. SECURITY CLASSIFICATION OF THIS PAGE	19. SECURITY CLASSIFICATION OF ABSTRACT	20. LIMITATION OF ABSTRACT
"	..		

FOREWORD

The program associated with the experimental measurement of the aero-optic characteristics of hypersonic configurations reported herein was conducted by the Calspan-University at Buffalo Research Center (CUBRC) and its subcontractors Physical Research, Inc., University of Alabama-Huntsville/Aero Thermo Technology, Inc., Science and Technology Associates, Inc., and Sparta, Inc. under Contract No. F49620-91-C-0026 for the Air Force Office of Scientific Research (AFOSR). This preliminary study, to be followed by more comprehensive programs, began in February 1991 and continued through September 1991 with additional hardware delivery through February 1992.

At AFOSR, the program monitor was Dr. Leonidas Sakell. Commander H.A. Korejwo at the Strategic Defense Initiative Organization (SDIO) provided monitoring for SDIO.

At CUBRC, Michael S. Holden and Donald E. Adams compiled this report from CUBRC and its subcontractor sources. Dr. Anthony L. Russo was Executive Director of CUBRC and Dr. Holden was Program Manager throughout this preliminary study. Mr. Ronald F. Drzewiecki and Mr. Adams assisted with program management. Mr. George Duryea was a consultant on all phases of facility design and Messrs. Frank N. Valente and Joseph M. Bona were in charge of design. Designers included Messrs. Wolfgang G. Czerwinski, Edward J. Krafchak, Donald R. Lombard, and John H. Merritt. Dr. Donald W. Boyer provided performance predictions and Dr. Walter H. Wurster defined the instrumentation.

TABLE OF CONTENTS

LIST OF FIGURES

Section 1
INTRODUCTION

A key problem in the design of optical sensors for small hypersonic vehicle development is that while the existing design tools are potentially capable of providing good estimates of the cooling requirements, these techniques are incapable of accurate predictions of the aero-optic distortion of visual observation associated with turbulent mixing and flowfield radiation over the windows. These inadequacies are intrinsically related to the lack of understanding and inability to model turbulence and nonequilibrium chemistry in the hypersonic flight of optical sensors. Even for the simplest sensor configuration it is unlikely, even with an aggressive program of fundamental experiments and analysis, that aero-optic distortion of flowfield radiation will be predicted with the required accuracy within the near future. However, for velocities up to 14,000 ft/sec (4300 m/sec), it is possible to duplicate the flight environment over optical sensors in ground test facilities. Such a capability would serve to evaluate directly the aero-optical and aerothermal performance of candidate optical sensors as well as provide direct calibration of prediction techniques.

The principal regime of interest for aero-optical studies in hypersonic flow covers a range in velocities from 6 to 15 kft/sec (1.8 to 4.6 km/sec) and altitudes from 50 to 150 kft (15 to 46 km). Shown in Figure 1-1 are the reservoir pressures and temperatures which must be generated in ground test facilities to duplicate these flight conditions. To generate velocities of up to 14,000 ft/sec (4.3 km/sec) at an equivalent altitude of 75,000 ft (23 km) requires equilibrium reservoir temperatures approaching 14,000°F (8000K) and reservoir pressures close to 40,000 psia (280 MPa). While such conditions cannot be generated in facilities with long test times without freestream contamination, they can be produced in short-duration, high-energy shock tunnels. It is important to note that for stagnation temperatures above 8,000R (4400K), where real gas effects in air are important, reservoir pressures greater than 20,000 psi (140 MPa) are required to prevent significant levels of energy being frozen in non-equilibrium species in the gasdynamic expansion to hypersonic freestream conditions. The reservoir pressures required to prevent freestream non-equilibrium increase rapidly with increasing velocity and reach impractical levels over 16,000 ft/sec (4.9 km/sec).

During the five years prior to this program, a new, large high-energy shock tunnel, the LENS (Large Energy National Shock Tunnel) facility has been designed and partially constructed by the Calspan-University at Buffalo Research Center (CUBRC). This facility was designed to duplicate the re-entry corridor environment for flight velocities up to 14,000 ft/sec (4300 m/sec) to fill a critical gap in the Nation's hypersonic testing and research capability. The key gaps in technology which this facility addresses are associated with compressible transitional and turbulent flows, nonequilibrium flows and real gas air chemistry, and combustion for air breathing scramjet engines operating at Mach numbers up to 14. The design of the facility is based on the very successful 48-inch Shock Tunnel operated at Calspan. This new facility will be able to generate reservoir pressures up to 30,000 psi (200 MPa) and stagnation temperatures of 14,000R (8000 K). In the design of this facility, we have incorporated all of the important features that we have identified in the 30 years that we have been designing, building, and testing in high energy shock tunnels. This facility, shown in Figure 1-2 is a reflected shock tunnel with a 11-inch (28 cm) ID driver and an 8-inch (20.32 cm) ID driven tube. The driver section can be heated to

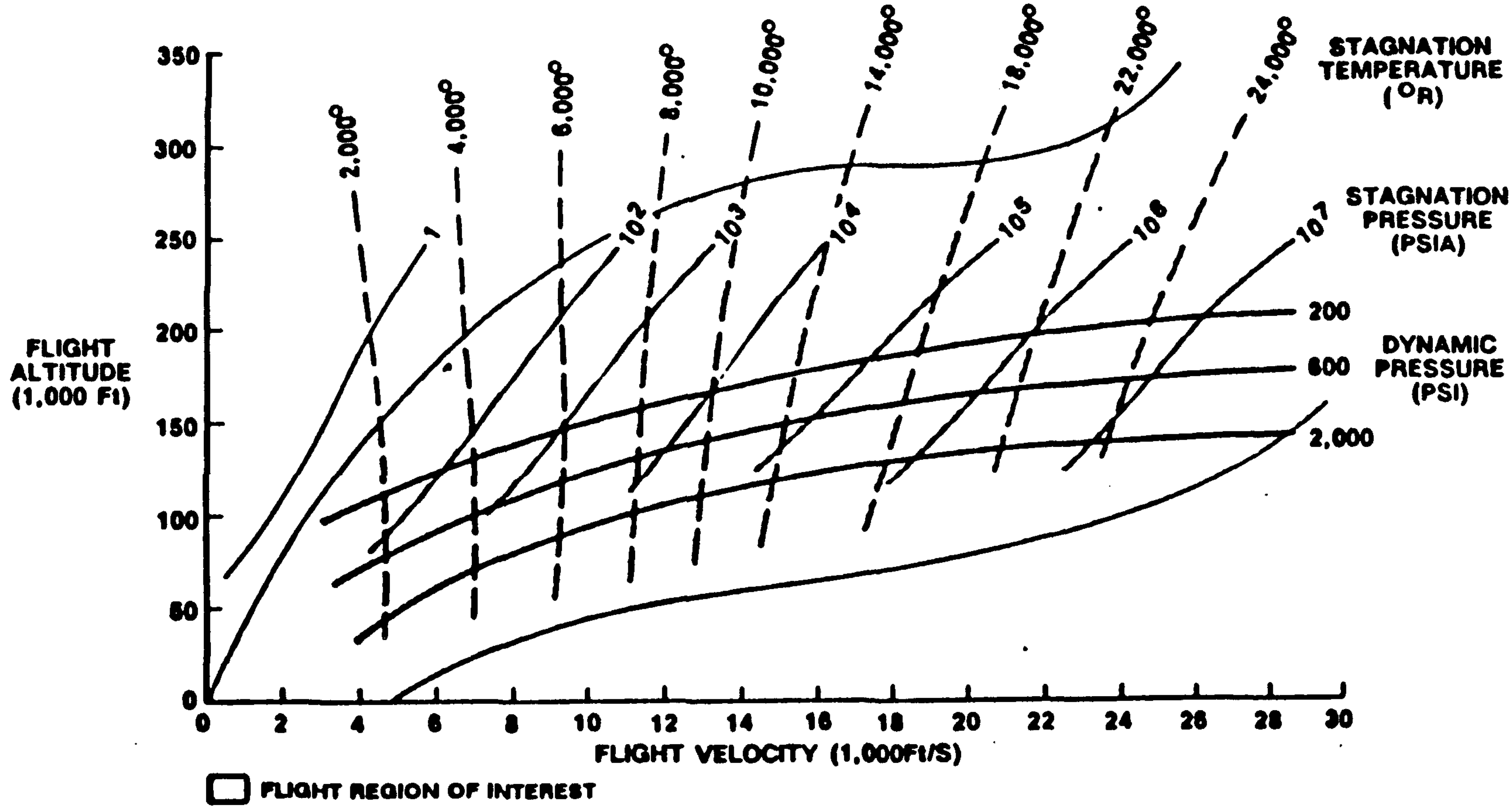

Figure 1-1 RESEVOIR CONDITIONS FOR GROUND TESTS FLIGHT DUPLICATION

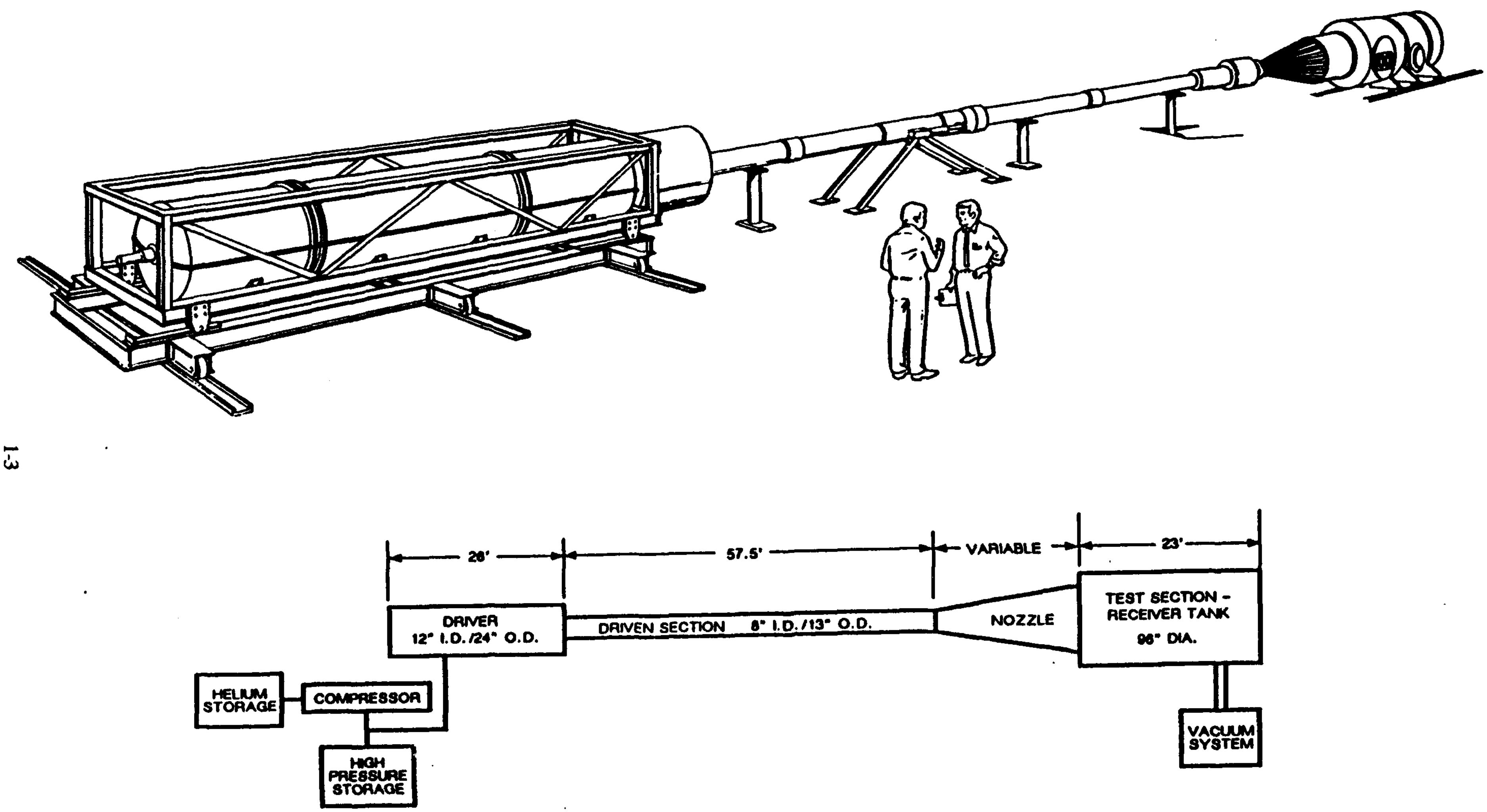

Figure 1-2 LARGE ENERGY NATIONAL SHOCK TUNNEL (LENS)

750°F and hydrogen or helium can be used as the driver gas. The Reynolds number/Mach number capabilities of the LENS facility are shown in Figure 1-3, with the Reynolds number based on a 4-foot (1.2 m) model length in the 8 ft (244 cm) test section. The total enthalpies which can be generated in this tunnel providing up to 14,000 ft/sec (4300 m/sec) are shown in Figure 1-4.

The optical performance of an optical sensor is controlled by the refraction and radiative environment introduced by the flow over the sensor. Non-uniform and turbulent refractive effects in the flow over an optical sensor degrade the optical performance of the IR optics. Also, radiative emission from high temperature air and coolants will reach the IR focal planes raising background levels and degrading performance. The definitive optical evaluation of optical sensors must be based on direct measurements of refractive and radiative levels produced in the flow. The refractive degradations can be measured with a combination of wavefront distortion and image formation diagnostics. The wavefront distortion produced by the flow over the optical sensor will be measured directly with holographic interferometry (HI). Pulsed laser holography is a convenient and accurate means for interferometric measurement of wavefront distortion. With the attendant specification of the optical aperture and wavelength, the focal plane intensity distribution is obtained through Fourier analysis. The image formation approach has the advantage of producing a real image (i.e., with actual lens elements) and recording real intensity distributions. By-passing the rather complex step used in HI of high resolution phase measurements and two-dimensional Fourier transform, the image formation systems measures the final results directly. The distinct disadvantage is that the optical degradation is wavelength and aperture dependent and therefore this evaluation is less comprehensive than the HI diagnostic. The HI diagnostic provides direct wavefront distortion measurements and image blur, MTF, PSF data through analysis. The imagery diagnostic provides direct measurement of image blur, MTF and PSF.

The radiative environment achieved in the high temperature flow over the optical sensor produces an increase in background level on the focal plane. Several lines of sight will be viewed with radiometers which will sense band radiation in the UV, visible, and near, mid and far infrared spectral regions. These radiation levels are expected to depend on incident gas velocity and density, and coolant gas and optical sensor design.

When carefully reconstructed and interpreted, these two sets of aero-optic measurements provide direct evaluation of optical sensor performance; however, they do not provide details of the structure of the flow over the nosetip and windows. For such measurements we require additional flowfield diagnostics (intrusive and nonintrusive) to provide point mean and fluctuating measurements of key flow properties. Here, we adopt the conservative approach of selecting only proven techniques or those methods which having worked successfully in a slightly different environment can be easily transitioned to obtain measurements in short duration hypervelocity flows. These techniques include electron-beam, emission spectroscopy, hot film, pitot pressure, and cross-beam correlation. If, for example, LIF were to be successfully demonstrated in an appropriate test facility, we would naturally consider the use of this potentially powerful technique in this program.

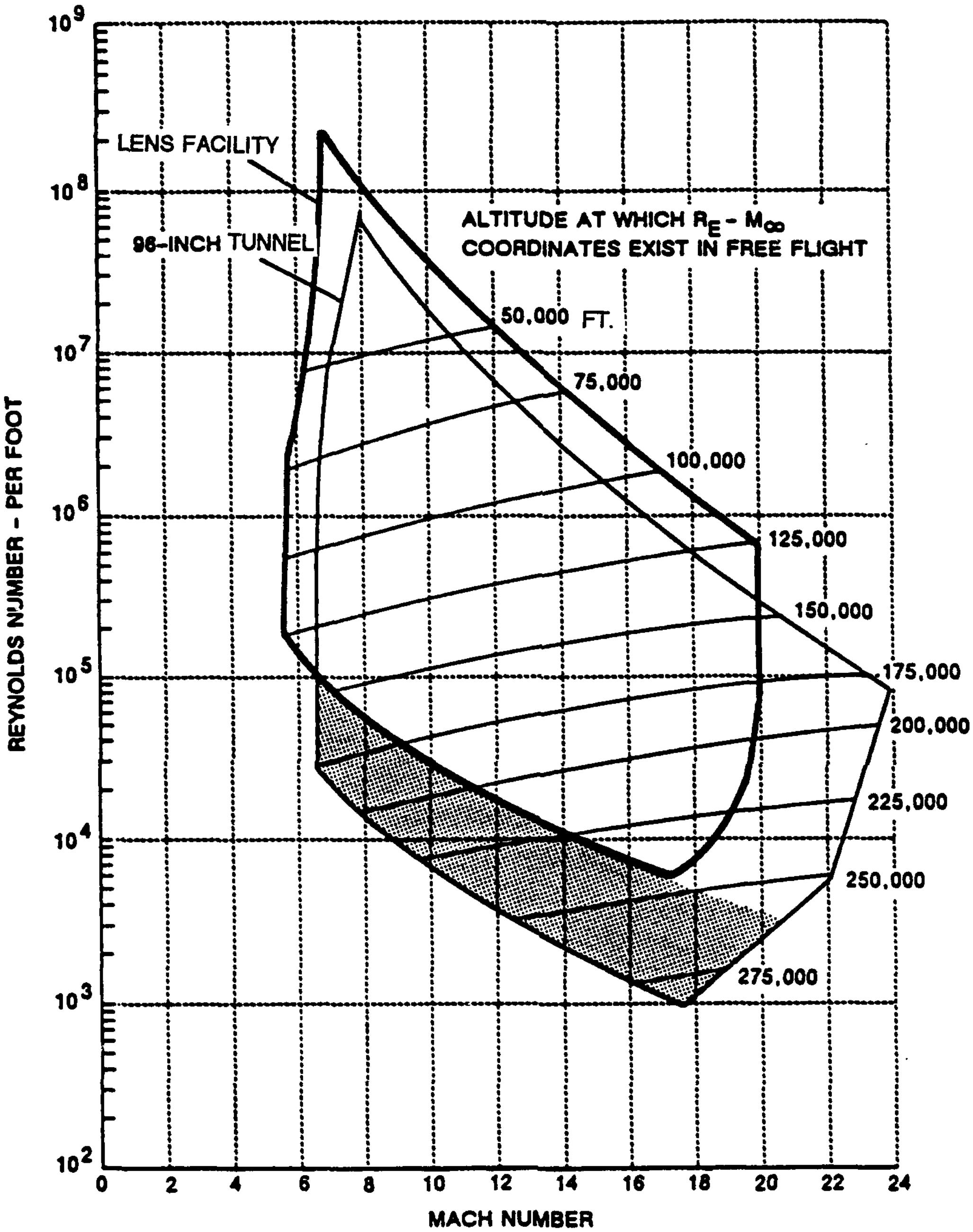

Re_{MAX} BASED ON $T_{\infty\ MIN} = 1.10\ T_{LOX}$

HIGH T_o, SHORT TEST TIME REGION ($t \leq 2$ ms) $T_o \geq 6000°$ R

Figure 1-3 HYPERSONIC SHOCK TUNNEL PERFORMANCE

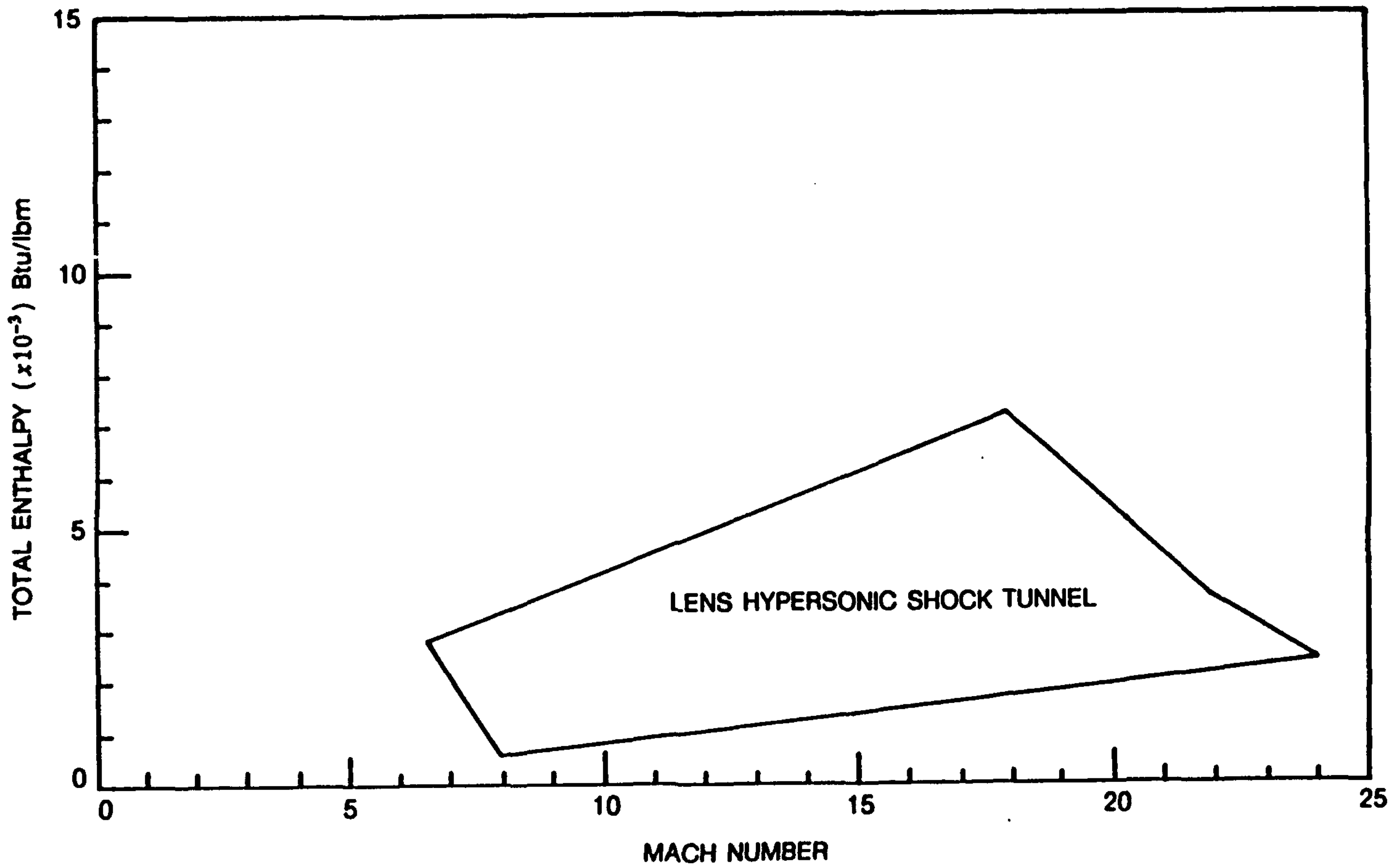

Figure 1-4 TOTAL ENTALPY VERSUS MACH NUMBER FOR LENS FACILITY

One of the important objectives of this program was to develop a capability to provide ground test measurements with aerothermal, flowfield, and aero-optical instrumentation which will be used in flight tests. This would open the exciting prospect of obtaining ground and flight tests measurements with identical instrumentation and optical sensor configurations at the same velocity and altitude conditions. Such a comparison would be of particular interest at velocities above 11,000 ft/sec when flowfield chemistry is important in both tunnel and flight tests.

This report first discusses the requirements for proper ground test simulation. The design and fabrication of the LENS facility during this preliminary study are included next. Following sections discuss the performance and instrumentation of the LENS facility, first flowfield and then aero-optic instrumentation. Sections 6 through 8 include analyses of facility performance, validation experiments, structural loading, and flight tests. This is a preliminary program and is expected to be followed by additional programs culminating in the experimental measurement of aero-optical characteristics of hypersonic configurations.

Section 2
GROUND TEST SIMULATION

2.1 Introduction

The construction of a ground-based facility to duplicate the flowfield environment around a hypersonic endo-atmospheric interceptor to evaluate optical seeker performance will provide a key element in the successful design of a ground-based ballistic-missile interception system. Because of the large heating loads to which such vehicles are subjected, an active coolant system (usually a gaseous film) must be used to prevent the degradation of the seeker window. However, the optical distortions to which light is subjected when it passes through such a cooled window can seriously compromise the performance of the seeker system. In this section of the report, we review the characteristics of a ground-based facility necessary to perform meaningful seeker head evaluation.

2.2 Simulation of Flows Around Endo-Interceptors

In the conduct of ground test studies simulating or duplicating the environment around an endo-interceptor, it is important to understand the parameters of key importance in the distortion of the electromagnetic waves as they are propagated through the shock layer and the shear layer of the interceptor. While the aero-thermal loads on an endo-interceptor may be simulated in a number of ground-based facilities, to duplicate the flowfield structure and radiation to obtain accurate measurements of aero-optic distortion requires a facility of significantly greater energy performance.

The key phenomena and major parameters that must be simulated over an interceptor vehicle are illustrated in Figure 2-1. On the relatively small seeker-head configurations, a key parameter that must be defined and controlled is the position of boundary layer transition. Not only is the heat transfer distribution strongly influenced by boundary layer transition, but also the mean flowfield structure, and the distributions of mean and fluctuating densities across the boundary layer are strongly dependent on the position of transition. Transition itself is dependent on the coolant blowing rate, on the Mach number and Reynolds number of the freestream, and on the seeker-head configuration. The flowfield structure over the forebody and, subsequently, over the windows is controlled principally by the velocity of the external flow and the coolant injection parameters for the forebody and windows. To correctly simulate coolant/flowfield mixing from the fluid dynamic viewpoint, it is important to duplicate the local convective Mach number of the injectant and the local Reynolds number of the flow. In simulating the major aero-optic characteristics of the flowfield, it is important that the density and the temperature characteristics of the flowfield be replicated. To achieve this, it is necessary that both the Reynolds number and the total enthalpy of the freestream be duplicated, together with the detailed injection characteristics of the forebody and windows. It is of key importance to duplicate the flowfield velocity to obtain the correct density profiles through the shock layer—and, hence, the correct aero-optic distortion—as illustrated in Figure 2-2. In Figure 2-2, we have shown typical density and velocity distributions through the shock layer generated in flight, in high-enthalpy shock tunnels, and in state-of-the-art high Mach number blowdown facilities. Basically, the magnitude of the density difference across the viscous

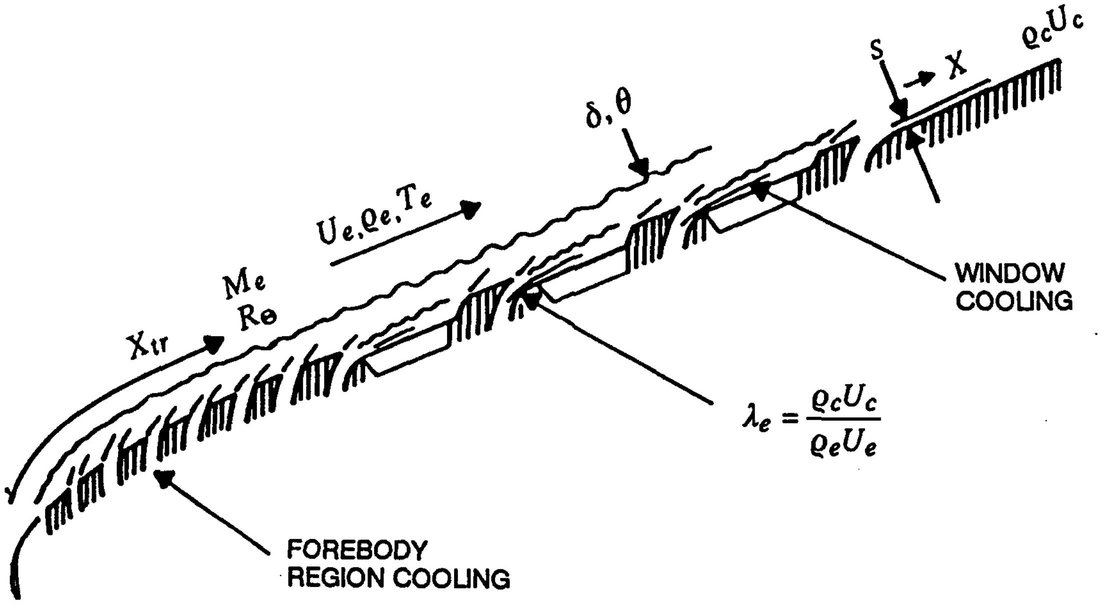

Figure 2-1 MAJOR PARAMETERS CONTROLLING APERTURE PERFORMANCE ASSOCIATED WITH FLOWFIELD PROPERTIES AND WINDOW CONFIGURATION

shock layer that controls the aero-optic distortion is directly related to the velocity. The convective Mach number across the shear layer, which is a key parameter in controlling the rate of mixing between the shock layer and the coolant flow, is also strongly influenced by velocity. Figure 2-2 also shows the magnitude of the optical distortion anticipated over a film-cooled seeker window in ground test facilities and flight. Here, we see that conventional low-velocity hypersonic facilities are capable of obtaining only 1/10 of the velocity and temperature ratios expected in flight.

Under a number of circumstances, it is also important to duplicate in the ground test facility the surface temperature that would be achieved in flight. In a shock tunnel, this can be achieved by pre-heating the seeker head by radiative or internal heating. Here, radiative heating employing laser or graphite heaters would appear to be the most attractive method.

While it is important to generate freestream velocity to duplicate the density profiles through the shock layer, it is also essential to obtain the correct total enthalpy of the flow (which is directly dependent on vehicle velocity) to obtain the correct flowfield chemistry and radiation. Figure 2-3 shows the important effects of freestream velocity on real-gas effects. For velocities below 5,000 ft/sec (1500 m/sec), which corresponds to the maximum velocity attainable by most conventional hypersonic blowdown facilities, such as NSWC Tunnel 9 and AEDC Tunnel C, the gas may be regarded as basically ideal. For velocities between 5,000 and 10,000 ft/sec (1500 and 3000 m/sec), progressively more energy is being absorbed by molecular vibration of the diatomic molecules of oxygen. Oxygen dissociation begins to occur in the shock-layer stagnation region at velocities around 10,000 ft/sec (3000 m/sec). The shuttle reactions involving the formation of nitric oxide (NO) also become a significant factor in the energy balance at these flow velocities. For velocities close to 14,000 ft/sec (4300 m/sec), the oxygen is almost completely dissociated, and significant electronic plasma effects begin to occur. At this velocity, nitrogen dissociation begins to occur; this process continues and is complete at velocities just under 20,000 ft/sec (6100 m/sec), where both the nitrogen and oxygen molecules in the shock layer become fully dissociated. At these and greater velocities, a shock layer is dominated by plasma effects.

Figure 2-4 shows that, while most conventional hypersonic facilities are unable to generate the velocities to provide simulation of gas effects, the shock tunnel will provide the flows of up to 14,000 ft/sec (4300 m/sec). Although it is possible to generate velocities above 14,000 ft/sec (4300 m/sec) in conventional and piston driven shock tunnels, extremely high pressures are required in the reservoir to prevent non-equilibrium effects associated with dissociation in the freestream at the exit of the nozzle. Whatever the nature of the tunnel, whether it be a conventional shock tunnel or a conventional blowdown tunnel, the reservoir requirements to simulate velocities and densities are exactly the same.

Figures 2-5, 2-6, and 2-7 show the typical performance of conventional blowdown and shock tunnel hypersonic facilities in terms of the major parameters of importance for interceptor performance—total temperature, Mach number, and Reynolds number. In terms of the Mach number and Reynolds number conditions that are important for transition simulation and aero-thermal heating, while there are a number of flight segments that cannot be duplicated in ground test

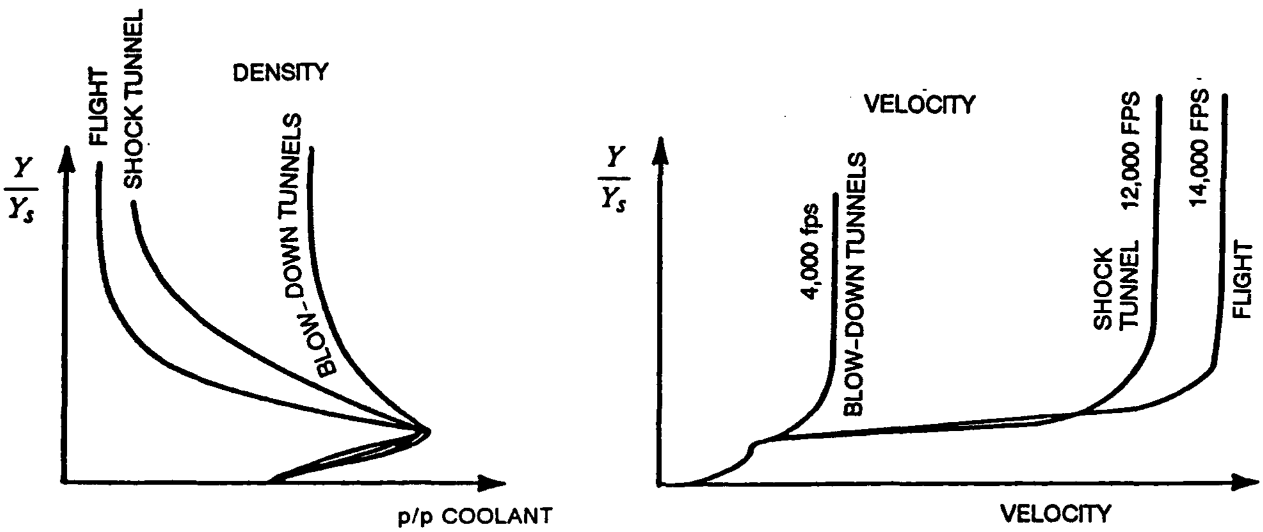

	Flight	AEDC	NSWC	Shock Tunnel
$\Delta_{p/p_{STP}}$	4	0.4	0.4	3.7
M_c	4	1	1	3.7
$\sigma_\lambda = 3.5$	1	0.1	0.1	0.87
U_∞ (ft/sec)	14,000	4,000	4,000	13,000
$T_o°(R)$	14,000°	1,900°	2,000°	13,000°

Figure 2-2 IMPORTANCE OF VELOCITY SIMULATION IN GROUND TEST FACILITIES TO ESTABLISH THE CORRECT SHOCK LAYER DENSITY PROFILES OVER INTERCEPTOR

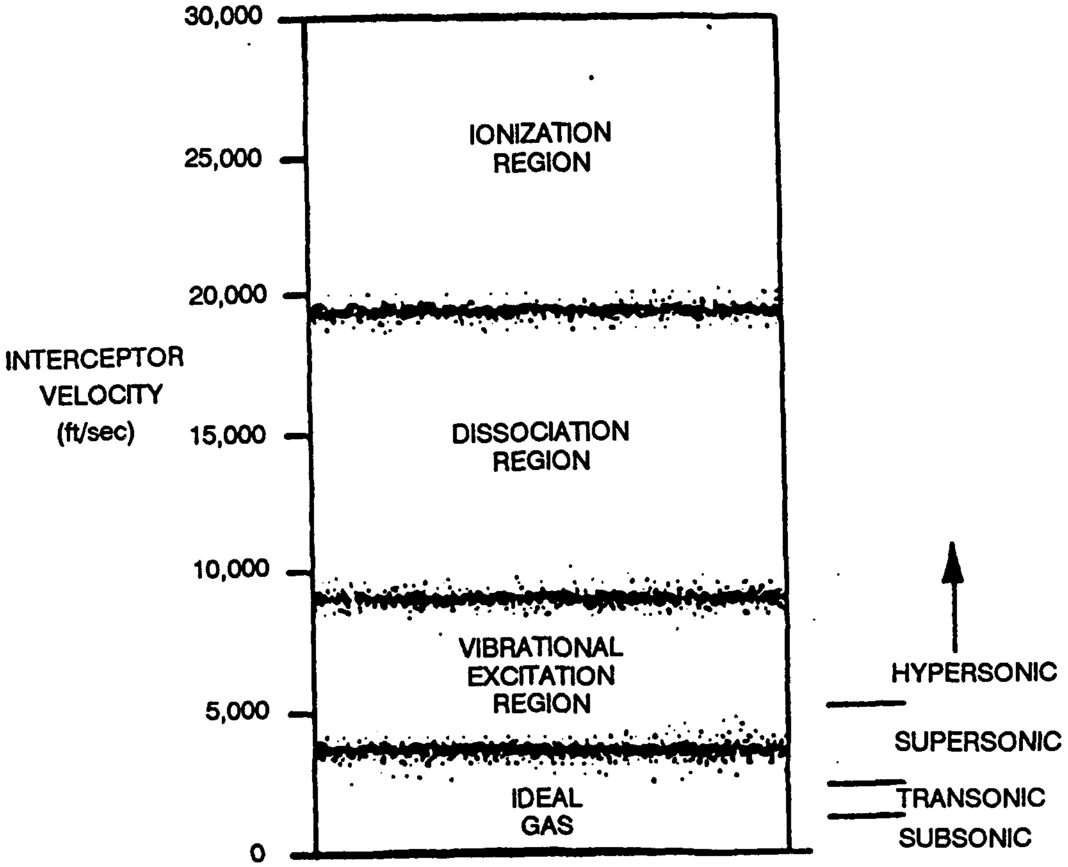

Figure 2-3 REAL GAS EFFECTS IN INTERCEPTOR SHOCK LAYER AS A FUNCTION OF VEHICLE VELOCITY

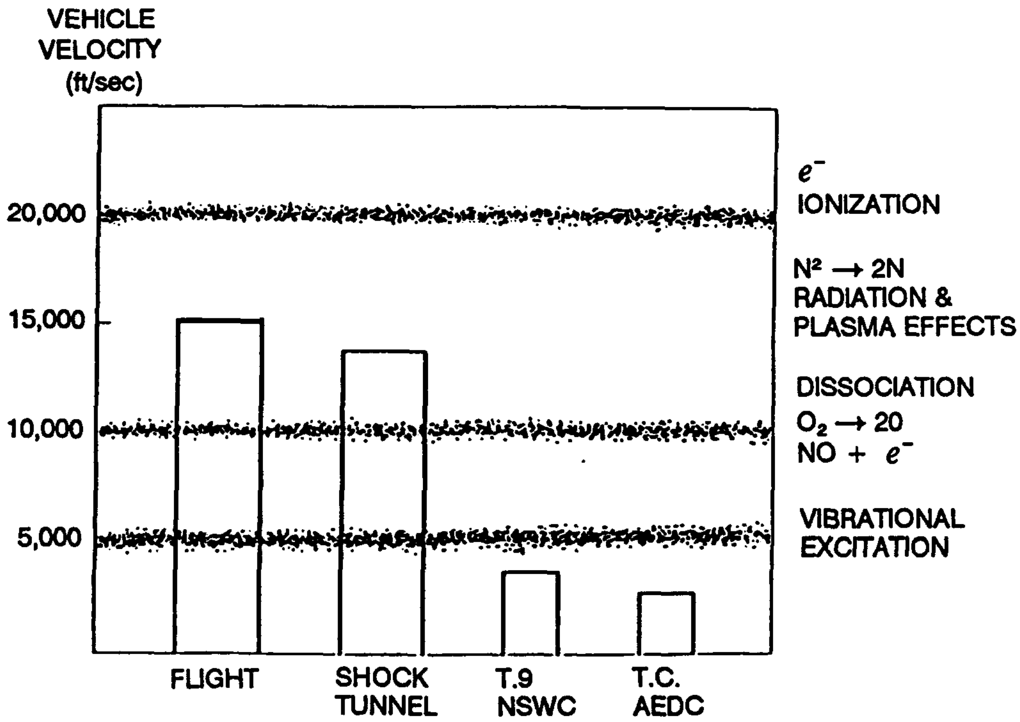

Figure 2-4 SIMULATION OF REAL GAS EFFECTS AND FLOW CHEMISTRY IN GROUND TEST FACILITIES

facilities, the key homing portion of the flight can be duplicated. However, to obtain the correct density and temperature distributions in the shock layer, the key simulation parameters are total temperature and Reynolds number. To obtain the correct Mach number, Reynolds number, and total temperature simulation for interceptor detection and homing, the only facilities capable of generating the clean flow conditions required are shock tunnels.

Figure 2-8 shows the reservoir pressure and temperature conditions required. It can be seen that, in order to generate conditions to duplicate an interceptor flying at 14,000 ft/sec (4300 m/sec) at 100,000 ft (30 km), one must generate stagnation temperatures of the order of 14,000°R (8000K) at pressure levels of the order of 30,000 psi (200 MPa). Under these conditions, Reynolds numbers of the order of 10^6/ft would be generated. It is possible to generate non-dissociated high-velocity flows without the requirement for extremely large stagnation pressures if the shock tunnel is operated in a non-reflective mode. However, the test times generated in such facilities are so short (on the order of 500 microseconds) that meaningful experimental programs with models involving surface injection are highly questionable.

2.3 Characteristics of the Large Energy National Shock Tunnel (LENS)

Design Features of LENS

The LENS is being constructed specifically for the purpose of generating hypervelocity flows to duplicate the flow over small endo-interceptors traveling as speeds up to 14,000 ft/sec (4300 m/sec). The test conditions and major freestream parameters for the LENS facility can be computed with the information presented in Figure 2-9. The operating range with the existing nozzle is Mach 11 to 18 for stagnation temperatures up to 14,000°R (8000K). The test conditions in terms of Mach number and Reynolds number are shown in Figure 2-9. The velocity/altitude performance of the LENS facility is shown in Figure 2-10. LENS is a large, high-pressure but conventional, shock tunnel that is based on an upgrade of the existing 48" shock tunnel and utilizes a number of features that have been developed over the past 25 years of shock tunnel development and testing at Calspan. In the design of this facility, particular care was taken in developing a contamination-free hypersonic flow and in isolating the loads associated with operation of the tunnel from the model support system and the aero-optic instrumentation. The design is based on a 8-inch-diameter shock tube, driven by a 11-inch-diameter driver. The tunnel layout of the LENS configuration is shown in Figure 2-11. The driver section of the tunnel heated to 750°F, and, because it is ordinarily operated with hydrogen, it has a stainless steel liner to prevent hydrogen embrittlement. The driver and heater section of the tunnel are mounted on a carriage, which recoils with the tunnel as it is fired. The firing of the tunnel is controlled by a double-diaphragm rig via which the pressure in the intermediate chamber is vented to fire the tunnel. Because flowfield chemistry and cleanliness are of prime importance in this facility, all components that come in contact with the test gas are constructed from stainless steel. A centerbody apparatus, which utilizes a fast-acting plug valve to close the nozzle throat, is used to terminate the flow once the useful slug of air has been exhausted from the end of the shock tube. A Mach 11 to 18 contoured fiberglass nozzle is used in this tunnel. However, to handle the large loads generated by the recoil of the driver, a metal corset, which surrounds the fiberglass nozzle is used to prevent overloading the

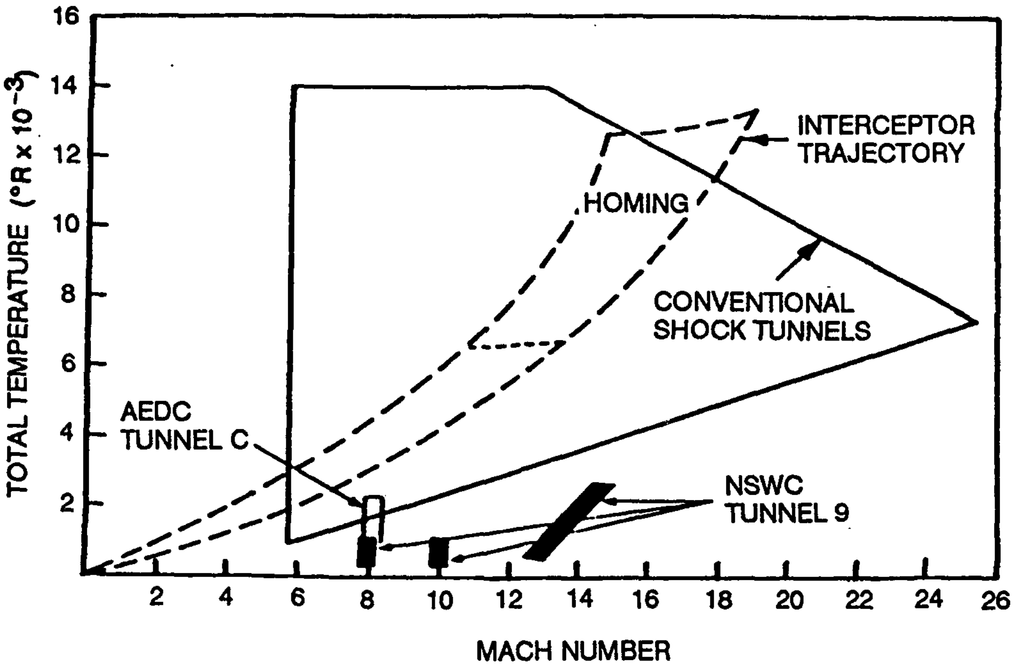

Figure 2-5 FREESTREAM PARAMETERS IN MAJOR HYPERSONIC GROUND TEST FACILITIES (TOTAL TEMPERATURE VS MACH NUMBER)

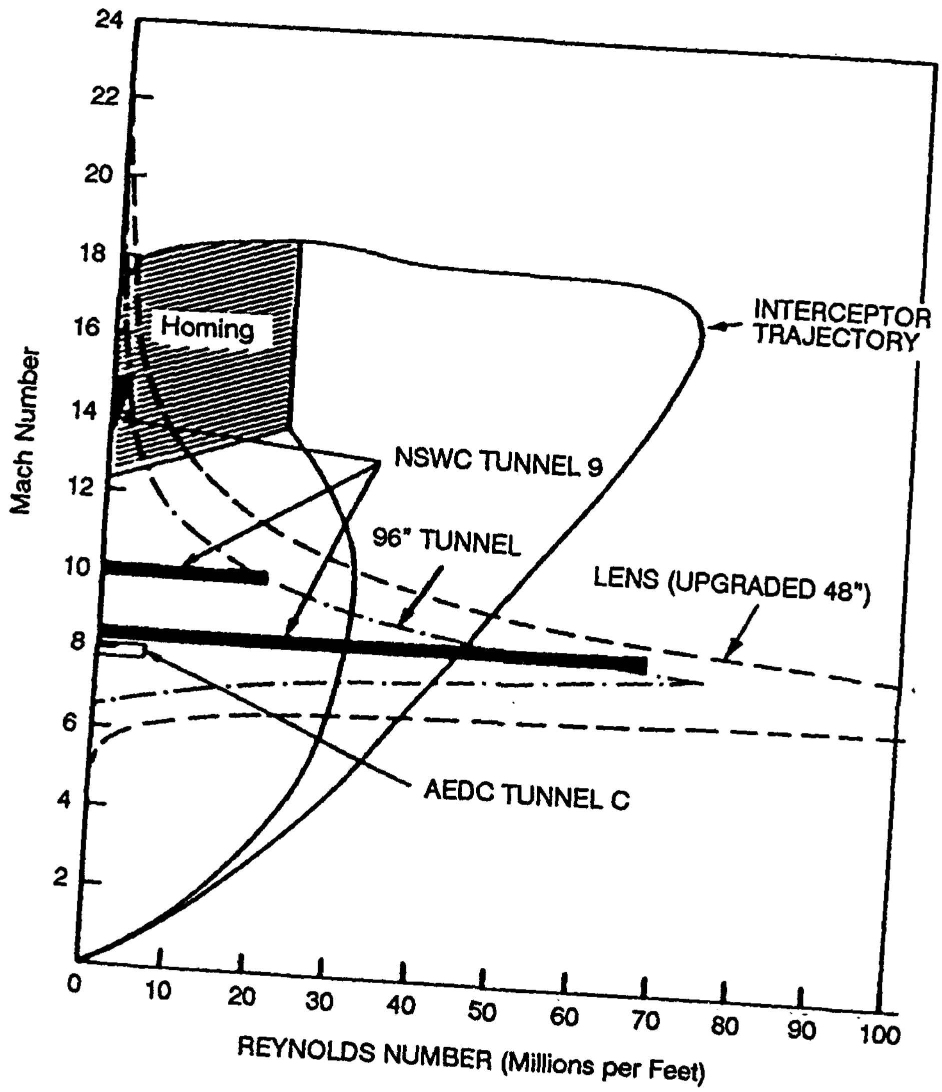

Figure 2-6 MAJOR FREESTREAM PARAMETERS DEVELOPED IN MAJOR GROUND TEST FACILITIES (MACH NUMBER VS REYNOLDS NUMBER)

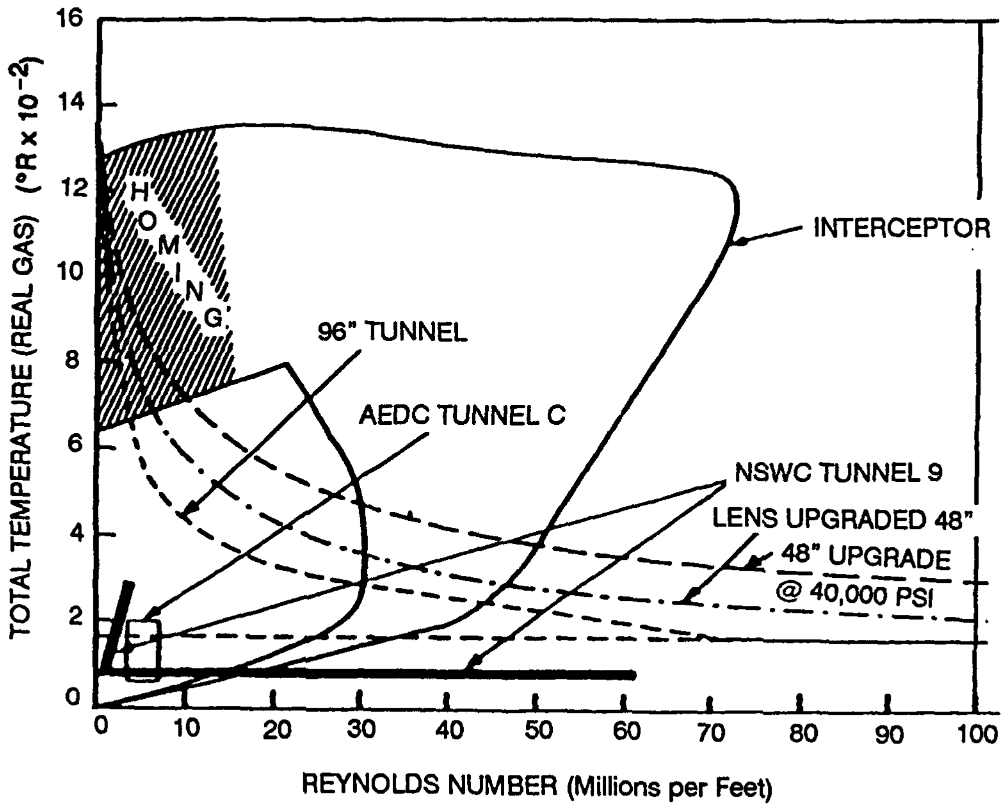

Figure 2-7 MAJOR FREESTREAM PARAMETERS DEVELOPED IN MAJOR GROUND TEST FACILITIES (TOTAL TEMPERATURE VS REYNOLDS NUMBER)

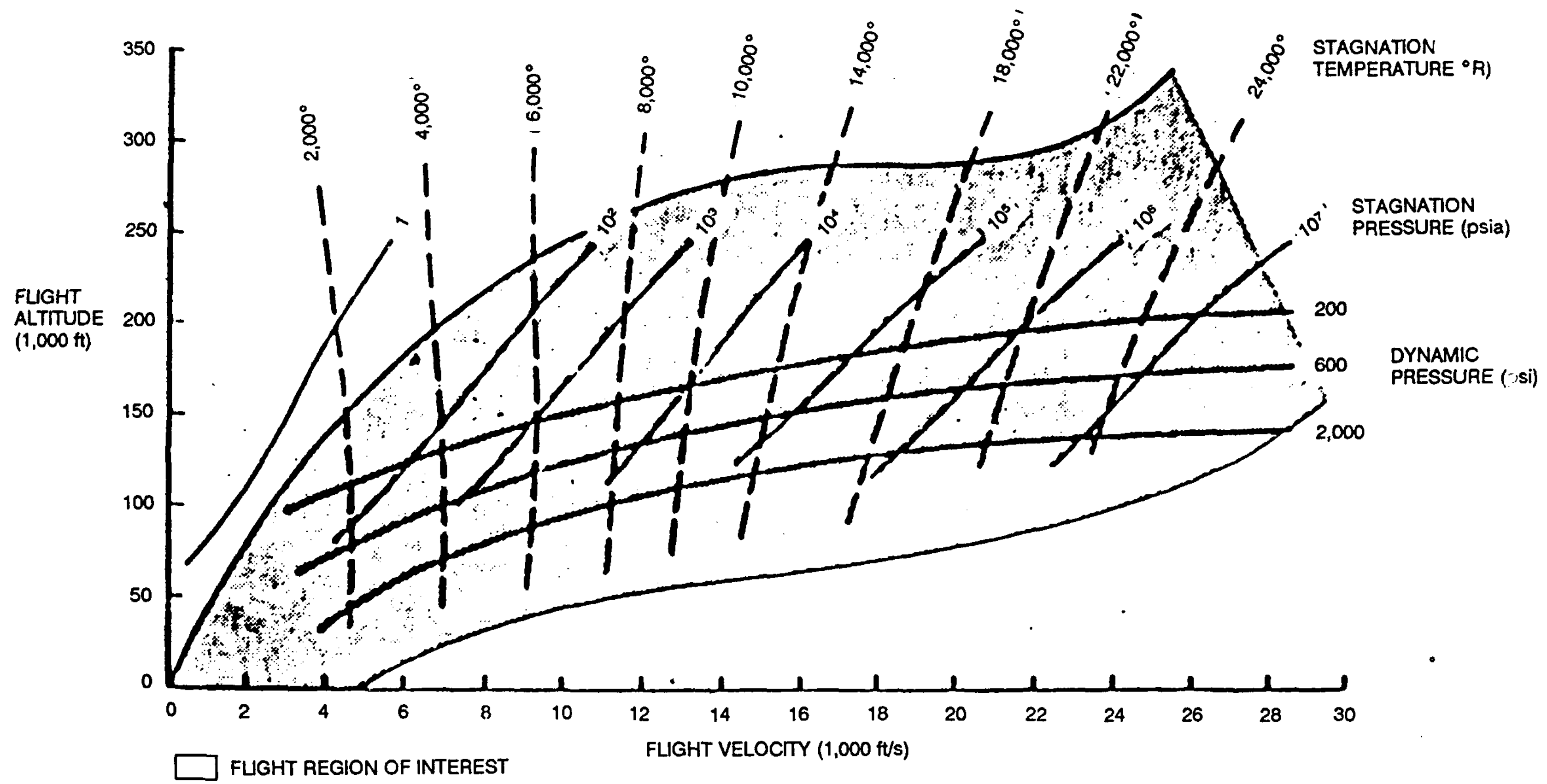

Figure 2-8 STAGNATION TEMPERATURE AND PRESSURE REQUIREMENTS FOR SIMULATING HYPERSONIC FLIGHT

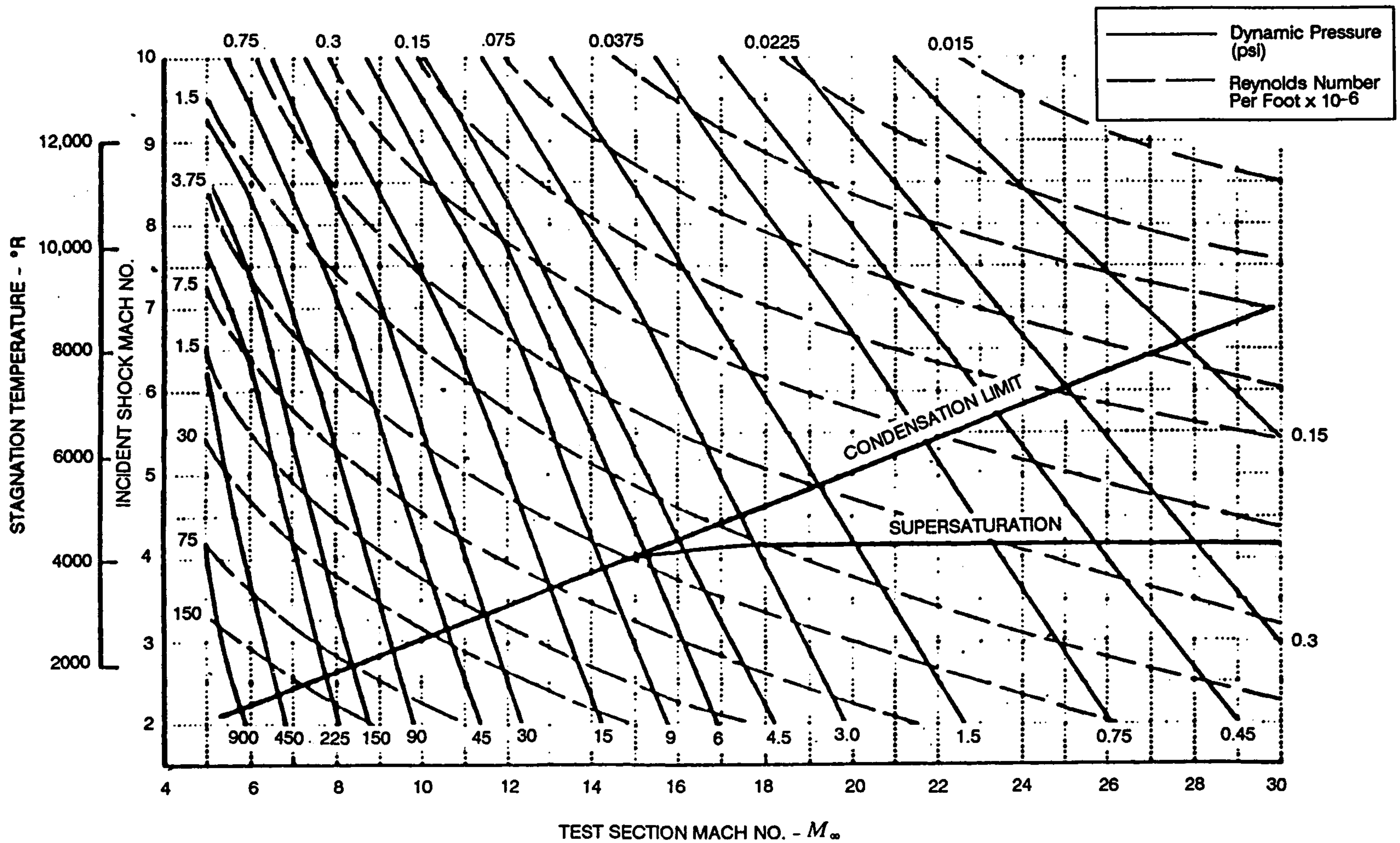

Figure 2-9 OPERATING CHARACTERISTICS - LENS HYPERSONIC SHOCK TUNNEL (30,000 PSIA NOZZLE SUPPLY PRESSURE), CHEMICAL EQUILIBRIUM

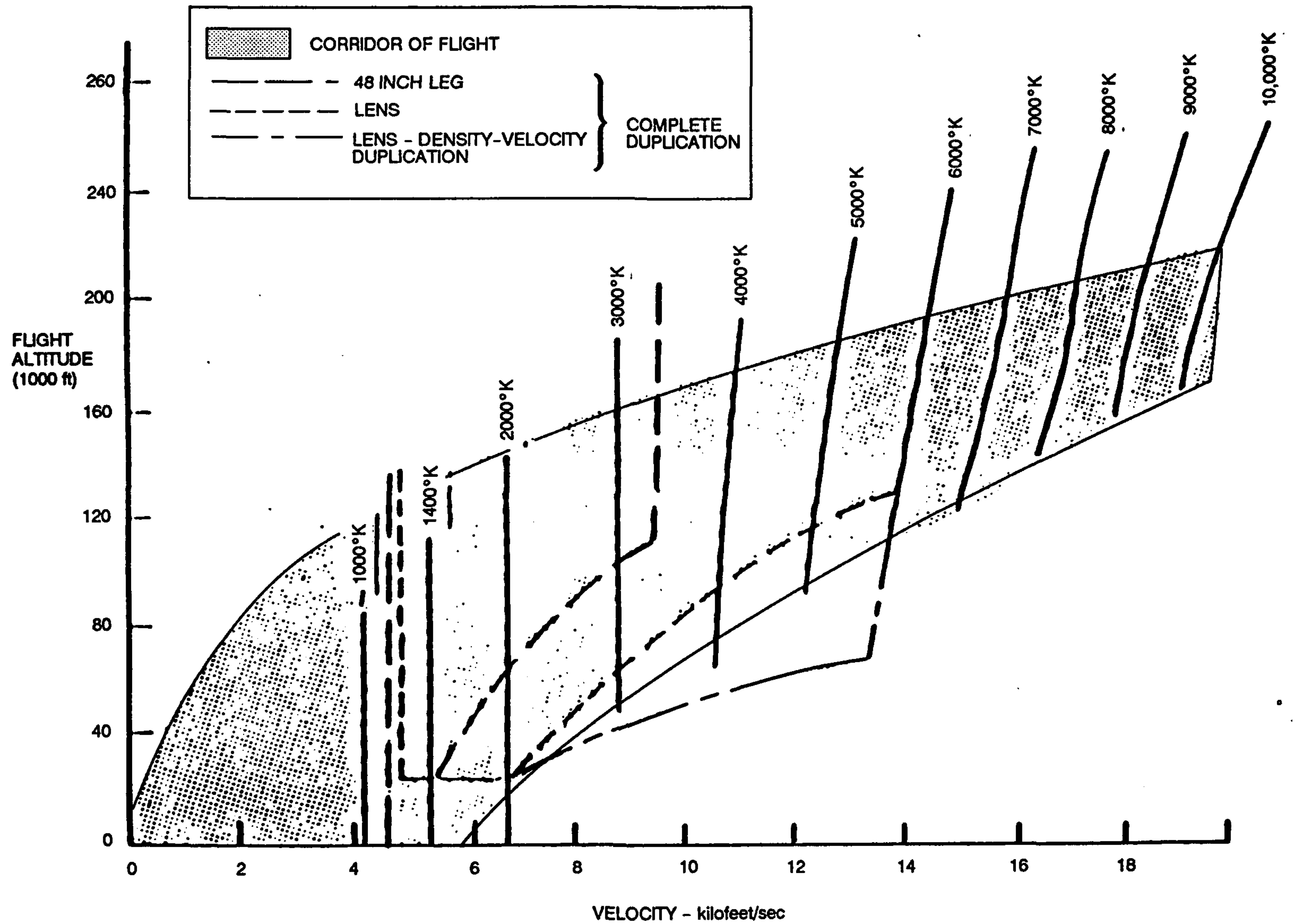

Figure 2-10 VELOCITY/ALTITUDE PERFORMANCE OF LENS FACILITY FOR GROUND TEST DUPLICATION

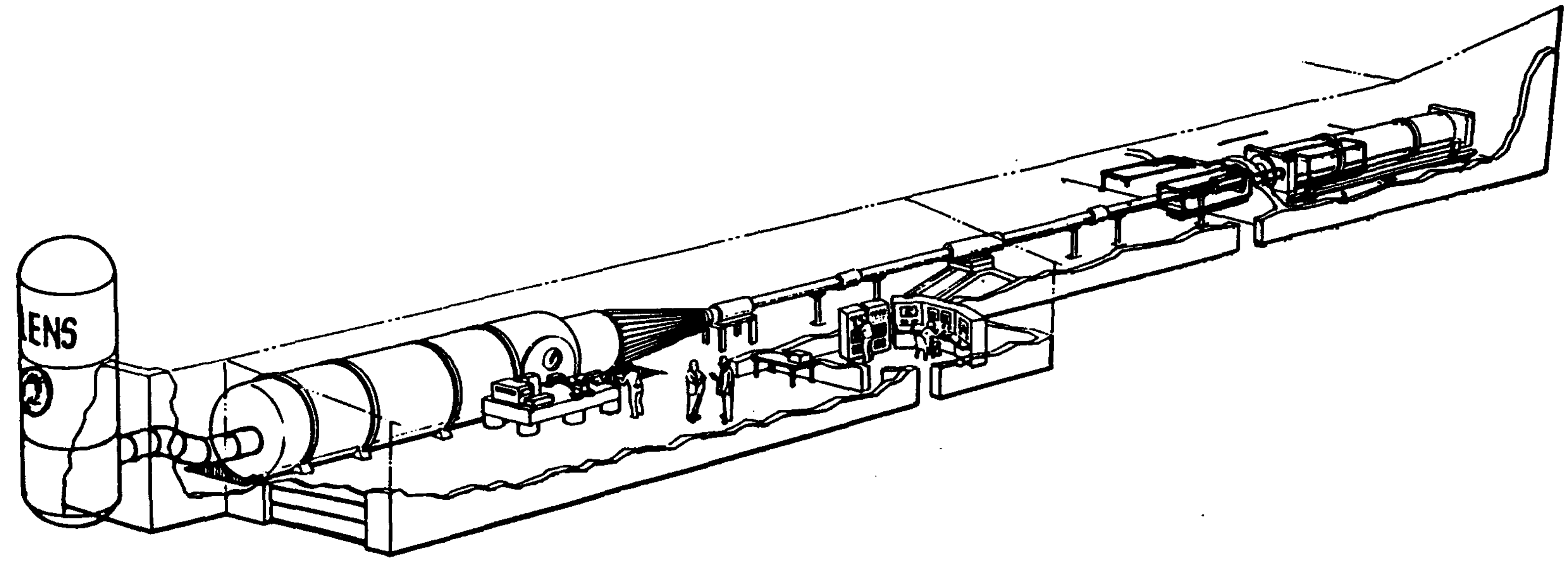

Figure 2-11 INSTALLATION LAYOUT OF LARGE ENERGY NATIONAL SHOCK TUNNEL (LENS)

fiberglass. Because of the large volume of gas contained in the high-pressure driver, a large test section volume is required to prevent the pressure level in the test section from exceeding that necessary to fracture the schlieren windows. If the centerbody valve fails to operate, then additional volume provided by a ballast tank, which is coupled to the test section through a large-volume pipe isolated through a diaphragm, is used to prevent overpressurization of the test section.

Test Conditions for Seeker Evaluation

The large dimensions of the driver and driven tubes allow us test times up to 18 milliseconds for operation at low incident Mach numbers, with contamination-free test times of the order of 3 to 4 milliseconds at 14,000 ft/sec (4300 m/sec). The test conditions that have been selected for the validation studies, the studies where we will compare measurements in different facilities with flight tests, are shown in Figure 2-12. Freestream and model measurements have been made to compare the performance of NSWC Tunnel 9 and the LENS facility to establish the equivalence of the air flows. Measurements at an altitude equivalent of 75,000 ft (23 km) will then be made at a velocity of 10,000 ft/sec (3000 m/sec) for direct comparison with flight tests. These studies will be conducted with both air and nitrogen to examine real-gas effects. At 120,000 ft (37 km), measurements will be made at velocities of both 10,000 ft/sec (3000 m/sec) and 14,000 ft/sec (4300 m/sec). Again, these studies for direct comparison with flight tests will be conducted with nitrogen and air environments to examine real-gas effects. These test conditions are replotted in Figure 2-13, highlighting the important real-gas effects. LENS test conditions in terms of stagnation and freestream test parameters are presented in Figure 2-14. Measurements at the higher velocities will enable examination of the important high-enthalpy and real-gas effects on the flowfield structure and radiation associated with a hypervelocity endo-interceptor vehicle.

2.4 Aero-Optical Model Support and Optical Bench System

Design of the support system for the aero-optical studies is one of the most important aspects of the construction of the aero-optic evaluation facility. The requirement that neither the model nor the optical bench move more than 10 microradians during the run time places a stringent demand on this design. The basic sting system (shown in Figure 2-15) is not attached to the test section of the tunnel and, thus, is not subjected to the large acceleration loads associated with the tunnel recoil. The lower half of the support system is mounted on two massive rods that pass through the test section via four sets of rolling seals and are attached to the concrete floor beneath the test section. The massive (40,000-lb) (18,000 kg) upper half of the support system is suspended on four rubber blocks such that this system has a natural frequency of under 20 hertz and, thus, will totally isolate the model attached to it from recoil loads for the 4 to 18-millisecond run time of the tunnel. Fairings (see Figure 2-16), which are attached to the test section of the tunnel, are employed to prevent the model support structure from being exposed to the airloads, leaving only the model and the source plate exposed in the airflow. The optical bench system (see Figure 2-17), which contains the optical components used for holographic and infrared evaluations of seeker-head performance, is mounted inside the model. The entire optical bench system is at atmospheric pressure and temperature conditions.

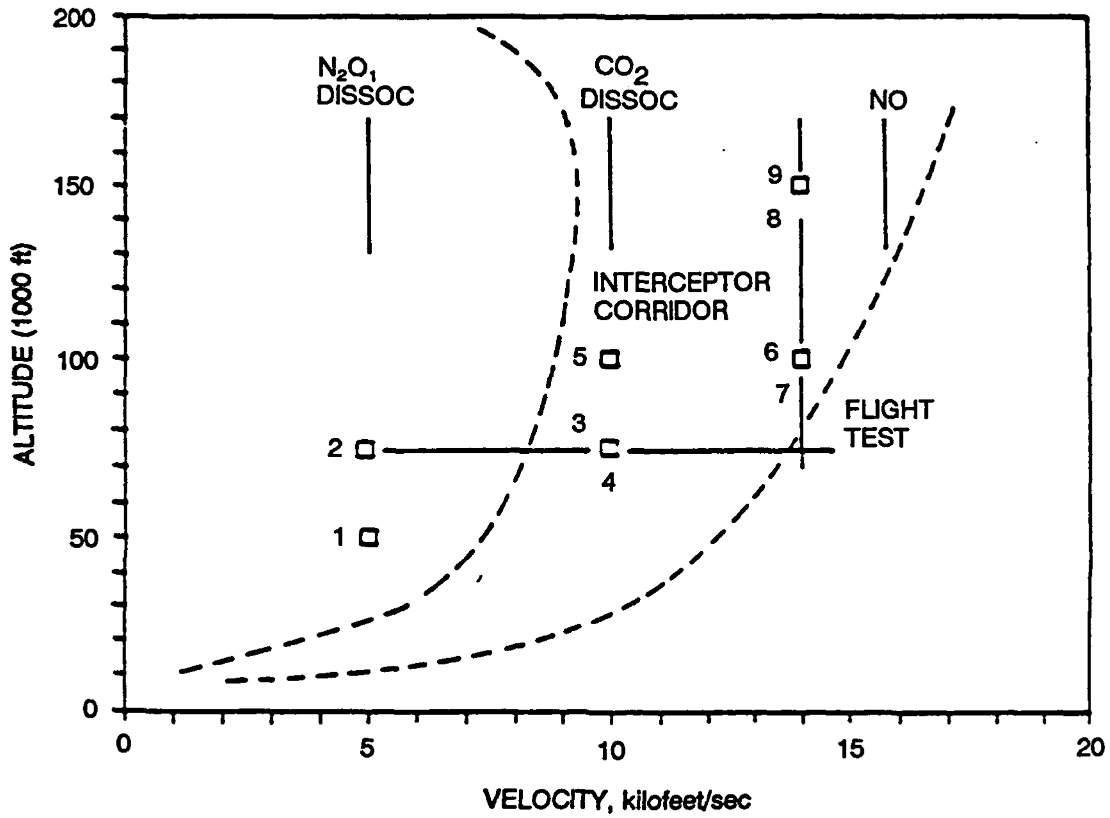

Figure 2-12 SAMPLE TEST CONDITIONS FOR AERO-OPTIC SENSOR GROUND TEST STUDIES

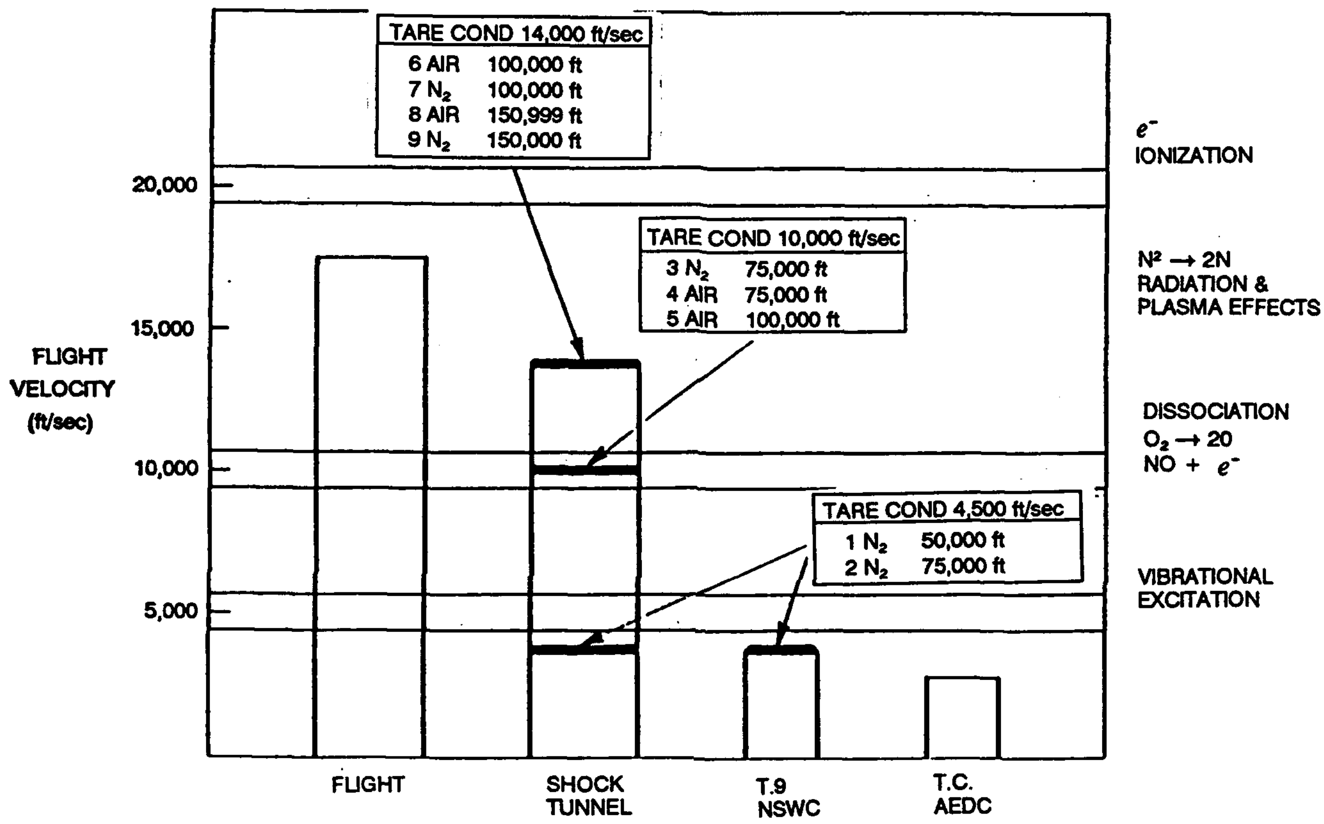

Figure 2-13 SIMULATION OF REAL GAS AND FLOW CHEMISTRY EFFECTS IN AERO-OPTICAL STUDIES IN GROUND TEST FACILITIES

	Shock Tunnel Operating Conditions			Shock Tunnel Test Conditions at Exit-Plane of D-Nozzle							
Driver	T_o (°K)	P_o (atm.)	d (in.)	U_∞ (ft/sec)	M_∞	ρ_∞ (Slugs/ft³)	Altitude (kft)	T_∞ (°R)	P_∞ (psia)	Dynamic Press (psia)	Re/ft
H_2	6200	1200	0.66	14020	10.8 Flt = 13.4	6.37×10^{-6}	136	700	5.4×10^{-2}	4.34	1.9×10^5
H_2	600	1500	0.964	13560	9.4 Flt = 13.5	1.77×10^{-5}	113	870	0.185	11.3	4.4×10^5
He	3500	1500	1.6	9340	9.3 Flt = 9.55	9.0×10^{-5}	79	420	0.045	27.3	2.7×10^6
He	1560	1500	1.6	5856	11	1.83×10^{-4}	40	116	0.25	22	11.0×10^6

Figure 2-14 TYPICAL TEST CONDITIONS FOR VALIDATION STUDIES TO BE CONDUCTED IN THE CALSPAN 96" SHOCK TUNNEL AND LENS GROUND TEST FACILITIES

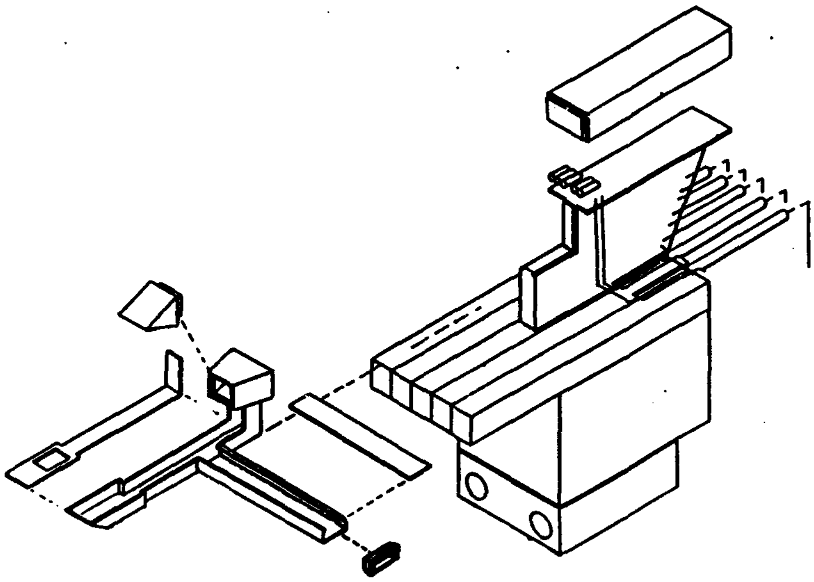

Figure 2-15 MODEL SUPPORT SYSTEM FOR 96" SHOCK TUNNEL AND LENS FACILITY STUDIES

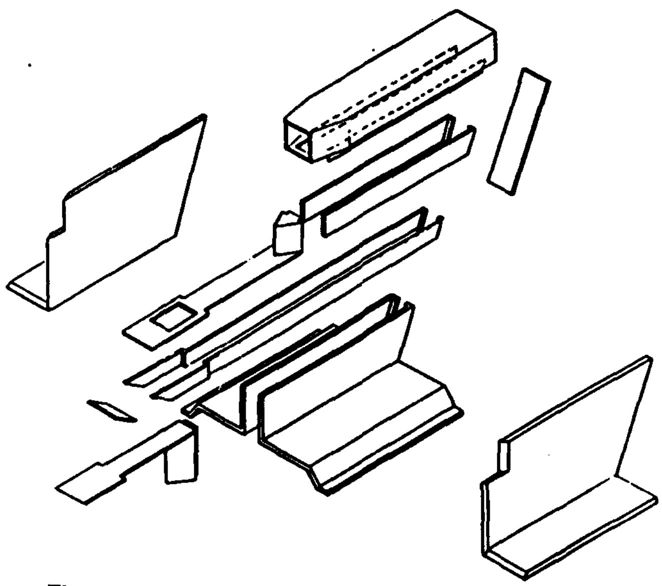

Figure 2-16 MODEL AND SUPPORT FAIRINGS

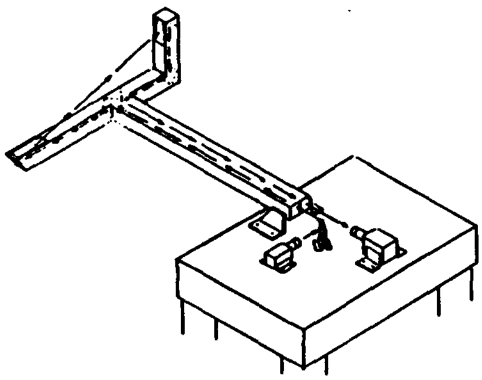

Figure 2-17 SCHEMATIC OF OPTICAL TUBE

Section 3
DESIGN AND FABRICATION OF LENS FACILITY

Prior to the beginning of this program, the basic design and even partial construction of the LENS facility had been completed. However, it was determined that redesign was required in two areas. Initially it was planned to make a separate driver for using helium or hydrogen as driver gas. By redesigning the driver including the use of a stainless steel liner, a single driver could be used with both helium and hydrogen and nearly the same test conditions could be produced. This would save a considerable amount of expense.

In addition, the facility was redesigned to produce the cleanest (lowest particle contamination and chemical impurities) test gas possible. This was necessitated by the requirement of a contaminant-free optical path for measurements of aero-optical seekerhead performance. This redesign included stainless steel driven tubes and joints between driven tubes that would not open up during a test run. The stainless steel tubes will preclude the formation of minute rust particles on interior tube walls which could contaminate the flow. It was believed that the joints in other shock tunnels could open slightly and capture and release contaminants on subsequent runs and therefore a new joint was designed with a metal-to-metal seal on the tube bore and clamping forces sufficient to prevent any separation. Significant efforts were devoted to the elimination of sources of chemical contamination, such as those which could be introduced by oils and lubricants.

In addition, detailed design drawings including revisions were made for a number of parts. The following items were designed and/or complete specification packages produced:

Test Section
Driver Tube Liner
Test Section Vacuum Pump
Hydrogen Gas Detection System
Control Console
Numerous Miscellaneous Parts for Control Console
Test Section Schlieren Windows
Centerbody Section
Double Diaphragm Section
Double Diaphragm and Centerbody Nut Carriages Stress Analysis
Driver Tube Heater
Driver Tube Carriage
Building Modifications
Model Support and Optical Bench System
Ballast Tank
A total of 33 drawings and 33 drawing revisions
were completed

In addition, fabrication of the following items was contracted and completed in this program:

Double Diaphragm Parts

Driver Tube Heater

Driver Tube Carriage

Forgings for Driven Tubes

Forgings for Centerbody Parts

Control Console Cabinets

Section 4
PERFORMANCE AND INSTRUMENTATION OF THE LENS FACILITY

4.1 INTRODUCTION

The shock tunnel is essentially a blow-down facility with a shock compression heater. A shock tunnel is constructed from three major components, the driver tube, the driven tube, and the nozzle and test section. The driven tube is connected to the driver through a fast-acting valve called a double-diaphragm rig, which is opened rapidly to start the tunnel. A fast-acting centerbody, connected between the driven tube and the nozzle, is used to terminate the flow through the test section to prevent model damage from diaphragm particles. The operation of the LENS is shown with the aid of a wave diagram in Figure 4-1. The tunnel is started by rupturing the double diaphragm, which permits high-pressure gas in the driver section to expand into the driven section and, in so doing, to generate a normal shock that propagates through the lower pressure air. A region of high-temperature, high-pressure air is produced between this normal-shock front and the gas interface (often referred to as the contact surface) between the driver and driven gas. When the primary or incident shock strikes the end of the driven section, it is reflected, leaving a region of almost stationary, high-pressure, heated air. This air is then expanded through a nozzle to the desired freestream conditions in the test section.

The duration of the flow in the test section is controlled by the interactions between the reflected shock, the interface, and the leading expansion wave generated by the non-stationary expansion process occurring in the driver section. We normally control the initial conditions of the gases in the driver and driven sections so that the gas interface becomes transparent to the reflected shock interaction. This is known as operating under "tailored-interface" conditions. Under these conditions, the test time is controlled by the time taken for the driver/driven interface to reach the throat, or the leading expansion wave to deplete the reservoir of pressure behind the reflected shock; the flow duration is said to be either

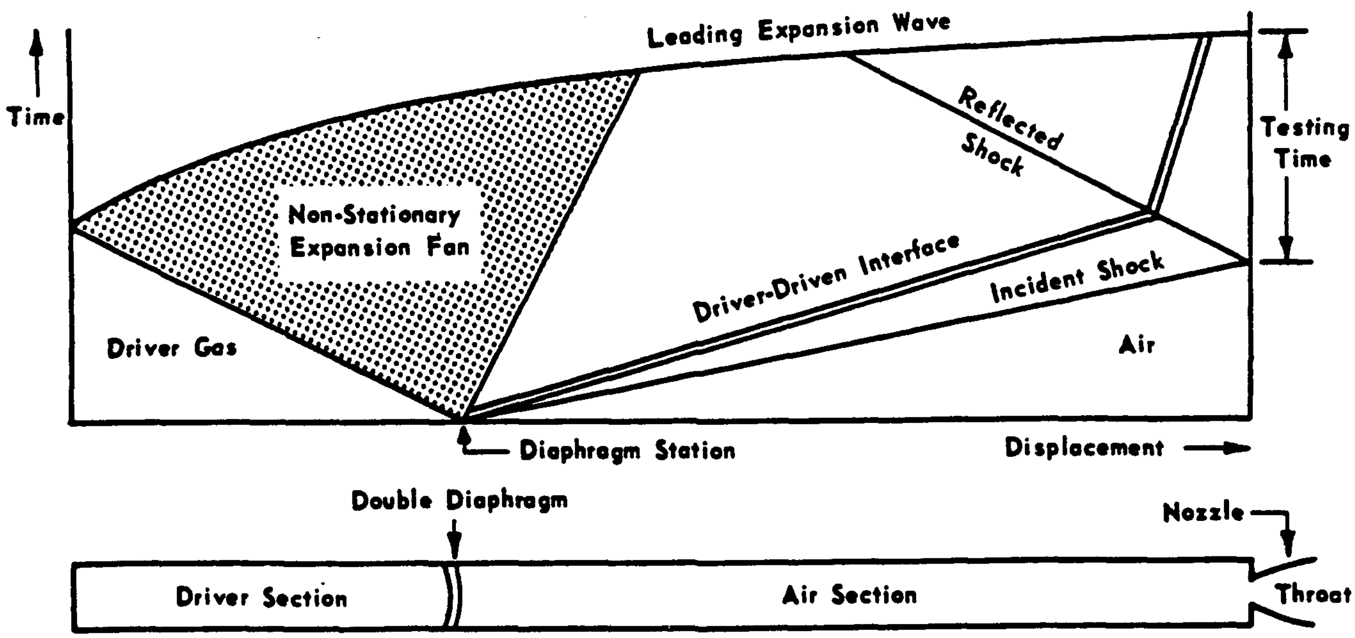

Figure 4-1 Wave Diagram for Tailored-Interface Shock Tube

Figure 4-1 WAVE DIAGRAM FOR TAILORED-INTERFACE SHOCK TUBE

driver–gas–limited or expansion–limited, respectively. Low M_i can be used to achieve up to 25 milliseconds of test time. When performed under these conditions at high pressures and high Reynolds numbers, the test running times are longer than for piston–driven tunnels with comparable stagnation temperatures, and the reservoir conditions and flow quality are superior to those of piston–driven tunnels. This results from the fact that the test gas is processed by a simple reflected shock, rather than by the multiple shocks of piston–driven tunnels. A further consequence is that the freestream conditions can be calculated far more accurately in a shock tunnel.

Note that when sensitive high–frequency instrumentation is used in the very severe heating conditions encountered in interaction regions in hypervelocity flow, running times longer than 20 milliseconds can result in damage to or destruction of the sensing element due to overheating.

4.2 OPERATING CHARACTERISTICS OF LENS FACILITY

Flight Corridor

The Hypersonic Shock Tunnel is capable of simultaneously duplicating velocity (i.e., enthalpy) and density over a wide range of hypersonic flight conditions. This range of conditions referenced to a typical continuous flight corridor is shown in Figure 4-2 for the Calspan 48-inch shock tunnel and the LENS facility. Reservoir temperatures associated with the velocity range of interest are also shown for reference purposes.

Shown in Figure 4-3 are the reservoir pressures and temperature which must be generated in gound test facilities to duplicate these flight conditions. To generate velocites of up to 14,000 ft/sec at an equivalent altitude of 75,000 requires equilibrium reservoir temperatures approaching 14,000°R and reservoir pressures close to 40,000 psia. While such conditions cannot be generated in facilites with long test times without freestream contamination, they can be produced in short-duration high-energy shock tunnels. It is important to note that for stagnation temperatures above 8,000°R, where real gas effects in air are

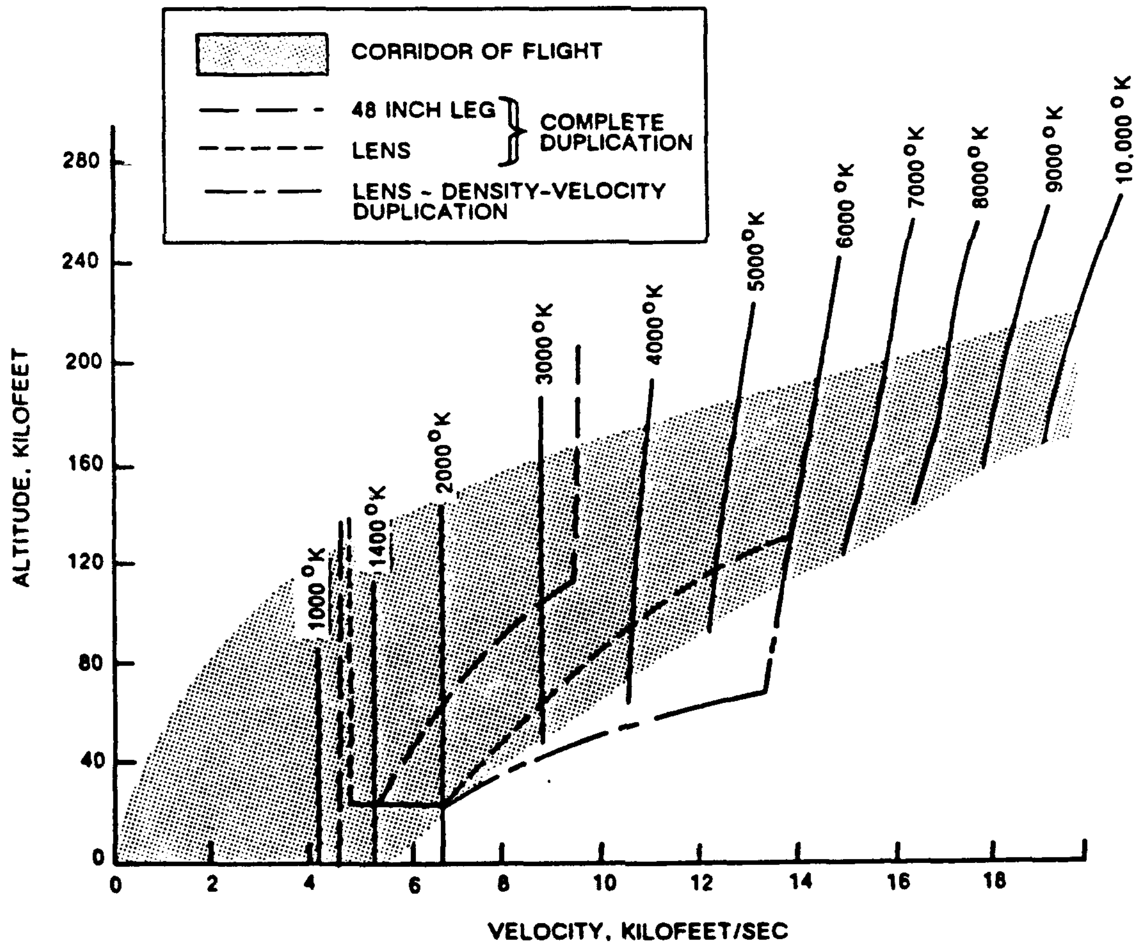

Figure 4-2 PERFORMANCE RANGE OF CALSPAN HYPERSONIC SHOCK TUNNEL

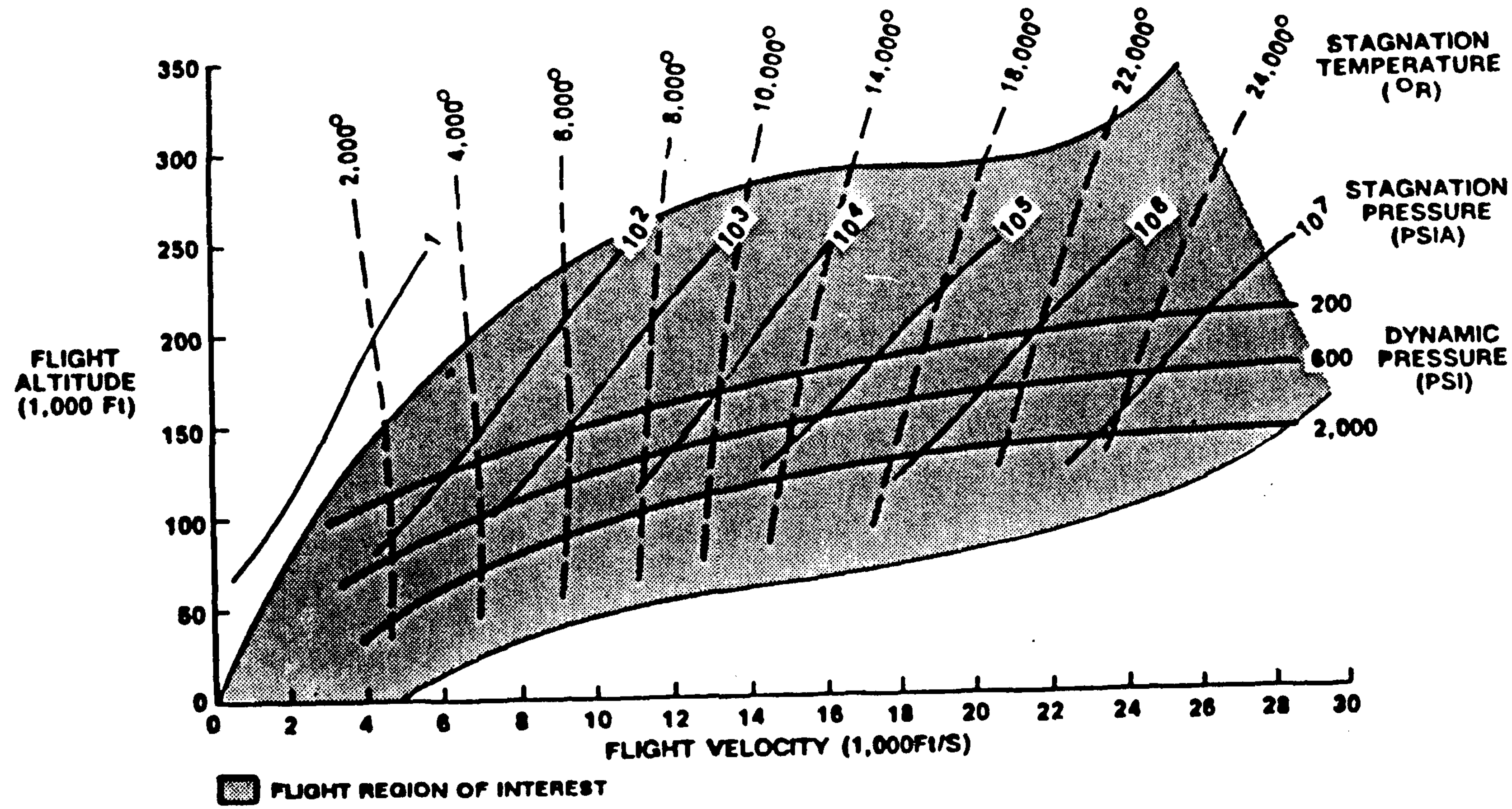

Figure 4-3 RESERVOIR CONDITIONS FOR GROUND TEST FLIGHT DUPLICATION

important, reservoir pressures greater than 20,000 psi are required to prevent significant levels of energy being frozen in non-equilibrium species in the gasdynamic expansion to hypersonic freestream conditions.

For certain flow phenomena (e.g., blunt bodies), the important parameters to be duplicated are the density-altitude and the flight velocity. These two parameters then insure duplication of freestream momentum ($\varrho_\infty U_\infty{}^2$)and energy ($1/2\varrho_\infty U_\infty{}^3$). Duplication of density-altitude and freestream velocity in the shock tunnel implies a higher freestream static temperature than in flight and, hence, a lower Mach number and unit Reynolds number. However, for inviscid flows that are Mach number independent, the lower flow Mach number imposes no restriction provided it is hypersonic (*i.e.*, $M_\infty \geq 5$).

M_i is the primary parameter governing the supply temperature (T_o) of the air behind the reflected shock. Figure 4-4 shows the relationship between M_i, T_o and the total enthalpy H_o. The effect of supply pressure (P_o) of the air behind the reflected shock on T_o is also shown for 100 and 1,000 atmospheres. In making tunnel performance calculations, it is convenient to use the Mach number (M_i) of the shock wave traveling down the shock tube as a reference parameter.

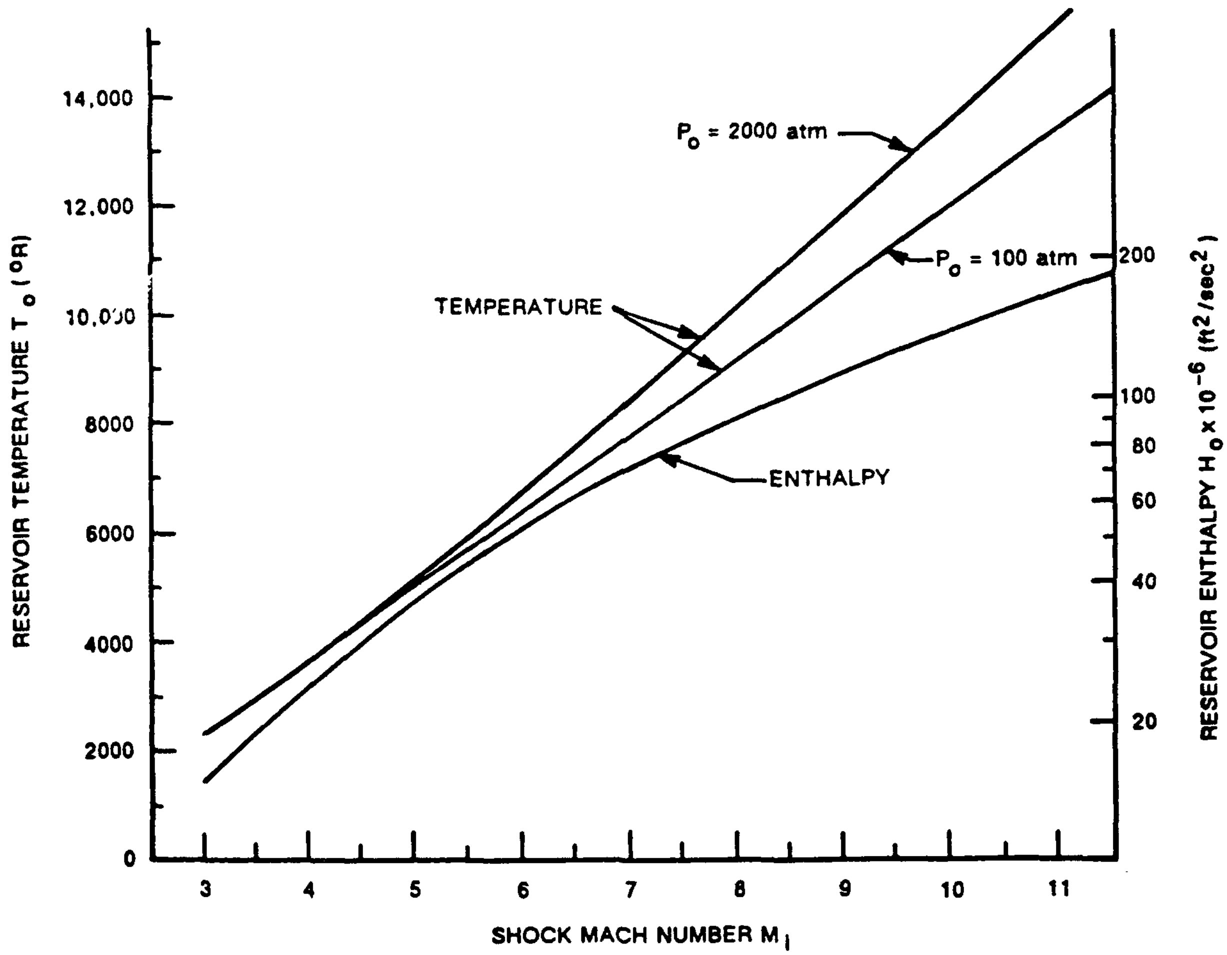

Figure 4-4 **RESERVOIR TEMPERATURE AND ENTHALPY AS A FUNCTION OF SHOCK MACH NUMBER**

Reynolds Number/Mach Number

The performance[4] of the tunnel covers Reynolds numbers (per foot) from 10^3 to 10^8 and Mach numbers from 5.5 to 24. This Reynolds number/Mach number simulation range is presented in Figure 4-5 The constant-altitude lines shown are those at which a vehicle would need to fly to achieve the combinations of Reynolds number per foot and Mach number shown.

It is useful to present the overall capability of the LENS as shown in Figure 4-6 for representative nozzle air supply pressure levels of 4,000 psia and 30,000 psia. The figure relates the test Mach number, the dynamic pressure, and the freestream Reynolds number to the incident shock Mach number. The highest Reynolds numbers are achieved with the weakest incident shocks (i.e., at the lowest stagnation temperatures). Also shown are the values of M_i required to duplicate flight enthalpies, as are those required to avoid air condensation. The minimum operating temperature is generally taken as that at which oxygen condenses in the test section. Although an increase in unit Reynolds number can be achieved by operating below the condensation limit (References 2 and 3), past experience has indicated that it is necessary to operate at freestream static temperatures approximately 10% above that at which oxygen condensation occurs to ensure valid data. This operational philosophy is reflected in Figure 6.

Test-Section Conditions

Test-section conditions are calculated under the assumption of isentropic flow from the reservoir to the test section. The test conditions can be computed assuming the test air to be in thermodynamic equilibrium or nonequilibrium.

A. Equilibrium

The calculations for test conditions assuming thermodynamic equilibrium in the test section include the vibrational heat capacity of the diatomic oxygen and nitrogen in air.

Test-section static temperature is obtained by equating the total enthalpy generated in the shock tube to the stagnation enthalpy in the test section. The test-section static temperature is then:

$$T\infty = \frac{h_o}{\overline{C}_{p\infty_{AVG}}}\left[1 + \frac{\gamma_\infty - 1}{2} \frac{C_{p\infty}}{\overline{C}_{p\infty_{AVG}}} M_\infty^2\right]^{-1}$$

where	T_∞	=	test-section static temperature
	h_o	=	total enthalpy
	$\overline{R}$	=	specific gas constant
	M_∞	=	test section Mach number
	$C_{p\infty_{AVG}}$	=	specific heat at constant pressure
	$\overline{C}_{p\infty_{AVG}}$	=	averaged specific heat at constant pressure
	γ_∞	=	$\dfrac{C_p\infty/\overline{R}}{(C_p\infty/\overline{R} - 1)}$

Now, $C_{p\infty}$ and $\overline{C}_{p\infty_{AVG}}$ are functions of T_∞; hence, the calculation of T_∞ for a given M_∞ involves an iterating computation.

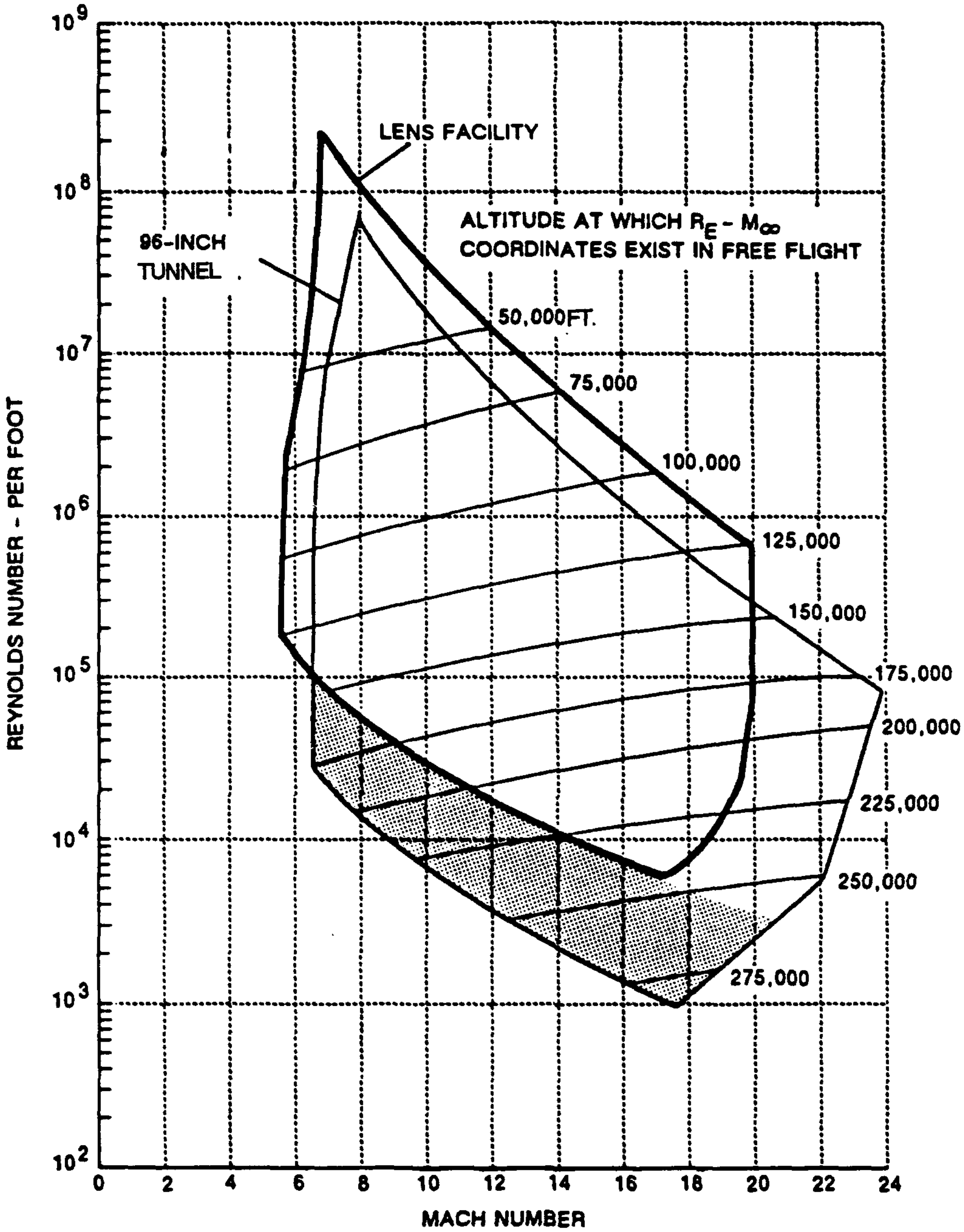

Re_{MAX} BASED ON $T_{\infty\ MIN} = 1.10\ T_{LOX}$

HIGH T_o, SHORT TEST TIME REGION ($t \leq 2$ ms) $T_o \geq 6000°$ R

Figure 4-5 **LENS HYPERSONIC SHOCK TUNNEL PERFORMANCE**

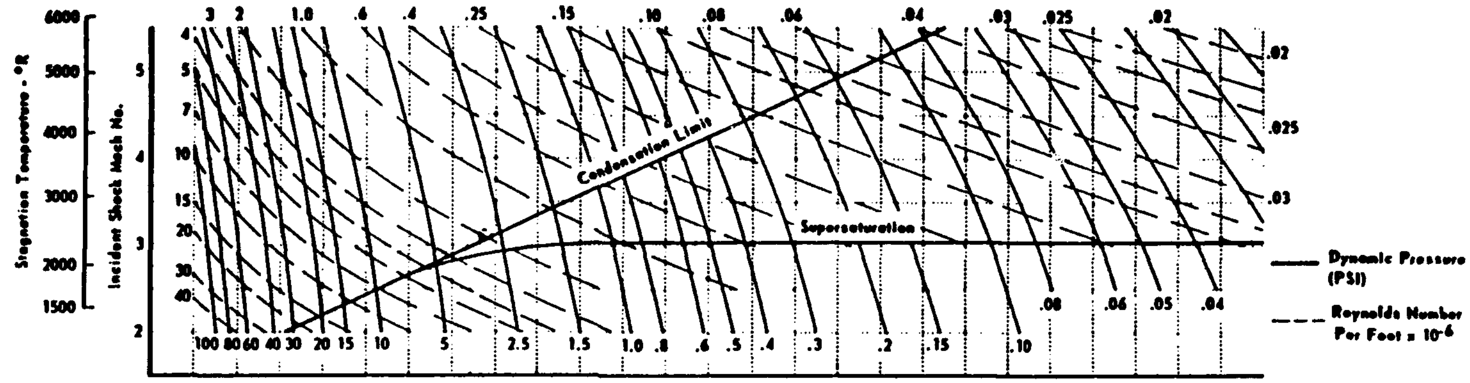

Operating Characteristics - 48" Hypersonic Shock Tunnel - 4000 PSIA Nozzle Supply Pressure

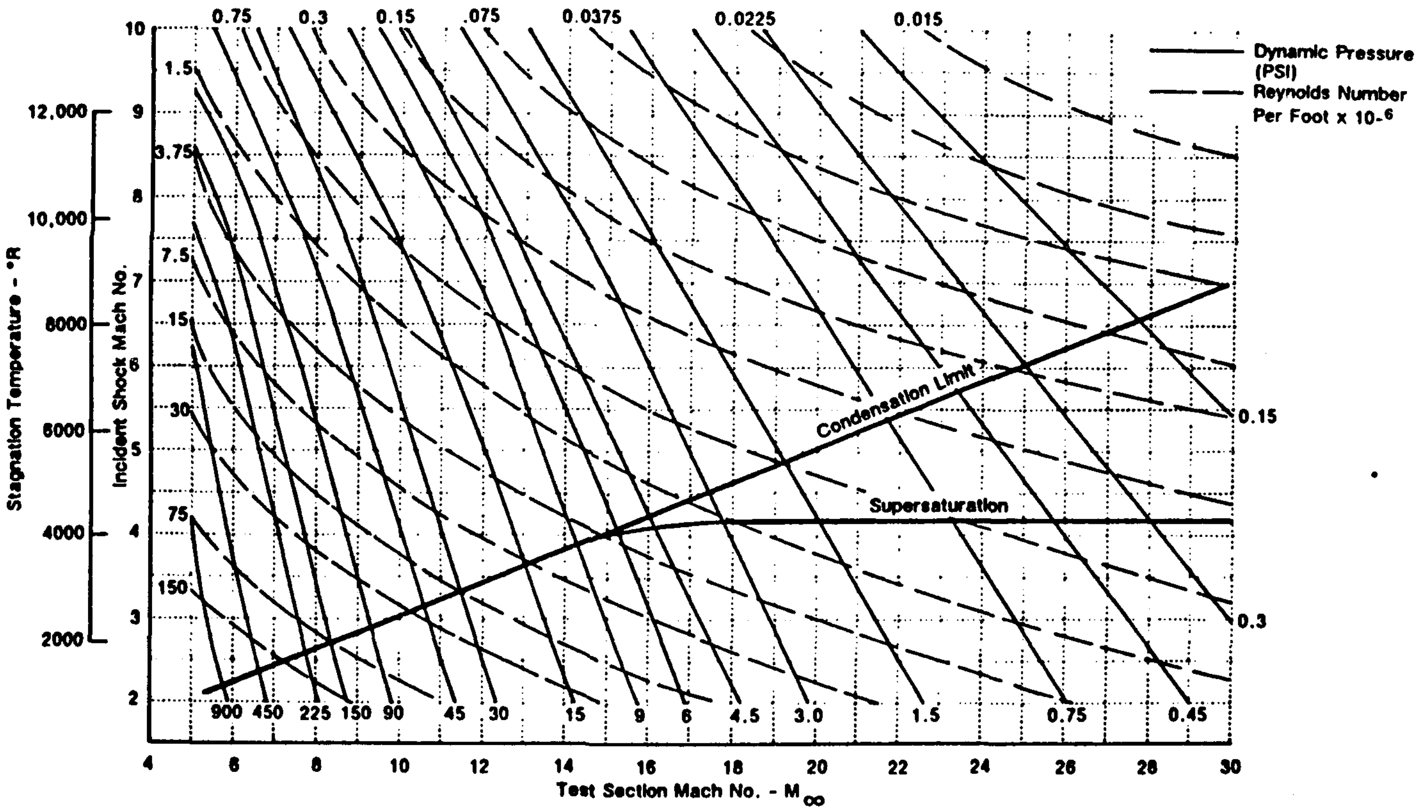

Figure 4-6 **Operating Characteristics - 96" Hypersonic Shock Tunnel - 30,000 psia Nozzle Supply Pressure – Chemical Equilibrium**

The test-section static pressure is determined as follows:

$$P_\infty = P_{ref}\left(\frac{T_\infty}{T_{ref}}\right)^{\frac{\gamma}{\gamma-1}} \exp\left(\frac{S_{ref}}{\bar{R}} - \frac{S_o}{\bar{R}}\right)$$

where S_o = entropy of test air including vibrational contributions

$\frac{S_{ref.}}{\bar{R}}$ = 30.56

$P_{ref.}$ = 0.001 psia

$T_{ref.}$ = 500°R

γ = specific heat ratio for air composed of 20.98% O_2, 78.08% N_2, 0.93%A

The values of $S_{ref.}$ are obtained from Reference 4 for air at some arbitrary state obeying the perfect gas laws.

The dynamic pressure is:

$$q_\infty = \frac{1}{2}\varrho_\infty u_\infty^2$$

where

$$\varrho_\infty = \frac{p_\infty}{\bar{R}T_\infty},\ u_\infty = \sqrt{\gamma_\infty \bar{R} T_\infty}\ M_\infty$$

The test-section stagnation pressure is obtained by solving the Rankine-Hugoniot normal shock equation at the test-section Mach number and can be shown to be:

$$P'_o = p_\infty\left[1 + \gamma_\infty M_\infty^2\left(1 - \frac{\xi}{2}\right)\right]$$

where ξ is the ratio of the density ahead of the shock wave to that after the shock.

B. Nonequilibrium

For air-supply temperatures above 5800°R, at which some dissociation takes place, care must be taken to include nonequilibrium effects in the nozzle expansion.[5,6] In general, the expansion process is so rapid that finite-rate chemical relaxation processes cannot maintain equilibrium composition, and some residual amounts of dissociated gas species remain when the air reaches the test section. The effects on specific heats, static enthalpy, and molecular weight of the residual dissociated gas species and associated frozen chemical energy need to be taken into account in the determination of freestream conditions. For exact computation of these effects, CUBRC has available a computer solution for nozzle expansions with finite-rate chemistry. Solutions for the effects of nonequilibrium in the nozzle expansion on tunnel test-conditions have been obtained for a wide range of tunnel–supply conditions and nozzle geometries, and new solutions can be obtained for a specific test.

An appropriate solution has been developed that generalizes the computer solutions so that the nonequilibrium effects, including residual (or "frozen") energy in vibration, for a specified test condition can be handcalculated to good accuracy. The frozen atomic specie mole fraction, η_A, static enthalpy loss through freezing, h_f, and effect of vibrational freezing on entropy, S_{V_F}/R_o are found from graphical presentations of the exact solutions. The ratios of nonequilibrium to equilibrium values in the freestream are then:

$$\frac{T_{N.E.}}{T_{EQ}} = \frac{\left[\left(1+\frac{h_f}{2h_o}\right)\left(1+\frac{\eta_A}{2}\right)\right]^{2/5(1+\frac{2}{5}\eta_A)} \eta_A^{\;2/5\eta_A} \left[f(T_o,P_o)\right]^{\eta_A} \exp\left(\left(-\frac{2}{5}+\frac{6}{25}\eta_A\right)\frac{S_{V_F}}{R_o}\right)}{\left(\frac{A}{A^*}\right)^{\frac{4\eta_A}{25}}}$$

$$\frac{P_{N.E.}}{P_{EQ}} = \left[\left(1+\frac{h_f}{2h_o}\right)\left(1+\frac{\eta_A}{2}\right)\right]\frac{T}{T_{EQ}}$$

$$\left(\frac{M_{N.E.}}{M_{EQ}}\right)^2 = \frac{1-\frac{h_f}{h_o}}{\left(1+\frac{43}{70}\eta_A\right)\frac{T}{T_{EQ}}}$$

where	T_o, P_o	=	reservoir temperature and pressure
	h_f/h_o	=	fraction of total enthalpy frozen into dissociation and vibrational excitation
	η_A	=	mole fraction of atomic species
	A/A^*	=	local area ratio
	S_{V_F}/R_o	=	non–dimensional entropy of the gas at the temperature of vibrational freezing

N.E. and EQ as subscripts refer to nonequilibrium and equilibrium conditions, respectively

This approximate analysis has also been applied to aerodynamic shapes to determine those conditions for which knowledge of freestream nonequilibrium is important; these results assist in the assessment of the degree of accuracy to which the nonequilibrium effects must be determined for a given test.

Testing Time

The duration of steady airflow is limited in the tailored case by the downstream propagation of expansion waves from the driver section, which, upon arrival at the downstream end of the driven tube, decrease the pressure and temperature of the nozzle supply gas. A second factor, which limits the available test time at higher incident shock speeds, is the penetration of the interface by the driver gas and the

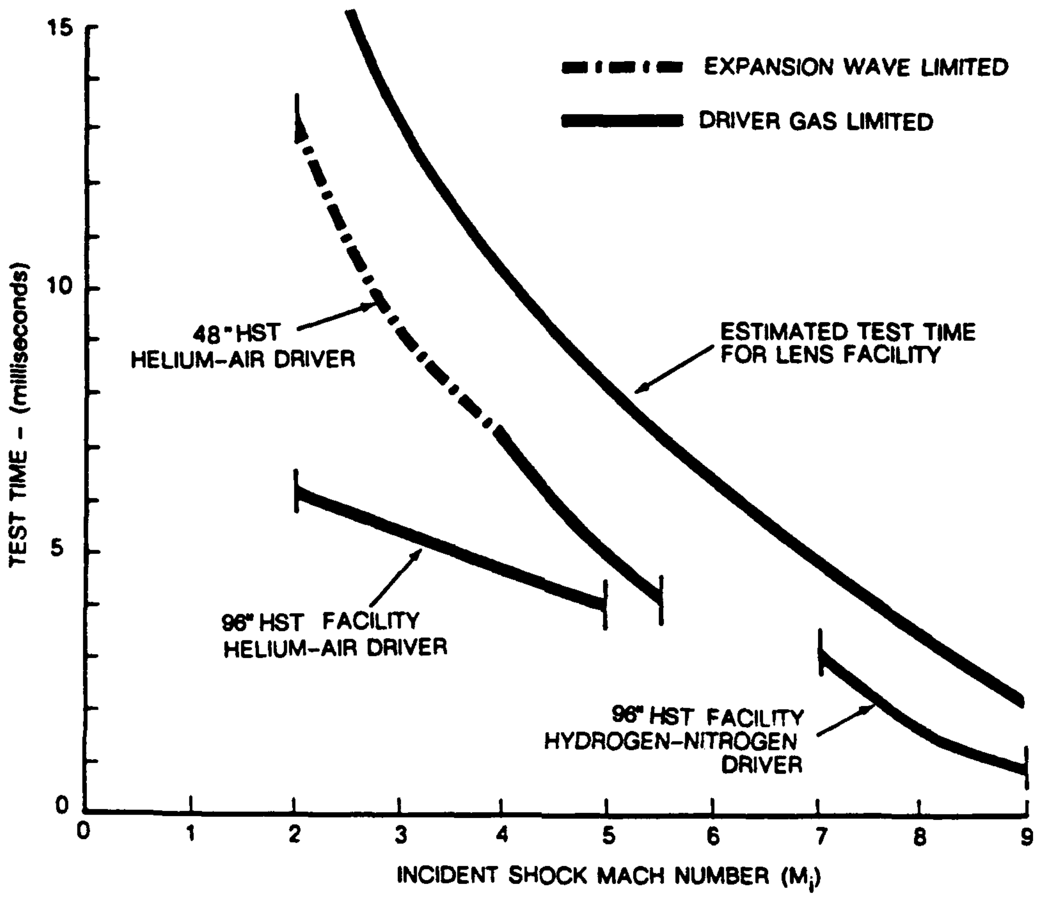

Figure 4-7 TEST TIME AVAILABLE FOR TAILORED-INTERFACE OPERATION

resulting early arrival of driver gas in the test section. This phenomenon has been studied both experimentally and theoretically, and test-time limitations based upon it are well known.[15] The testing time for various operating conditions are shown in Figure 4-7. Additional test time can be attained in the 48-inch leg at incident shock speeds below 3.5 by increasing the driver length to 40 feet.

Observations on Boundary Layer Transition in Hypersonic Flows

Experimental measurements of boundary transition on sharp flat plates and cones made in many different studies conducted in the Calspan 48- and 96-inch shock tunnels, which have the same nozzle configurations as the LENS facility, form the basis for the correlations presented herein. We have also selected measurements and observations from ballistic range and downrange shots for comparison. It is clear from the studies of Pate and Schueler[37] and extensive measurements made at NASA/Langley that boundary layer transition on models in wind tunnel studies is influenced by the freestream pressure environment. In general, our studies were conducted at Mach and Reynolds numbers considerably larger than those in the studies of Pate and Schueler. Thus, the magnitude of the noise radiated from the tunnel walls and the intensity on the axis should be significantly less in these facilities. A direct result of Pate and Schueler's findings is that a decrease in the tunnel size, for the same freestream conditions, should decrease the transition Reynolds number. However, transition measurements (shown in Figure 4-8) made in the A and D nozzles, which have exit diameters of 24 inches and 48 inches, respectively, do not exhibit this scale effect, even though a unit Reynolds number variation is evident in the correlation. Predictions based on Pate and Schueler's correlation suggest that transition Reynolds numbers of over 200 million should be anticipated for our test conditions, which is clearly well in excess of physically meaningful values. Expressing transition in terms of the Reynolds number based on the momentum thickness at transition onset, we can compare our measurements with the results of earlier studies conducted in the ballistic range and in full-scale flight tests as shown in Figure 4-9. Here, we have included measurements from cone and flat plate studies; we can see that, although our transition measurements on flat plates are consistently larger than those on cones, both sets of measurements are in essential agreement with ballistic range and flight tests. It is clear that, in these tests, the position of transition was influenced by factors more complex than those governing transition in the tests conducted by Pate and Schueler. Whether the fluctuating pressure level of the freestream is the principal factor influencing transition, as indicated by the measurements of Stainback, Fisher, and Wagner,[38] or whether this quantity is directly related to parameters that themselves govern transition remains to be determined.

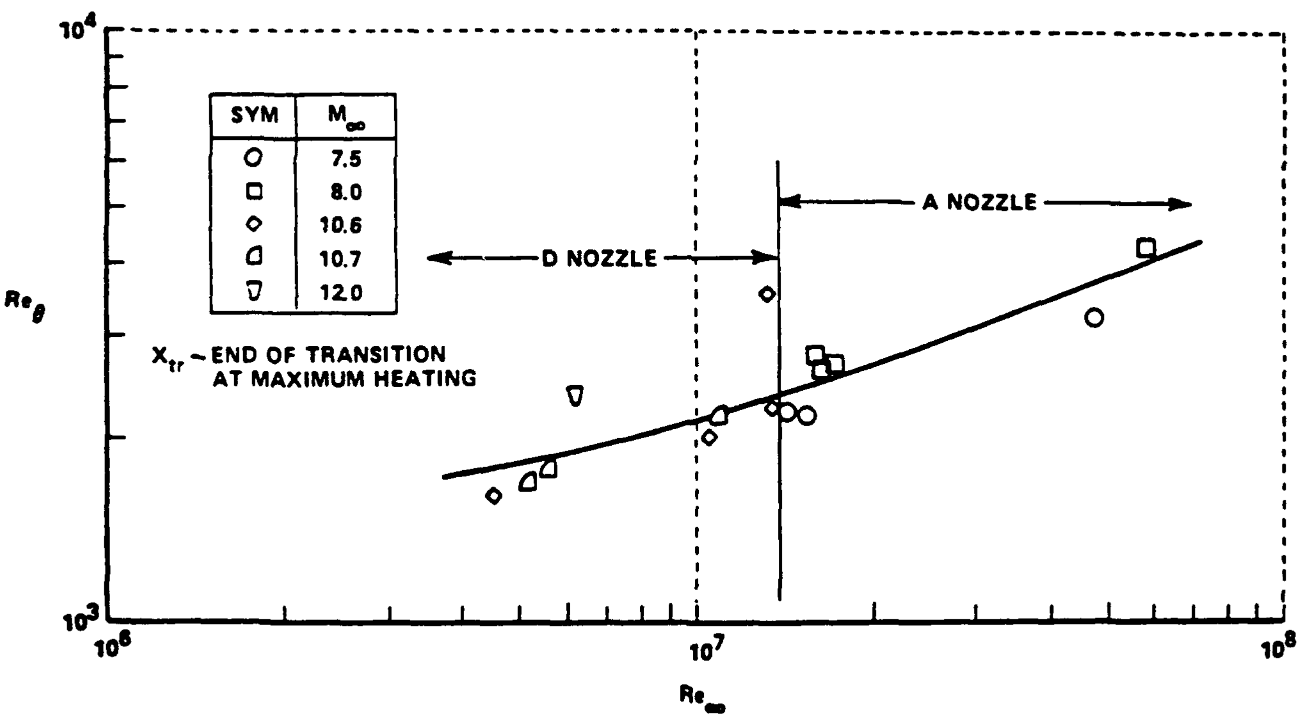

Figure 4-8 CORRELATION OF TRANSITION SHOWING THE EFFECTS OF TUNNEL SIZE

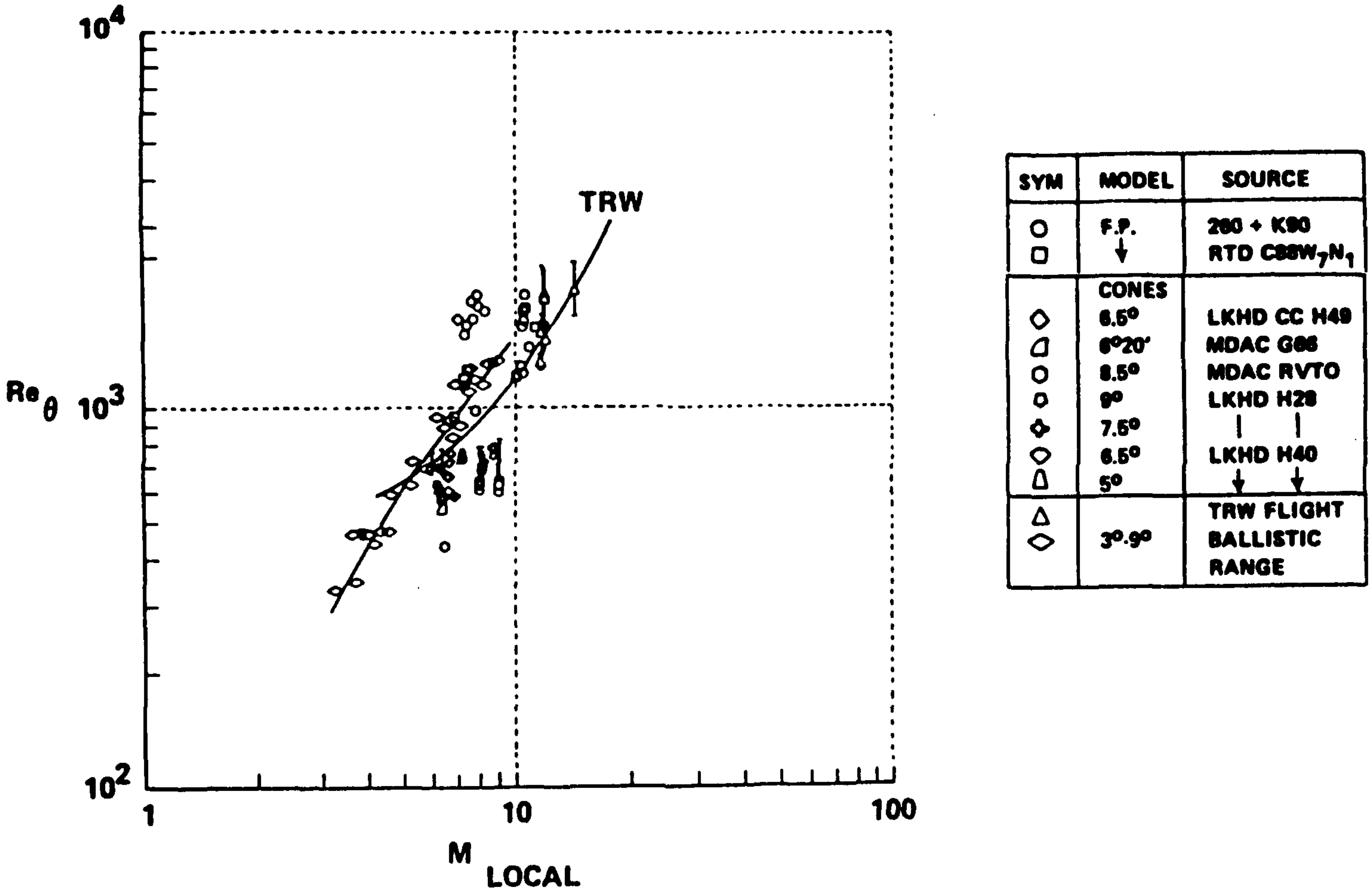

Figure 4-9 **CORRELATION OF TRANSITION MEASUREMENTS IN THE CALSPAN SHOCK TUNNELS WITH BALLISTIC AND DOWNRANGE MEASUREMENTS**

4.3 GENERAL AIRFLOW DATA AND CALIBRATION

The test conditions generated by each nozzle are functions of several variables: nozzle throat size; air supply pressure and temperature; and, in the case of a conical nozzle, axial station in the test section. The lateral distribution of pitot pressure has been surveyed in each nozzle for many combinations of these variables; examples are shown in the lower-left-hand corners of Figures 4-10 and 4-11.

Airflow data from many runs of a particular nozzle configuration are averaged for each run, and the average values are normalized to standard conditions as shown inFigures 4-10 and 4-11to indicate their dependence on supply conditions. The theoretical trends are established based upon the best available boundary layer information[14]. It has been found that data taken in the 96-inch leg duplicate that obtained in the 48-inch leg. Therefore, the M∞ vs. M_i curves are applicable to both legs of the tunnel within their respective limits, and to the LENS shock tunnel.

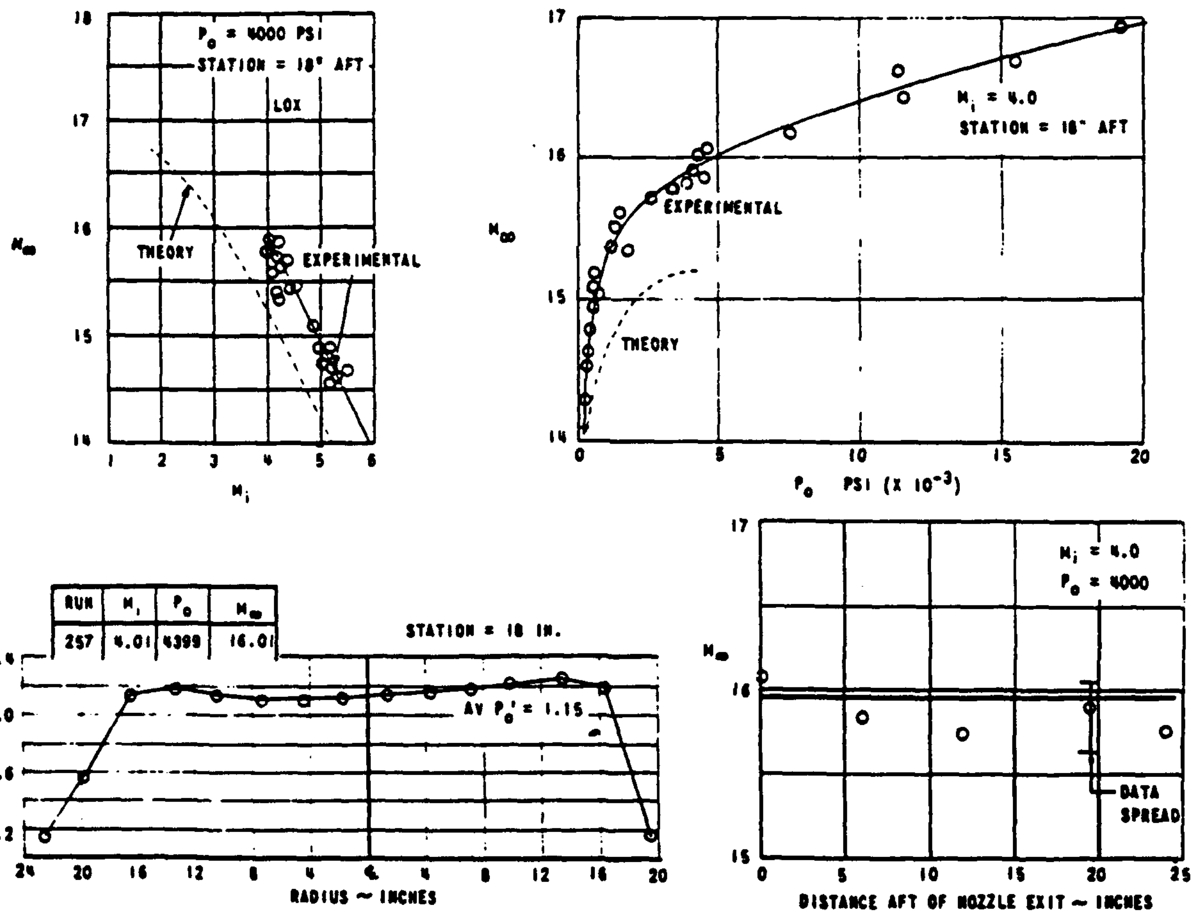

Figure 4-10 AIRFLOW CALIBRATION - 4-FOOT CONTOURED "D" NOZZLE, D* = 0.5 INCH

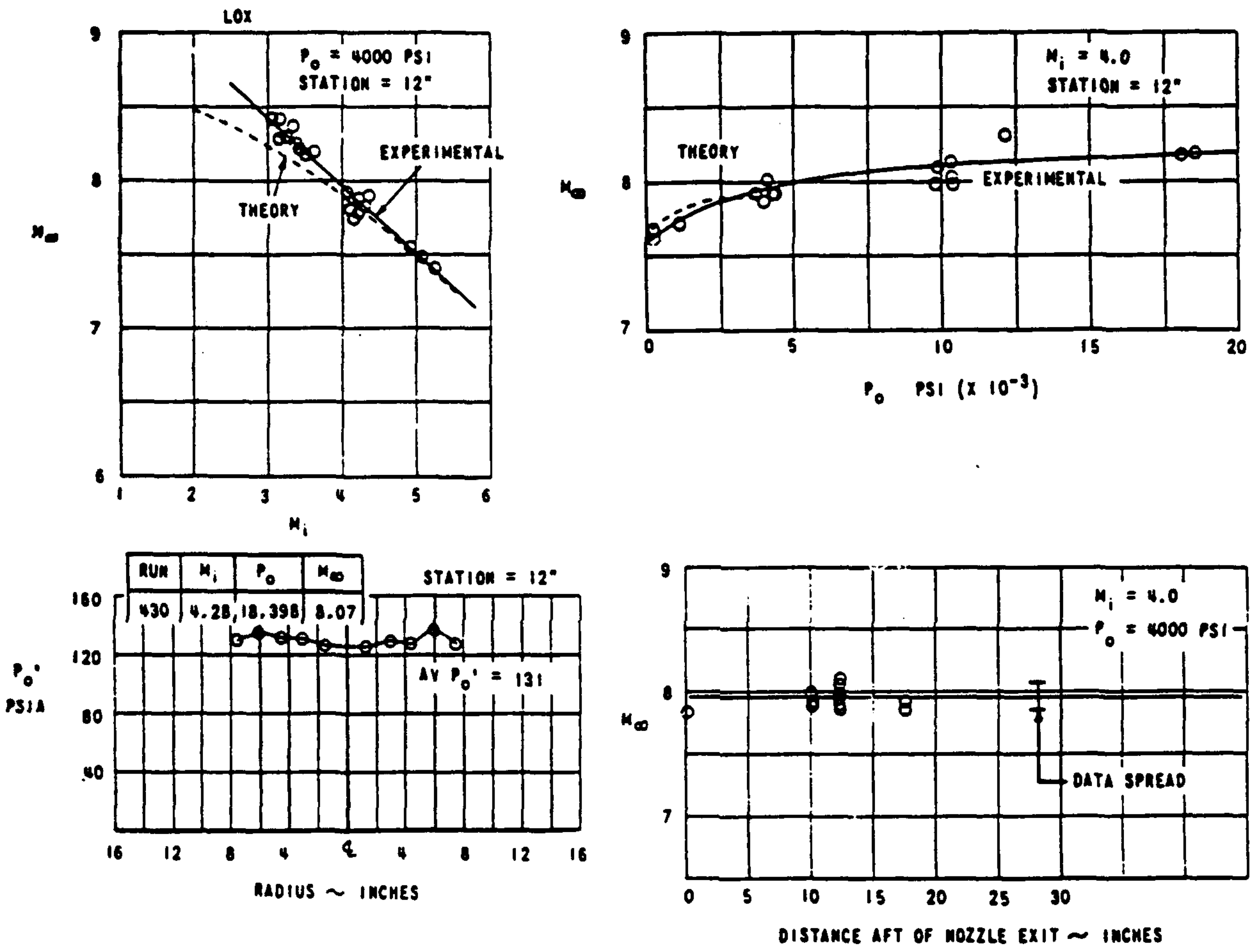

Figure 4-11 AIRFLOW CALIBRATION—2-FOOT CONTOURED "A" NOZZLE

4.4 Surface and Flowfield Instrumentation for Aerothermal Studies

Review of Measurement Techniques

We have examined and surveyed the potential instrumentation that could be of use in obtaining surface and flowfield measurements. Particular emphasis was placed on measurements of the fluctuating density and temperature fields, as these properties directly control the aero-optic characteristics of the flowfield. In terms of wall quantities, we have in hano excellent means of measuring surface pressure, heating rate, and skin friction. Heating-rate measurements using "thin films" (thin-film resistance thermometers) also provide key information on the position of transition. Mean flow measurements under low-enthalpy conditions can be made with pitot pressure and total temperature intrusive probes. It is also possible to obtain direct measurements of concentration under these conditions. Holographic interferometry and velocimetry are possible to obtain measurements of density or velocity. Holographic interferometry can be used to obtain flowfield density information. At this point, however, it is questionable whether laser doppler velocimetry (LDV) techniques are capable of measuring at the high velocities we anticipate in our experimental studies; and laser-induced fluorescence (LIF), while an extremely important potential technique, is yet to be used successfully in large-scale facilities. For flowfield fluctuation measurements, very few definitive techniques are available. High-frequency pitot pressure measurements have been made and will be used to determine principally turbulent scale size. Density measurements can be made with electron beams, and this technique would be employed first in a validation experiment.

Surface Measurement Technique

Thin-film heat transfer instrumentation has the capabilities of measuring both mean and fluctuating heat transfer rates up to frequencies of 1 MHz. High-frequency Kulite pressure gages are capable of accurately providing the mean pressure and the fluctuating level up to typically 300 kHz. Skin friction instrumentation using floating-element balances is capable of measuring up to 5 kHz in frequency response which basically must be regarded as a mean measurement. Thin-film and calorimeter heat transfer elements are illustrated in Figures 4-12 and 4-13, and a description of these techniques can be found in Reference 1.* The skin friction gage used in earlier programs in the shock tunnel is shown in Figure 4-14. The gage is based on a single-component force balance and contains extensive accelerometer compensation.

---

* 1. "Large Energy National Shock Tunnel (LENS)—Description and Capabilities," Calspan-UB Research Center, February 1991.

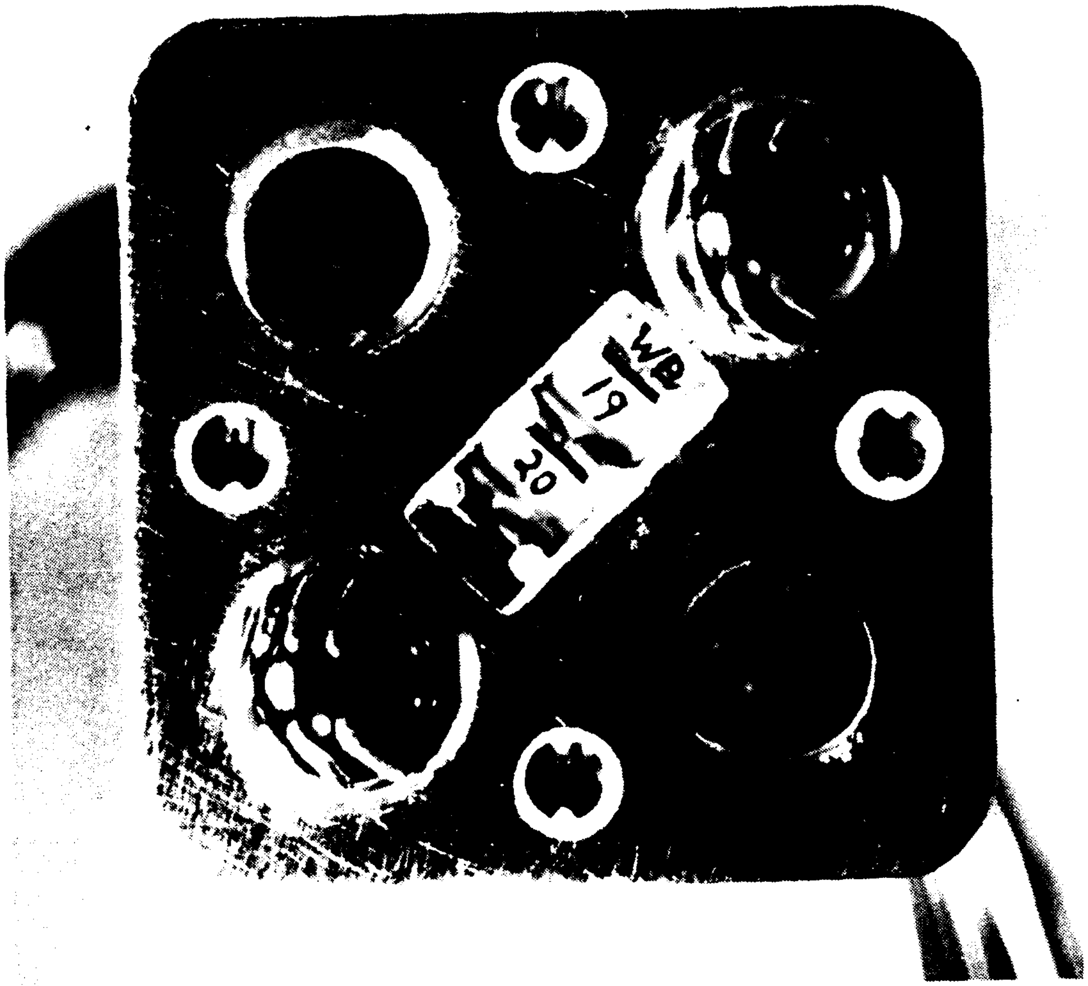

Figure 4-12 THIN FILM HEAT TRANSFER INSTRUMENTATION

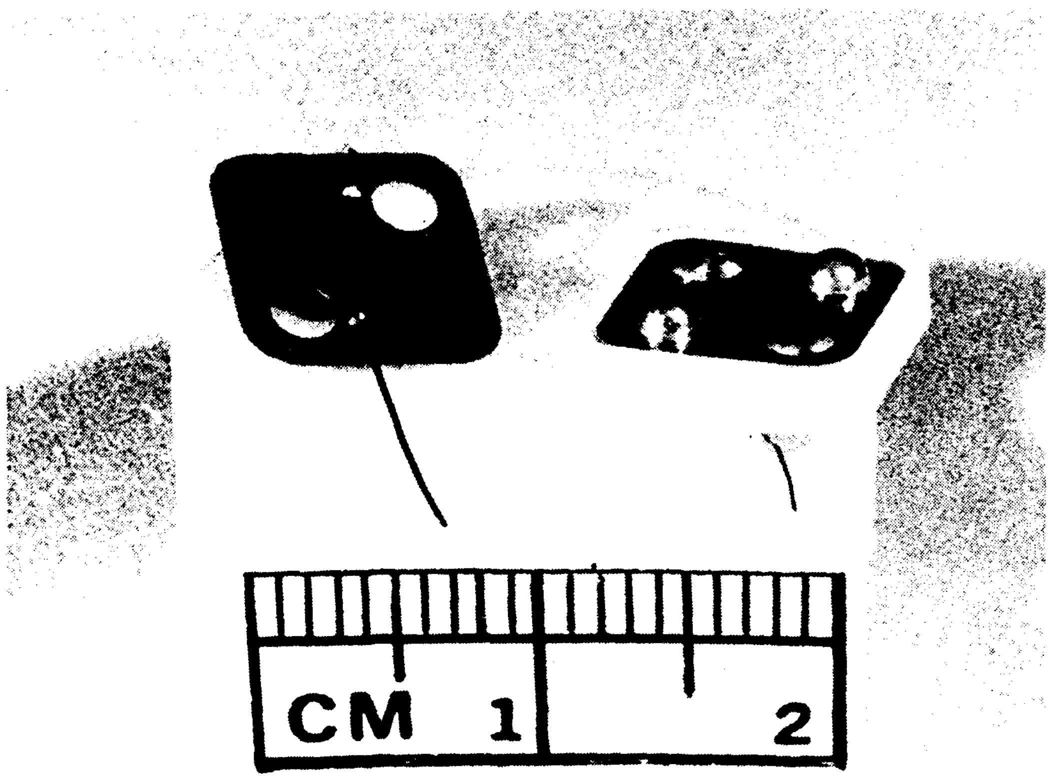

Figure 4-13 TYPICAL CALORIMETER INSTRUMENTATION TO BE USED IN LENS FACILITY

Intrusive Flowfield Measurements

Three sets of instrumentation will be used to probe the flowfield under low-enthalpy conditions. These are mean-frequency pitot probes, total temperature probes, and thin-film probes. A typical probe assembly is shown in Figure 4-15. The Kulite-based high-frequency pitot probes have a frequency response of 300 kHz. The total temperature gages and the thin-film gages will give us the ability of measuring fluctuations of up to 1 kHz. Both the pitot pressure and thin-film instruments can be used to obtain turbulent scale size in the mixing region of the flowfield.

Non-Intrusive Flowfield Instrumentation

We will be using a number of non-intrusive flowfield measurement techniques during the validation studies. Later, we hope to incorporate more techniques, such as LIF, as these techniques mature. As mentioned above, we will use holographic interferometry to determine the distribution of the density in the flowfield. This will enable us to determine the boresight shift for direct comparisons with the boresight-shift data obtained from line-of-sight measurement through the window. We have used the electron-beam technique in earlier shock tunnel studies to obtain mean and fluctuating density measurements across turbulent boundary layers in hypersonic flow. Static temperature measurements can also be obtained at the same point that the density measurements are made. A typical electron-beam setup, in which measurements were made across a 6° cone, is shown in Figure 4-16. The mean and fluctuating densities across the boundary layer are determined by measuring the mean and fluctuating intensities of emitted light at the measurement stations across the boundary layer. Typical measurements of the density and temperature distributions across a 0.6-inch-thick boundary layer over the cone are shown in Figures 4-17 and 4-18. The static temperatures at the various measurement stations across the boundary layer can be deduced from measurements of the fluorescence spectra. It can be seen that large fluctuations in density occur in the middle of the viscous layer that give rise to serious aero-optic distortion. By correlating the outputs from the 10 individual measurement stations across the boundary layer, it is possible to obtain measurements of the turbulent scale size as well as the density and temperature across the flow.

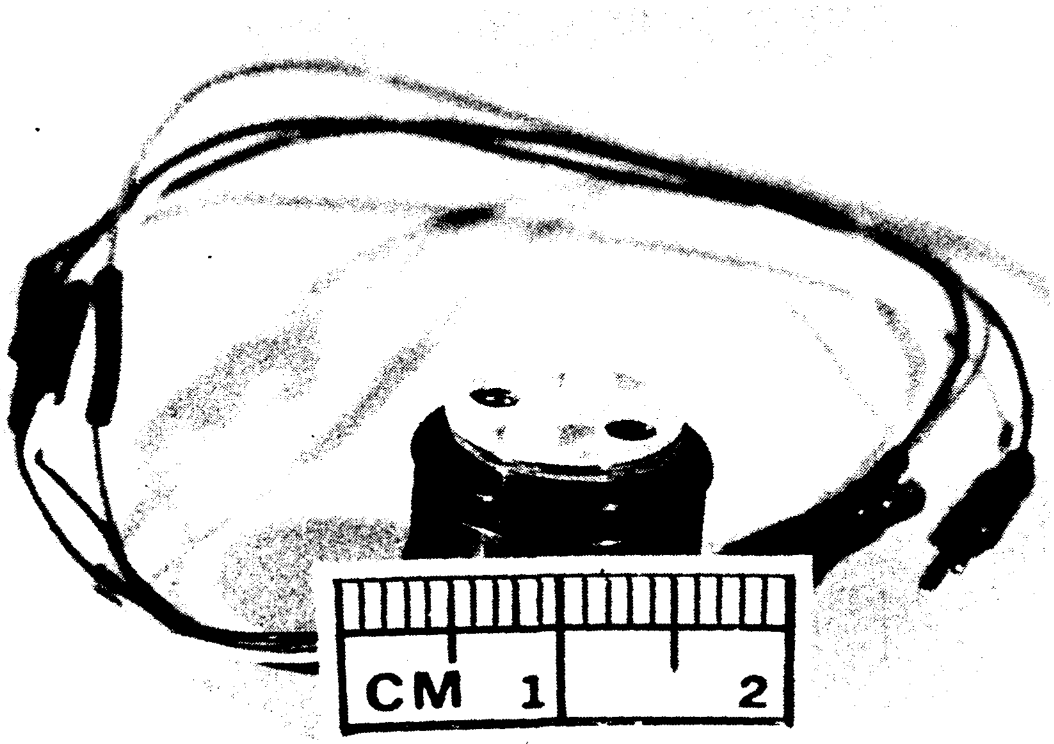

Figure 4-14 TYPICAL SKIN FRICTION GAGE INSTRUMENTATION TO BE USED IN LENS FACILITY

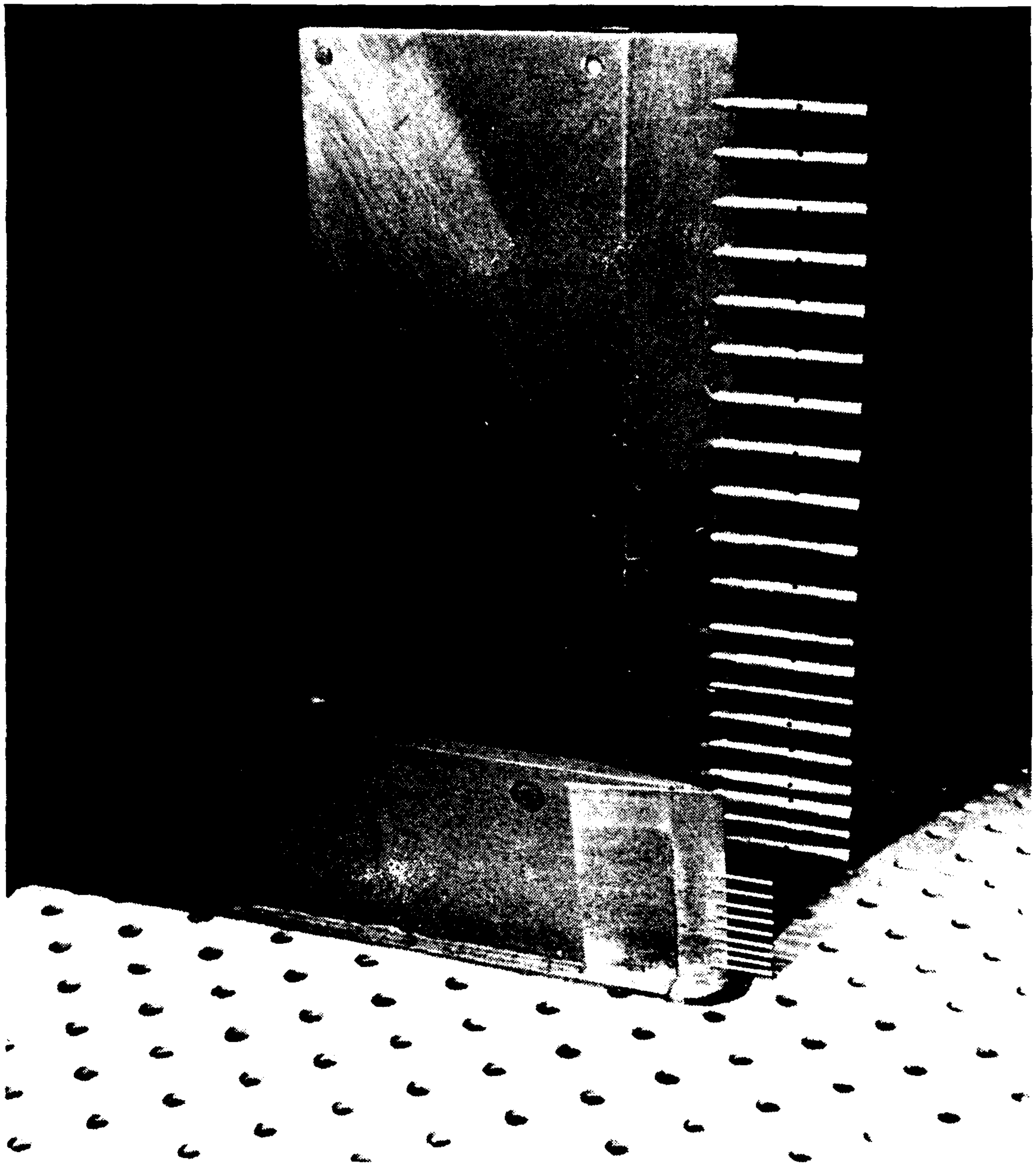

Figure 4-15 SHOCK LAYER AND BOUNDARY LAYER RAKES FOR FLOWFIELD STUDIES

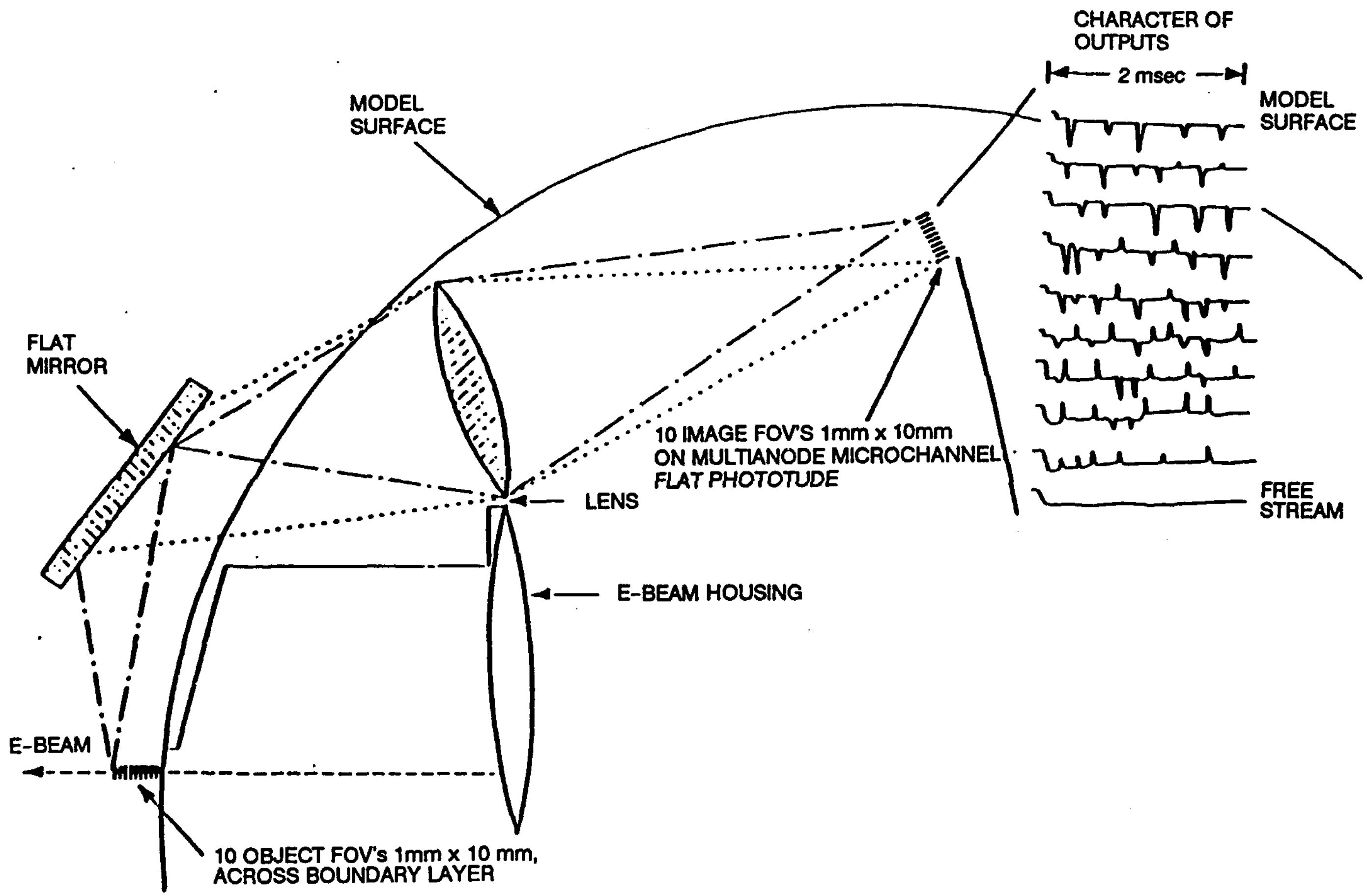

Figure 4-16 OPTICS AND DETECTOR CONFIGURATION FOR ELECTRON-BEAM STUDIES

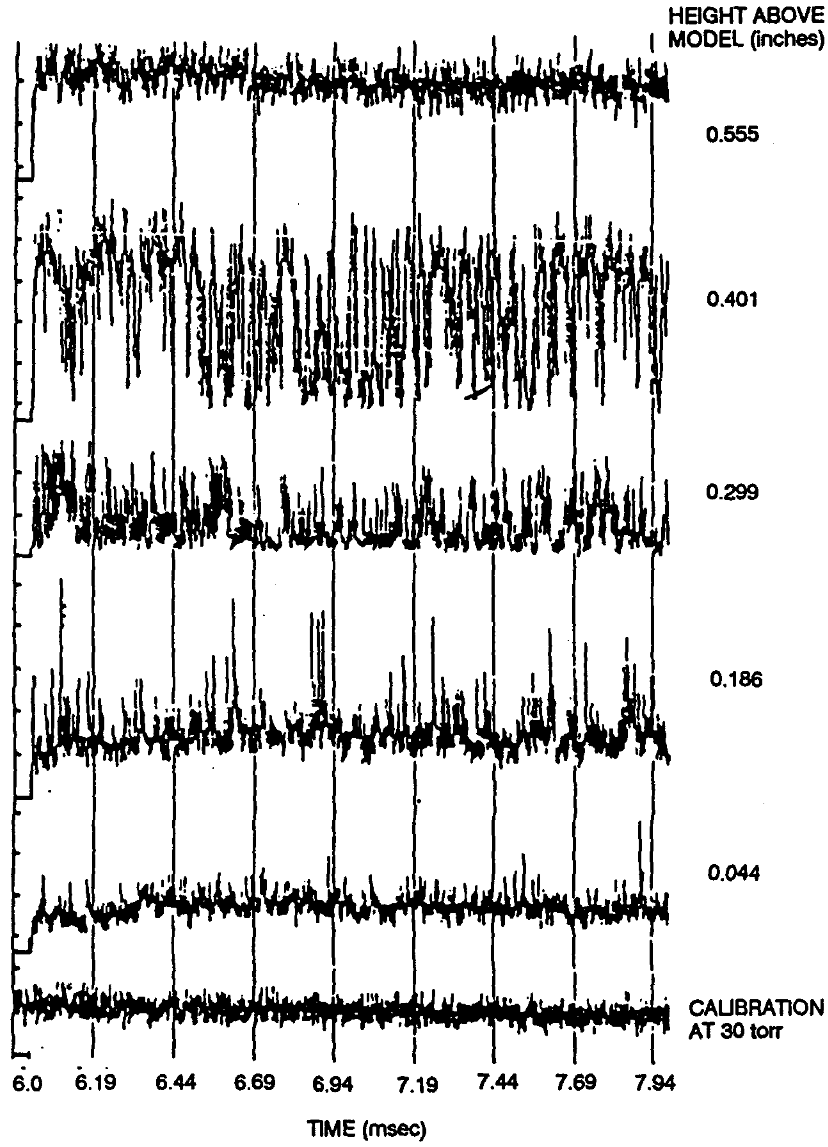

Figure 4-17 ELECTRON-BEAM DENSITY FLUCTUATION MEASUREMENTS ACROSS TURBULENT BOUNDARY LAYER ON CONICAL VEHICLE

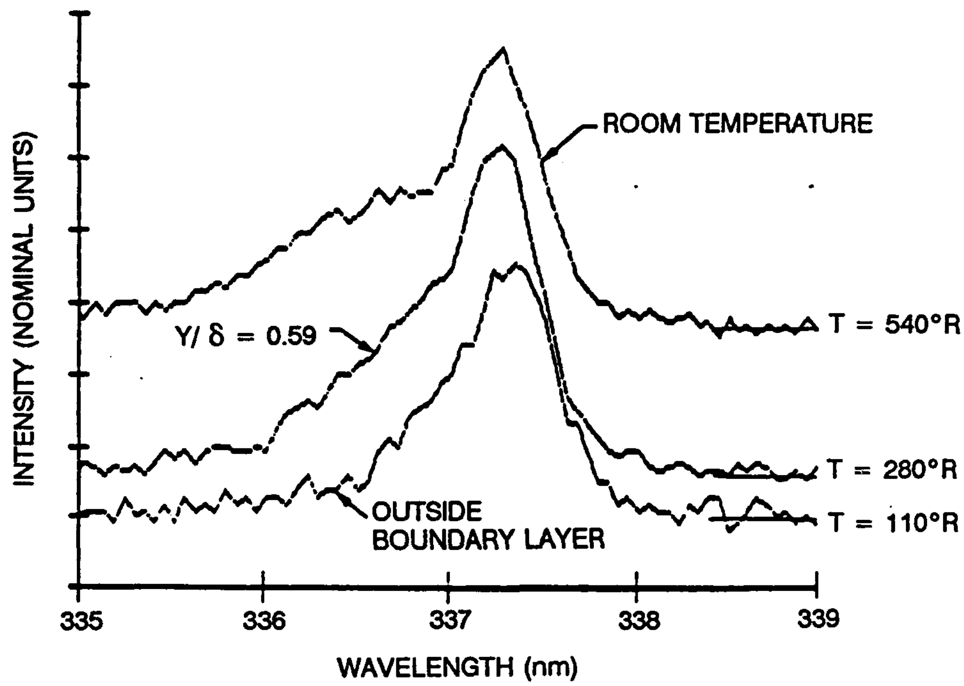

Figure 4-18 FLOWFIELD TEMPERATURE MEASUREMENTS USING ELECTRON BEAM (FLUORESCENCE SPECTRUM N^2 SECOND POSITIVE TRANSITION, $C^3 - B^3$ (0,0))

4.5 REFERENCES

1. Bird, K.C., and Burke, A.F., "The Use of Conical and Contoured Expansion Nozzles in Hypervelocity Facilities," Calspan Report No. 112, January 1962.

2. Daum, Fred L., "Air Condensation in a Hypersonic Wind Tunnel," AIAA Journal, Vol. 1, No. 5, May 1963.

3. Griffith, B.J., Deskins, H.E., and Little, H.R., "Condensation Tests in Hotshot Tunnels," Third Hypervelocity Technique Symposium, March 17–18, 1964.

4. Reece, J.W., "Shock Tube Theory for Real Air with Application to Wind Tunnel Testing and to Flight Simulation," Calspan Experimental Facilities Division Report WTH-003, October 1958.

5. Boyer, D.W., Eschenroeder, A.Q., and Russo, A.L., "Approximate Solutions for Nonequilibrium Air Flow in Hypersonic Nozzles," Report No. AEDC-TN-60-181, August 1960.

6. Burke, A.F., Curtis, J.T., and Boyer, D.W., "Nonequilibrium Flow Consideration in Hypervelocity Wind Tunnel Testing," Calspan Report No. AA-1632-Y-1, May 1962.

7. Curtis, J.T., Burke, A.F., and Hayman, R.A., "An Analytical and Experimental Study of the Ionized Flowfield about a Hemisphere Cylinder and its Effect on the Radiation Pattern of a Slot Antenna," Report No. AFCRL-63-339, August 1963.

8. Andre, S.N., "Study of Antenna Voltage Breakdown in a Shock Tunnel," Final Technical Report AFCRL-68-0253 (Calspan Report No. UB-2344-E-4), January 1967–April 1968 CONFIDENTIAL.

9. Boyer, D.W., "Ionization Nonequilibrium Effects on a Magneto-gasdynamic Interaction on the Stagnation Region of an Axisymmetric Blunt Body," Report No. ASD-TDR-62-1078, March 1963.

10. Garberoglio, J.E., Dukowicz, J.K., and Romeo, D.J., "Experimental Investigation of Turbulent Near Wakes in Hypersonic Flow," Calspan Report No. WTH-032, January 1968.

11. Rogers, C.E., and Mason, R.P., "Some Recent Advances in Short-Duration Aerodynamic Testing Techniques," presented at The Second AIAA Aerodynamic Testing Conference, Los Angeles, CA, September 1966.

12. Young, M.C., and Tripp, B.R., "Short-Pulse Coherent Doppler Radar Measurements of Backscatter from Hypersonic Wakes," Calspan Report No. 162, January 1968.

13. Wallace, J.E., and Duryea, G.R., Jr., "Porous Leading Edge Development and Experiments on Transpiration Effects for a Blunt Plate in Hypersonic, Laminar Flow," AFFDL-TR-66-33, Vol. III, September 1966.

14. Burke, A.F., "Turbulent Boundary Layers on Highly Cooled Surface at High Mach Numbers," Calspan Report No. 118, November 1961.

15. Bird, K.D., Martin, J.F., and Bell, T.J., "Recent Developments in the Use of the Hypersonic Shock Tunnel as a Research and Development Facility," presented at the Third Hypervelocity Techniques Symposium, Denver, CO, March 1964.

16. Beal, J.L. et al., "Review Report on CAL Studies of the Breakup of Drops During Reentry," Calspan Report No. AA-2121-Y, March 1967.

17. Martin, J.F., Duryea, G.R., and Stevenson, L.M., "Instrumentation for Force and Pressure Measurements in a Hypersonic Shock Tunnel," Calspan Report No. 113, January 1962.

18. Bogdan, L., "Instrumentation Techniques for Short-Duration Test Facilities," Calspan Report No. WTH-030, March 1967.

19. MacArthur, R.C. and Martin, J.F., "Use of Field Effect Transistors in Shock Tunnel Instrumentation Circuits," Proceedings of the 2nd International Congress on Instrumentation in Aerospace Simulation Facilities, Stanford University, Stanford, CA, 29-31 August 1966.

20. MacArthur, R.C., "The Development of High Output Miniaturized Pressure Transducers for Shock Tunnel Testing," AFAPL-TR-68-37, April 1968.

21. Vidal, R.J., "Transient Surface Temperature Measurements," Calspan Report No. 114, March 1962.

22. Bogdan, L., "High-Temperature, Thin-Film Resistance Thermometers for Heat Transfer Measurements," Calspan Report No. HM-1510-Y-6, February 1963.

23. Rogers, C.E., Bogdan, L., Kinzly, R.E., and Stratton, J.E., "A Thermal Mapping Technique for Shock Tunnels and a Practical Data-Reduction Procedure," AIAA 7th Aerodynamic Testing Conference, Palo Alto, CA, September 13-15, 1972 (AIAA Paper No. 720-1031).

24. Sheeran, W.J., and Duryea, G.R., "The Application of the Accelerometer Force Balance in Short-Duration Testing," presented at the AIAA 4th Aerodynamic Testing Conference, Cincinnati, OH, April 28-30, 1969 (AIAA Paper No. 69-351).

25. MacArthur, R.C., "Transducer for Direct Measurement of Skin Friction in a Hypersonic Shock Tunnel," Calspan Report No. 129, August 1963.

26. MacArthur, R.C., "Contoured Skin Friction Transducers," Calspan Report No. AN-2403-Y-1, August 1967.

27. Wallace, J.E., "Hypersonic Boundary Layer Measurements Using an Electron Beam," Calspan Report No. AN-2112-Y-1, August 1968.

28. Holden, M.S., "Shock Wave-Turbulent Boundary Layer Interaction in Hypersonic Flow," AIAA Paper No. 72-74, paper presented at the AIAA 10th Aerospace Science Meeting, San Diego, CA, 17-19 January 1972.

29. Holden, M.S., "Shock Wave-Turbulent Boundary Layer Interaction in Hypersonic Flow," Calspan Report No. AI-2920-A-1, July 1973.

30. Holden, M.S., "A Preliminary Experimental Study of the Turbulent Near Wake in High Reynolds Number Hypersonic Flow," Calspan Report No. AB-5211-A-1, January 1973.

31. Harvey J., Bergman, R.C., and Holden, M.S., "An Experimental Study of Hypersonic Turbulence on a Sharp Cone," AIAA Paper No. 89-1866.

32. Havener, G., Holden, M.S., and Azevedo, D., "Preliminary Application of Holographic Interferometry to Study Hypersonic Regions of Shock Wave/Boundary Layer Interactions," AIAA Paper No. 87-1194.

33. Rudy D.H., Thomas, J.L., Kumar, A., and Gnoffo, P.A., "A Validation Study of Four Navier-Stokes Codes for High Speed Flows," AIAA Paper No. 89-1838.

34. Holden, M.S., Nowak, R.J., Olsen, G.C., and Rodriguez, K.M., "Experimental Studies of Shock Wave/Wall Jet Interaction in Hypersonic Flow," AIAA Paper No. 90-0607.

35. Seymour, P.J., "Techniques for Evaluation of Unsteady Heat Flux From Film Gages," Master of Science Thesis at University of Buffalo, 1982.

36. Wittliff, C.E., "Hypersonic Shock Tunnel Heat Transfer Tests of the Space Shuttle SILTS Pod Configuration," AIAA Paper No. 83-1535.

37. Pate, S.R., Schueler, C.J., "An Investigation of Radiated Aerodynamic Noise Effects on Boundary-Layer Transition in Supersonic and Hypersonic Wind Tunnels," AIAA Paper No. 68-375.

38. Stainback, P.C., Fisher, M.C., Wagner, R.D., "Effects of Wind Tunnel Disturbance on Hypersonic Boundary-Layer Transition," AIAA Paper No. 72-181.

39. Watkins, W., "Comparisons of a Full Navier-Stokes Computational Model with High Mach Number Combustor Test Data," AIAA Paper No. 90-5217.

40. Dunn, M.G. and Lordi, J.A., "Measurement of Electron Temperature and Number Density in Shock-Tunnel Flows. Part II: $NO^+ + e^-$ Dissociative Recombination Rate in Air. AIAA J. 7, 2099, November 1969.

41. Dunn, M.G. and Lordi, J.A., "Measurement of $O_2^+ + e^-$ Dissociative Recombination in Expanding Oxygen Flows." AIAA J. 8, 614, April 1970.

42. Dunn, M.G. and Lordi, J.A., "Measurement of $N_2^+ + e^-$ Dissociative Recombination in Expanding Nitrogen Flows." AIAA J. 8, 339, February 1970.

43. Dunn, M.G., "Measurement of $C^+ + e^- + e^-$ and $CO^+ + e^-$ Recombination in Carbon Monoxide Flows." AIAA J. 9, 2184, November 1971.

44. Boyer, D.W., "Experimental Studies of Flush-Mounted Electrostatic Probes in Collision-Dominated Hypersonic Ionized Flows," Sandia Laboratories (Albuquerque) Report SC-CR-72-3145, July 1972.

45. Boyer, D.W. and Touryan, K.J, "Experimental and Numerical Studies of Flush Electrostatic Probes in Hypersonic Ionized Flows: I. Experiment." AIAA J. 10, 1667, December 1972.

46. Dunn, M.G., Blum, R.J, Swift, C.T., Beck, F.B., and Grantham, W.C., "Antenna Admittance Determination of Electron Density." AIAA J. 11, 1018, July 1973.

47. Boyer, D.W., Bein, G.P. and Andre, S.N., "Studies of Microwave Transmission through a Hypersonic Air Plasma." Sandia Laboratories Report SC-CR-67-2710, June 1967.

48. Bein, G.P. and Boyer, D.W., "Microwave Transmission in a Pure Air Plasma," AIAA Paper 66-173. Paper presented at AIAA Plasmadynamics Conference, Monterey, California, March 2-4, 1966.

49. Boyer, D.W. and Andre, S.N., "Theoretical and Experimental Studies of Microwave Interaction Effects in a Hypersonic Air Plasma," Sandia Laboratories Report SC-CR-72-3164, October 1972.

50. Boyer, D.W. and Bitikofer, D.R., "Analytical and Experimental Studies of Microwave Interaction with a Hypersonic Air Plasma," Calspan Report No. AA-2053-Y-1, AFCRL-67-0201, February 1967.

51. Boyer, D.W., Bitikofer, D.R., and Neubauer, R.A., "Experimental Studies of Pulsed Microwave Breakdown Effects in a Hypersonic Air Plasma," Calspan Report No. AA-2053-Y-2, AFCRL-68-0145, February 1968.

Section 5
AERO-OPTIC INSTRUMENTATION
Physical Research, Inc.

5.1 Overview of Aero-Optics Effects

The optical effects of the turbulence depend on the scale and level of fluctuation in the index of refraction. For air or nitrogen coolant gas, the index of refraction is directly proportional to density. Alternatively, when a second gas type is used for the coolant, perhaps helium or carbon dioxide, the index of refraction of the mixture depends on the local concentration of each constituent and number density. When a monotonic gas (i.e., helium is used, the mixing layer is essentially composed of two gases, air and helium. However, when higher molecular weight gases (i.e., carbon dioxide) are used, chemical reactions may occur in the high temperature portion of the mixing layer. In this case, the local composition of the mixing layer will include a variety of species or constituents. In all cases, the scale and level of the fluctuation in the index of refraction of the mixture determine the optical properties of the mixing layer.

Optical propagation through the nonuniform media induces wavefront distortion in the collected target radiation, as different rays collected by the sensor aperture encounter different optical path lengths in the coolant turbulence. The variation in the optical path length within the aperture distorts the otherwise planar wavefront, and magnitude of the distortion is characterized by its variance from a plane wave. The spatial frequency at which the phase changes across the aperture is characterized by a length scale which is typically taken as equal to the nominal dimension of the turbulence cells. For a planar wavefront, the sensor telescope will form a nearly diffraction limited image on the focal array. The basic characteristics of the image are its brightness and its size. The brightness is expressed as a Strehl ratio, which is the ratio of the peak brightness to the diffraction limited brightness and the image size is expressed in angular dimensions which encircles or encloses a large fraction of the collected energy. These image properties begin to degrade as the RMS distortion increases above 1/10 wave. As the distortion exceeds 1/3 wave the image becomes dramatically degraded.

5.2 Introduction

Hypersonic endo-atmospheric interceptors, which utilize optical seekers, experience strong aero-optical distortions produced by coolant turbulence in the flow over the seeker window. Flow induced optical distortions produce boresight shifting and blurring of target images. Bore-sight shifting of the target can be corrected by advanced guidance algorithm. However, the more dramatic effects of target blurring results in large reductions in image brightness, due to spreading of the collected target energy over a larger number of pixels. The following are several problems caused by strong target blurring:

1) the peak intensity of the target image is dramatically reduced from the diffraction-limited value;

2) in the presence of "real-world" background noise sources (i.e., detector noise, natural or nuclear; and flow luminosity), reduced image brightness will delay target acquisition to shorter ranges and reduce homing times;

3) increase in image size to 5 or 10 times the diffraction limited image is a source of uncertainty in target line-of-sight, which contributes to miss distance.

Background

The effects of coolant turbulence on wavefront distortion and the resultant focal plane intensity distribution are illustrated in Figure 5-1. The shear layer formed between the hot shock layer gases on the interceptor forebody and the injected coolant on the sensor window is characterized by large velocity and temperature gradients. Since the pressure is relatively constant over the sensor window, the density varies inversely with the temperature. The strong velocity gradient results in rapid development of turbulence levels, which are characterized by large fluctuations in the gas velocity, temperature and density. The characteristic dimension of the turbulence cells, or the integral scale, grows with the thickness of the mixing layer. The mixing layer thickness grows as the flow moves over the sensor window. The radiative induced degradation of focal plane imagery is illustrated in Figure 5-2.

Figure 5-1

TURBULENCE INDUCED REFRACTIVE EFFECTS ON FOCAL PLANE IMAGERY

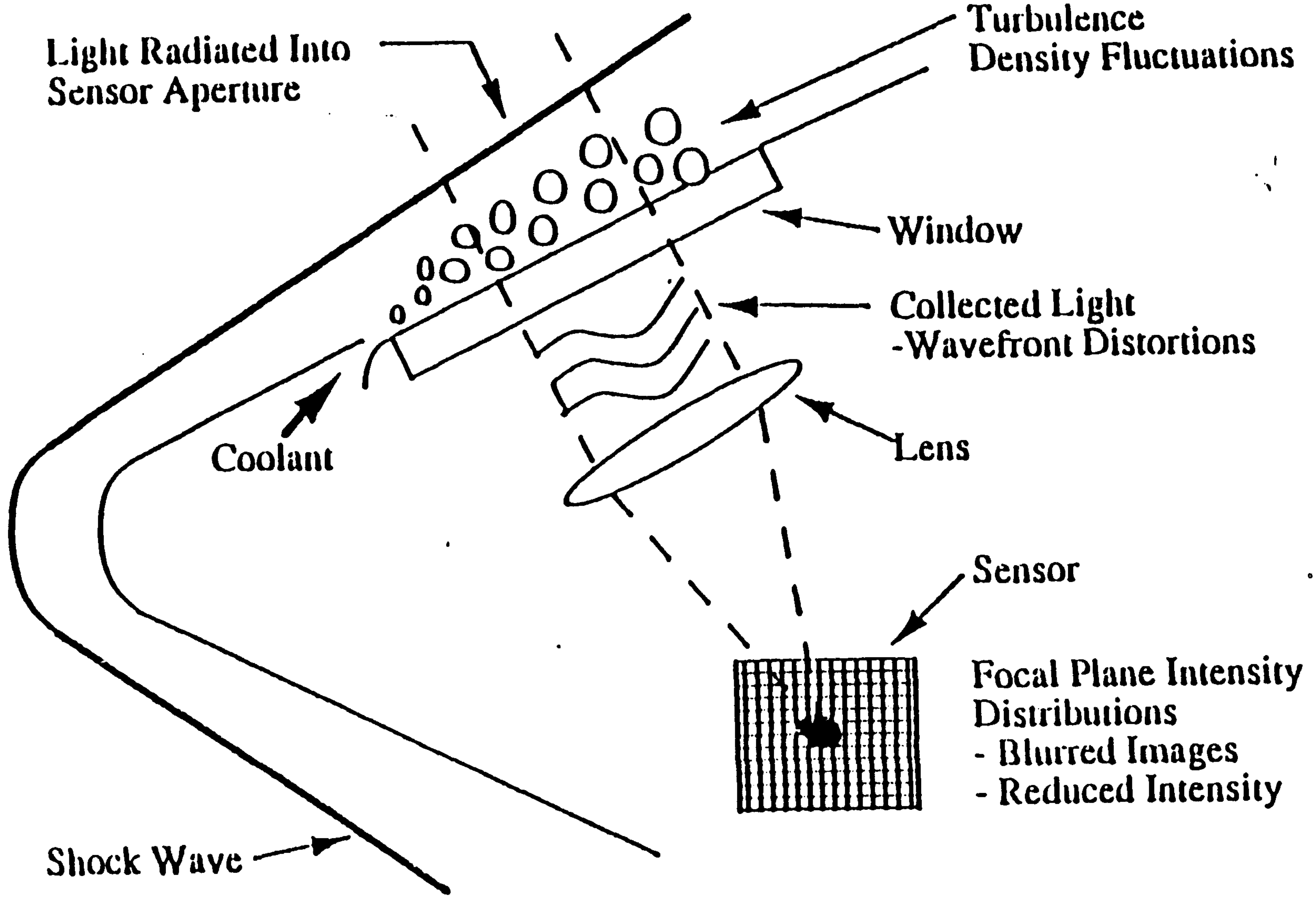

Figure 5-2

RADIATIVE INDUCED DEGRADATION OF FOCAL PLANE IMAGERY

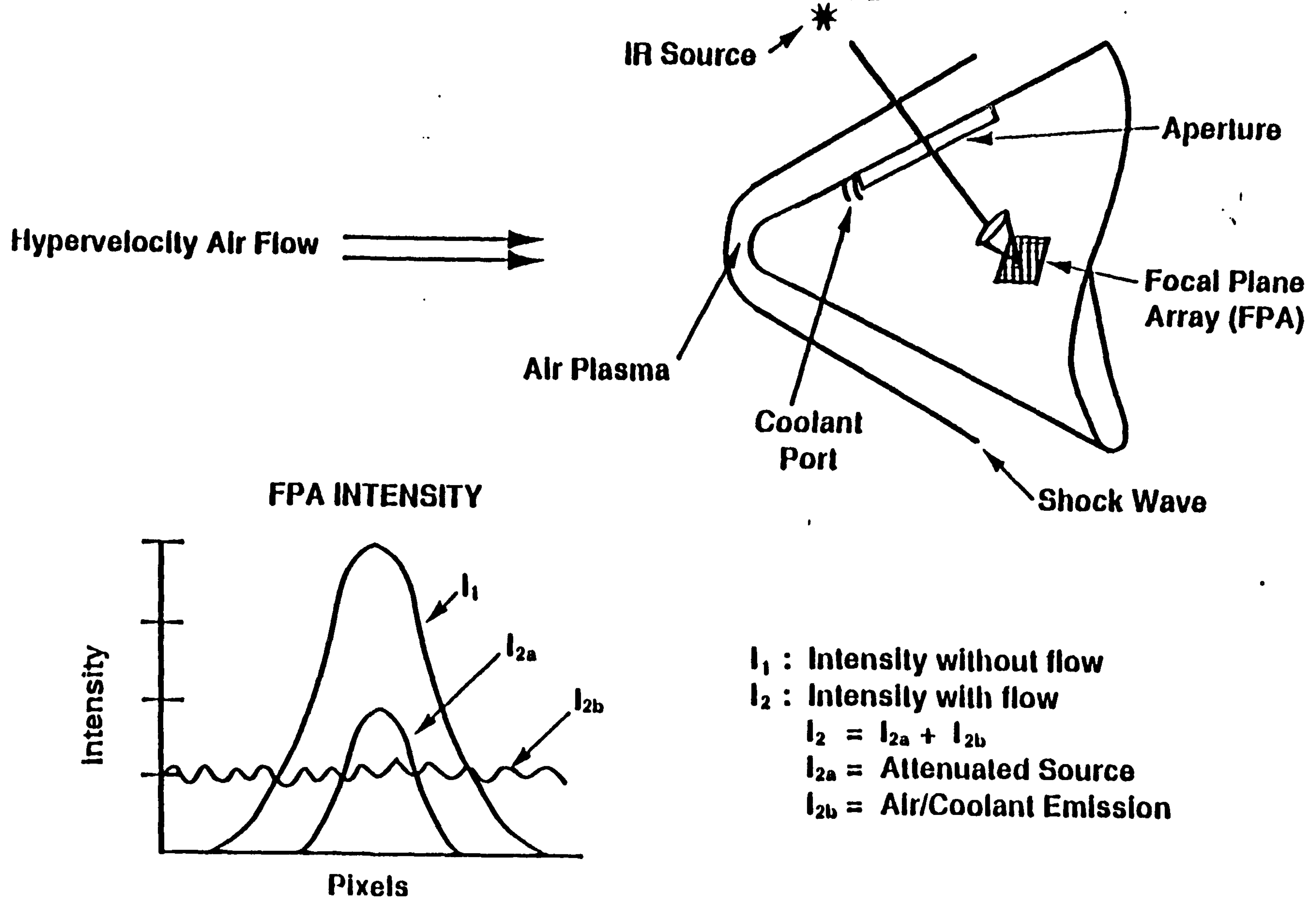

5.3 Instrumentation

The AOEC objective is to establish a center in which aero-optic performance capabilities of seeker window designs can be consistently evaluated in ENDO-LEAP environments. The six tasks are (1) develop and fabricate instruments, (2) software development, (3) calibration, (4) install and test, (5) data reduction and analysis, and (6) reporting. These tasks are further subdivided in Figure 5-3.

Five (5) instrumentation systems as delineated in Figure 5-4 will be developed and installed in the AOEC facility for the the purpose of:

Holography
Imagery
Boresight/Jitter
Radiometry
Spectrometry

providing sensor performance evaluation.

The wedge seeker window material will be fused silica with transmission from 0.28 to 2.3 μm. The window dimensions are for a 2 inch beam diameter, (i.e., 3.2" x 4.5" x 5"). The window frame accommodates the coolant system. The light source aperture windows provide 20 and 40 degree LOS optical paths. These windows will also be fused silica and utilize flush mount frame design. IR window materials were identified as ZnS, ZnSe and Ca F_2. Additional information is shown in Figure 5-5.

The optical system will be coupled to the LOS through beam ducts, designed to operate in the UV, VIS and IR bands, as shown in Figure 5-6. LOS angles will range from 20-60 degrees. Stable platforms exist within the beam ducts to mount optical components. An optical aperture of 50.0 mm diameter is available.

HI is a powerful diagnostic system which has been successfully used to measure wavefront distortions in previous aero-optics tests.

The AOEC HI system, as shown in Figure 5-7, will record up to six (6) holograms at variable time separations, (spacing from 1 - 100 ms). This repetition will provide an evolution of wavefront

Figure 5-3

Overview of Task 10:

AERO-OPTICS INSTRUMENTATION TASK

AOEC Objective: To establish a center in which aero-optic performance capabilities of seeker window designs can be consistently evaluated in ENDO LEAP mission environments.

I. Develop and Fabricate AO Instrumentation
   A. Wavefront Sensing (Holographic Interferometry)
   B. BSE
   C. Imaging: Visible, IR
   D. IR Radiometry, Spectrometry

II. Software Development
   A. Interferogram Analysis
   B. Data Acquisition
   C. Data Management (KDEC)

III. Calibration

IV. Install Instrumentation and Support Test Series
   A. 96"
   B. LENS
   C. NSWC

V. Reduction and Analysis of Data

VI. Reporting

Figure 5-4
AOEC INSTRUMENTATION

I. Holographic Interferometry

II. Point Source Imagery

- Visible
- IR (2-5 μm)

III. Line of Sight/Jitter

- Band Radiometers
- Spectrometers

Figure 5-5

Windows and Window Frames for Wedge Seeker and Sting Light Source Aperture

- Wedge Seeker Window
  - Fused Silica (.28 micron - 2.3 microns)
  - 3.2" x 4.5" x .5"
  - Frame design accomodates wedge seeker coolant system

- Light Source Aperture Windows
  - 20° LOS: 3.2" x 8" x .75"
  - 40° LOS: 3.2" x 4.9" x .75"
  - Fused Silica
  - Flush mount frame design

- Window materials for IR studies in progress
  - ZnS, ZnSe: .7 μm to LWIR
  - CaF_2: Covers visible and MWIR
  - Will order by Nov. 1, 1991

Figure 5-6

LINE-OF-SIGHT ORIENTATION

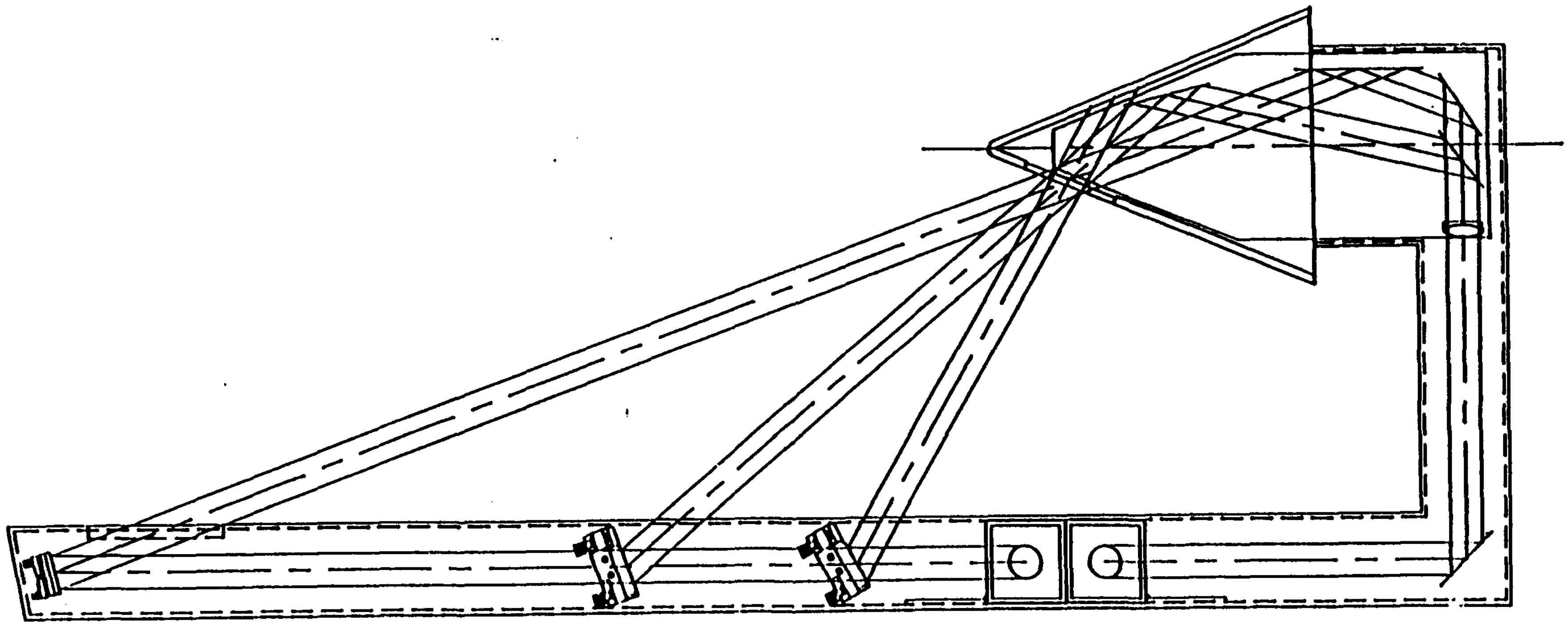

Figure 5-7

HOLOGRAPHIC INTERFEROMETRY

OBJECTIVE:

- RECORD 2 TRIPLE EXPOSURE HOLOGRAMS, SPACED BY $\Delta t=100\mu sec$, WITH ANGULARLY CODED REFERENCE BEAMS.
- SHOW EVOLUTION OF OPD ERRORS IN 100 μsec INTERVALS.
- PHASE SHIFTING WAVEFRONT ANALYSIS VIA DOUBLE-PLATE RECONSTRUCTION PROVIDES $>\lambda/100$ WAVEFRONT ERROR.

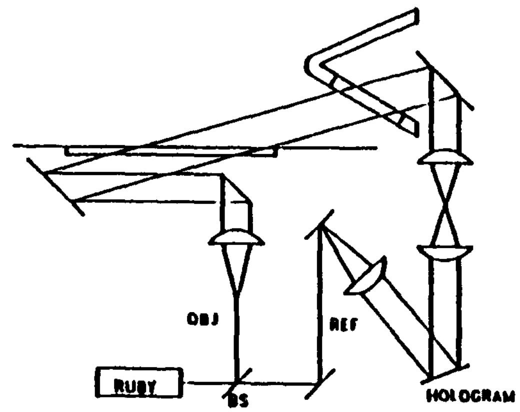

SPECIFICATIONS:

- (6) WAVEFRONTS RECORDED EVERY Δt μs
- PULSE SPACING, Δt, VARIABLE FROM 1 TO 400 μs
- HOLOGRAMS RECORDED AT 0.69μm
- SPATIAL RESOLUTION ALONG WAVEFRONT IS BETTER THAN 100μm (f/20)

EXPECTED RESULTS:

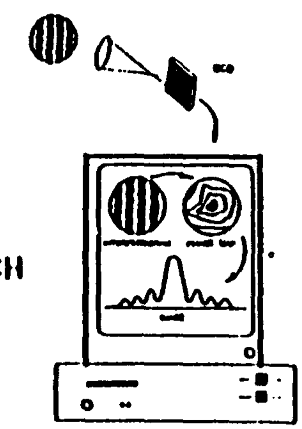

- WAVEFRONT OPD, ϕ(X,Y) AND RMS DISTORTION EACH OF 6 HOLOGRAMS
- PROPAGATE EACH OPD TO FOCAL PLANE TO DETERMINE:
  - IR POINT SPREAD FUNCTION,PSF
  - IR MODULATION TRANSFER FUNCTION,MTF

errors and statistical information. The holograms are exposed in the red band, (ruby = 0.69 μm), and will utilize an F20 telescope to resolve better than 100 μm in spatial dimensions across the wavefront. When weak wavefront distortions are to be measured and high accuracy is needed, advanced HI analysis will be used to achieve accuracy better than 1/100 waves. Software will be available to provide point spread and modulation transfer functions for IR bands.

PSI systems using visible and IR wavelengths will be available to provide imagery. The visible system will utilize coherent light and several coherent optical components to provide PSF's in rapid succession, perhaps 100 μm intervals. For example 16 images will be exposed on 128 x 128 pixels sectors of a 512 x 512 pixel CCD camera, all during a 3.2 ms period of facility operation. The visible system will use a HeNe laser, 0.63 μm. The exposure time of each image will be variable from 1-100μs, or longer. The sensor telescope will provide four pixel samples across the diameter of the Airy disc. These systems are shown in Figure 5-8.

The IR PSI system will utilize a black body source and an IR sensor. The black body will be subresolved and appear as a point source to the sensor. The IR system will utilize a small FPA (≈200 x 200 pixels) with 1000 frame/sec readout. Each frame will contain a single image. Again, any Airy disc diameter of four pixels is available. The IR PSI system will be available in bands within the 1-5 μm range.

Visible and IR imaging systems have been described. The visible device uses a laser and CCD camera. Acoustic-optic beam deflectors will scan the LOS during the short duration test, allowing image exposure durations form 1 ms to 200 ms. The IR device used a black body source and an IR sensitive FPA. The FPA would be PtSi or InSb and achieve a frame rate of 1000/sec. Further description is given in Figure 5-9.

The visible and IR PSI instrument specification requirements for wavelength, optical component materials, camera technology, frame rate, integration times, and applicability are identified in Figure 5-10.

BSE system will be available to measure LOS offsets produced by aero-optics. The BSE will utilize LOS of 20, 40 and 60 degrees. The centroid sensor will be sampled at 10Mhz and have frequency response over 1Mhz. The centroid sensor range/accuracy will be 1.5 milliradian and 10 μradian, respectively, as shown in Figure 5-11.

Figure 5-8

POINT SOURCE IMAGERY

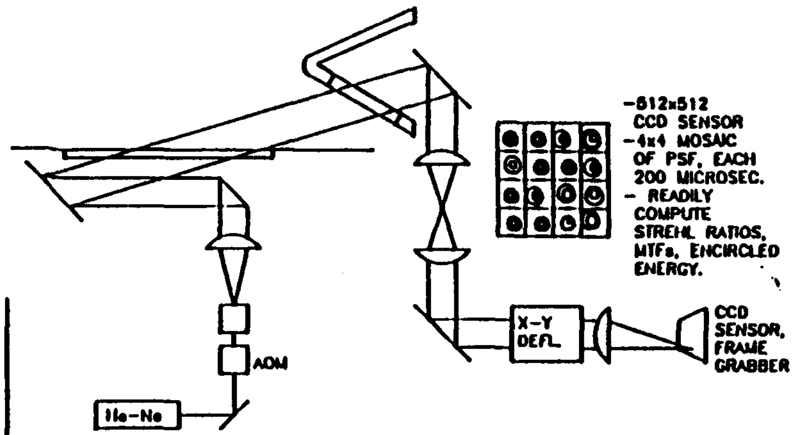

Objective:

- o Obtain images of PSF at 200 microsec intervals, before, during and after passage of shock wave.
- o For each PSF image, compute:
  - – 86% Encircled energy diameter
  - – Strehl Ratio
  - – MTF

Specifications:

- o PSF imaged every 200 microsec, 16 times, over 3.2 msec duration.
- o Each PSF imaged onto 128x128 portion of 512x512 CCD camera.
- o Wavelength = .633 micron.
- o Provide plot of 86% encircled energy diameter vs. time (<30 minute turn around time).
- o Provide 16 MTF plots showing its evolution inn time (1–2 hour turn-around).
- o Short exposure (< 1 μsecond).
- o Long exposure (100 μsecond).

Expected results:

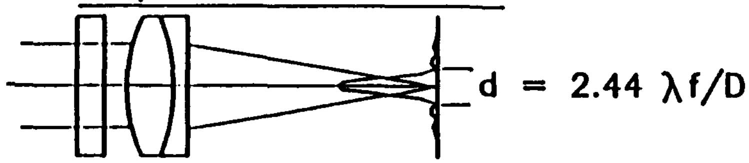

- o For wavelength= .633 micron, D=50mm, airy disc diameter is 30 microrad.
- o Pick f such that airy disc is four pixels wide.
- o If BSE = 1 millirad, then PSF will remain within 128 x 128 pixel grid reserved for it.

Figure 5-9

IMAGING/POINT SPREAD FUNCTION EVALUATION

❑ Visible

- Collimated HeNe source.
- Silicon CCD camera.
- Can be used to corroborate Holographic Interferometry results.
- Acousto-Optic beam scanning allows PSF measurement every 100-200 μ sec, exposures down to 1μ sec.

❑ Infrared

- Blackbody source.
- IR sensitive (PtSi, InSb), high frame rate (~1000 fps) cameras.
- More realistic imaging evaluation - effects of boundary layer emission/absorption become relevant.
- Possible collaboration with Aerojet.

Figure 5-10

Requirements for Point Source Imaging Instrumentation

	Visible	Infrared
Source	HeNe Laser	Blackbody, broadband
Wavelength	.633 micron	1 - 5.4 micron
Suitable Materials for Beam Tube Lenses and Windows	Glass, Fused Silica (CaF_2: NUV to MWIR)	ZnS, ZnSe: LWIR CaF_2: MWIR
Camera Technology	Si CCD	InSb or PtSi
Frame Rate	30 Hz (Will be upgraded for LENS.)	1000 Hz, 900 Hz
Integration time available (Short times: Jitter statistics (Long times: Improved sensor SNR.)	1 microsecond to 10 milliseconds (Acousto-Optic modulator)	Several microseconds to 1 millisecond (Electronic gating)
Predominant Nature of Image Degradation	Image blur diameter increases in direct response to density fluctuations across window.	IR radiation emitted by heated coolant gases forms increases backgound intensity, decreasing SNR and effective dynamic range Worst case: IR background can blind (saturate) sensor.

Figure 5-11

BORESIGHT ERROR

Objective:

Measure variations in centroid position of point spread function due to turbulence and shock wave.

Specifications:

- 10 MHz A/D Rate
- Three Lines of Sight:
  - −20 degrees
  - −40 degrees
  - −60 degrees
- Approximately 10 microradians positional accuracy.
- Approximately 1.5 milliradians Field of View.

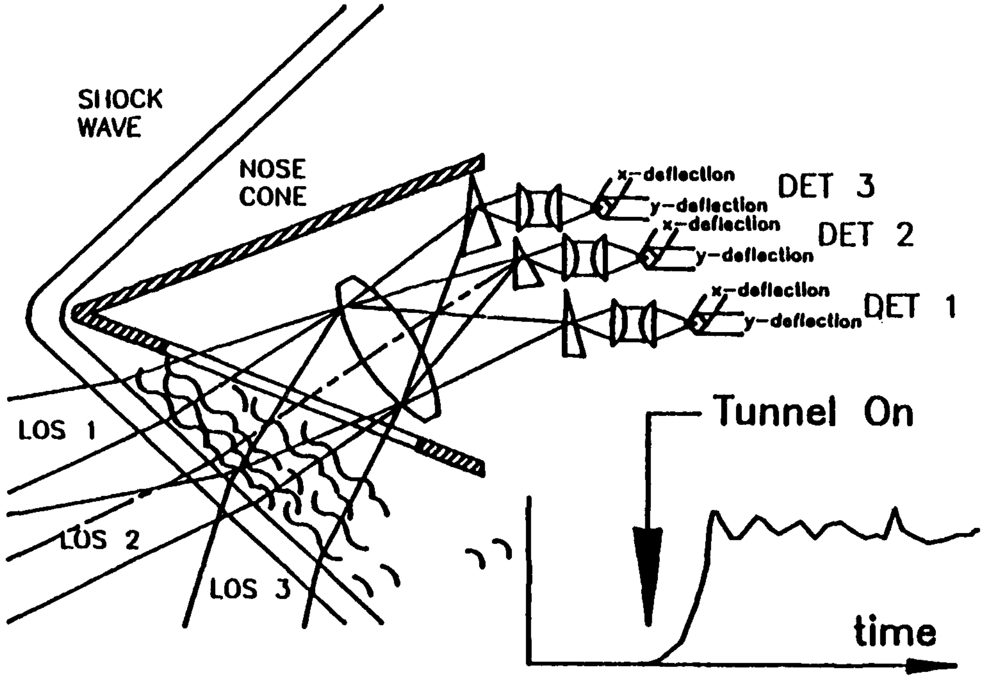

Expected Results:

- BSE due to shock wave refraction, approximately 1 milliradian.
- Jitter levels due to sub–aperture turbulence approximately 20–100 microradians.

An IR radiometer will be available to measure the absorption/emission of the shock/coolant layer, as shown in Figure 5-12. The sensor will look through the flow and a chopper wheel at a black body, before, during and after a run. The chopper frequency will be up to 10Khz. Sensor response will be available up to 10ms and in the MWIR and LWIR bands.

The IR spectrometer (Figure 5-13) will be available to measure spectral radiance in the SWIR, MWIR and LWIR bands. The spectral resolution will be 0.1 μm or better. A black body reference will provide calibration.

5.4 Programmatic Issues

Six tasks are planned to accomplish the aero-optic instrumentation task; including (1) hardw e, (2) software, (3) calibration, (4) testing, (5) data reduction and (6) documentation. The sche is shown in Figure 5-14. The hardware task will design and fabricate the instrumentation systems described in the previous charts. Software to operate instrumentation and to analyze data will be designed, implemented and integrated with the hardware instrumentation systems. Calibration of each instrument will be achieved first in the laboratory and later in the shock tunnel facility. Testing will be initiated after installation of the instrumentation systems into the LENS facility. Data reduction will be performed in parallel with the test activities.

The program plan for the 96" hypersonic shock tunnel (HST) test includes test objectives, instrumentation requirements and task plans (Figure 5-15). The test objectives are to measure RMS wavefront distortion, image degradation and Line-of-Sight deflection. Image resolution parameters (PSF and MTF) will be computed. The instrumentation requirements incorporate the use of the PRi holocamera, holographic reconstruction, fringe analysis, and tunnel-laboratory interface tubes. The task plan includes the initial modification and adaptation of the existing holocamera reconstruction, analysis, and instrumentation and of the design, assembly and installation of the tunnel-lab-interface tubes. The task plan is finalized by the conduct of the test through data analysis, reduction and report.

PRi will install and conduct a holograph measurements experiment on wedge tare models in the 96" facility in the Fall of '91. A top view of the optical system, the beam coupling tubes and the tare model is shown in Figure 5-16.

Holographic Interferometry (HI) is accomplished through the interference of wavefronts, as shown in Figure 5-17. In one case, the wavefronts are recorded before and during the flow; and in the

Figure 5-12

INFRARED RADIOMETRY

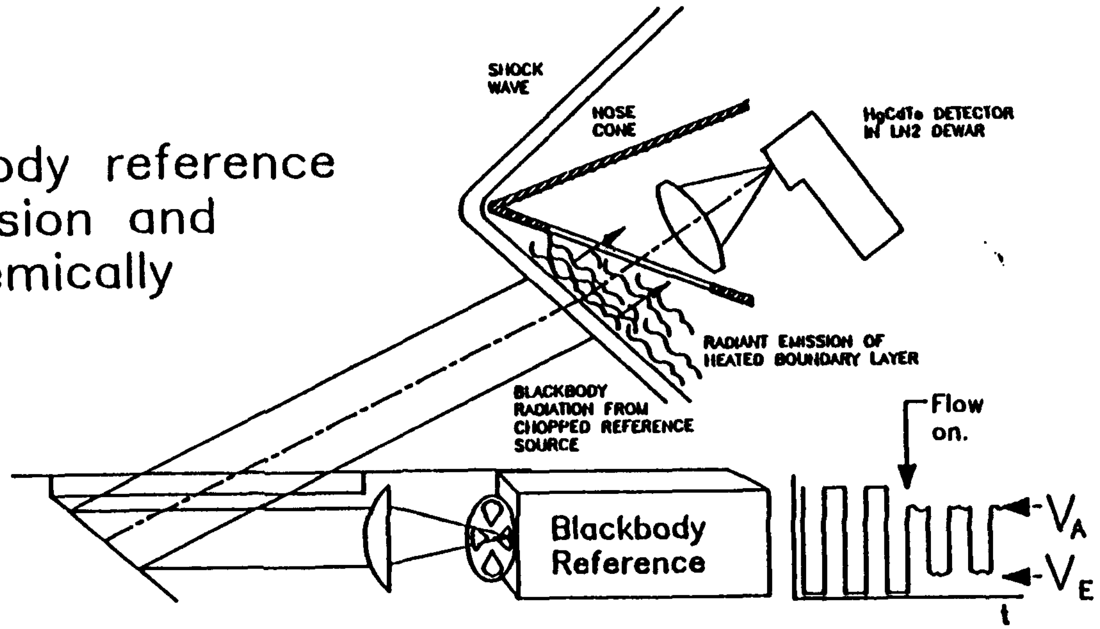

Objective:
Using chopped blackbody reference source, measure emission and absorption due to chemically active mixing layer.

Specifications
- o 10 microsecond detector decay time.
- o HgCdTe for 8–12 microns.
- o InSb for 1–5 microns.

Expected results:
- o Emission: V_E

$$V_E = \left[\int R_D(\lambda) L(\lambda) d\lambda \right] \frac{A_{det} A_{pupil}}{f^2}$$

- o Absorption: V_A

$$V_A = \left[\int R_D(\lambda) \exp[-\alpha(\lambda) z] L_{BB}(\lambda) d\lambda \right] \times \frac{A_{det} A_{pupil}}{f^2}$$

Figure 5-13

INFRARED SPECTROMETER

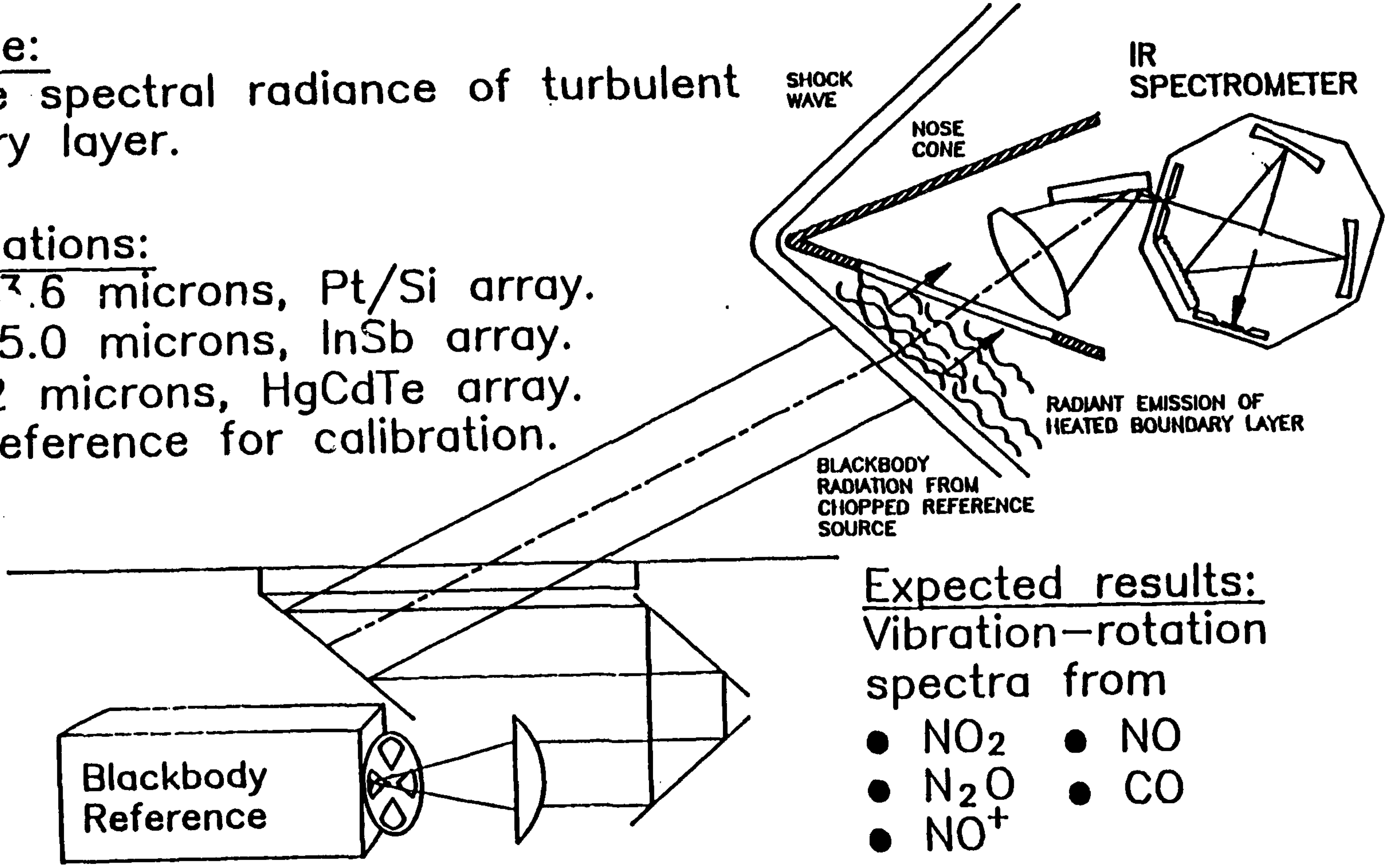

Objective:
Measure spectral radiance of turbulent boundary layer.

Specifications:
- 1.3–3.6 microns, Pt/Si array.
- 2.5–5.0 microns, InSb array.
- 8–12 microns, HgCdTe array.
- BB reference for calibration.

Expected results:
Vibration–rotation spectra from
- NO_2
- NO
- N_2O
- CO
- NO^+

Figure 5-14

TASK 10 - AERO-OPTIC INSTRUMENTATION SCHEDULE

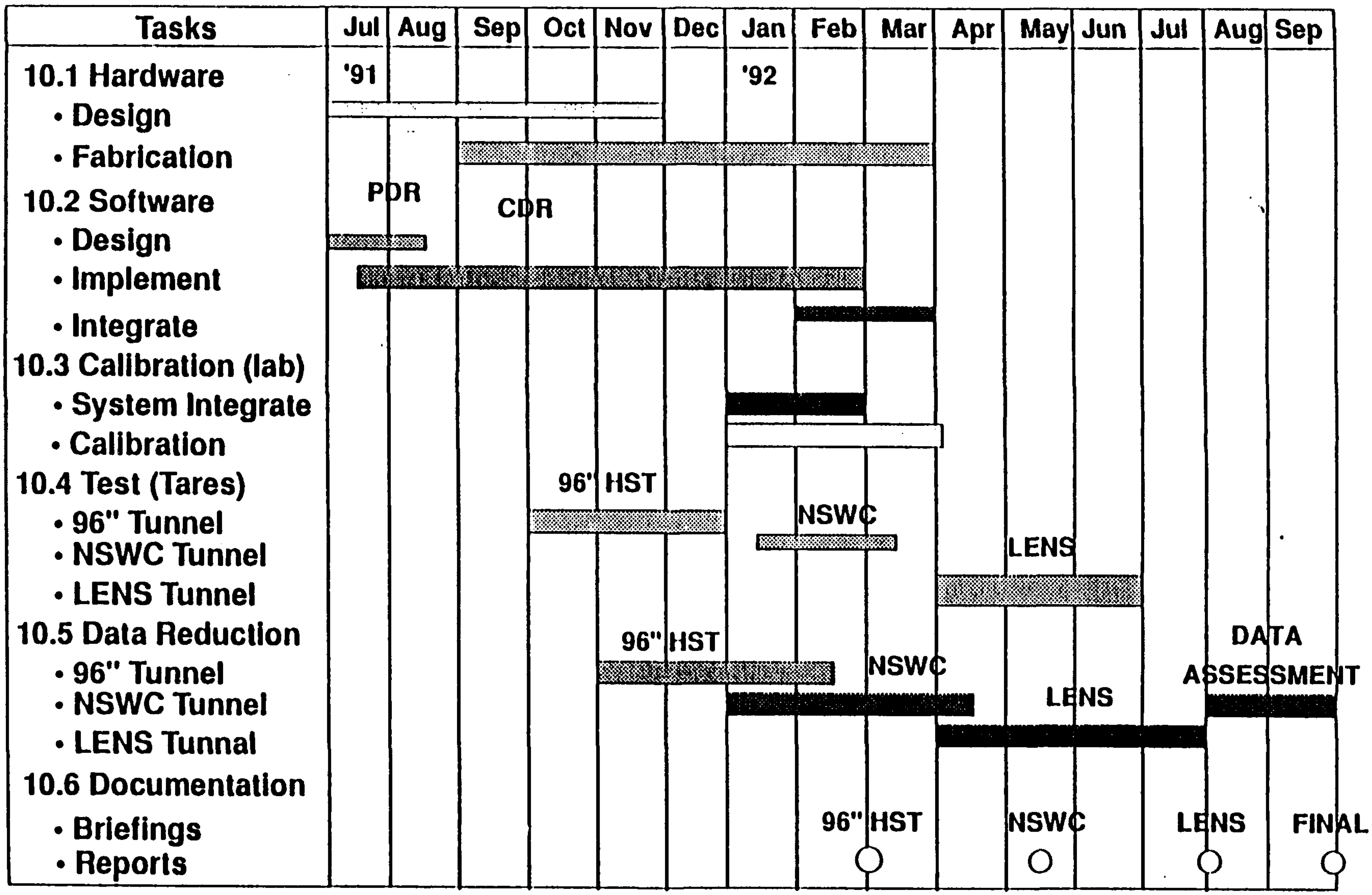

Figure 5-15
PROGRAM PLAN FOR 96" TEST

- ❑ Test Objectives
  - Measure OPD(x,y), RMS wavefront disturbance at aero-optic window of CALSPAN wedge seeker model
  - Compute image resolution parameters – PSF, MTF
  - (• IR Imaging – Possible schedule acceleration)
- ❑ Instrumentation Requirements
  - Wavefront sensor: PRi Holocamera (DPH)
  - Hologram reconstruction, fringe analysis
  - Tunnel-laboratory interface tubes
- ❑ Task Plan
  - Modify existing holocamera, reconstruction & analysis, instrumentation
  - Design, assemble and install tunnel-lab interface tubes
  - Tests, data analysis and reduction
  - Final report

Figure 5-16

PRI HOLOCAMERA CONFIGURATION FOR 96" TEST - FALL '91

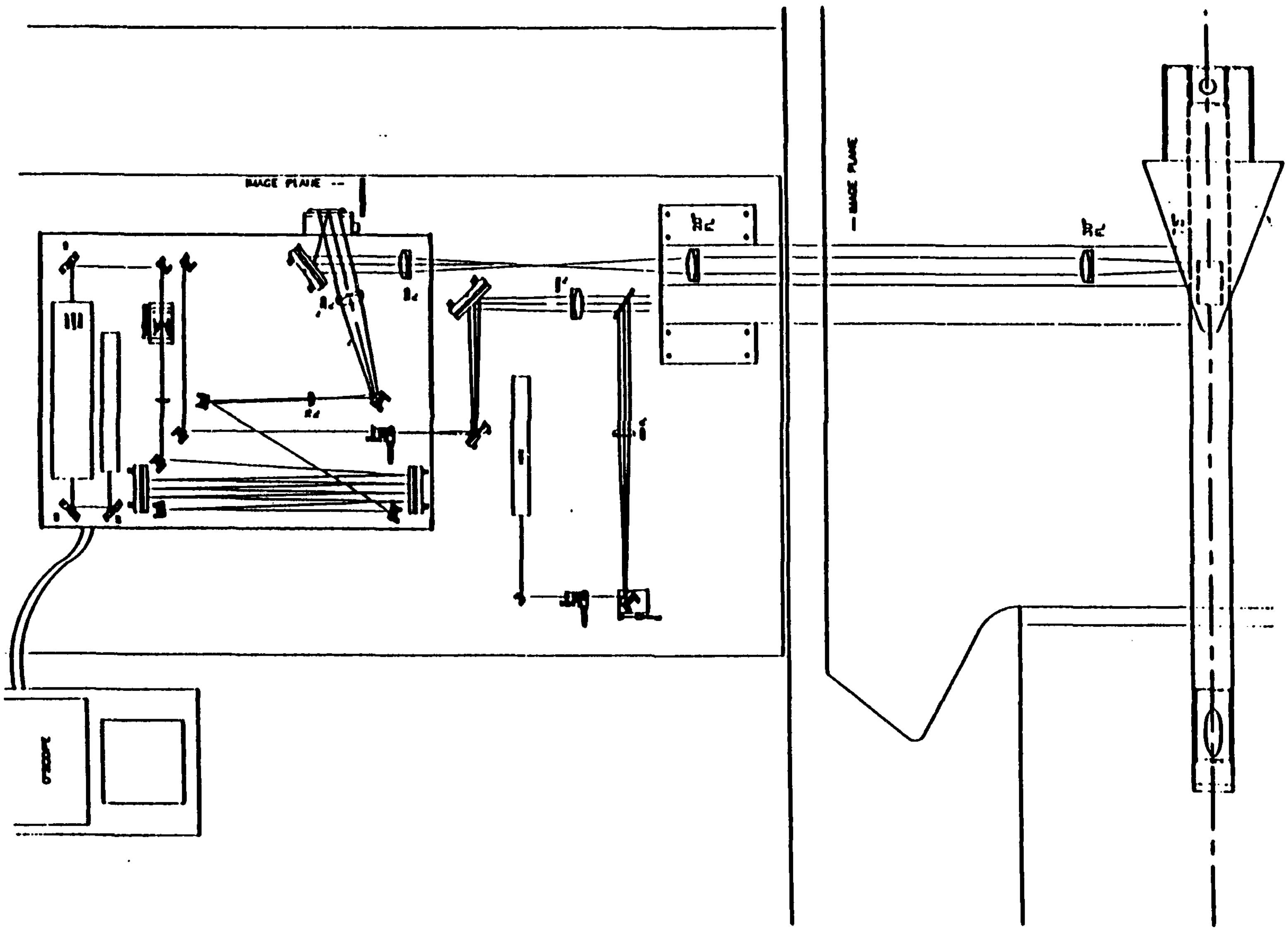

Figure 5-17

Wavefront Sensing via Holographic Interferometry

o Record: Two exposures, at times t_1 and t_2.

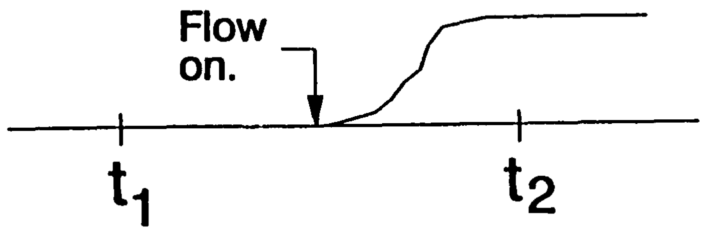

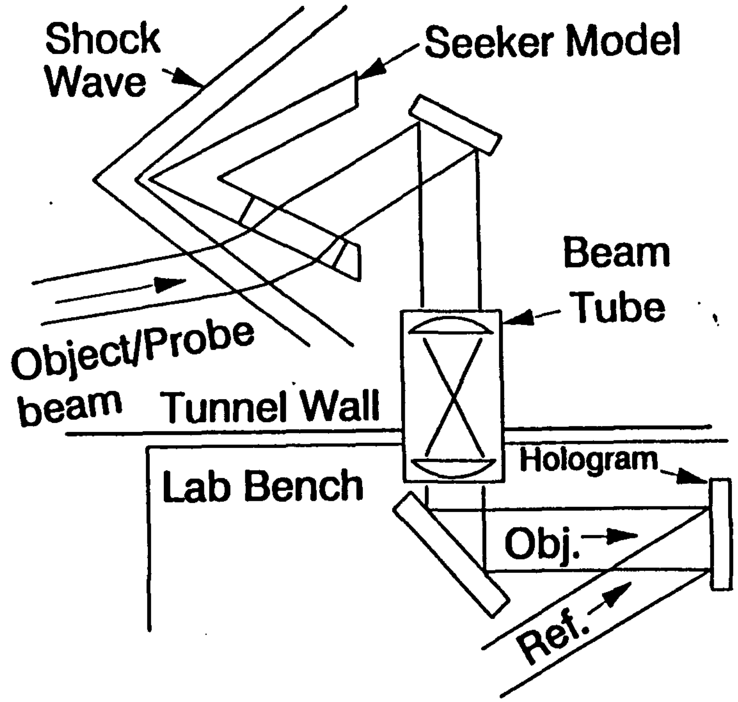

o Develop

o Reconstruct:

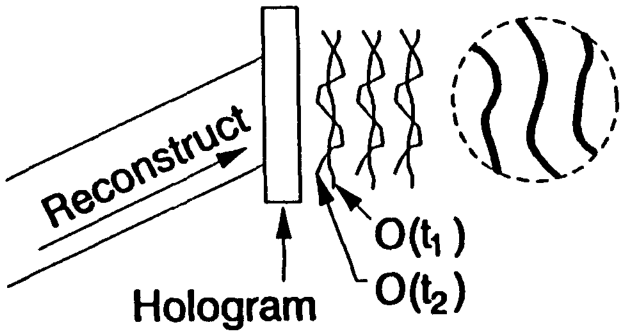

o Fringe analysis:

- o OPD(x,y)
- o RMS Wavefront error
- o PSF
- o MTF

other case both wavefronts are recorded during the flow. The holograms are recorded on high resolution film which requires wet chemical processing. The drying step completes the hologram process. The hologram plates are illuminated with a CW laser to reconstruct the flow and without flow wavefronts. The interference of these two wavefronts creates fringes which represent the flow induced phase distortions. Image analysis is used to measure the phase map, RMS phase and associated PSF and MTF.

The holographic methods are accomplished through "Double-Plate" or "Double-Pulse" techniques (Figure 5-18). For the Double-Pluse technique, holograms are exposed before and during the flow on individual plates. These plates are placed together in reconstruction, hence "Double-Plate", and the resulting interferogram depicts an absolute phase map of the flow field. For the Double-Pluse technique, both holograms are exposed during the flow on a single plate. This plate is illuminated in reconstruction, in which each hologram replays a wavefront. The resulting interference depicts the difference between the two stored wavefronts. As such, the Double-Pulse technique is ideally suited for measurements of turbulence.

The seeker model and light source aperture requirements deal mostly with vibration and flow on quality across the optical path. The structure must not transmit vibration to the optical platform and the optical windows must not be distorted by mounting frame torques or through distortion of the structure. The design of the structure must not disrupt the quality of the optical path. As such, the structure must be aligned with the flow and its leading edge and its surface must be designed to minimize the boundary layer influence on the window.

The TLI structures are the model support tube, the beam optics tube and the wind shields (Figure 5-19). The model support tube, MST, includes the seeker model, the source window, mechanical isolation from the tunnel walls and the wind shields, and air tight bellows between the MST and the tunnel walls. The beam optics tube, BOT, is housed within the MST and is suspended from the optical platform which sits on the facility floor. The BOT does not contact the MST. The optical beam (2 inch, diameter) is coupled through the BOT and pointed through the light source aperture window in the MST. The wind shield deflects strong airflows from the MST and is mounted to the tunnel structures.

The OBT design includes mechanical and optical specifications. The mechanical specifications are for table mounting, light source windows for 20 and 40 degree LOS viewing angles, access ports for mirror and lens adjustment, 4 x 4 inch cross section for in flow sections, lense and mirror mounts and seeker head optical platform. The optical components are mirrors and lenses. The

Figure 5-18

BASELINE HOLOGRAPHY CONFIGURATION

Double-Plate	Double-Pulse
<u>Steps</u> 1. Expose TARE hologram in vacuum on Plate 1 prior to run. 2. Expose FLOW hologram on Plate 2 during flow. 3. Combine holograms in double-plate reconstruction. 4. Interferogram gives OPD map of entire flow; i.e., mean & fluctuation flow.	<u>Steps</u> 1. Expose two holograms on one plate during flow. 2. Holograms separated in time by 1 - 800 μs. 3. Reconstruction gives time difference, $OPD(t_1) - OPD(t_2) = \Delta OPD$ 4. Interferogram depicts changes or effects of turbulence

Figure 5-19

TUNNEL-LAB INTERFACE STRUCTURE

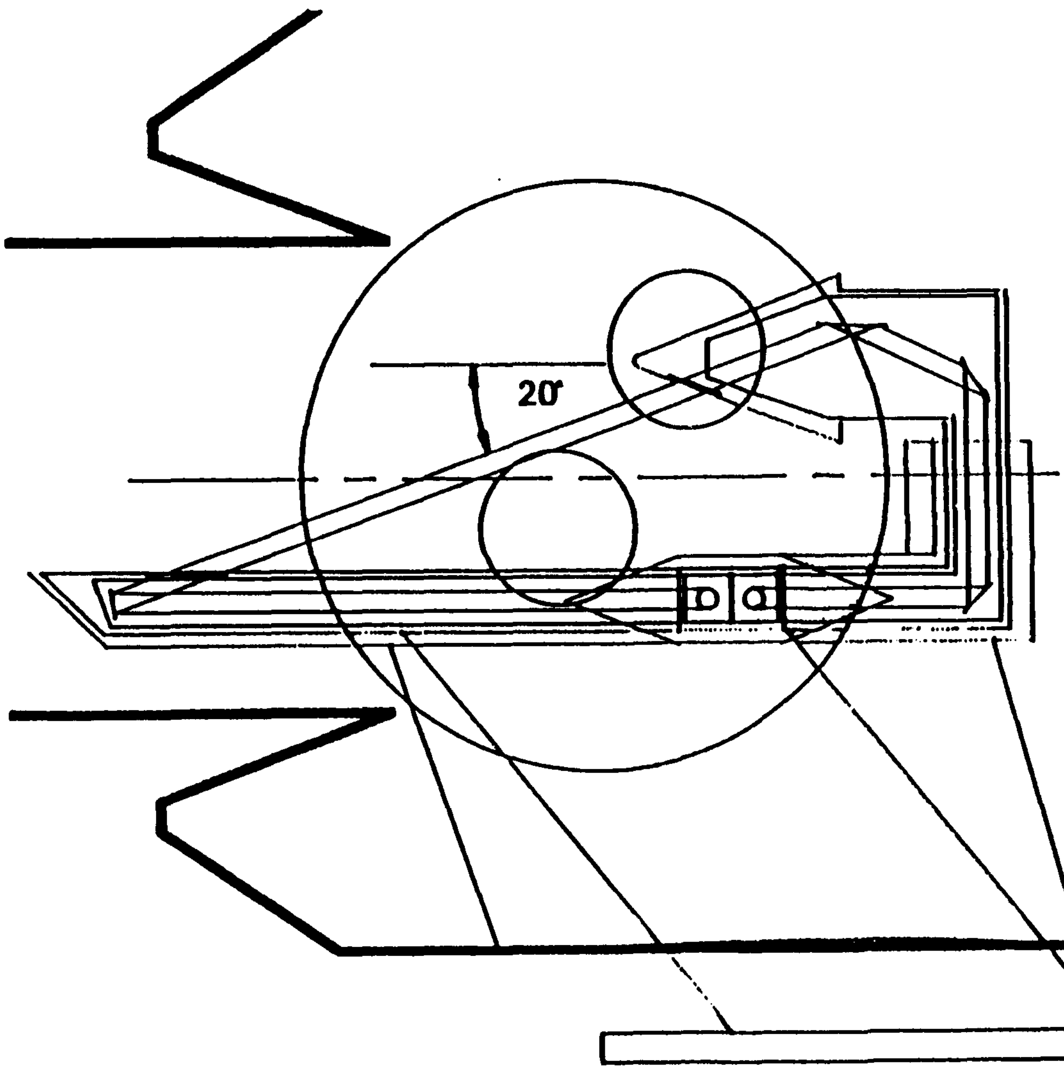

- MODEL SUPPORT TUBE:
  - SEEKER MODEL
  - SOURCE WINDOW
  - MECHANICALLY ISOLATED FROM TUNNEL WALLS AND WIND SHIELD
  - AIR TIGHT BELLOWS TO TUNNEL
- BEAM OPTICS TUBE:
  - ISOLATED FROM MODEL SUPPORT TUBE
  - MOUNTED TO EDGE OF OPTICS TABLE
  - 2" BEAM DIAMETER
  - HOUSES BREADBOARD FOR MODEL INSTRUMENTATION
- WIND SHIELD:
  - DEFLECTS SHOCK FROM MODEL SUPPORT TUBE
  - MOUNTED TO TUNNEL

optical specifications of the mirrors are defined by a 2 inch beam diameter and for high reflection in visible and IR bands. More complete specifications are given in Figure 5-20.

The preliminary design (Figure 5-21) of the Optical Beam Tube (OBT) achieves a weight of 70 pounds and a 5x5 inch crossection with 0.25 inch wall thickness. The OBT mounts on the optical platform and houses the relay mirrors and lenses.

A tunnel airflow quality test is planned to measure the background levels of optical distortion due to LSA window turbulence and freestream turbulence. This test is shown schematically in Figure 5-22. A MIMIC model is identified to mimic the LSA window flow. The optical experiment measures twice the background level produced by the LSA.

The conceptual design was completed in September 91. The detail design, fabrication and assembly will be completed in the Fall of 1991. The installation and test will be completed in the Winter of 1992. This schedule is further delineated in Figure 5-23.

PRi will interact with BAA and ENDO LEAP contractors to insure that sensor apertures can be evaluated in the AOEC facility with a minimum of alterations. It is expected that the generic refractive/radiative evaluation instruments under development for the AOEC facility will form the basis for evaluation of BAA and ENDO LEAP contractors' sensor apertures. Tasks completed in the BAA integration efforts are summarized in Figure 5-24. BAA seeker aperture concepts are categorized into optical, millimeter wave and dual mode systems in Figure 5-25.

The following tasks will be completed during a follow-on study:

Optical seekerhead evaluation capability will be achieved for refractive and radiative degradations.

Existing holography instrumentation will be reconfigured to perform early parameter design experiments, 96" test.

Based on these prototype experiments, the final design parameters for the A-O instrumentation will be selected and constructed.

Provisions for instrumentation adaptation to BAA and Prime contractor seekerhead designs will be made.

Final A-O instrumentation suite will be tested in LENS facility to achieve calibration of facility and evaluation capability.

Figure 5-20

Optical Beam Tube Design Specifications

Mechanical Design

- Tabletop mount.
- Two light source aperture modules: 20° & 40° LOS.
- Access ports for mirror and lense adjustment.
- 4" x 4" Cross sectional area on in-flow portion.
- Mounts for lenses and mirrors.
- Seeker head platform that serves as optics breadboard.

Optical Components

- Mirrors:
  - 3" diameter
  - Front surface aluminized
  - Suitable for both Visible and IR.
- Relay lenses
  - Visible: Glass achromats
  - Broad band IR: ZnS or ZnSe (.7 µm - 12 µm)
  - Visible-to-MWIR: CaF_2 (Under evaluation).

Preliminary Design of Optical Beam Tube

- o Houses mirrors and lenses that interface tunnel and lab bench.
- o Approximately 70 lbs. (Al), 5" x 5" ID, .25" wall thickness.
- o Preliminary design review w/ CALSPAN scheduled for Sept. 5, '91.
- o Final design review set for Sept. 25, '91.
- o Tunnel installation to be completed Nov. 13, '91.

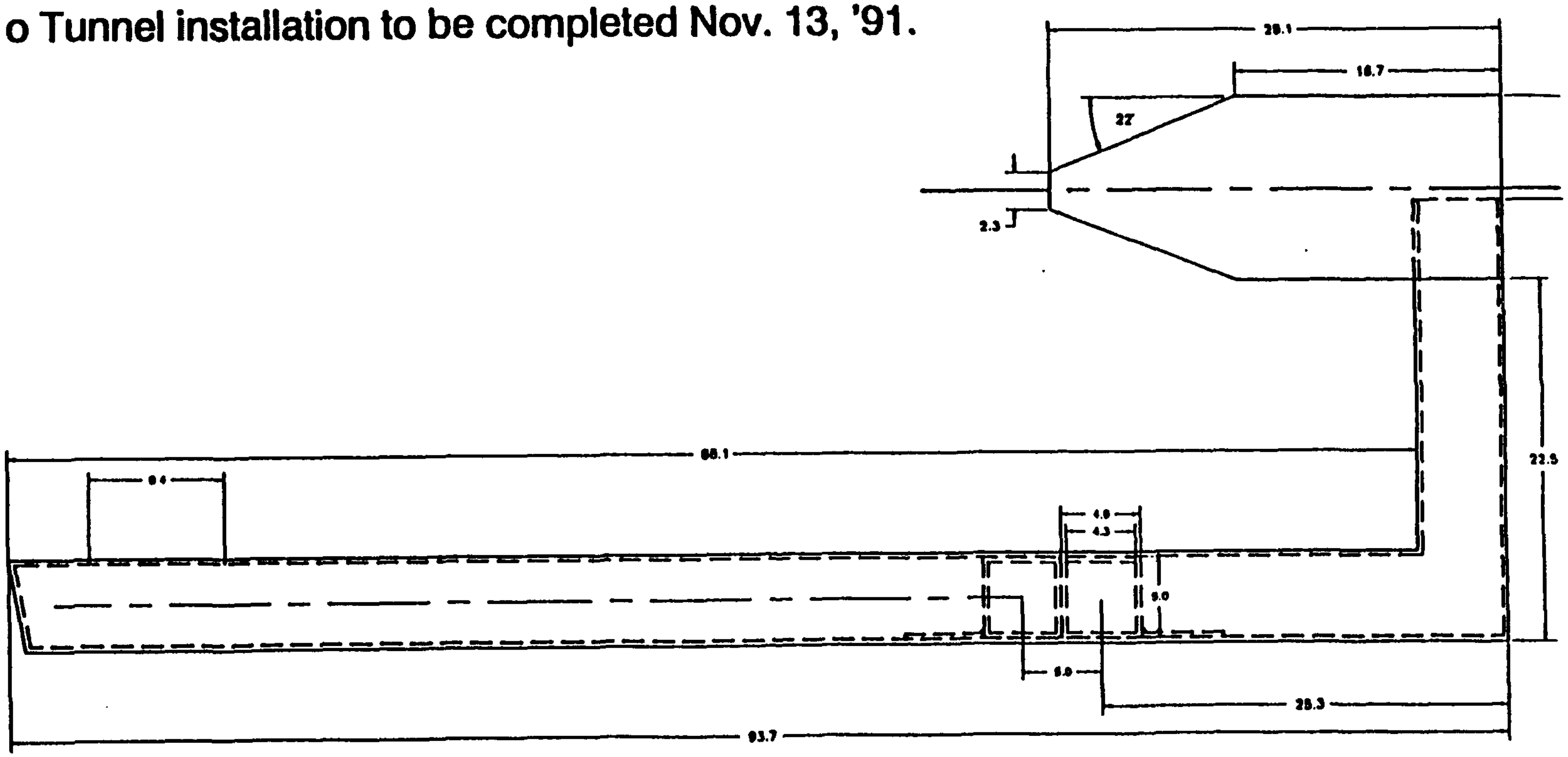

Figure 5-22

Characterization of turbulence/air flow over probe beam source window.

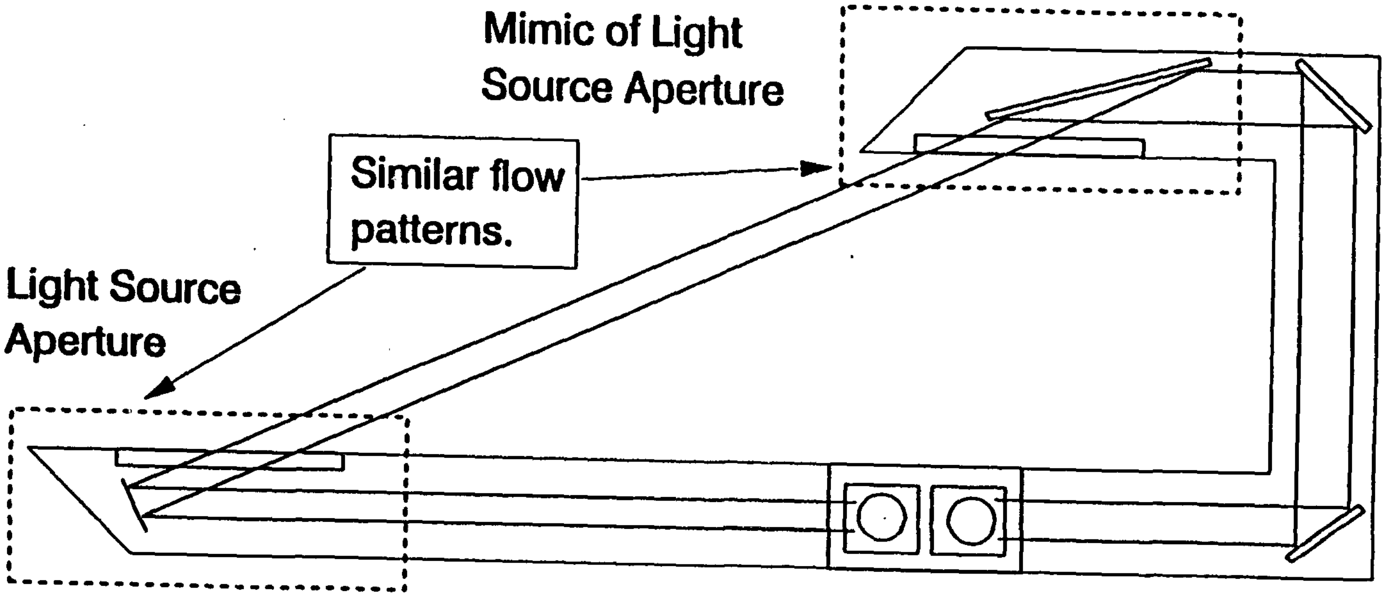

- o Mean square wavefront error measured will be twice the amount contributed solely by turbulent flow over light source aperture.
- o Expected contributions to wavefront error: LSA vs. Aero-optic window

Dual LSA:
Expected wavefront variance, $\sigma = 2 \times \sigma(\text{LSA})$

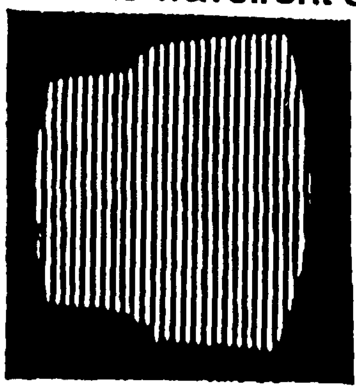

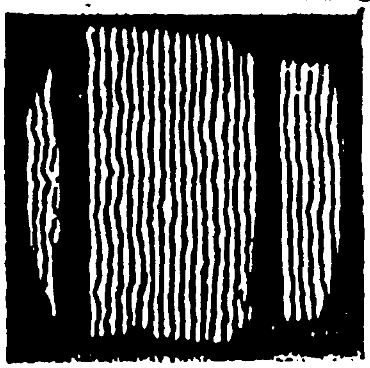

LSA + AOW:
Expected wavefront variance, $\sigma = \sigma(\text{LSA}) + \sigma(\text{AOW})$
(HEDI, AEDC, 1987)

Figure 5-23

PRESENT STATUS OF 96" TEST PREPARATIONS

Tasks	Status
Conceptual Design (Holocamera and optics tube)	Complete
Detailed Design	Will commence immediately after PDR, September 5, 1991
Final Design (Critical Design Review)	CDR September 30, 1991
Fab/Assemble	Shipping to CUBRC, October 25, 1991
Install	No-flow test holograms, November 15, 1991
Tests, Data Reduction	From Nov '91 to Feb '92

Figure 5-24

SUMMARY OF BAA INTEGRATION EFFORTS

- Reviewed short document overviewing 22 different aperture concepts.
- Seeker catagories:
  - 14 - optical
  - 6 - MMW
  - 2 - dual mode
- Objective: Integration of A/O instrumentation suite with 14 - Optical and 2 - dual mode.
- Initial review suggests that wavefront, imagery, BSE and jitter instrumentation can be adapted to many of the BAA concepts.
- Requirement: Coordinate with BAA contractors to establish interface requirements and produce A/O instrumentation configurations.

Figure 5-25

BAA SEEKER APERTURE CONCEPTS

	OPTICAL	MMW/IR	MMW
1) DIAMOND WINDOW	X		
2) RECESSED WINDOW	X		
3) HOLOGRAPHIC LENS	X		
4) FISH EYE VARIANT	X		
5) MULTI-SPECTRAL WINDOW	X		
6) REAL-TIME A/O COMPENSATION	X		
7) FISH EYE	X		
8) FACETED DOME	X		
9) INTERNALLY.COOLED WINDOW	X		
10) AEROSPIKE	X		
11) MULTIPLE APERTURE	X		
12) MICROLENS WINDOW	X		
13) ENHANCED APERTURE	X		
14) REVOLVING WINDOW			X
15) DUAL MODE DOME		X	
16) DIAMOND COATED DOMES			X
17) SILICON NITRIDE			X
18) COOLED CERAMIC			X
19) REACTION BONDED SiN			X
20) CERAMIC RADOME			X
21) MMW/IR DUAL MODE		X	
22) THIN WINDOW	X		

Section 6
ANALYSIS OF FACILITY PERFORMANCE AND VALIDATION EXPERIMENTS

University of Alabama-Huntsville/Aero-Thermo Technology, Inc.

6.1 INTRODUCTION

The design and development of a small effective seekerhead is one of the most important and difficult challenges in the development of advanced endo-atmospheric interceptors. The program at CALSPAN-UB is based on the potential to reduce significantly the scale of an endo interceptor. This scale reduction potential was demonstrated in recent intensive and successful miniaturization programs. While the size of the sensor head can potentially be reduced, however, the aperture of the system is much more difficult to downsize. Retaining aperture size on a smaller seekerhead can be achieved only by increasing the percentage of the nosetip through which the target is viewed. This naturally leads to placing the optical components in the more severe aerothermal environment close to the small nosetip. For the design of such a seekerhead, effective cooling and aero-optical performance become the key issues.

Designing a small sensor head with a large usable aperture requires a very sophisticated window and cooling system configuration. Basically the coolant injection system must occupy a very small part of the surface area and yet provide an effective coolant layer with a minimum of optical distortion. The basic problem in seekerhead development is that while the current design tools are potentially capable of providing good estimates of the cooling requirements, these techniques do not accurately predict the aero-optic distortion associated with turbulent mixing and flowfield radiation over the windows. These inadequacies are intrinsically related to a lack of understanding and inability to model turbulence and nonequilibrium chemistry in hypersonic flight. Even for the simplest seekerhead configuration it is unlikely, even with an aggressive program of fundamental experiments and analysis, that aero-optic distortion or flowfield radiation will be predicted with the required accuracy in the near future. However, because of the relatively small size of advanced endo-atmospheric seekerheads for velocities up to about 14,000 ft/sec, it is possible to duplicate the flight environment in ground test facilities. The LENS facility is under development at Calspan-UB Research Center to evaluate directly the aero-optic and aerothermal performance of candidate seekerheads as well as provide direct calibration of prediction techniques.

In Section 6-2 we discuss our initial efforts to select state-of-the-art flow solvers with capabilities for determining the inherent salient flowfield features such as turbulence and reacting chemistry. In addition, the codes selected are capable of treating interceptor nosetip and forebody transpiration cooling in turbulent flows at hypersonic speeds.

The information in Section 6-3 presents the capabilities and solution techniques for two state-of-the-art flow solvers with the desired capabilities to support the Calspan-UB effort. Section 6-4 presents results obtained from these two codes compared to experimental data. Parameters investigated include grid structure, number of grid points, chemistry model and turbulence model. The experimental data utilized are from Calspan's 48" and 96" shock tunnels. In Section 6-5 the results for predictions of the flow in the LENS "D" nozzle are presented; and finally in Section 6-6, calculations are reported for the flowfield properties over a model to be used in the validation experiments in the LENS facility.

6.2 BACKGROUND

The General Aerodynamic Simulation Program (GASP) was chosen because it appears to be the state-of-the-art in CFD, offering many options including upwinding, chemical kinetics, numerical solution methods, blocking and nonequilibrium thermodynamics. However, the one shortcoming which GASP presently has is a deficiency in turbulence modeling. GASP currently uses the simple algebraic model to Baldwin-Lomax (Ref. 1) to determine eddy viscosity. This was orignally developed to predict heat transfer and skin friction for simple flat plate boundary layer flows and the spreading of two-dimensional shear layers. Using this model, the GASP code was used to predict the wall quantities, heat transfer and pressure for the experimental conditions reported by Holden et.al. in Ref. 2 for a wall bounded shear layer and a wall bounded shear layer/shock interaction experiment shown in Fig. 6-1. Results of these calculations, presented in Section 6-4, show reasonable agreement for pressure and good agreement for heat transfer when the grid is adjusted properly.

A second code chosen to predict the wall quantities of this experiment was the Multiphase All-Speed Transient Flow Solver (MAST), Ref. 3. This code is a two-dimensional, pressure based, time dependent Navier-Stokes solver, which has a highly developed k-e model to determine the eddy viscosity coefficient. The purpose of these calculations was to demonstrate improved accuracy when using an appropriate turbulence model and the deficiencies of using a simple algebraic formulation.

6.3 CODE DESCRIPTION

6.3.1 The General Aerodynamic Simulation Program (GASP)

The GASP code is capable of solving the complete (Reynolds-averaged) Navier Stokes (NS) equations on structured hexagonal meshes. Subsets of the complete NS equations, including Thin-Layer Navier-Stokes, Parabolized Navier-Stokes, (PNS), and

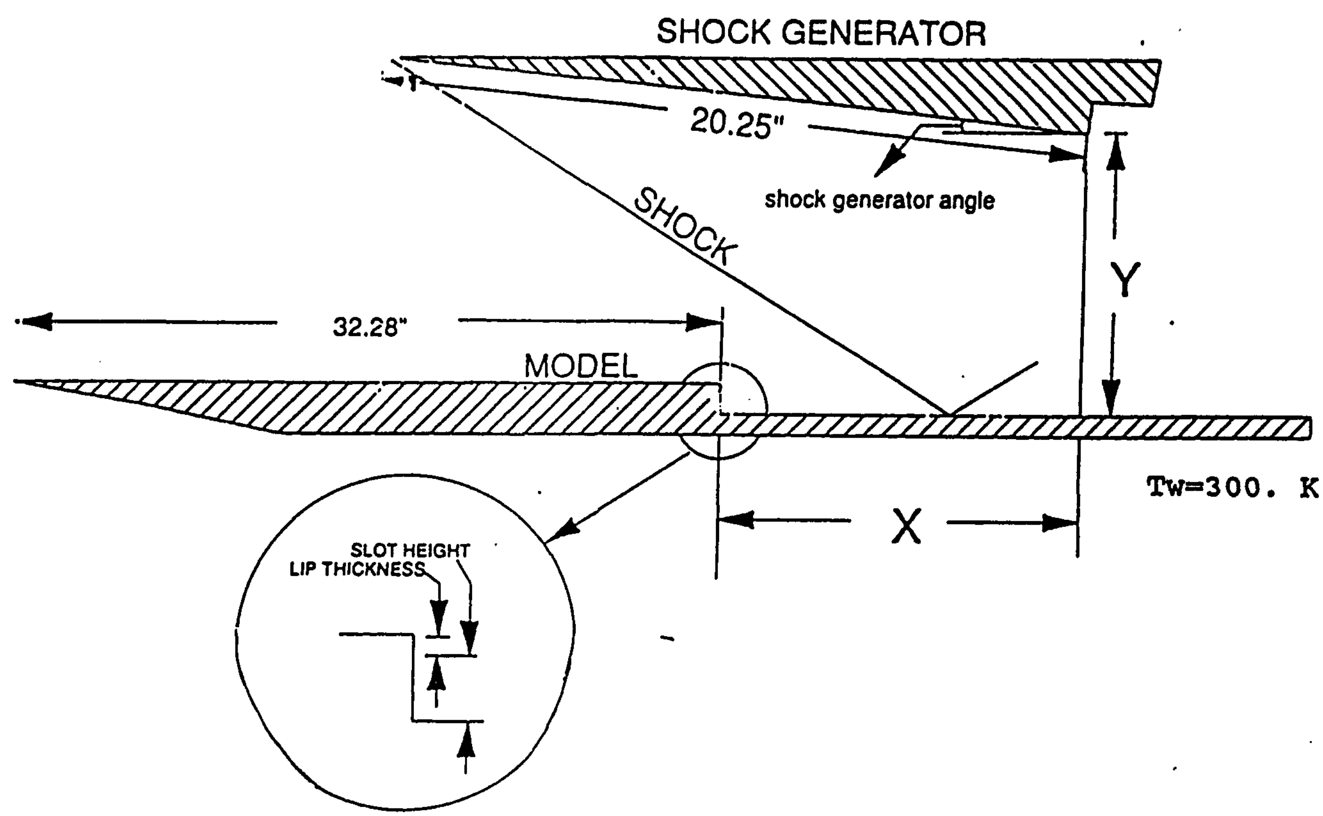

Figure 6-1 - SHOCK GENERATOR DIAGRAM

Aero Therme Technology (AT2)
HB:ct 7/26/91

Euler equations may also be solved. GASP provides the user with various time integration/solution algorithm choices, ranging from explicit to implicit factored/relaxation algorithms. Space-marching regions of supersonic inviscid flows as well as PNS. simulations are allowed and can be mixed with regions whose behavior is elliptic in character. GASP incorporates a general multi-block or zonal feature that allows the user to construct grids by piecing together individual blocks of grids. The patched grid interface is contrained to be one-to-one correspondence. There are no constraints, however, on how blocks can be linked together. Moreover, the choice of solution procedures among the zones is quite flexible.

The present calculations were made from solutions of the full Reynolds-averaged Navier-Stokes equations using multiple block grids. Numerical experiments were conducted to determine the effect of grid densities on the wall quantities. With the blocking capabilities of GASP, gridding changes were made in the zones of interest near the wall and just downstream of the coolant jet while maintaining the same external flow structure and grid density.

The discretization of the inviscid fluxes can be accomplished by means of flux-splitting techniques. Originally developed for a perfect gas, these methods have been extended to flows in chemical equilibrium, and to mixtures out of chemical and thermal equilibrium. These techniques are very accurate and robust when used for transonic, supersonic and hypersonic flows, and are fully compatible with the conservative finite-volume, shock-capturing approaches found in GASP. For the calculations presented here, the approximate Riemann solver due to Roe was used. Previous experience has shown this to be somewhat less robust but more accurate than some of the other flux-splitting techniques.

The slot cooling experiment of Holden et.al., simulated by this numerical study, utilized helium as the coolant. The gas model used for the GASP calculations was based on a mixture of nitrogen and oxygen to simulate the free stream and helium for the coolant.

Baldwin-Lomax Turbulence Model

The algebraic turbulence model used for these calculations is based on the Baldwin and Lomax model, Ref. 1. When turbulent flow analyses are required, the viscous coefficients are modified as follows:

$$\mu_{Total} = \mu = \mu_T$$

$$\frac{\kappa_{total}}{Pr} = \frac{\kappa}{Pr} + \frac{\mu_T}{Pr_T}$$

where μ is the turbulent viscosity, and Pr is the turbulent Prandtl number ≅0.9. For bounded flows the turbulent viscosity is computed from

$$\mu_T = Re\ \varrho\ \ell\ \underline{V}$$

where

$$\ell = \ell_0 d\,(1 - e^{-d+/\bar{A}+})$$

$$d = \sqrt{(x - x_w)^2 + (y - y_w)^2 + (z - z_\omega)^2}$$

$$d^+ = \sqrt{Re\ \varrho_2\ \omega\ d^2/\mu_w}$$

$$V = \ell\omega$$

6-3-2 Multiphase All-Speed Transient Flow Solver (MAST)

The MAST code solves the complete Reynolds-averaged Navier-Stokes equations on a body-fitted generalized non-orthogonal grid system. This code was developed at UAH for a typical sub/supersonic spray combustion condition. The governing equations of the gas phase are solved by means of a control-volume based finite-difference method in a time-marching fashion. A second order accurate, central differencing scheme is used for the diffusion terms, and a TVD type upwind scheme is used for the convection term. The implicitly coupled pressure and velocity equations are solved by an operator-splitting algorithm (Ref. 3), with individual equations being solved by an efficient conjugate gradient matrix solver. In the MAST code, a generalized equilibrium chemistry subroutine, utilizing the minimization of Gibbs free energy (Ref. 4) technique, was used for thermophysical properties of the multi-species gas mixture with the aid of the JANAAF data base.

Turbulence in the flow field is accounted for by means of an eddy viscosity formulation based on the two equation k-e model. With this model, the effective transport coefficient for momentum and energy are given by:

$$\mu\ \mathrm{eff} = \mu + \mu_t$$

$$\frac{\mathrm{Keff}}{Pr} = \frac{K}{Pr} + \frac{\mu_t}{Pr_t}$$

where μ_t is to be

$$\frac{\mu_t}{\rho} = C_\mu \frac{k^2}{\varepsilon},$$

and Pr is the turbulent Prandtl number (≅0.9). Turbulence quantities k and e are solved by their respective transport equations as follows.

$$\frac{\partial}{\partial t}(\rho k) + \frac{\partial}{\partial x_i}(\rho\, U_i k) = \frac{\partial}{\partial x_i}\left[\left(\mu + \frac{\mu_t}{\delta_k}\right)\frac{\partial k}{\partial x_i}\right]$$

$$- \rho\,\overline{u'_i u'_j}\,\frac{\partial U_i}{\partial x_j} - \frac{\mu_t}{\rho^2}\,\frac{\partial \rho}{\partial x_j}\,\frac{\partial P}{\partial x_j} - \rho\varepsilon \qquad (1)$$

$$\frac{\partial}{\partial t}(\rho\varepsilon) + \frac{\partial}{\partial x_i}(\rho\, U_i \varepsilon) = \frac{\partial}{\partial x_i}\left[\left(\mu + \frac{\mu_t}{\delta\varepsilon}\right)\frac{\partial \varepsilon}{\partial x_i}\right]$$

$$- C_1\,\frac{\varepsilon}{k}\left[\rho\,\overline{u'_i u'_j}\,\frac{\partial U_i}{\partial x_j}\right] - \frac{\mu_t}{\rho^2}\,\frac{\partial \rho}{\partial x_j}\,\frac{\partial P}{\partial x_j} - C_2\rho\,\frac{\varepsilon^2}{k} \qquad (2)$$

The constants appearing in equations (1) and (2) have the values:

$$\delta_{k} = 1.0,\ \delta_{\varepsilon} = 1.3,\ C_1 = 1.43\ \ C_2 = 1.92$$

and the Reynolds stresses are related to the mean flow gradients by the Boussinesq equation:

$$- \rho\,\overline{u'_i u'_j} = \mu_t\left[\left(\frac{\partial \mu_i}{\partial x_j} + \frac{\partial \mu_j}{\partial x_i}\right) - \frac{2}{3}\,\frac{\partial U_k}{\partial x_k}\,S_{ij}\right]$$

$$- \frac{2}{3}\,\rho k\, S_{ij}$$

The boundary conditions for the flow fields and turbulence quantities as well as the temperature field are applied by means of the "wall functions" (Ref. 5). In the wall function formulation, the boundary conditions for velocities, k, e, and temperature are not applied at the wall but are applied one point away from the wall. This wall boundary condition treatment has the advantage of eliminating extra fine grids very near the wall. The behaviors of the field variables were then prescribed by the universal functions based on the equilibrium layer profiles as follows:

$$\frac{U\rho}{u^*} = \frac{1}{k}\ln\left[Ey_p\, u^*/\nu\right] = \frac{1}{k}\ln\left[Ey^+\right]$$

$$\frac{Tp\text{-}Tw}{q^*} = \frac{\delta_T}{k}\ln\left[Ey_p\, u^*/\nu\right] + \delta_T P\sigma$$

and u* is the friction velocity, evaluated as

$$\tau_w = -\left[\frac{\rho\, k\, C_\mu^{1/4} k_p^{\ 1/2}}{\ln\left[Ey^+\right]}\right] U_p \quad ,$$

and q is evaluated as

$$\frac{qn}{\rho Cpu^*}$$

$$P\delta \text{ is given as: } \quad 9\left(\frac{\delta_L}{\delta_T} - 1\right)\left(\frac{\delta_L}{\delta_T}\right)^{-1/4}$$

Finally, the wall functions for k and e are given as:

$$k = C\mu^{-1/2} U^{*2}$$

and

$$\varepsilon p = \frac{1}{x y_p} \; C\mu^{3/4} \, kp^{\;3/2}$$

Results presented in Section 4 were obtained from the MAST code and were solved on a single block 59 X 71 grid. Total storage requirement for the problem was approximately 0.43 megawords on the CRAY XMP-24.

6.4 COMPARISON OF CODE PREDICTIONS IN FILM COOLING MEASUREMENTS

Results of the calculations presented here are shown to demonstrate the accuracy and applicability of the two CFD codes chosen to predict flow properties about high performance endo-atmospheric interceptors.

The experimental configuration depicted in Fig. 6-1 shows a shock generator and a slot for a wall jet of coolant. The experimental study was conducted to determine the interaction between a planar shock wave and a wall jet produced by slot cooling in a turbulent hypersonic flow. The studies were conducted in the 48-inch shock tunnel at Calspan at a freestream Mach number of 6 and a Reynolds number of 35 x 10^6. The planar wall jet was generated from 40 transverse nozzles of two heights, 0.08 and 0.12 inches producing a flow Mach number of 3. The nozzles were operated at pressures which produced exit pressures matching the freestream and also pressures higher and lower than freestream. Helium was used as the coolant for the cases investigated here.

The shock wave from a two-dimensional shock generator impinged on the lower plate thus producing a separated flow in the shock/coolant layer region. Results of the experiments show that shocks could easily disperse the coolant. Moreover, the peak heating in the reattachment region was not significantly reduced by even high levels of coolant flow rates. Calculations for three cases taken from Ref. 2 were performed.

6.4.1 Results for Simple Wall Jet Cooling (Run 44)

The first case was Run 44 which was a case where no impinging shock interacts with the coolant layer. Calculations were made with both the GASP and MAST codes to compare the performance of the respective turbulence models discussed in Section 6.2. The freestream and helium coolant exit conditions are listed in Table 1.

		case 44	case 50	case 56
Air	M	6.43	6.4264	6.4362
	T (K)	141.43	139.89	136.03
	P (N/m2)	7348.39	7375.32	6882.49
	Angle D	0.	8.	8.
	X (inch)	6.88	6.88	6.798
	Y (inch)	3.5	3.167	1.959
He	M	3.	3.	3.
	T K	73.34	73.34	73.34
	P (N/m2)	5647.50	7487.71	13086.25

Freestream and Helium Coolant Exit Conditions

TABLE 1

Three grid densities were used for the GASP calculations to determine if a grid dependence was present and if the solution converged to the correct pressure and heat transfer levels as the grid became finer.

Three grids become increasingly finer in the region downstream of the wall jet and are designated I, II and III. In Fig. 2a,b,c the nondimensional y+ dimension at the first grid point off the wall is plotted versus distance down the wall. The y+ for the grid on the flat plate ahead of the wall jet is constant for all three cases. However, aft of the wall jet it is easy to see y+ becomes increasingly smaller as the grid becomes finer.

In Fig. 6-3 the predicted pressure is plotted for the three grids used for the GASP calculations. The experimental data show a great deal of scatter where one would not expect a wide deviation such as the flat plate region in front of the wall jet. In Ref. 2, schlieren photographs show nonuniform flow and shock waves on the flat plate area

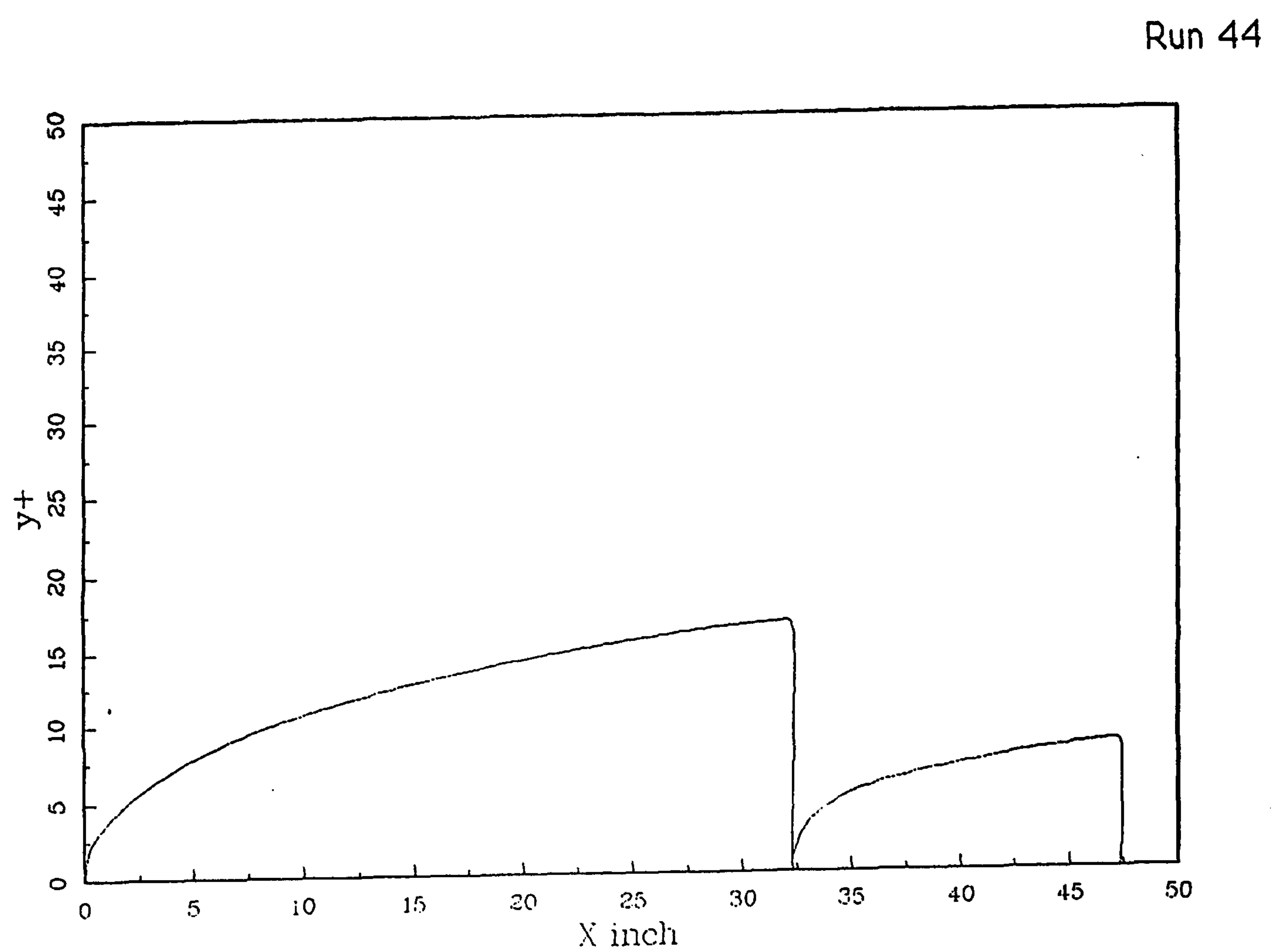

Figure 6-2a - Y+ at the First Grid Point (Grid I)
GASP CODE

Aero Thermo Technology (AT2)
HB:cl 7/26/91

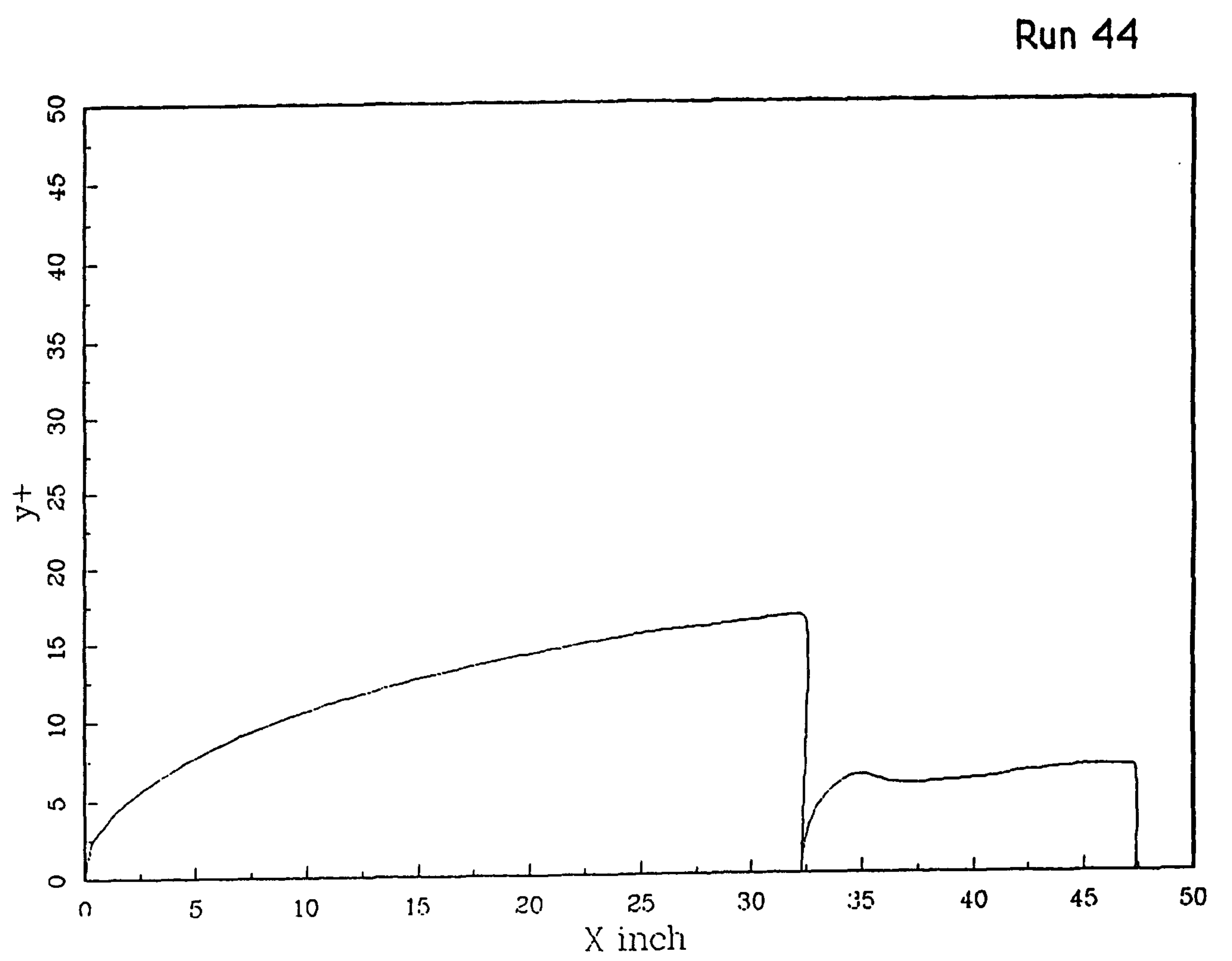

Run 44
y+
0
5
10
15
20
25
30
35
40
45
50
X inch

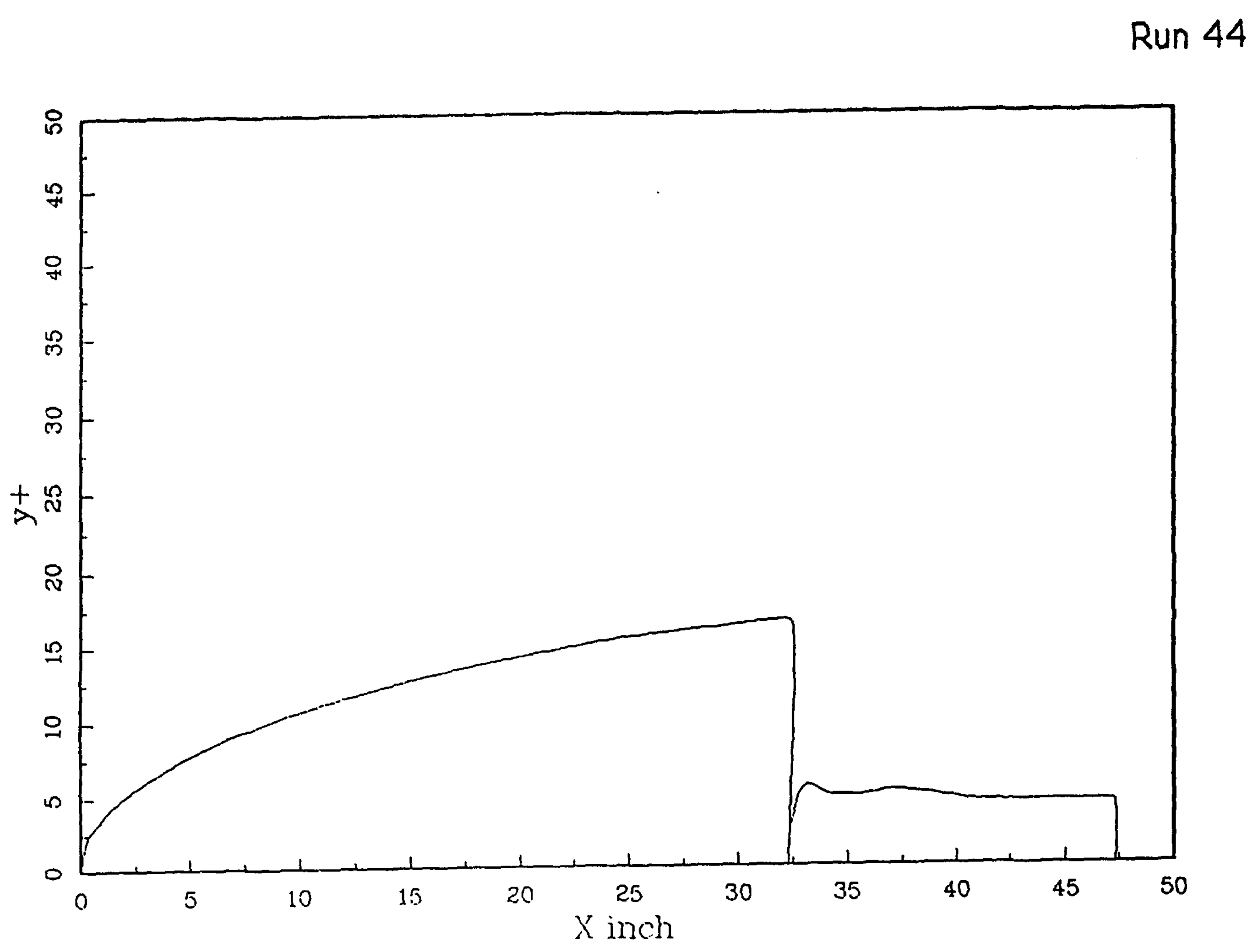

Figure 6-2c - Y+ at First Grid Point (Grid III)
GASP CODE

Aero Thermo Technology (AT2)
HB:cl 7/26/91

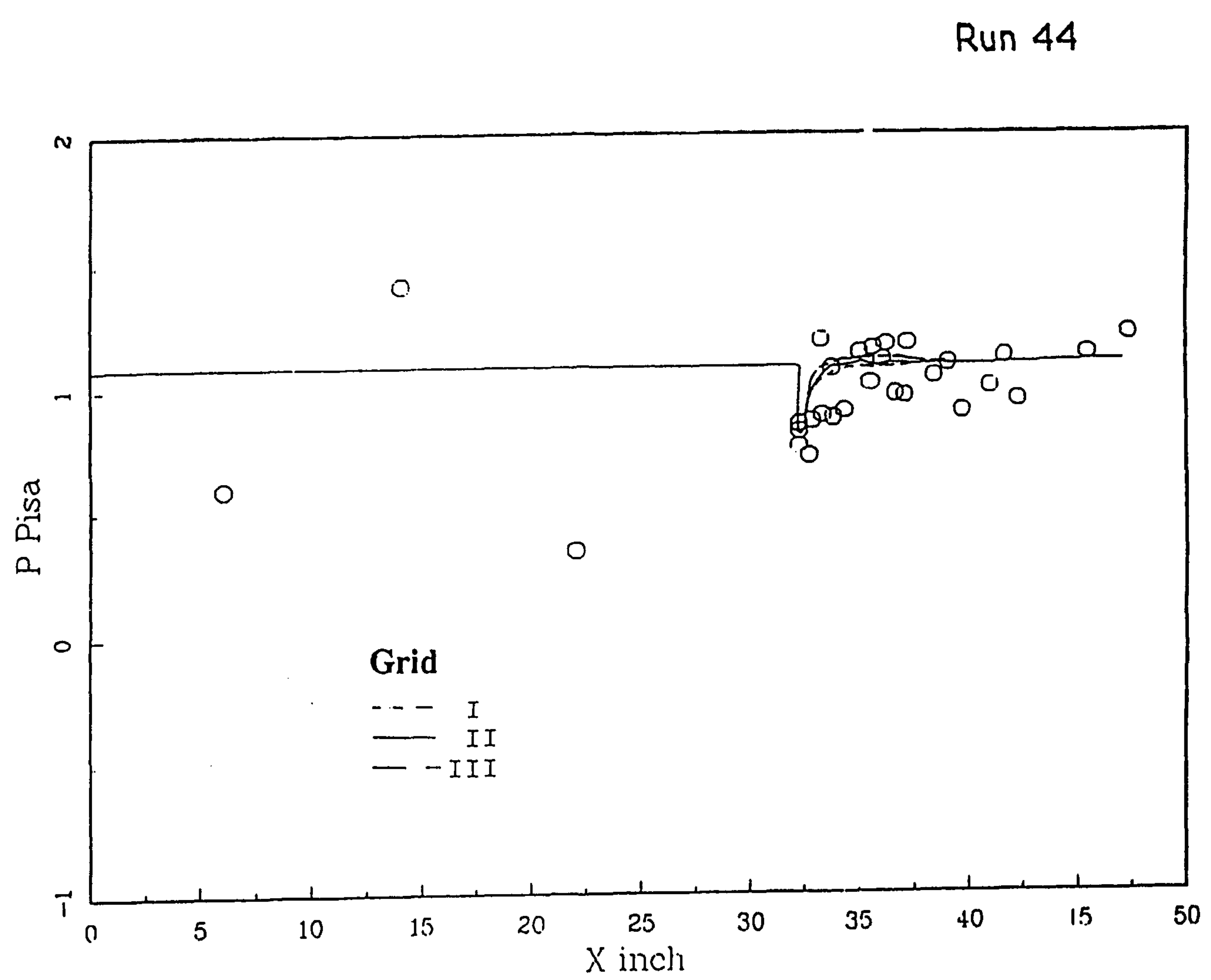

Figure 6-3 - PREDICTED WALL PRESSURE (GASP CODE)

Aero Thermo Technology (AT2)
HB:ct 7/26/91

indicating a disturbance in the flow which could possibly cause the wide scatter in the pressure data. Predicted pressure for all three grids shows fair agreement with the experimental data.

GASP heat flux predictions along the wall using the three grids are shown in Fig. 6-4. The turbulent flat plate predictions ahead of the wall jet show good agreement with the data as might be expected since the Baldwin-Lomax turbulence model was used. At locations downstream of the wall jet outlet, the grid dependence is shown for the three grids. The best agreement with the experimental data was for the case with the medium density grid. Further refinement of the grid caused GASP to overpredict the heat transfer.

Density contours of the helium coolant are shown in Fig. 6-5 for the wall jet region. The extent of turbulent mixing diffusion of the helium in to the freestream can be seen.

In Fig. 6-6 the predicted pressure, shown on expanded scale taken from calculations with the MAST code, is shown. Agreement with experiment is well within the experimental scatter.

The MAST code prediction for heat transfer is shown in Fig. 6-7 for Run 44. Agreement with experiment is excellent on the flat plate portion upstream of the wall jet and also downstream of the wall jet thus indicating that the k-e turbulence model is appropriate in both regions. For these calculations a 59 x 71 grid was used, and no grid dependence was noted when several grid densities were used.

6.4.2 Results for Shock/Coolant Layer Interaction (Run 56)

Calculations were made for Run 56 conditions with the GASP code and two grid densities in the wall jet region. For this case, the freestream and helium wall jet exit conditions are also given in Table 1.

In Fig. 6-8a,b the grids used for these calculations are shown. The grids are the same for the region upstream of the wall jet exit. Downstream of the exit plane, however, Grid I has a 30 x 39 density, while Grid II has a 36 x 32. For these calculations the non-dimensional y+ of the first grid point away from the wall is shown in Fig. 6-9a,b for both grids. This figure also shows that the y+ for Grid I is closer to the wall and should give better resolution of the heat transfer.

Figure 6-10 shows the wall pressure for this case. Predicted pressure upstream of the wall jet shows agreement within the experimental scatter of the data. The data show a steep rise in pressure due to the shock impingement downstream of the jet exit at a station of about 32.5 inches. The predicted pressure rise occurs at a station of about 35.0 inches which corresponds more closely with the heat transfer rise shown in Fig. 6-11. The slope of the rise approximates that of the data; however, it occurs downstream of the actual

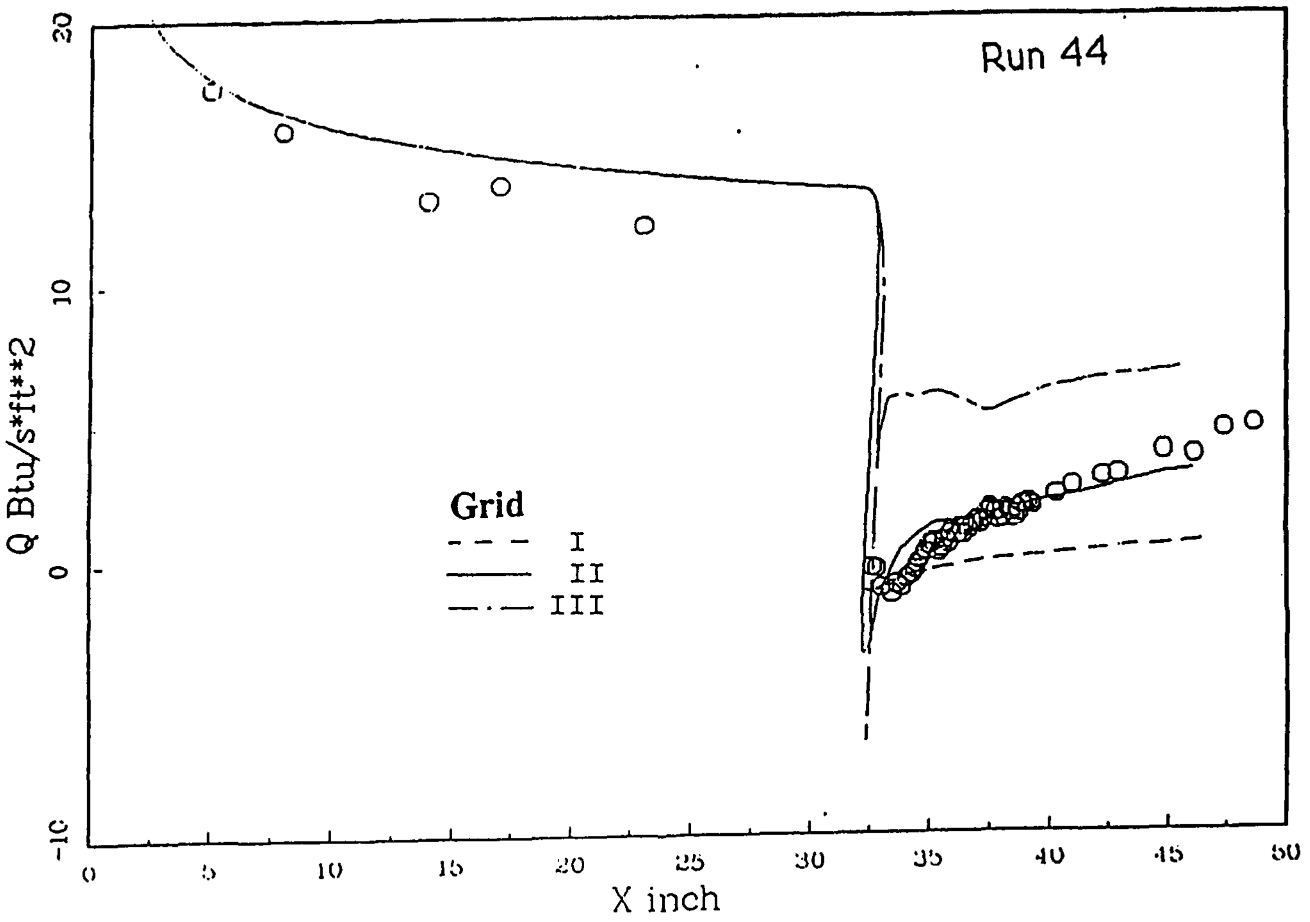

Figure 6-4 - Predicted Heat Flux (GASP CODE)

Aero Thermo Technology (AT2)
HB:ct 7/26/91

Run 44

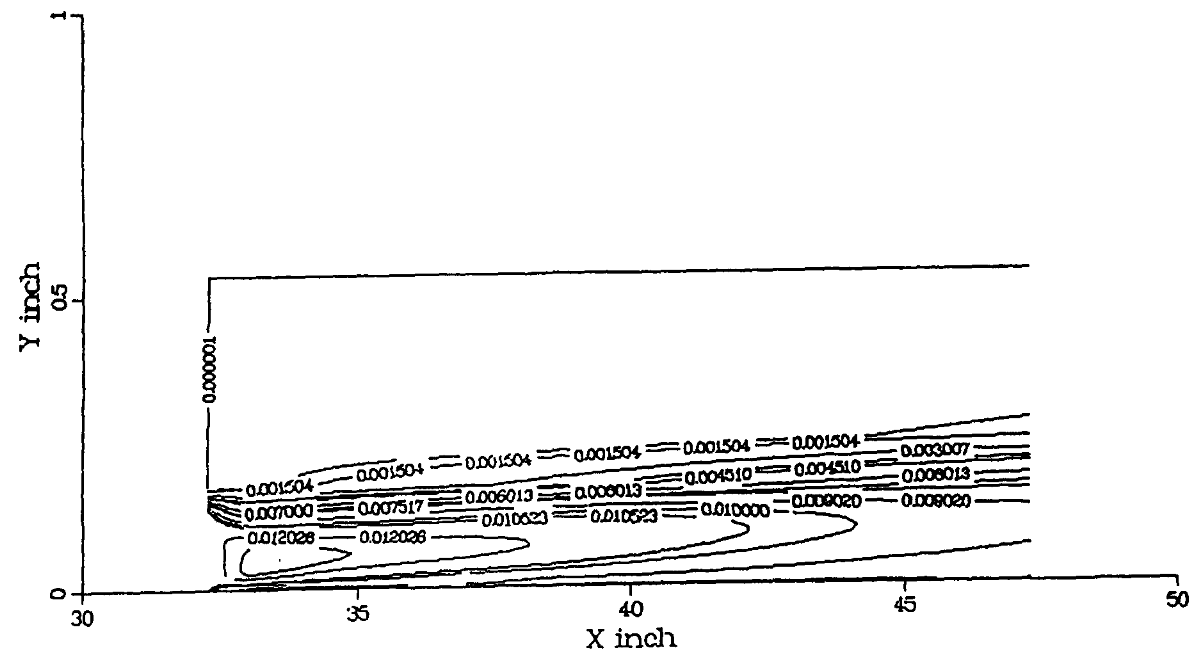

Figure 6-5 - He Coolant Density Contours (kg/m**3) (GASP CODE)
ZONE 2

Aero Thermo Technology (AT2)
HB:cl 7/26/91

Wall pressure

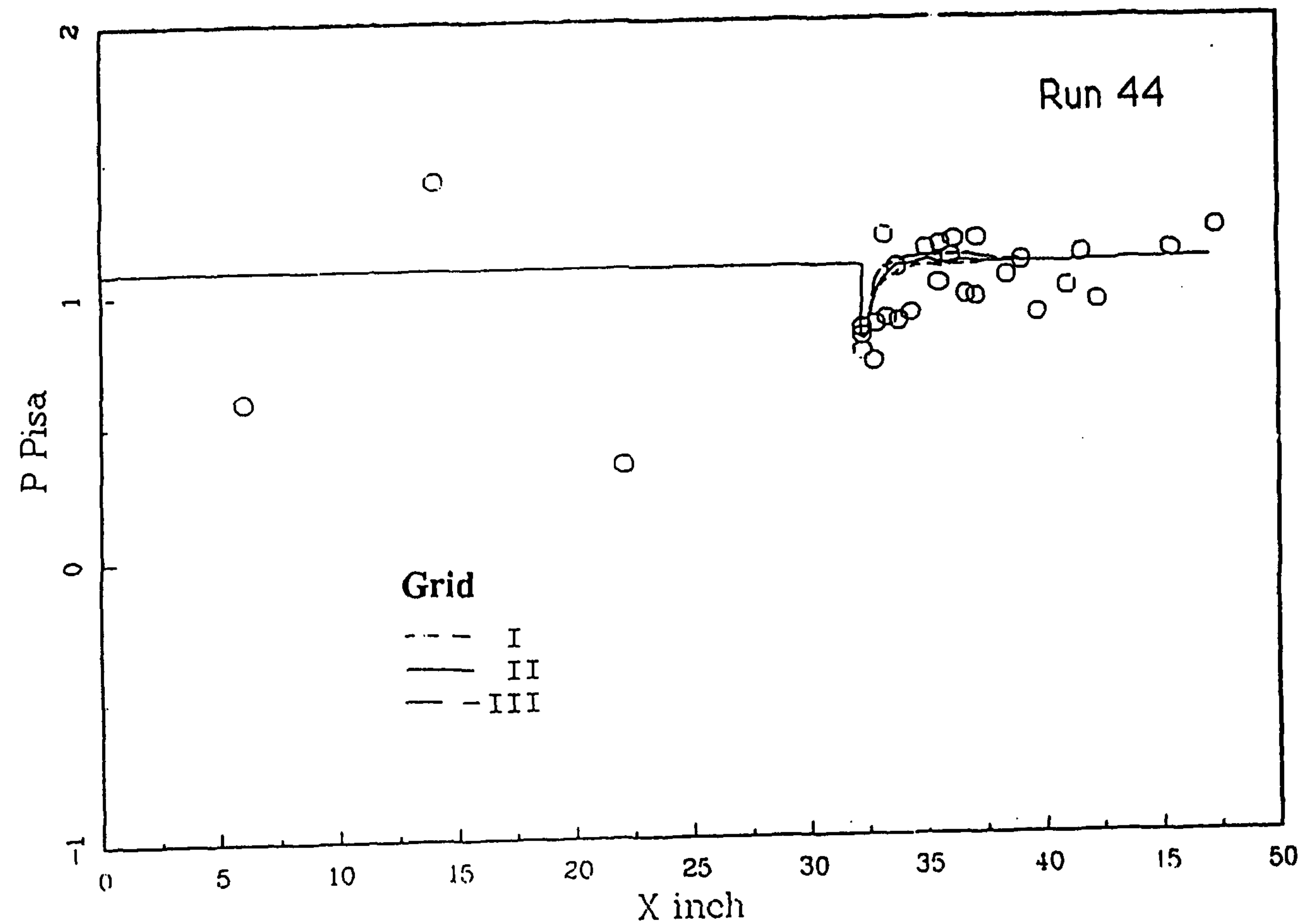

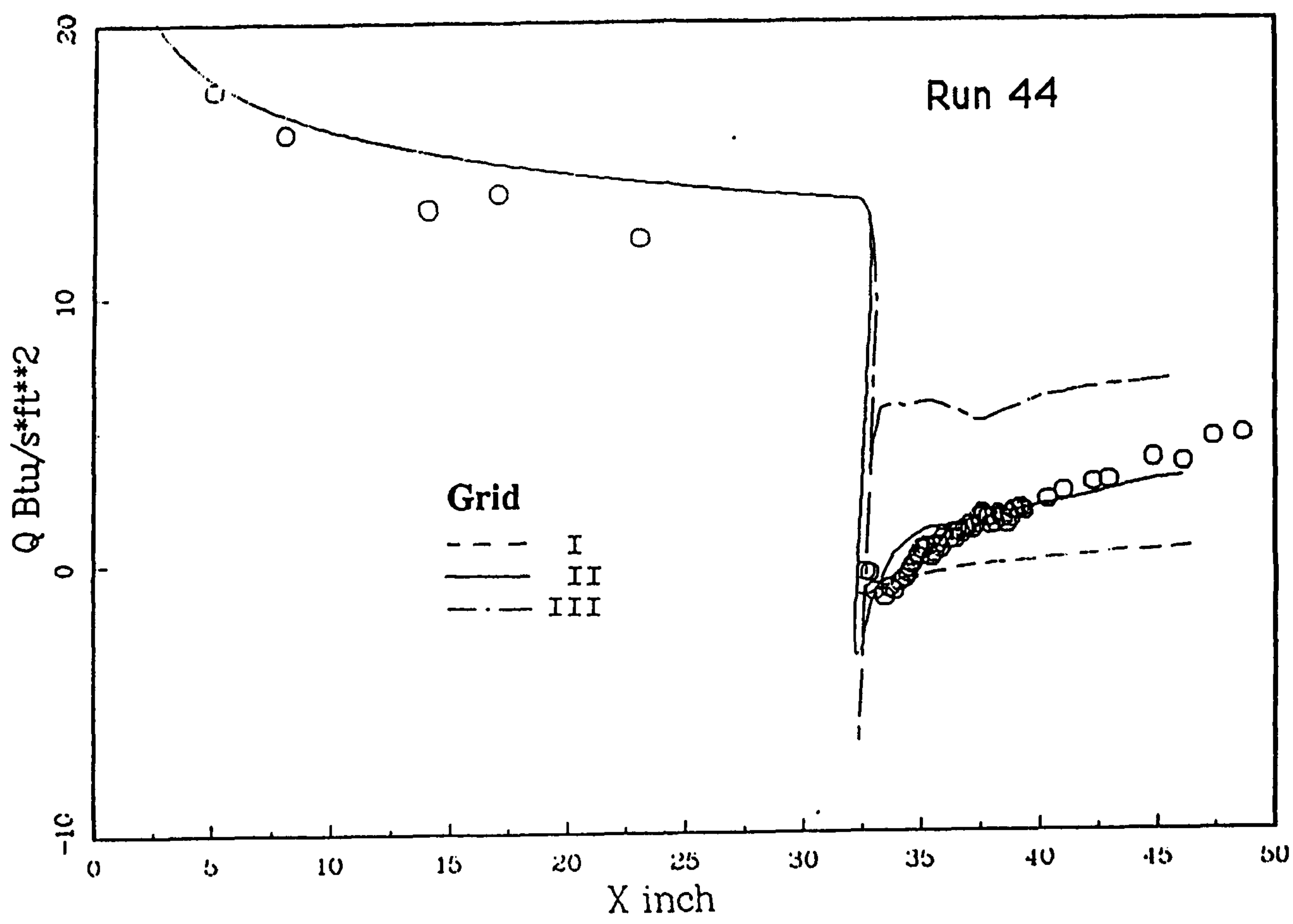

Figure 6-7 - Predicted Heat Flux (MAST CODE)

Aero Therme Technology (AT2)
HB:el 7/26/91

Grid Point

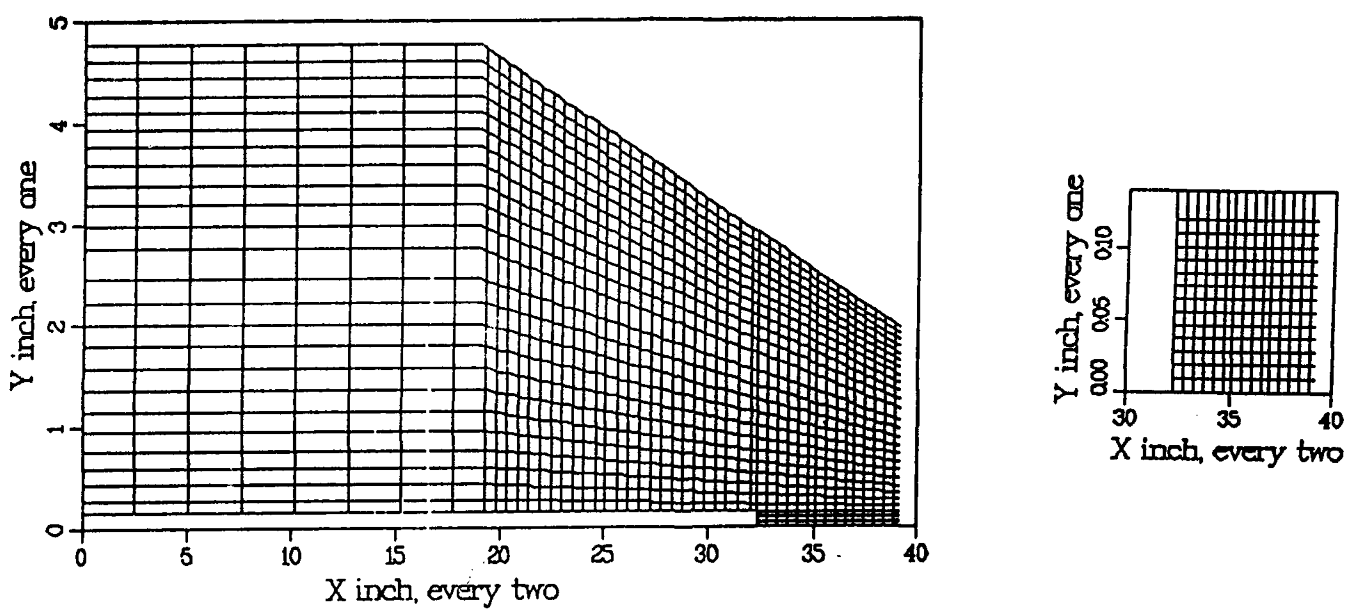

Case 56 I

Zone1 66x25
Zone2 30x39

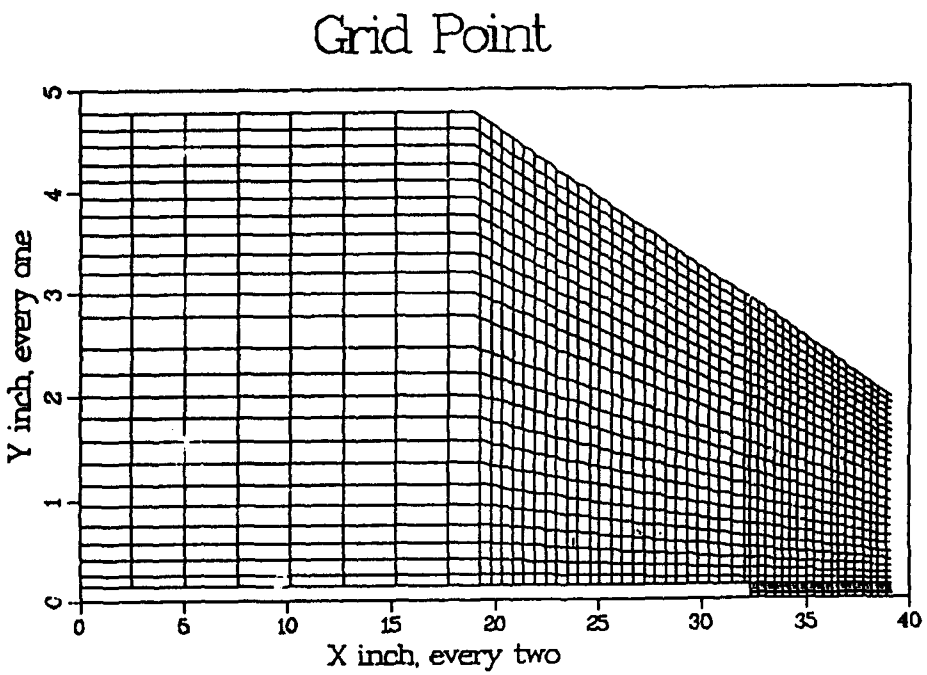

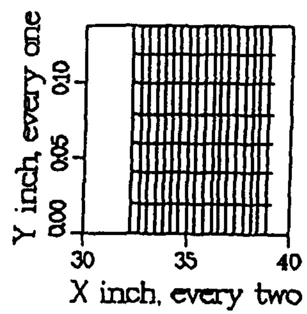

Case 56 II

Zone1 66x25
Zone2 36x32

Figure 6-8b - Grid II DENSITY (Run 56)

Aero Thermo Technology (AT2)
HB:ct 7/26/91

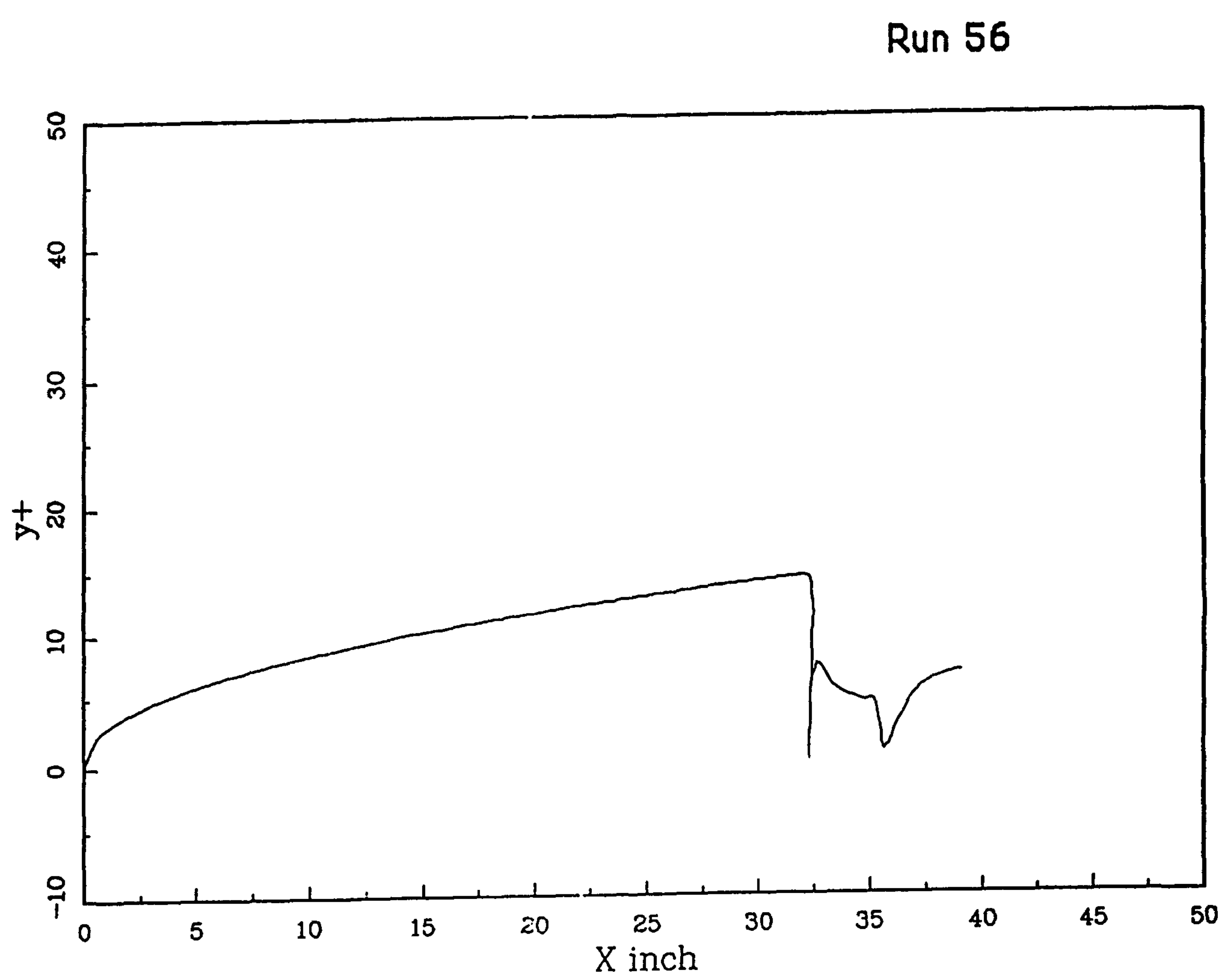

Figure 6-9a - Y+ at the First Grid Point (GRID I)

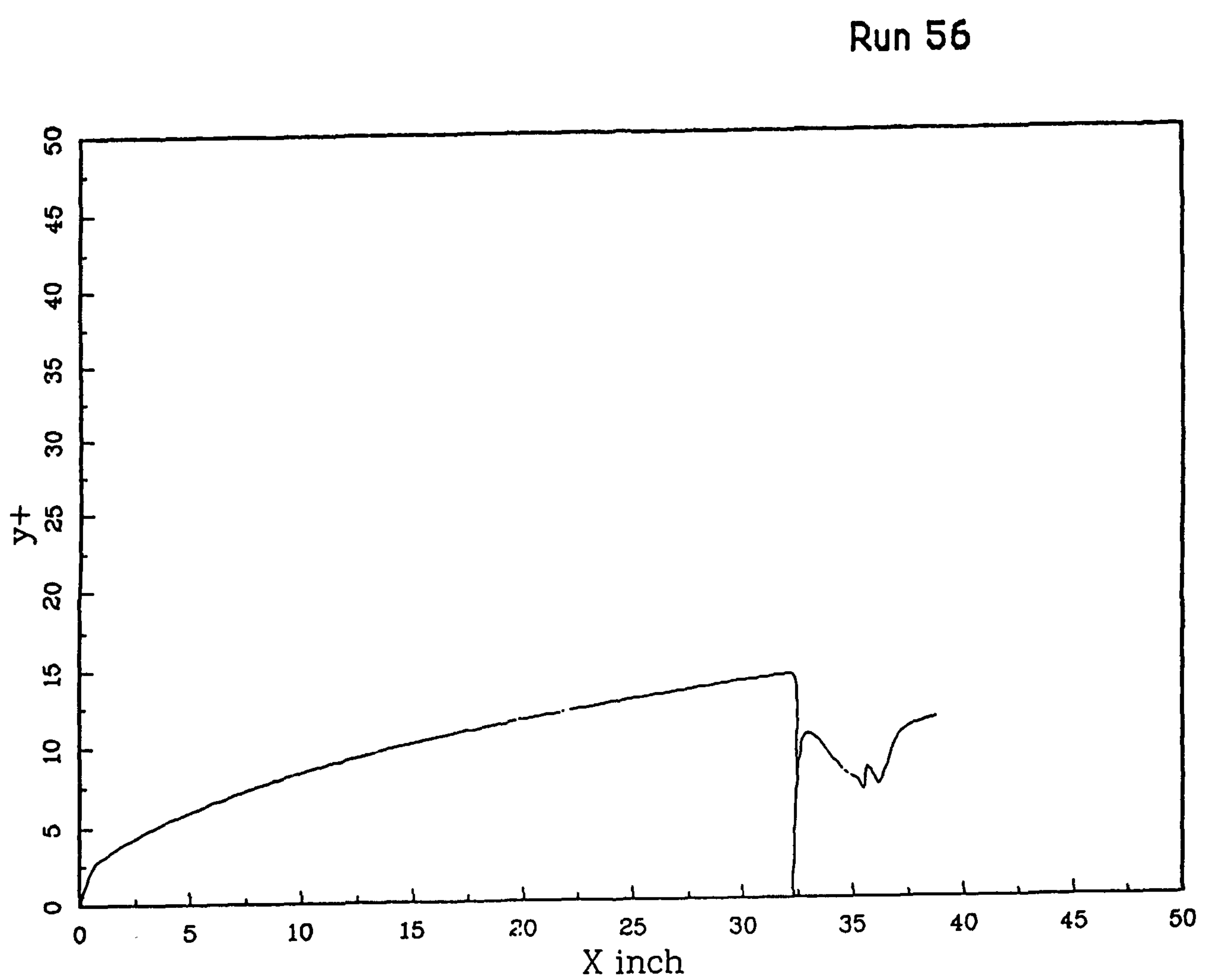

Figure 6-9b - Y+ at the First Grid Point (GRID II)

Aero Thermo Technology (AT2)
HB:ct 7/26/91

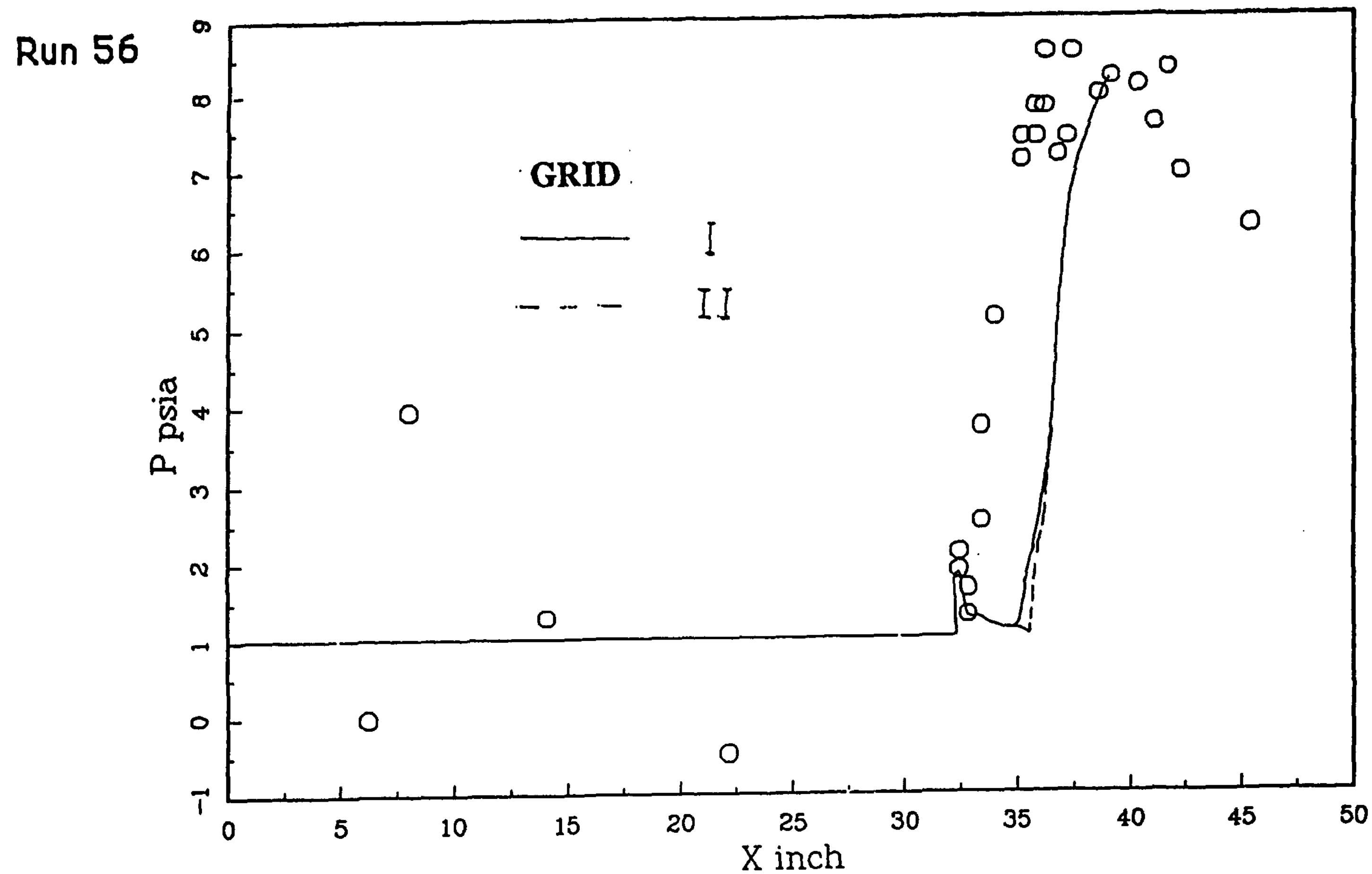

Figure 6-10 - Predicted Wall Pressure (GASP CODE)

Aero Thermo Technology (AT2)
HB:xl 7/26/91

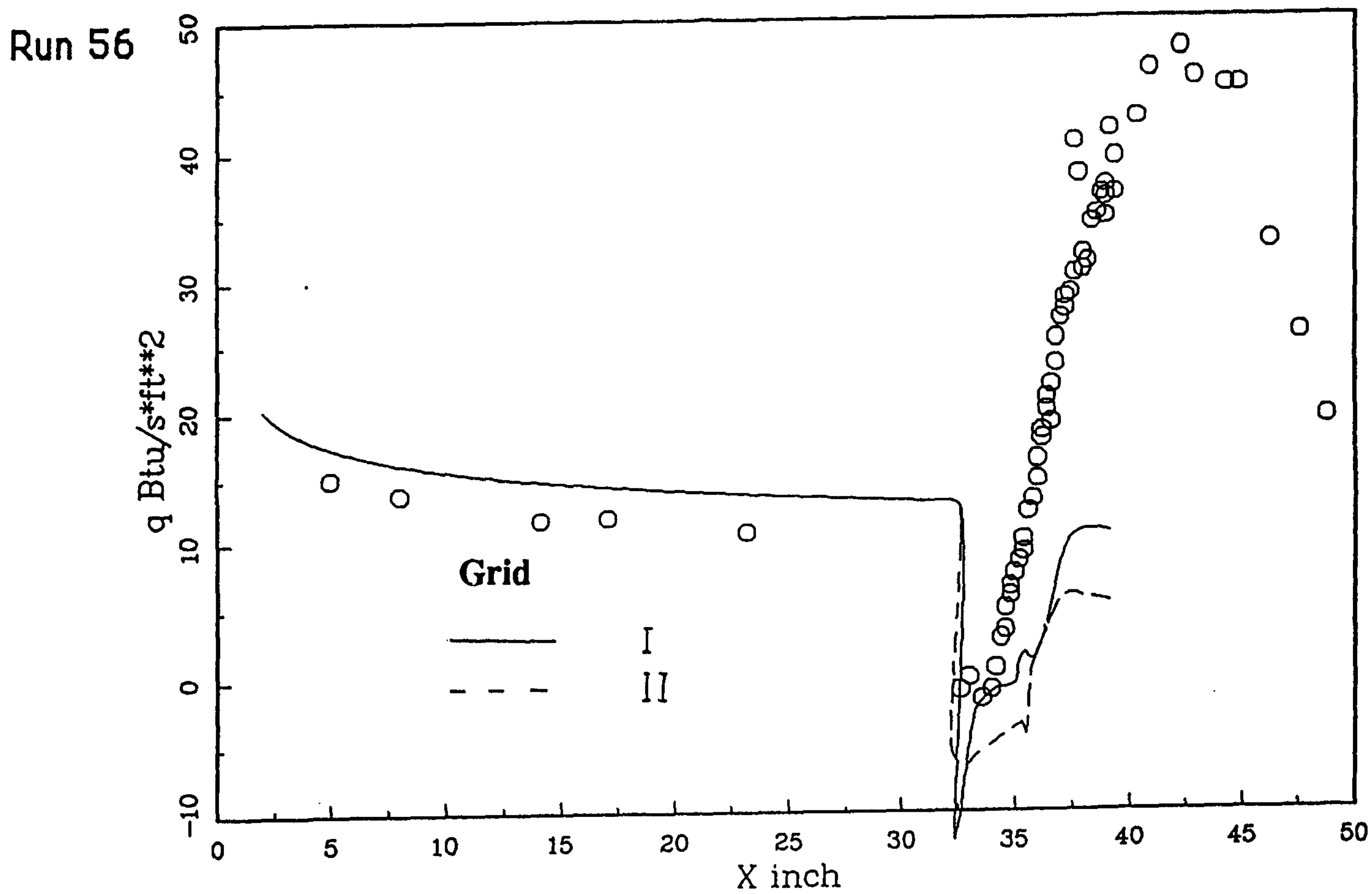

Figure 6-11 - Predicted Heat Flux (GASP CODE)

Aero Thermo Technology (AT2)
HB:ct 7/26/91

location because of the inadequate turbulence model. Pressure predictions for both grids are in agreement.

The heat transfer prediction shown in Fig. 6-11 for Grids I and II agree with the flat plate data upstream of the wall jet. At the wall jet and shock/coolant layer interaction region, however, the GASP code predictions are in disagreement with the data due to the lack of a suitable turbulence model for a shock interaction region.

6.4.3 Results for the Shock/Coolant Layer Interaction (Run 50)

Calculations were made for the Run 50 conditions using the MAST code with a single 59 x 71 grid. For this case the freesteam and helium wall jet exit conditions are presented in Table 1.

In Fig. 6-12 a qualitative plot of the Mach contours is shown for the entire flowfield. The gradients depict the shock and shock/coolant layer interaction region. MAST shock waves are not as sharp as GASP shocks because the shock capturing numerics in GASP are superior.

Comparison between calculated surface pressure, shown in Fig. 6-13, and the experimental data shows excellent agreement. The location of the shock impingement, separation and reattachment is quite good. The magnitude of the peak pressure at the reattachment point is also excellent.

In Fig. 6-14 heat transfer prediction is compared with the experimental data. Agreement is good upstream of the jet exit and most of the coolant jet region. Heat transfer through the separated region is also good. However, the peak reattachment heating was over predicted by the MAST code even though the location was in agreement with the experimental data.

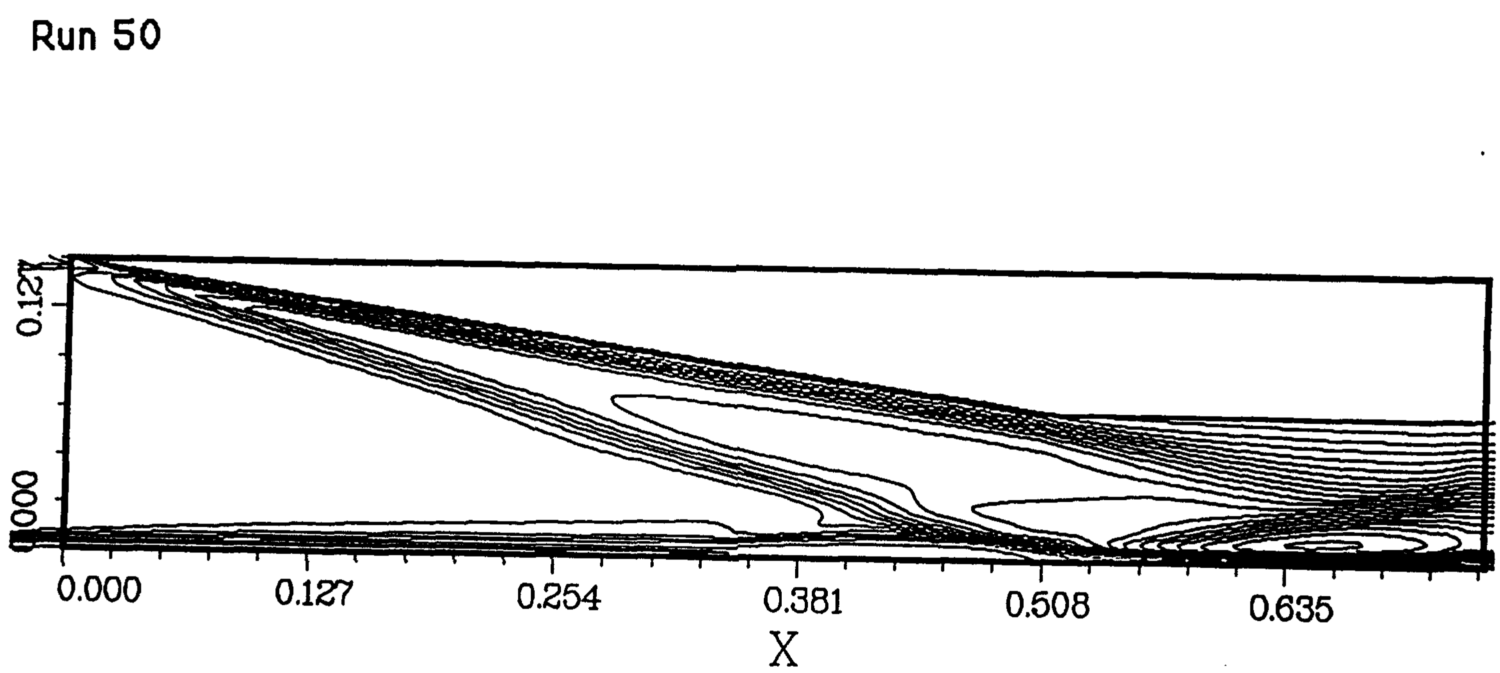

Figure 6-12 - Mach Number Contours (MAST CODE)

Aero Therm Technology (AT2)
HB:ct 7/26/91

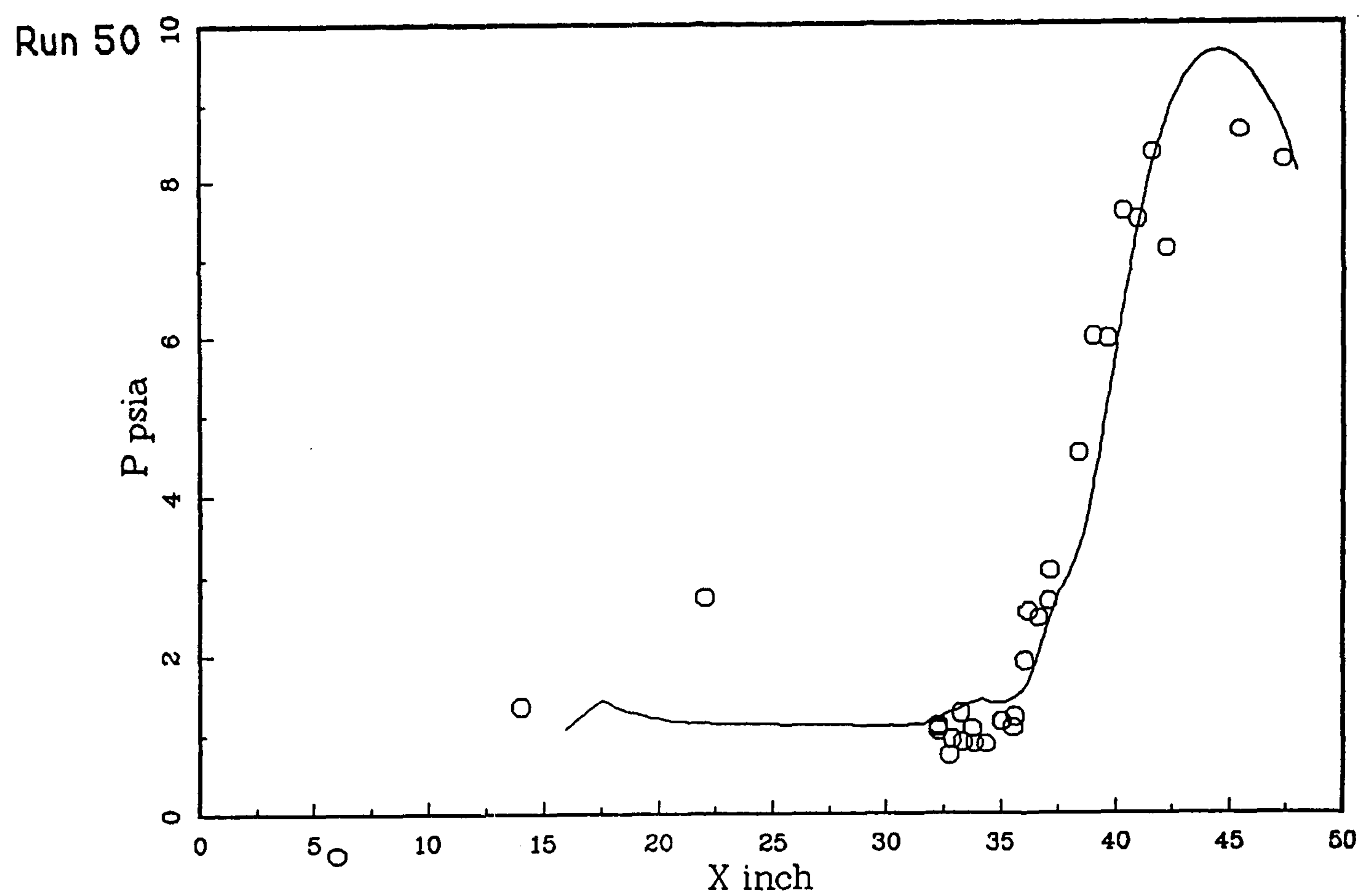

Figure 6-13 - Predicted Wall Presssure (MAST CODE)

Aero Thermo Technology (AT2)
HB:ct 7/26/91

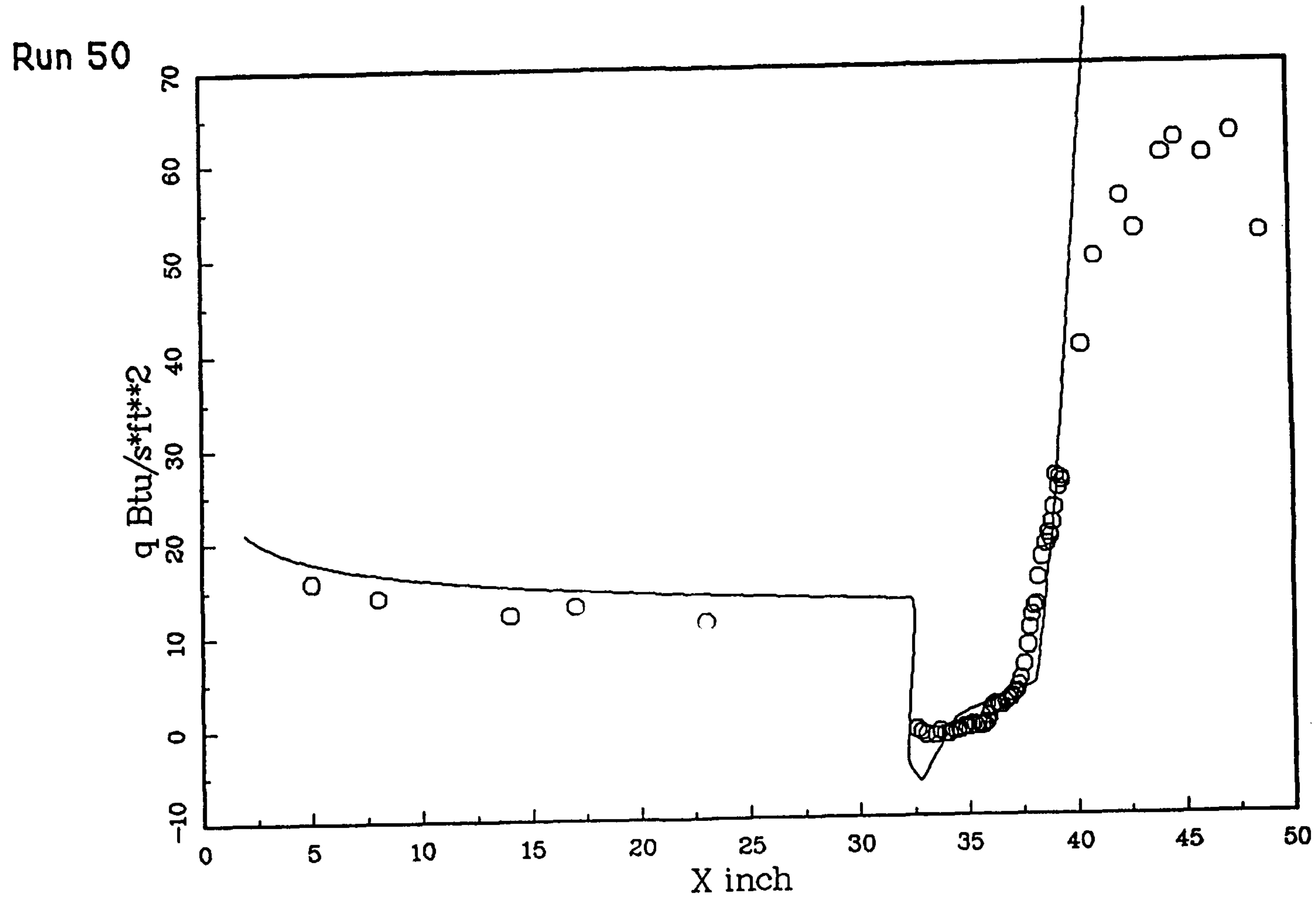

Figure 6-14 - Predicted Heat Flux (MAST CODE)

Aero Thermo Technology (AT2)
HB:ct 7/26/91

6.5 PREDICTION OF HYPERSONIC NOZZLE PERFORMANCE

Preliminary calculated results are presented for the Calspan-UB Research Center "D" nozzle. The data shown in Table 1 are for the shock tunnel operating conditions that were utilized to initialize the nozzle calculations. The nozzle wall contour was curve fit utilizing the coordinates presented in Table 2. Two different contours were curve fit corresponding to throat diameters of 1.6 inches and 0.964 inches.

TABLE 1

CASE	DRIVER	To (^{0}K)	Po (ATM)	Throat Dia. (inches)
1	Helium	1560	1500	1.6
2	Helium	3500	1500	1.6
3	Hydrogen	6000	1500	0.964
4	Hydrogen	6200	1200	0.66

Fig. 6-15 depicts a typical grid structure generated for the calculation of the nozzle flow properties. The grid was arranged to provide high nodal density in the region of large gradients and correspondingly fewer grid points in the regions where gradients are small.

Calculations were performed utilizing k-ε turbulent viscosity models with a wall function to predict the boundary layer growth on the nozzle wall. The finite rate chemistry model used is from Ref. 5 and comprises 6 species with 11 reactions as shown in Table 3. Fig. 6-16 shows the Mach number contours for the operating conditions of CASE 2. Note that both the nozzle wall curvature effects as well as the wall boundary layer effects are well outside of the flow region where test models well be located. Approximately 75% of the flow appears to be very uniform as it approaches the exit plane of the nozzle.

Figures 6-17 and 6-18 present contours of the pressure and temperature for CASE 2. Exit plane profiles of Mach number, pressure, temperature and velocity are shown in Figures 6-19 through 6-22, respectively.

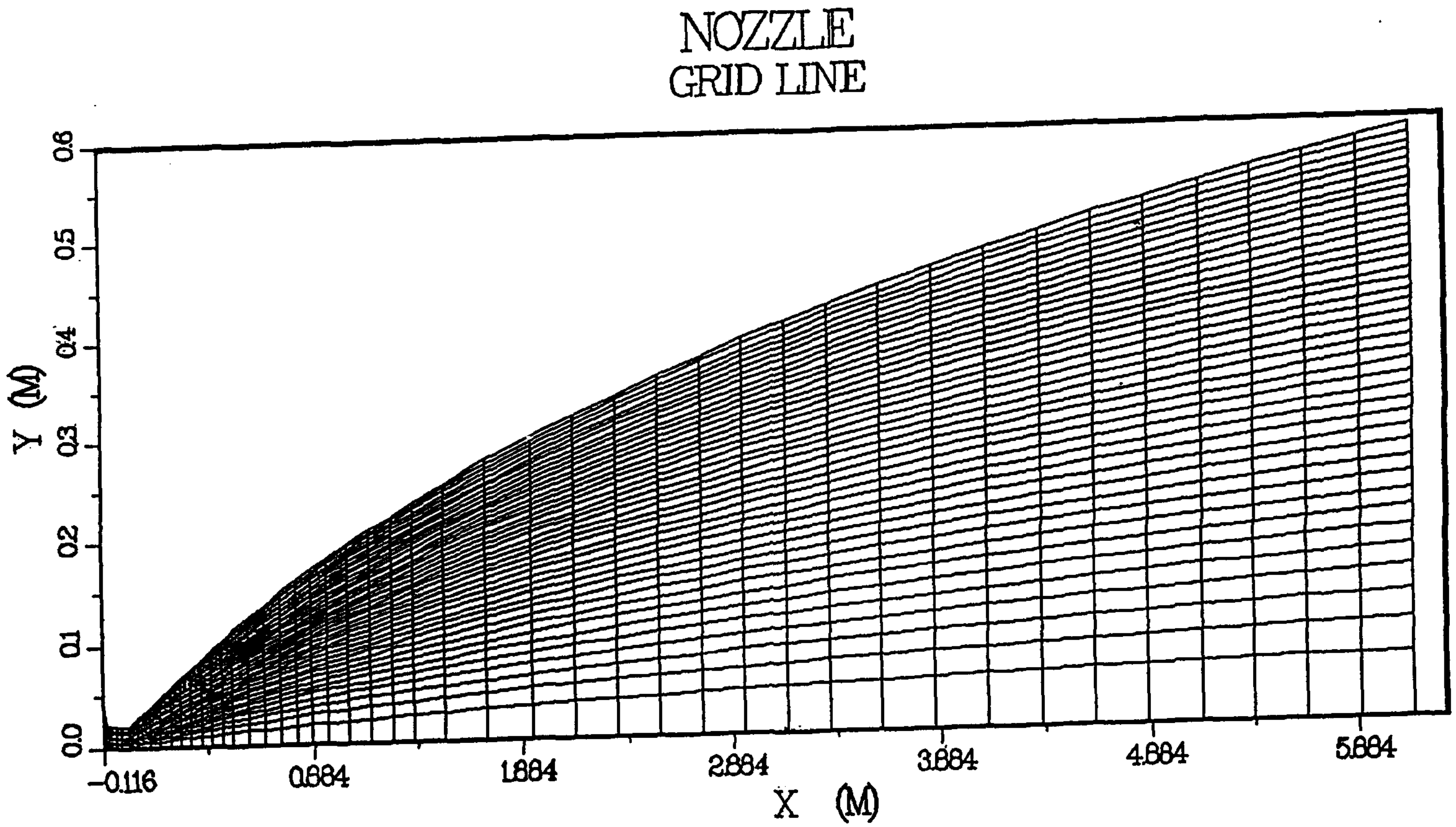
NOZZLE
GRID LINE
Y (M)
0.0
0.1
0.2
0.3
0.4
0.5
0.6
X (M)
-0.116
0.884
1.884
2.884
3.884
4.884
5.884

Figure 6-15

X,Y COORDINATES FOR CALSPAN'S "D" NOZZLES

.660"		.968"		1.600"		1.843"		2.400"	
X	Y	X	Y	X	Y	X	Y	X	Y
-2.1313	1.2500	-2.9500	1.2500	-4.5710	1.4260	-5.2260	1.4340	0.0500	1.2013
-2.0943	1.0456	-2.9004	1.0793	-4.4460	1.3030	-5.1640	1.3730	0.1000	1.2050
-2.0573	0.9627	-2.8507	1.0102	-4.3210	1.2020	-5.1010	1.3200	0.1500	1.2113
-1.9832	0.8490	-2.7515	0.9152	-4.1960	1.1180	-4.9760	1.2320	0.1824	1.2168
-1.9092	0.7654	-2.6522	0.8454	-4.0710	1.0480	-4.8510	1.1650	1.0000	1.3684
-1.8352	0.6980	-2.5529	0.7892	-3.9460	0.9880	-4.7260	1.1110	2.0000	1.5539
-1.7611	0.6415	-2.4536	0.7420	-3.8210	0.9360	-4.6010	1.0650	3.0000	1.7393
-1.6871	0.5930	-2.3544	0.7015	-3.5710	0.8600	-4.4760	1.0260	4.0000	1.9248
-1.5390	0.5140	-2.1558	0.6356	-3.3210	0.8150	-4.2260	0.9680	5.0000	2.1103
-1.3910	0.4533	-1.9573	0.5849	-3.1200	0.8000	-3.9760	0.9360	6.0000	2.2957
-1.2429	0.4068	-1.7587	0.5461	0.0000	0.8000	-3.7260	0.9230	7.0000	2.4812
-1.0948	0.3724	-1.5602	0.5174	0.0500	0.8013	-3.5940	0.9215	8.0000	2.6667
-0.9468	0.3486	-1.3616	0.4975	0.1000	0.8050	0.0000	0.9215	9.0000	2.8521
-0.7987	0.3346	-1.1631	0.4859	0.1500	0.8113	0.0500	0.9228	9.6217	2.9674
-0.6506	0.3300	-0.9645	0.4820	0.1824	0.8168	0.1000	0.9265	10.6217	3.1530
0.0000	0.3300	0.0000	0.4820	1.0000	0.9684	0.1500	0.9328	11.6217	3.3370
0.0500	0.3313	0.0500	0.4833	2.0000	1.1539	0.1824	0.9383	12.6217	3.5200
0.1000	0.3350	0.1000	0.4870	3.0000	1.3393	1.0000	1.0899	13.6217	3.7000
0.1500	0.3413	0.1500	0.4933	4.0000	1.5248	2.0000	1.2754	14.6217	3.8780
0.1824	0.3468	0.1824	0.4988	5.0000	1.7103	3.0000	1.4608	15.6217	4.0530
1.0000	0.4984	1.0000	0.6504	6.0000	1.8957	4.0000	1.6463	16.6217	4.2260
2.0000	0.6839	2.0000	0.8359	7.0000	2.0812	5.0000	1.8318	17.6217	4.3960
3.0000	0.8693	3.0000	1.0213	8.0000	2.2667	6.0000	2.0172	18.6217	4.5650
4.0000	1.0548	4.0000	1.2068	9.0000	2.4521	7.0000	2.2027	19.6217	4.7310
5.0000	1.2403	5.0000	1.3923	10.0000	2.6376	8.0000	2.3882	20.6217	4.8950
6.0000	1.4257	6.0000	1.5777	11.0000	2.8231	9.0000	2.5736	21.6217	5.0570
7.0000	1.6112	7.0000	1.7632	11.7785	2.9674	10.0000	2.7591	22.6217	5.2170
8.0000	1.7967	8.0000	1.9487	12.7785	3.1530	11.1234	2.9674	23.6217	5.3760
9.0000	1.9821	9.0000	2.1341	13.7785	3.3370	12.1234	3.1530	24.6217	5.5330
10.0000	2.1676	10.0000	2.3196	14.7785	3.5200	13.1234	3.3370	25.6217	5.6880
11.0000	2.3531	11.0000	2.5051	15.7785	3.7000	14.1234	3.5200	26.6217	5.8410
12.0000	2.5385	12.0000	2.6905	16.7785	3.8780	15.1234	3.7000	27.6217	5.9930
13.0000	2.7240	13.0000	2.8760	17.7785	4.0530	16.1234	3.8780	28.6217	6.1440
14.0000	2.9095	13.4931	2.9674	18.7785	4.2260	17.1234	4.0530	29.6217	6.2920
14.3126	2.9674	14.4931	3.1530	19.7785	4.3960	18.1234	4.2260	30.6217	6.4390
15.3126	3.1530	15.4931	3.3370	20.7785	4.5650	19.1234	4.3960	31.6217	6.5850
16.3126	3.3370	16.4931	3.5200	21.7785	4.7310	20.1234	4.5650	32.6217	6.7290
17.3126	3.5200	17.4931	3.7000	22.7785	4.8950	21.1234	4.7310	33.6217	6.8720
18.3126	3.7000	18.4931	3.8780	23.7785	5.0570	22.1234	4.8950	34.6217	7.0130
19.3126	3.8780	19.4931	4.0530	24.7785	5.2170	23.1234	5.0570	35.6217	7.1530
20.3126	4.0530	20.4931	4.2260	25.7785	5.3760	24.1234	5.2170	36.6217	7.2910
21.3126	4.2260	21.4931	4.3960	26.7785	5.5330	25.1234	5.3760	37.6217	7.4280
22.3126	4.3960	22.4931	4.5650	27.7785	5.6880	26.1234	5.5330	38.6217	7.5640
23.3126	4.5650	23.4931	4.7310	28.7785	5.8410	27.1234	5.6880	39.6217	7.6990
24.3126	4.7310	24.4931	4.8950	29.7785	5.9930	28.1234	5.8410	40.6217	7.8330
25.3126	4.8950	25.4931	5.0570	30.7785	6.1440	29.1234	5.9930	41.6217	7.9650
26.3126	5.0570	26.4931	5.2170	31.7785	6.2920	30.1234	6.1440	42.6217	8.0960
27.3126	5.2170	27.4931	5.3760	32.7785	6.4390	31.1234	6.2920	43.6217	8.2260
28.3126	5.3760	28.4931	5.5330	33.7785	6.5850	32.1234	6.4390	44.6217	8.3550
29.3126	5.5330	29.4931	5.6880	34.7785	6.7290	33.1234	6.5850	45.6217	8.4820

TABLE 2

X,Y COORDINATES FOR CALSPAN'S "D" NOZZLES

D* = .660" X	.660" Y	.964" X	.964" Y	1.600" X	1.600" Y	1.843" X	1.843" Y	2.400" X	2.400" Y
30.3126	5.6880	30.4931	5.8410	35.7785	6.8720	34.1234	6.7290	46.6217	8.6090
31.3126	5.8410	31.4931	5.9930	36.7785	7.0130	35.1234	6.8720	47.6217	8.7350
32.3126	5.9930	32.4931	6.1440	37.7785	7.1530	36.1234	7.0130	48.6217	8.8590
33.3126	6.1440	33.4931	6.2920	38.7785	7.2910	37.1234	7.1530	49.6217	8.9830
34.3126	6.2920	34.4931	6.4390	39.7785	7.4280	38.1234	7.2910	50.6217	9.1050
35.3126	6.4390	35.4931	6.5850	40.7785	7.5640	39.1234	7.4280	51.6217	9.2270
36.3126	6.5850	36.4931	6.7290	41.7785	7.6990	40.1234	7.5640	52.6217	9.3480
37.3126	6.7290	37.4931	6.8720	42.7785	7.8330	41.1234	7.6990	53.6217	9.4680
38.3126	6.8720	38.4931	7.0130	43.7785	7.9650	42.1234	7.8330	55.6217	9.7040
39.3126	7.0130	39.4931	7.1530	44.7785	8.0960	43.1234	7.9650	57.6217	9.9380
40.3126	7.1530	40.4931	7.2910	45.7785	8.2260	44.1234	8.0960	59.6217	10.1670
41.3126	7.2910	41.4931	7.4280	46.7785	8.3550	45.1234	8.2260	61.6217	10.3940
42.3126	7.4280	42.4931	7.5640	47.7785	8.4820	46.1234	8.3550	63.6217	10.6170
43.3126	7.5640	43.4931	7.6990	48.7785	8.6090	47.1234	8.4820	65.6217	10.8380
44.3126	7.6990	44.4931	7.8330	49.7785	8.7350	48.1234	8.6090	67.6217	11.0550
45.3126	7.8330	45.4931	7.9650	50.7785	8.8590	49.1234	8.7350	69.6217	11.2690
46.3126	7.9650	46.4931	8.0960	51.7785	8.9830	50.1234	8.8590	71.6217	11.4810
47.3126	8.0960	47.4931	8.2260	52.7785	9.1050	51.1234	8.9830	73.6217	11.6900
48.3126	8.2260	48.4931	8.3550	53.7785	9.2270	52.1234	9.1050	75.6217	11.8960
49.3126	8.3550	49.4931	8.4820	54.7785	9.3480	53.1234	9.2270	77.6217	12.1000
50.3126	8.4820	50.4931	8.6090	55.7785	9.4680	54.1234	9.3480	79.6217	12.3010
51.3126	8.6090	51.4931	8.7350	57.7785	9.7040	55.1234	9.4680	81.6217	12.4990
52.3126	8.7350	52.4931	8.8590	59.7785	9.9380	57.1234	9.7040	83.6217	12.6960
53.3126	8.8590	53.4931	8.9830	61.7785	10.1670	59.1234	9.9380	85.6217	12.8890
54.3126	8.9830	54.4931	9.1050	63.7785	10.3940	61.1234	10.1670	87.6217	13.0810
55.3126	9.1050	55.4931	9.2270	65.7785	10.6170	63.1234	10.3940	89.6217	13.2700
56.3126	9.2270	56.4931	9.3480	67.7785	10.8380	65.1234	10.6170	91.6217	13.4580
57.3126	9.3480	57.4931	9.4680	69.7785	11.0550	67.1234	10.8380	93.6217	13.6430
58.3126	9.4680	59.4931	9.7040	71.7785	11.2690	69.1234	11.0550	95.6217	13.8250
60.3126	9.7040	61.4931	9.9380	73.7785	11.4810	71.1234	11.2690	97.6217	14.0060
62.3126	9.9380	63.4931	10.1670	75.7785	11.6900	73.1234	11.4810	99.6217	14.1850
64.3126	10.1670	65.4931	10.3940	77.7785	11.8960	75.1234	11.6900	101.6217	14.3620
66.3126	10.3940	67.4931	10.6170	79.7785	12.1000	77.1234	11.8960	103.6217	14.5370
68.3126	10.6170	69.4931	10.8380	81.7785	12.3010	79.1234	12.1000	105.6217	14.7100
70.3126	10.8380	71.4931	11.0550	83.7785	12.4990	81.1234	12.3010	107.6217	14.8810
72.3126	11.0550	73.4931	11.2690	85.7785	12.6960	83.1234	12.4990	109.6217	15.0510
74.3126	11.2690	75.4931	11.4810	87.7785	12.8890	85.1234	12.6960	111.6217	15.2180
76.3126	11.4810	77.4931	11.6900	89.7785	13.0810	87.1234	12.8890	113.6217	15.3840
78.3126	11.6900	79.4931	11.8960	91.7785	13.2700	89.1234	13.0810	115.6217	15.5490
80.3126	11.8960	81.4931	12.1000	93.7785	13.4580	91.1234	13.2700	117.6217	15.7120
82.3126	12.1000	83.4931	12.3010	95.7785	13.6430	93.1234	13.4580	119.6217	15.8730
84.3126	12.3010	85.4931	12.4990	97.7785	13.8250	95.1234	13.6430	121.6217	16.0320
86.3126	12.4990	87.4931	12.6960	99.7785	14.0060	97.1234	13.8250	123.6217	16.1900
88.3126	12.6960	89.4931	12.8890	101.7785	14.1850	99.1234	14.0060	125.6217	16.3460
90.3126	12.8890	91.4931	13.0810	103.7785	14.3620	101.1234	14.1850	127.6217	16.5010
92.3126	13.0810	93.4931	13.2700	105.7785	14.5370	103.1234	14.3620	129.6217	16.6540
94.3126	13.2700	95.4931	13.4580	107.7785	14.7100	105.1234	14.5370	131.6217	16.8060
96.3126	13.4580	97.4931	13.6430	109.7785	14.8810	107.1234	14.7100	133.6217	16.9560
98.3126	13.6430	99.4931	13.8250	111.7785	15.0510	109.1234	14.8810	135.6217	17.1050
100.3126	13.8250	101.4931	14.0060	113.7785	15.2180	111.1234	15.0510	137.6217	17.2520

TABLE 2 (CONTINUED)

X,Y COORDINATES FOR CALSPAN'S "D" NOZZLES

t = .660"		.964"		1.600"		1.843"		2.400"	
X	Y	X	Y	X	Y	X	Y	X	Y
102.3126	14.0060	103.4931	14.1850	115.7785	15.3840	113.1234	15.2180	139.6217	17.3980
104.3126	14.1850	105.4931	14.3620	117.7785	15.5490	115.1234	15.3840	141.6217	17.5430
106.3126	14.3620	107.4931	14.5370	119.7785	15.7120	117.1234	15.5490	143.6217	17.6860
108.3126	14.5370	109.4931	14.7100	121.7785	15.8730	119.1234	15.7120	145.6217	17.8280
110.3126	14.7100	111.4931	14.8810	123.7785	16.0320	121.1234	15.8730	147.6217	17.9680
112.3126	14.8810	113.4931	15.0510	125.7785	16.1900	123.1234	16.0320	149.6217	18.1080
114.3126	15.0510	115.4931	15.2180	127.7785	16.3460	125.1234	16.1900	151.6217	18.2460
116.3126	15.2180	117.4931	15.3840	129.7785	16.5010	127.1234	16.3460	153.6217	18.3820
118.3126	15.3840	119.4931	15.5490	131.7785	16.6540	129.1234	16.5010	155.6217	18.5180
120.3126	15.5490	121.4931	15.7120	133.7785	16.8060	131.1234	16.6540	157.6217	18.6520
122.3126	15.7120	123.4931	15.8730	135.7785	16.9560	133.1234	16.8060	159.6217	18.7860
124.3126	15.8730	125.4931	16.0320	137.7785	17.1050	135.1234	16.9560	161.6217	18.9180
126.3126	16.0320	127.4931	16.1900	139.7785	17.2520	137.1234	17.1050	163.6217	19.0480
128.3126	16.1900	129.4931	16.3460	141.7785	17.3980	139.1234	17.2520	165.6217	19.1780
130.3126	16.3460	131.4931	16.5010	143.7785	17.5430	141.1234	17.3980	167.6217	19.3060
132.3126	16.5010	133.4931	16.6540	145.7785	17.6860	143.1234	17.5430	169.6217	19.4340
134.3126	16.6540	135.4931	16.8060	147.7785	17.8280	145.1234	17.6860	171.6217	19.5600
136.3126	16.8060	137.4931	16.9560	149.7785	17.9680	147.1234	17.8280	173.6217	19.6850
138.3126	16.9560	139.4931	17.1050	151.7785	18.1080	149.1234	17.9680	175.6217	19.8090
140.3126	17.1050	141.4931	17.2520	153.7785	18.2460	151.1234	18.1080	177.6217	19.9320
142.3126	17.2520	143.4931	17.3980	155.7785	18.3820	153.1234	18.2460	179.6217	20.0530
144.3126	17.3980	145.4931	17.5430	157.7785	18.5180	155.1234	18.3820	181.6217	20.1740
146.3126	17.5430	147.4931	17.6860	159.7785	18.6520	157.1234	18.5180	183.6217	20.2940
148.3126	17.6860	149.4931	17.8280	161.7785	18.7860	159.1234	18.6520	185.6217	20.4120
150.3126	17.8280	151.4931	17.9680	163.7785	18.9180	161.1234	18.7860	187.6217	20.5300
152.3126	17.9680	153.4931	18.1080	165.7785	19.0480	163.1234	18.9180	189.6217	20.6470
154.3126	18.1080	155.4931	18.2460	167.7785	19.1780	165.1234	19.0480	191.6217	20.7620
156.3126	18.2460	157.4931	18.3820	169.7785	19.3060	167.1234	19.1780	193.6217	20.8770
158.3126	18.3820	159.4931	18.5180	171.7785	19.4340	169.1234	19.3060	195.6217	20.9900
160.3126	18.5180	161.4931	18.6520	173.7785	19.5600	171.1234	19.4340	197.6217	21.1030
162.3126	18.6520	163.4931	18.7860	175.7785	19.6850	173.1234	19.5600	199.6217	21.2150
164.3126	18.7860	165.4931	18.9180	177.7785	19.8090	175.1234	19.6850	201.6217	21.3260
166.3126	18.9180	167.4931	19.0480	179.7785	19.9320	177.1234	19.8090	203.6217	21.4360
168.3126	19.0480	169.4931	19.1780	181.7785	20.0530	179.1234	19.9320	205.6217	21.5450
170.3126	19.1780	171.4931	19.3060	183.7785	20.1740	181.1234	20.0530	207.6217	21.6530
172.3126	19.3060	173.4931	19.4340	185.7785	20.2940	183.1234	20.1740	209.6217	21.7610
174.3126	19.4340	175.4931	19.5600	187.7785	20.4120	185.1234	20.2940	211.6217	21.8670
176.3126	19.5600	177.4931	19.6850	189.7785	20.5300	187.1234	20.4120	213.6217	21.9730
178.3126	19.6850	179.4931	19.8090	191.7785	20.6470	189.1234	20.5300	215.6217	22.0780
180.3126	19.8090	181.4931	19.9320	193.7785	20.7620	191.1234	20.6470	217.6217	22.1820
182.3126	19.9320	183.4931	20.0530	195.7785	20.8770	193.1234	20.7620	219.6217	22.2850
184.3126	20.0530	185.4931	20.1740	197.7785	20.9900	195.1234	20.8770	221.6217	22.3870
186.3126	20.1740	187.4931	20.2940	199.7785	21.1030	197.1234	20.9900	223.6217	22.4890
188.3126	20.2940	189.4931	20.4120	201.7785	21.2150	199.1234	21.1030	225.6217	22.5890
190.3126	20.4120	191.4931	20.5300	203.7785	21.3260	201.1234	21.2150	227.6217	22.6890
192.3126	20.5300	193.4931	20.6470	205.7785	21.4360	203.1234	21.3260	229.6217	22.7880
194.3126	20.6470	195.4931	20.7620	207.7785	21.5450	205.1234	21.4360	231.6217	22.8860
196.3126	20.7620	197.4931	20.8770	209.7785	21.6530	207.1234	21.5450	233.6217	22.9840
198.3126	20.8770	199.4931	20.9900	211.7785	21.7610	209.1234	21.6530	235.6217	23.0810
200.3126	20.9900	201.4931	21.1030	213.7785	21.8670	211.1234	21.7610	237.6217	23.1770

TABLE 2 (CONTINUED)

X,Y COORDINATES FOR CALSPAN'S "D" NOZZLES

D* =	.660"		.964"		1.600"		1.843"		2.400"	
	X	Y	X	Y	X	Y	X	Y	X	Y
	202.3126	21.1030	203.4931	21.2150	215.7785	21.9730	213.1234	21.8670	239.6217	23.2720
	204.3126	21.2150	205.4931	21.3260	217.7785	22.0780	215.1234	21.9730		
	206.3126	21.3260	207.4931	21.4360	219.7785	22.1820	217.1234	22.0780		
	208.3126	21.4360	209.4931	21.5450	221.7785	22.2850	219.1234	22.1820		
	210.3126	21.5450	211.4931	21.6530	223.7785	22.3870	221.1234	22.2850		
	212.3126	21.6530	213.4931	21.7610	225.7785	22.4890	223.1234	22.3870		
	214.3126	21.7610	215.4931	21.8670	227.7785	22.5890	225.1234	22.4890		
	216.3126	21.8670	217.4931	21.9730	229.7785	22.6890	227.1234	22.5890		
	218.3126	21.9730	219.4931	22.0780	231.7785	22.7880	229.1234	22.6890		
	220.3126	22.0780	221.4931	22.1820	233.7785	22.8860	231.1234	22.7880		
	222.3126	22.1820	223.4931	22.2850	235.7785	22.9840	233.1234	22.8860		
	224.3126	22.2850	225.4931	22.3870	237.7785	23.0810	235.1234	22.9840		
	226.3126	22.3870	227.4931	22.4890	239.7785	23.1770	237.1234	23.0810		
	228.3126	22.4890	229.4931	22.5890	241.7785	23.2720	239.1234	23.1770		
	230.3126	22.5890	231.4931	22.6890	0.0000	0.0000	241.1234	23.2720		
	232.3126	22.6890	233.4931	22.7880						
	234.3126	22.7880	235.4931	22.8860						
	236.3126	22.8860	237.4931	22.9840						
	238.3126	22.9840	239.4931	23.0810						
	240.3126	23.0810	241.4931	23.1770						
	242.3126	23.1770	243.4931	23.2720						
	244.3126	23.2720								

Name of print file is dnozzles.dat

TABLE 2 (CONCLUDED)

REACTION KINETIC DATA EMPLOYED IN NUMERICAL CALCULATIONS

REACTION	THIRD BODY M	FORWARD RATE CONSTANT k_F (cm^3/mole sec.)
1. $O_2 + M \rightleftharpoons 2O + M$	O_2	$3.6 \times 10^{21}\ T^{-1.5} \exp(-\frac{117960}{R_o T})$
2. $O_2 + M \rightleftharpoons 2O + M$	O	$2.1 \times 10^{18}\ T^{-0.5} \exp(-\frac{117960}{R_o T})$
3. $O_2 + M \rightleftharpoons 2O + M$	N_2,Ar,N,NO	$1.2 \times 10^{21}\ T^{-1.5} \exp(-\frac{117960}{R_o T})$
4. $N_2 + M \rightleftharpoons 2N + M$	N_2	$3.0 \times 10^{21}\ T^{-1.5} \exp(-\frac{224990}{R_o T})$
5. $N_2 + M \rightleftharpoons 2N + M$	N	$1.5 \times 10^{22}\ T^{-1.5} \exp(-\frac{224990}{R_o T})$
6. $N_2 + M \rightleftharpoons 2N + M$	O_2,Ar,O,NO	$9.9 \times 10^{20}\ T^{-1.5} \exp(-\frac{224990}{R_o T})$
7. $NO + M \rightleftharpoons N + O + M$	O_2,N_2,Ar,O,N,NO	$5.2 \times 10^{21}\ T^{-1.5} \exp(-\frac{149960}{R_o T})$
8. $N + O_2 \rightleftharpoons NO + O$		$1.0 \times 10^{12}\ T^{0.5} \exp(-\frac{6200}{R_o T})$
9. $O + N_2 \rightleftharpoons NO + N$		$5.0 \times 10^{13} \exp(-\frac{75520}{R_o T})$
10. $O_2 + N_2 \rightleftharpoons NO + NO$		$9.1 \times 10^{24}\ T^{-2.5} \exp(-\frac{129120}{R_o T})$
11. $NO^+ + e^- \rightleftharpoons N + O$		$5.4 \times 10^{21}\ T^{-1.5}$

TABLE 3

Aero Thermo Technology (AT2)
HS:ct 4 Nov 1981

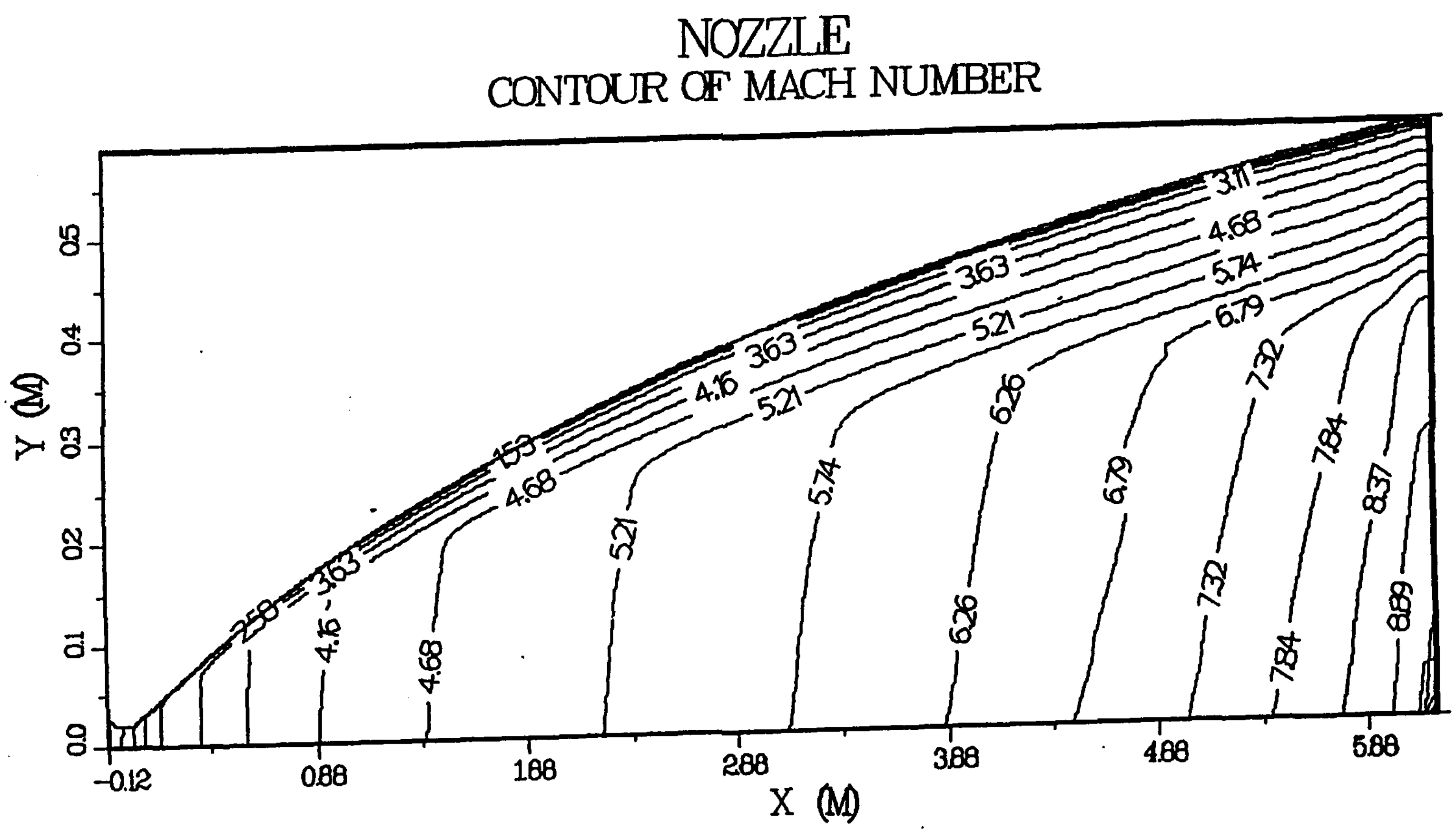
NOZZLE
CONTOUR OF MACH NUMBER
Y (M)
X (M)
0.0
0.1
0.2
0.3
0.4
0.5
-0.12
0.88
1.88
2.88
3.88
4.88
5.88
2.58
3.63
4.16
4.68
4.53
5.21
5.74
6.26
6.79
7.32
7.84
8.37
8.89
3.11

Figure 6-16

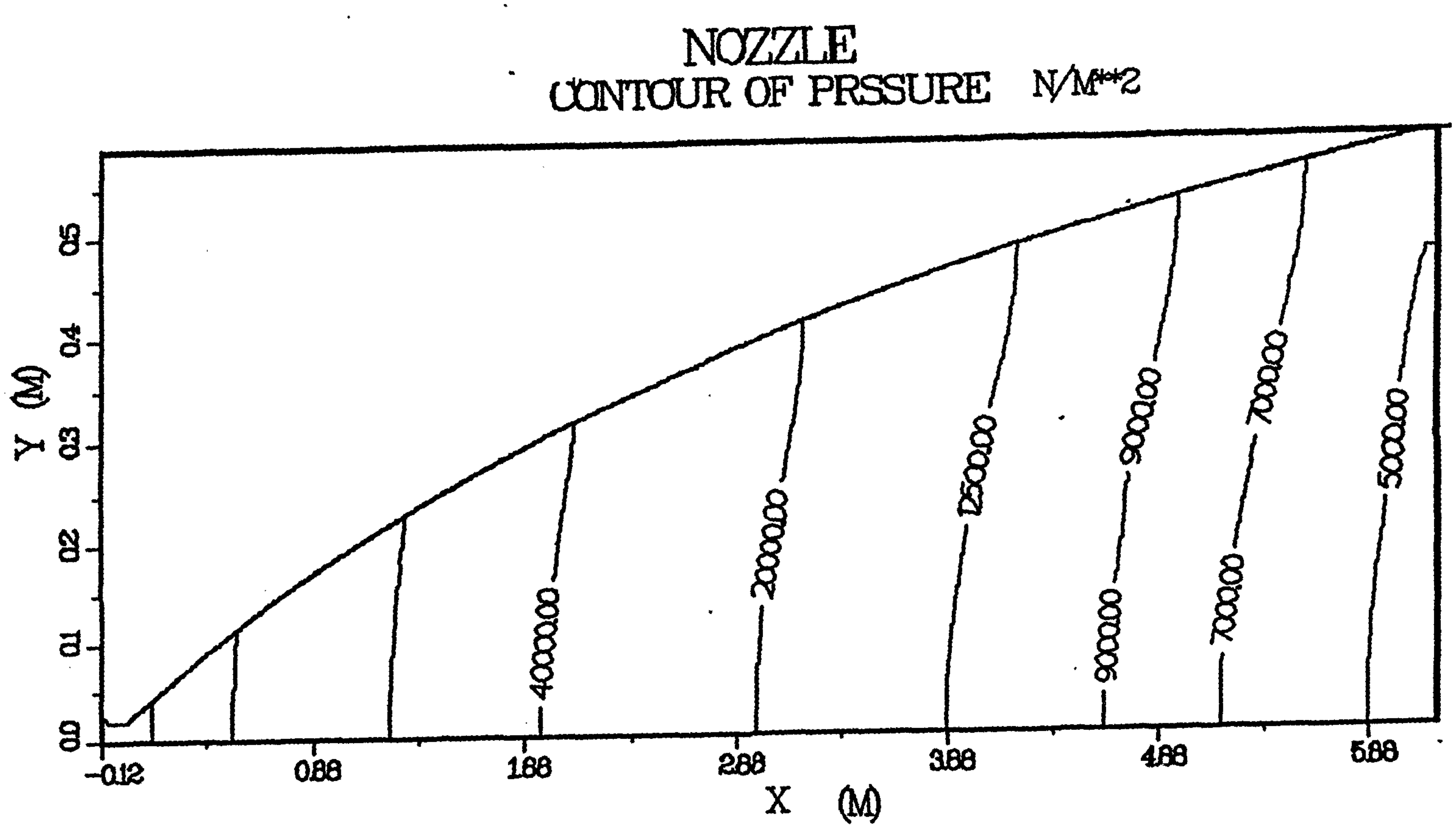
NOZZLE
CONTOUR OF PRSSURE N/M**2
Y (M)
X (M)
0.0
0.1
0.2
0.3
0.4
0.5
-0.12
0.88
1.88
2.88
3.88
4.88
5.88
40000.00
20000.00
12500.00
9000.00
9000.00
7000.00
7000.00
5000.00

Figure 6-17

NOZZLE
CONTOUR OF TEMPERATURE (°K)

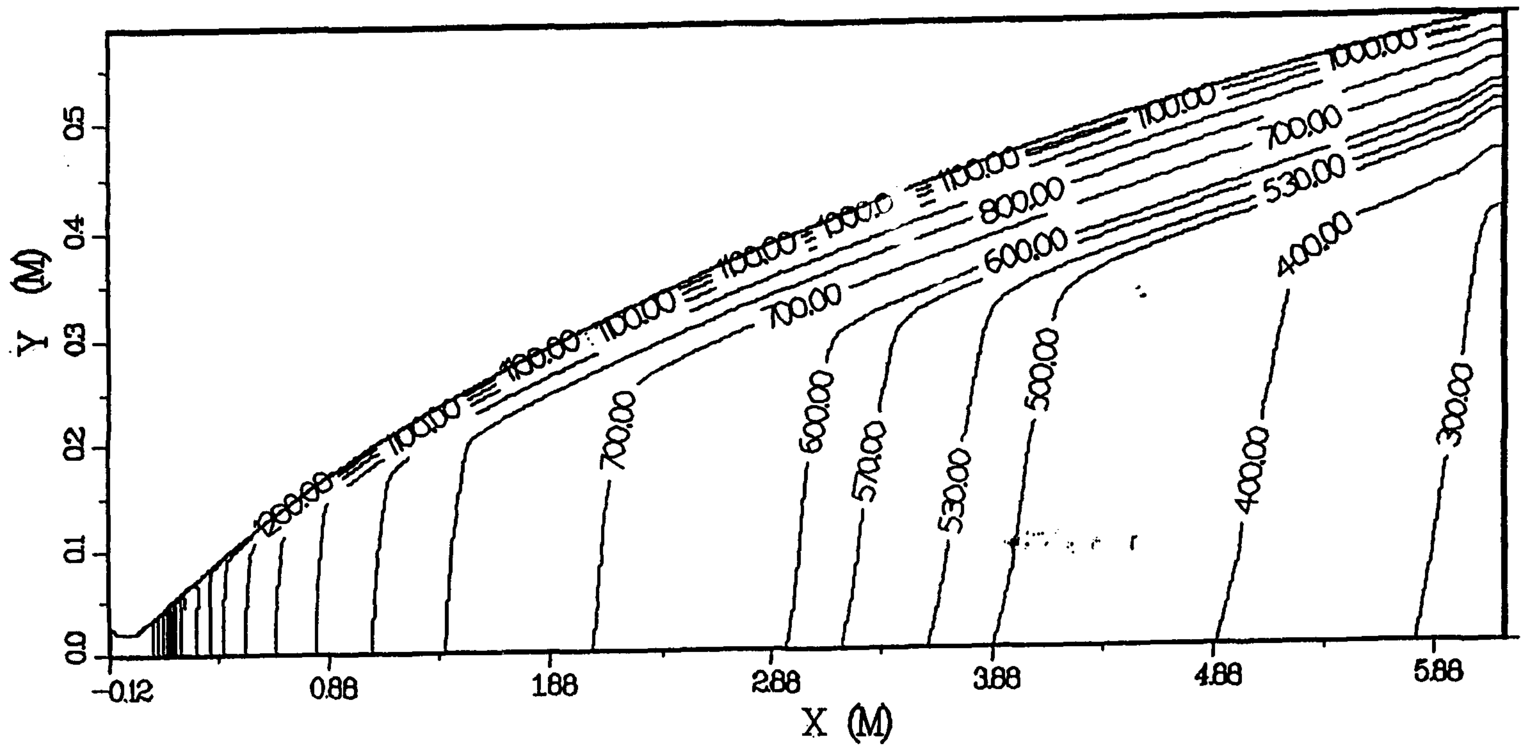

Figure 6-18

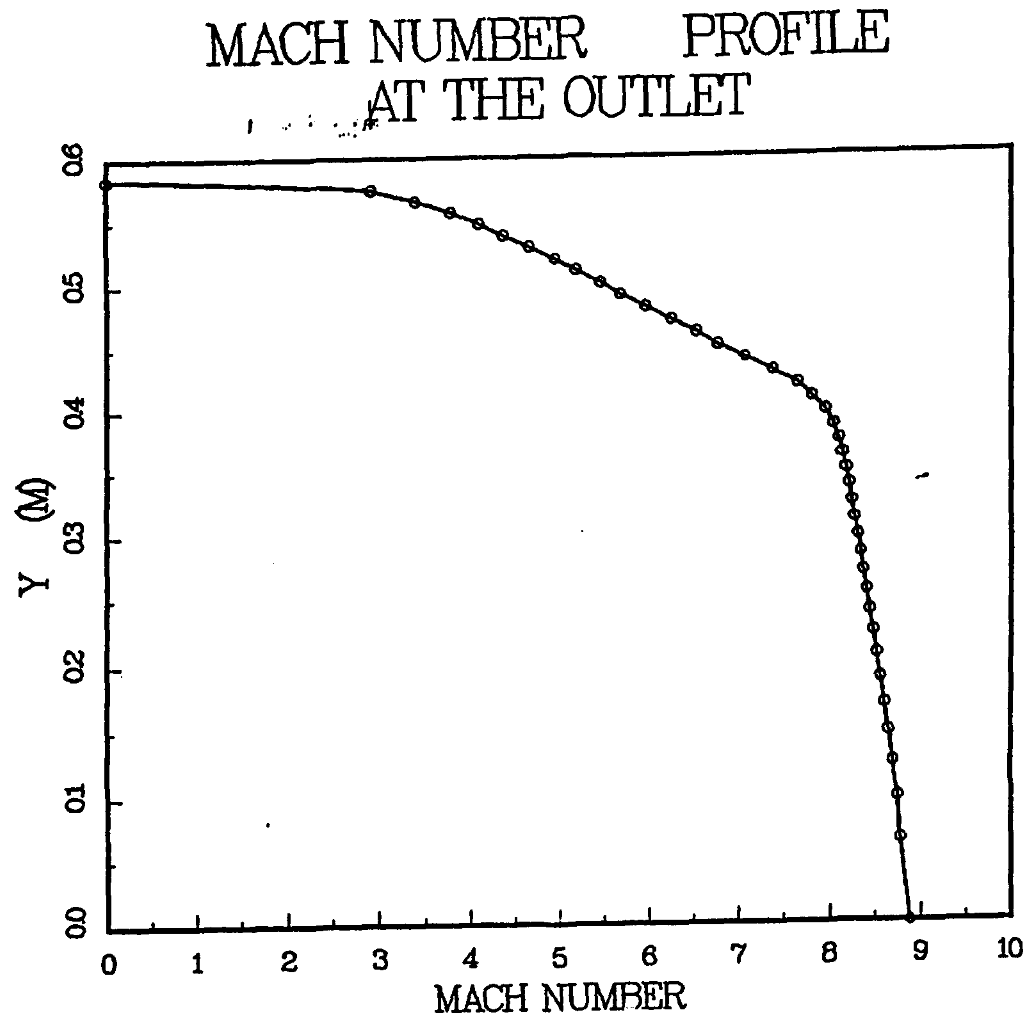
MACH NUMBER PROFILE
AT THE OUTLET
Y (M)
0.0
0.1
0.2
0.3
0.4
0.5
0.6
0
1
2
3
4
5
6
7
8
9
10
MACH NUMBER

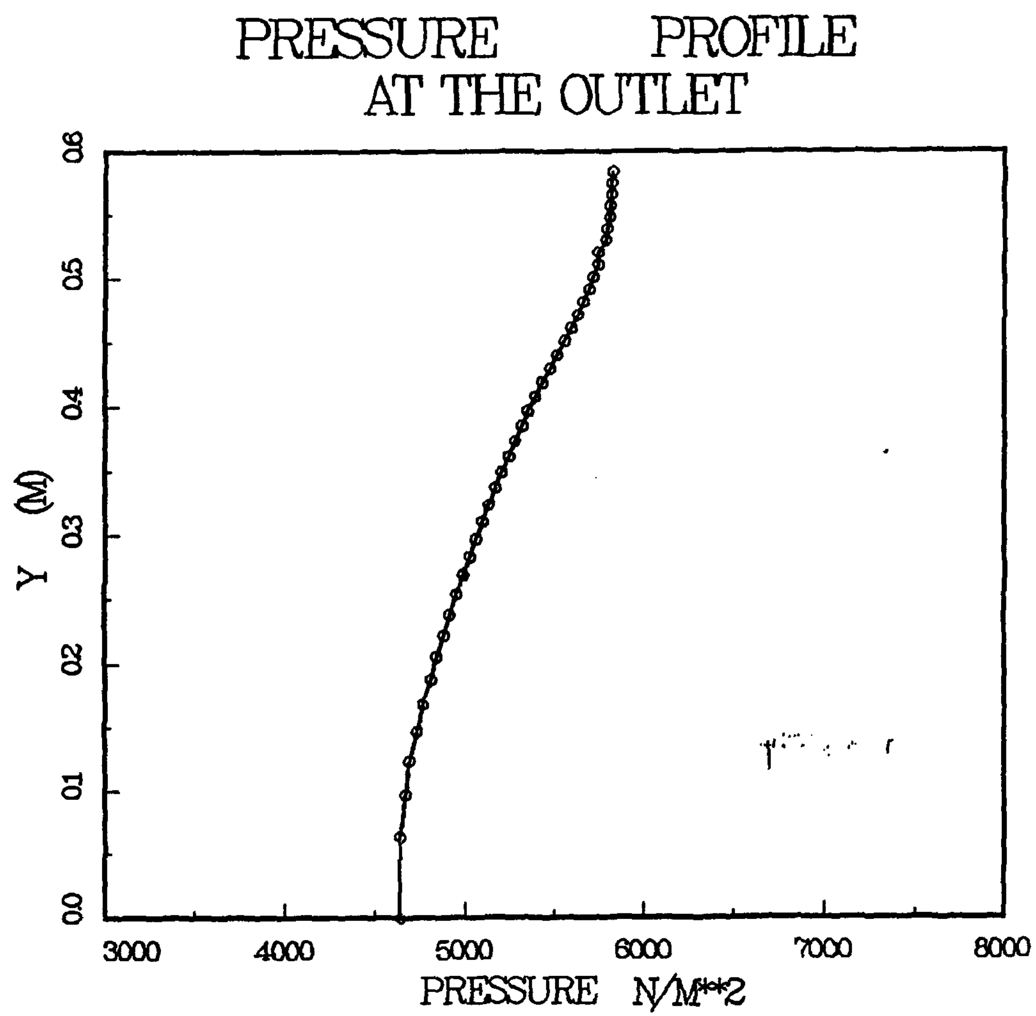
PRESSURE PROFILE
AT THE OUTLET
Y (M)
0.0
0.1
0.2
0.3
0.4
0.5
0.6
3000
4000
5000
6000
7000
8000
PRESSURE N/M**2

Figure 6-20

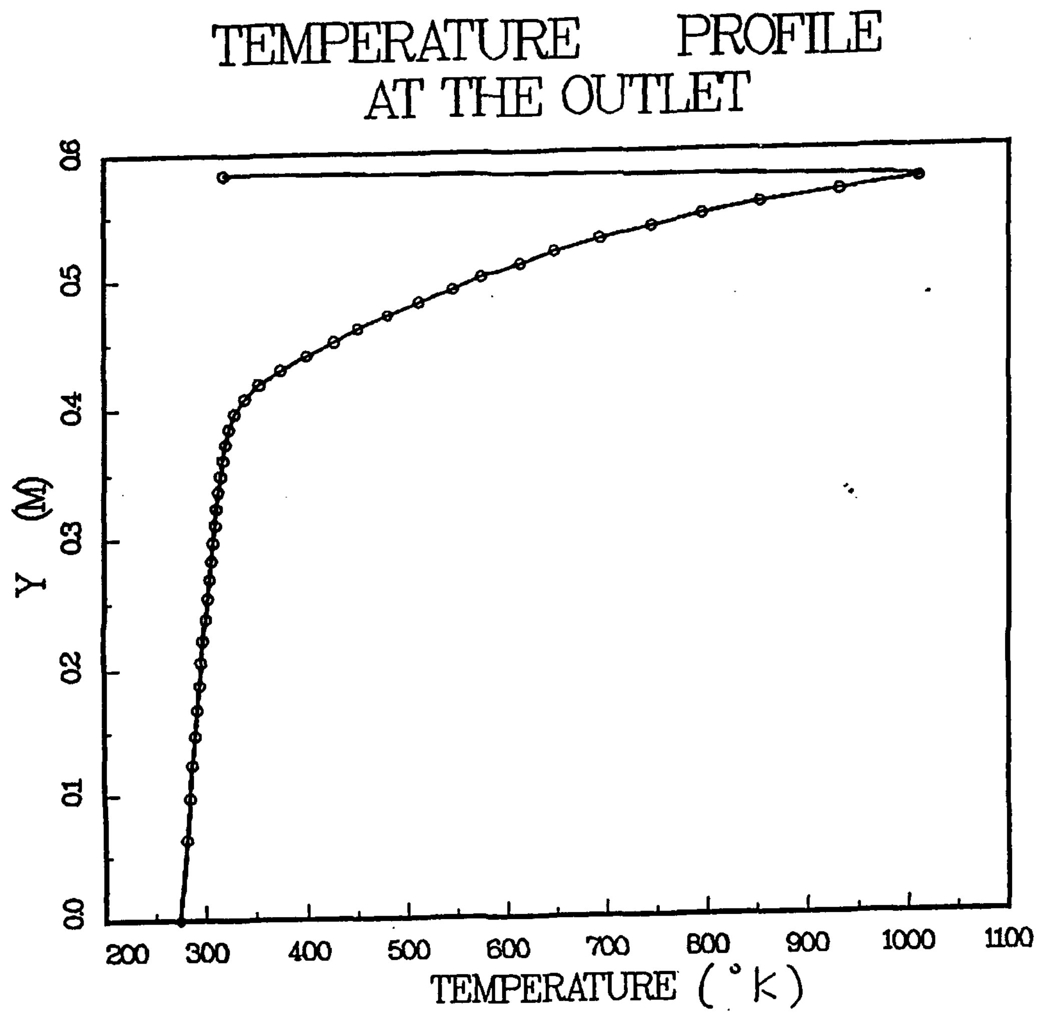
TEMPERATURE PROFILE
AT THE OUTLET
Y (M)
0.0
0.1
0.2
0.3
0.4
0.5
0.6
200
300
400
500
600
700
800
900
1000
1100
TEMPERATURE (°K)

Figure 6-21

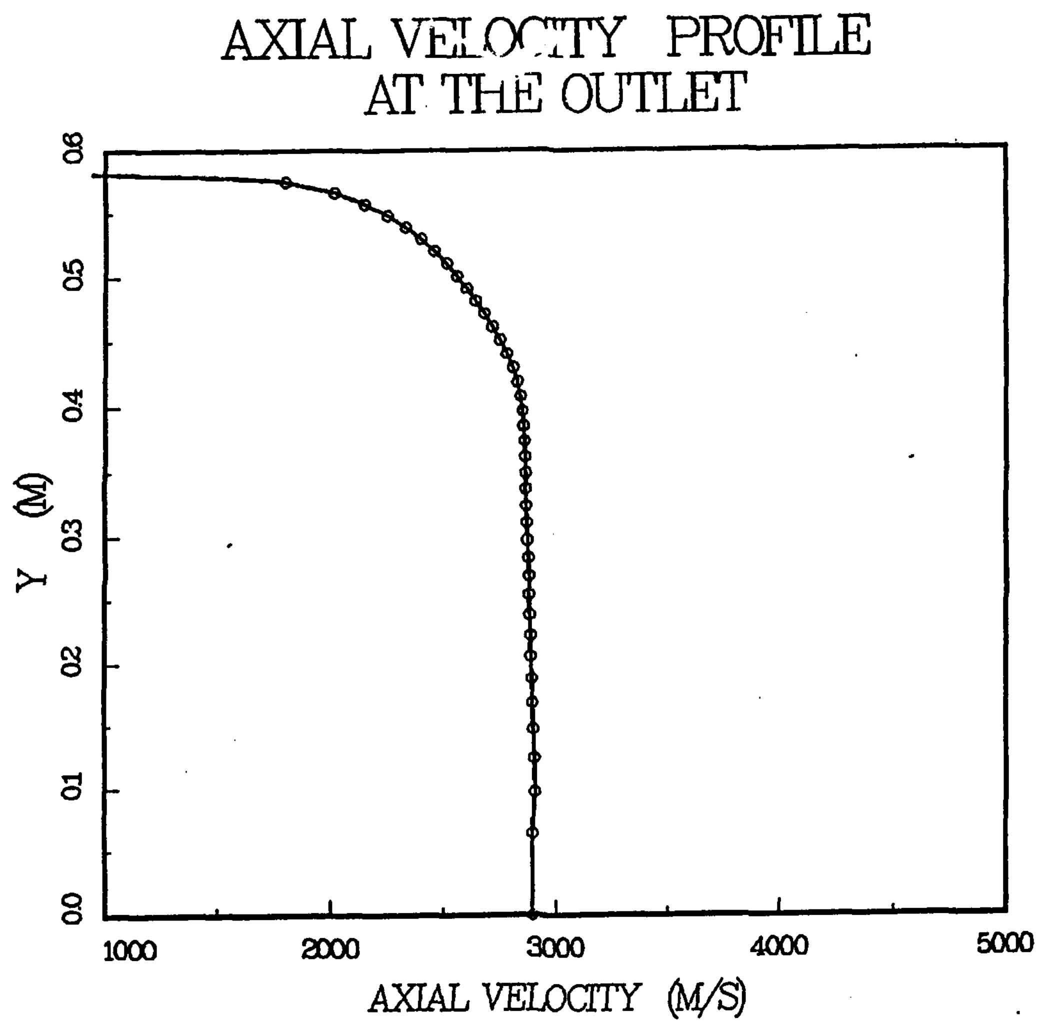
AXIAL VELOCITY PROFILE
AT THE OUTLET
Y (M)
0.0
0.1
0.2
0.3
0.4
0.5
0.6
1000
2000
3000
4000
5000
AXIAL VELOCITY (M/S)

Figure 6-22

6.6 PREDICTION OF FLOWFIELD AND SURFACE PROPERTIES OVER TARE TEST MODEL

The single aperture two-dimensional TARE configuration shown in Figure 6-23 was analyzed. Initial calculations were performed using the "D" nozzle exit conditions of Case 2 from Table 2. The solutions presented were calculated with a finite rate air chemistry model and utilized a k-ϵ turbulence model. The injectant nozzle exit height was 0.27 inches and the working gas was N_2, assumed to be stored at 300°K. The N_2 was expanded to a Mach 2 exit condition maintaining a balanced jet constraint at the interface with the main stream flow over the body.

Figure 6-24 presents the grid network which was set up for the solution of the flowfield. The grid was divided into four sections corresponding to: 1) nose, 21 x 21, 2) afterbody, 31 x 21, 3) window area, 61 x 41.

Mach contour plots are shown in Figure 6-25. These results clearly indicate the bow shock and subsequent wedge shock over the body as well as the slight disturbances created by the mixing of the coolant layer with the main stream flowfield. Figures 6-26 and 6-27 present the corresponding pressure and temperature contours.

Heat flux over the window is depicted in Figure 6-28. Note that the heating rate is negative (indicating cooling) over the entire length of the window. For the assumptions employed this indicates that the window is over cooled and thus the amount of coolant can be reduced. The next iteration planned will alter the injector size to reduce the coolant flow.

6.7 CONCLUSIONS

Calculations were made with two advanced CFD codes to predict the surface quantities, pressure and heat transfer, for two experimental configurations. Calculations with the GASP code were made to investigate the accuracy and robustness of the numerics for stressing calculations and to assess the need for further development and refinement, especially turbulence modeling. Calculations with the MAST code were made to determine if a more highly developed k-e turbulence model would increase the accuracy of the calculations.

SINGLE APERTURE TARE MODEL

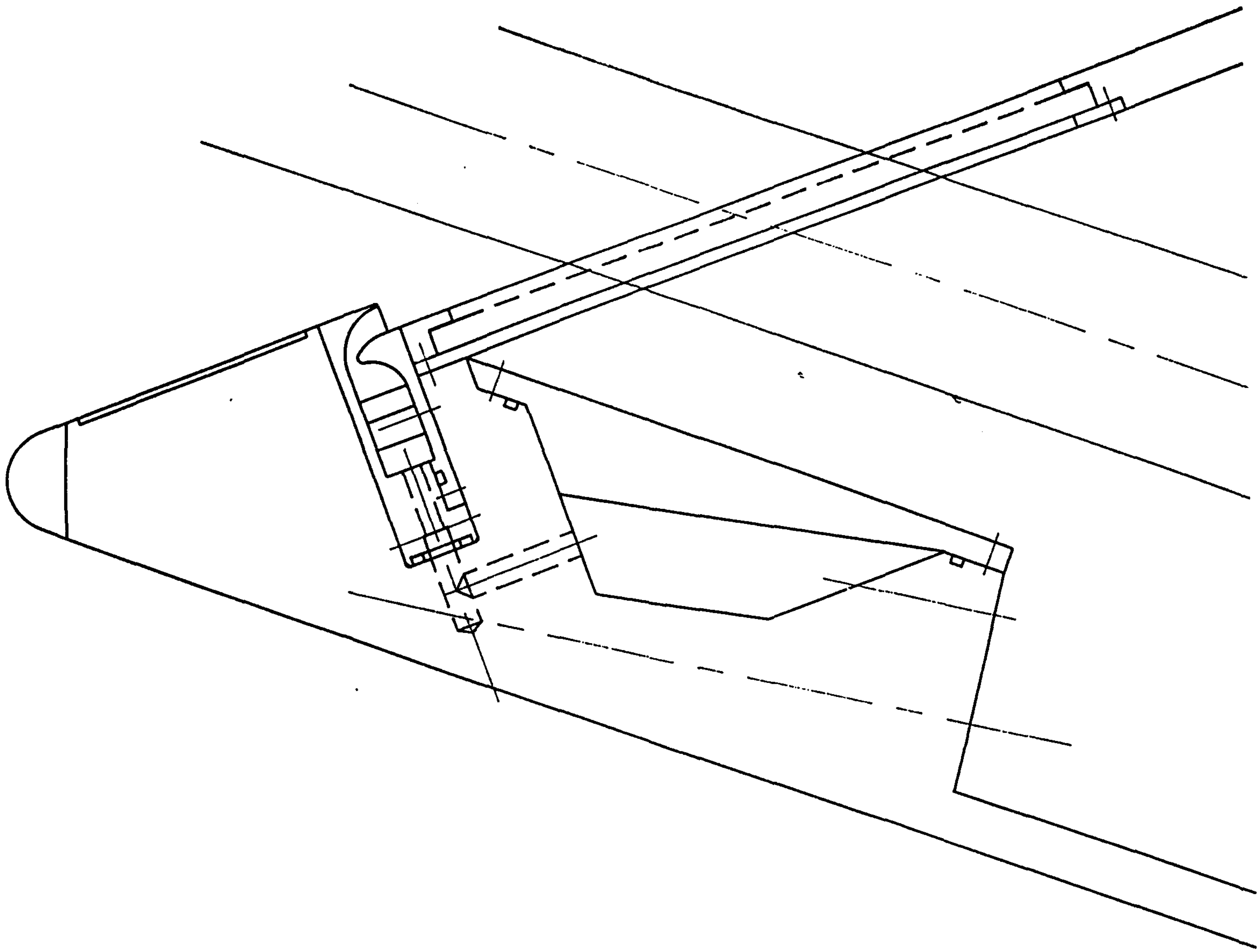

Grid Point

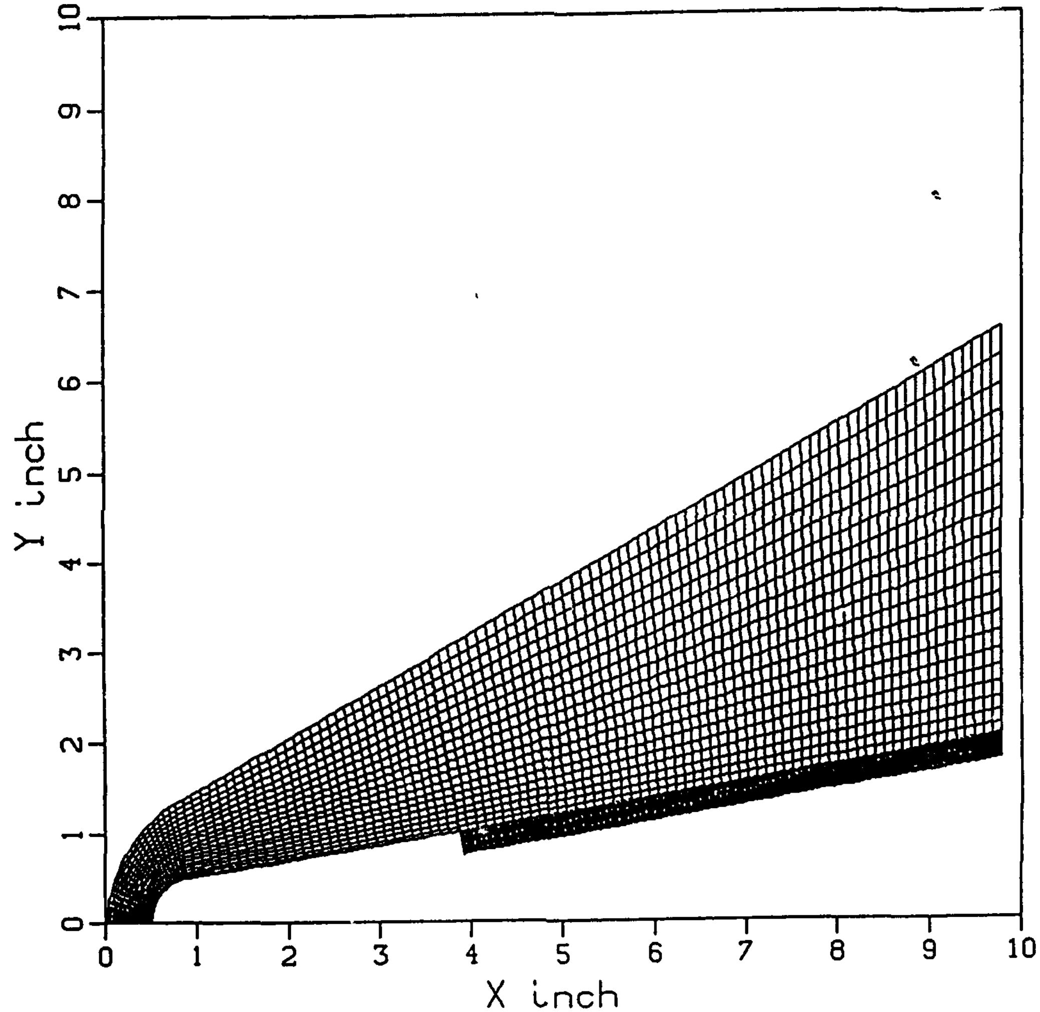

Figure 6-24

Mach number contour

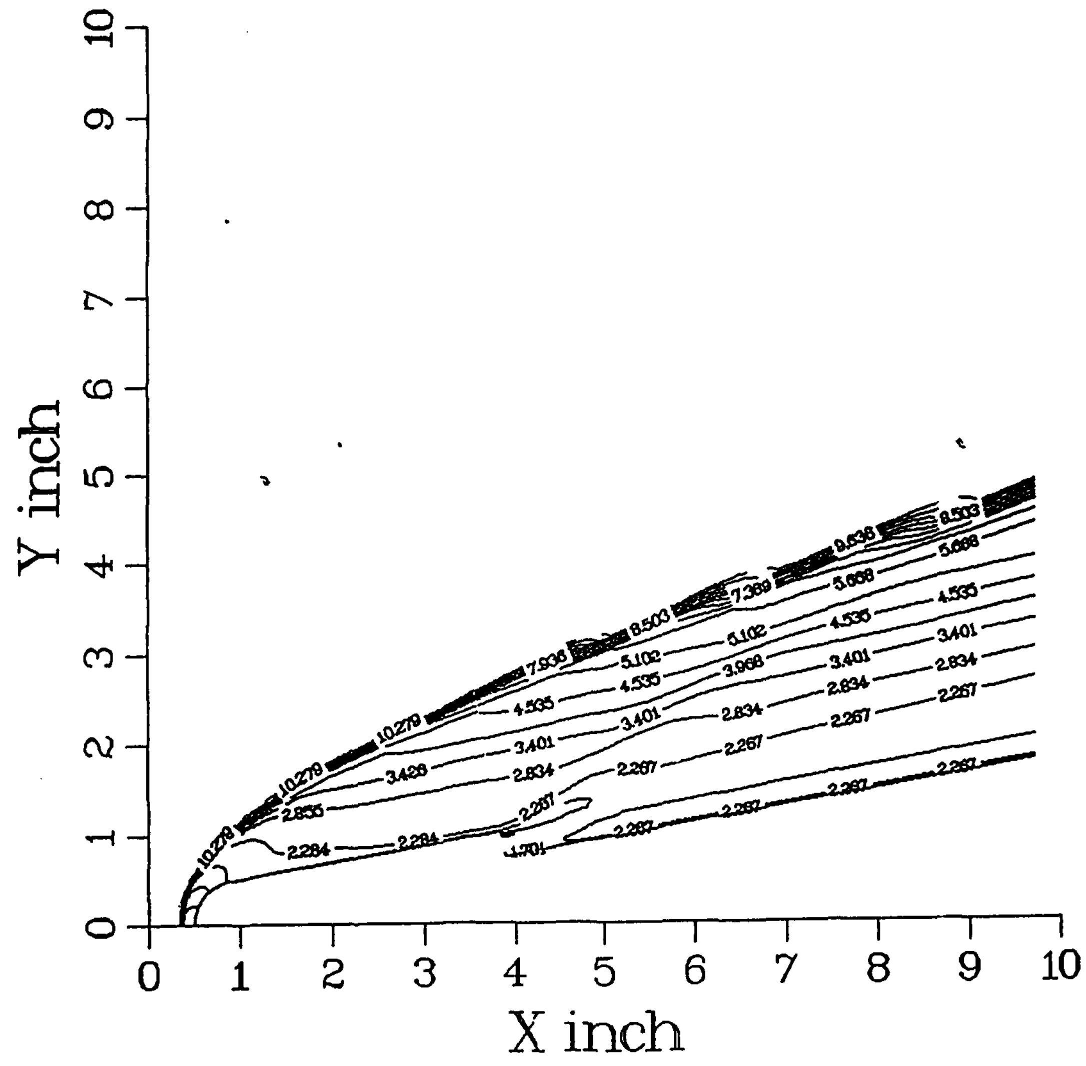

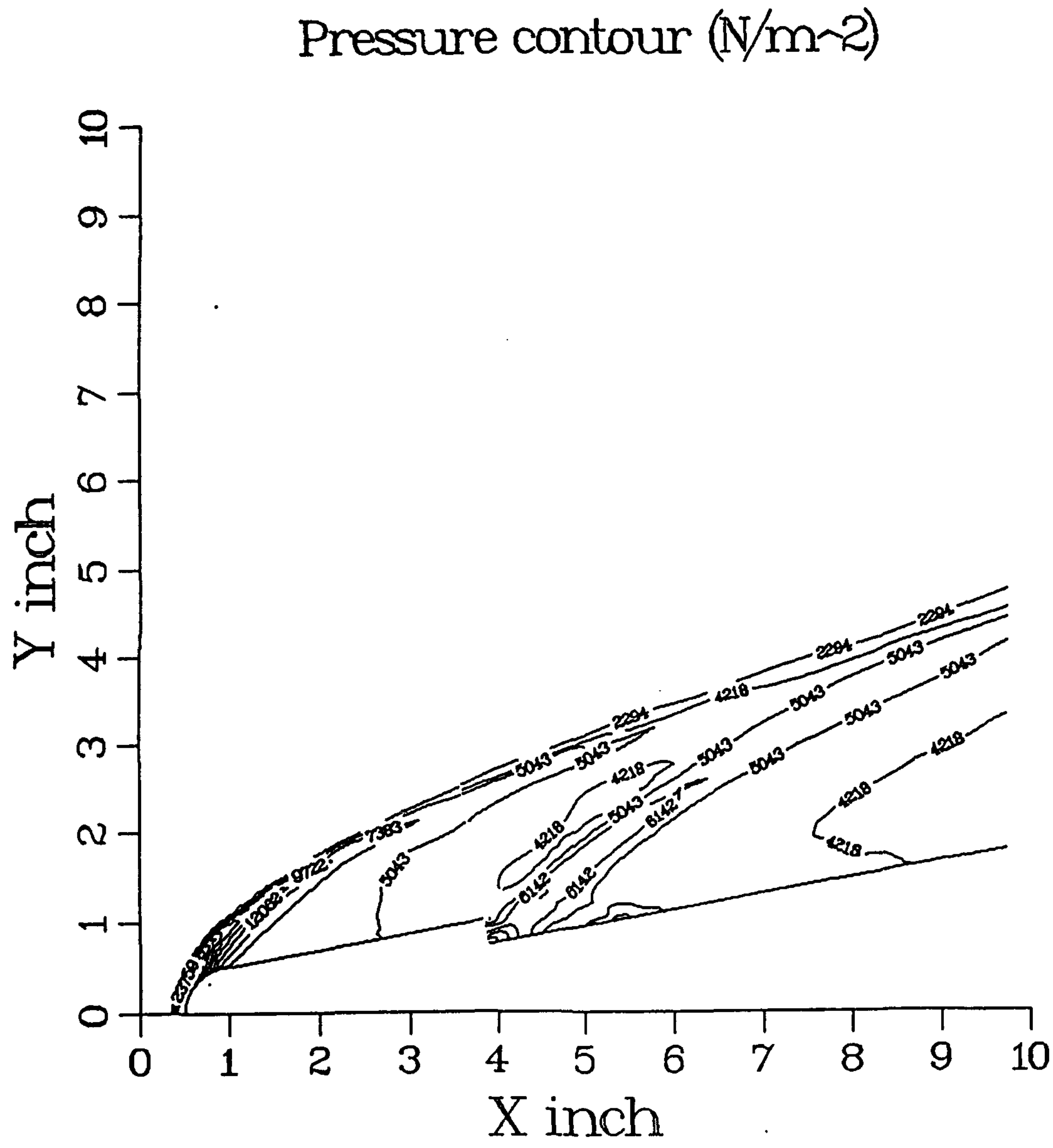
Pressure contour (N/m~2)
Y inch
X inch
0
1
2
3
4
5
6
7
8
9
10
2294
4218
5043
6142
7383
9722
12082
23759

Figure 6-26

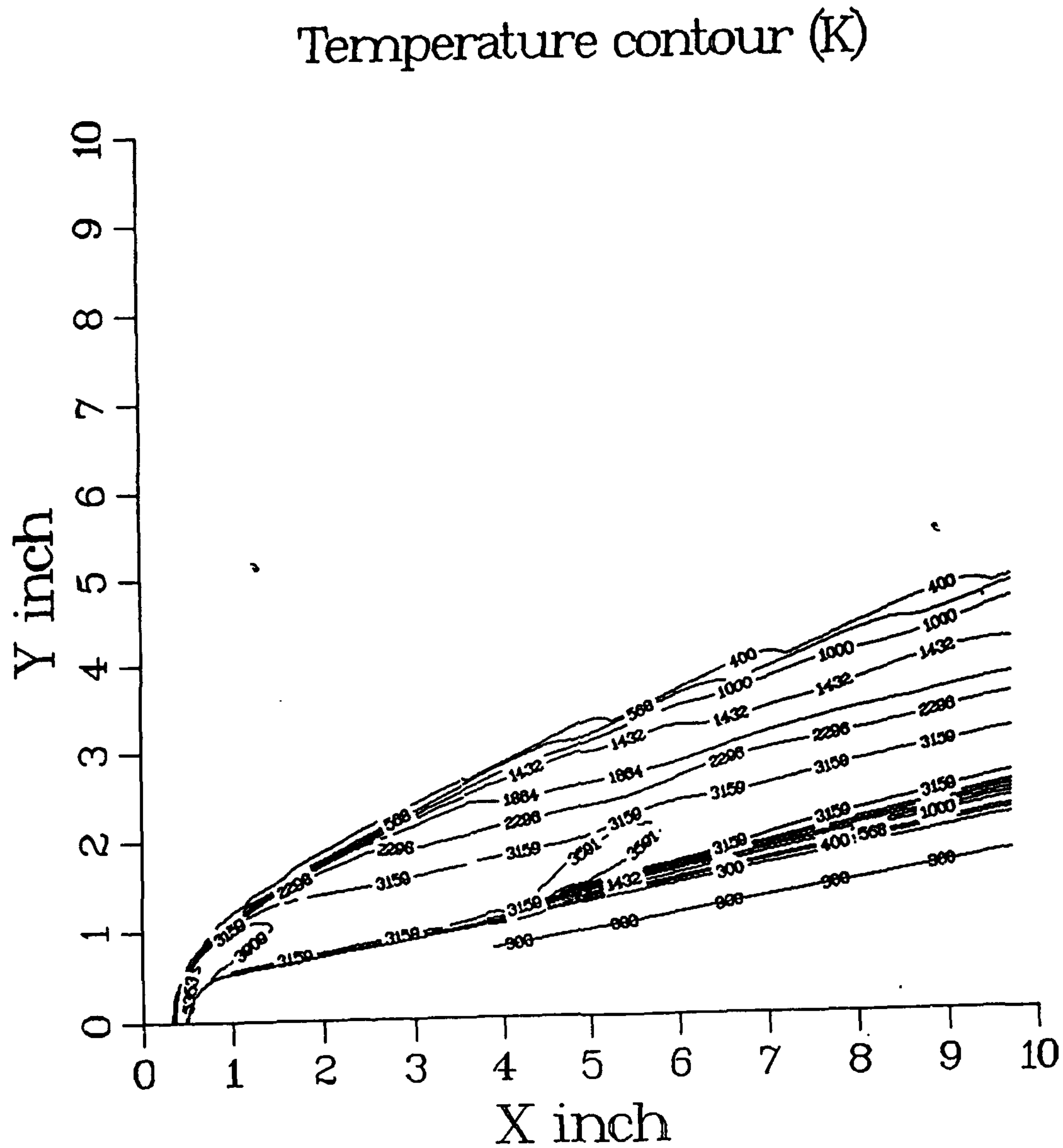

Figure 6-27

Heat Flux

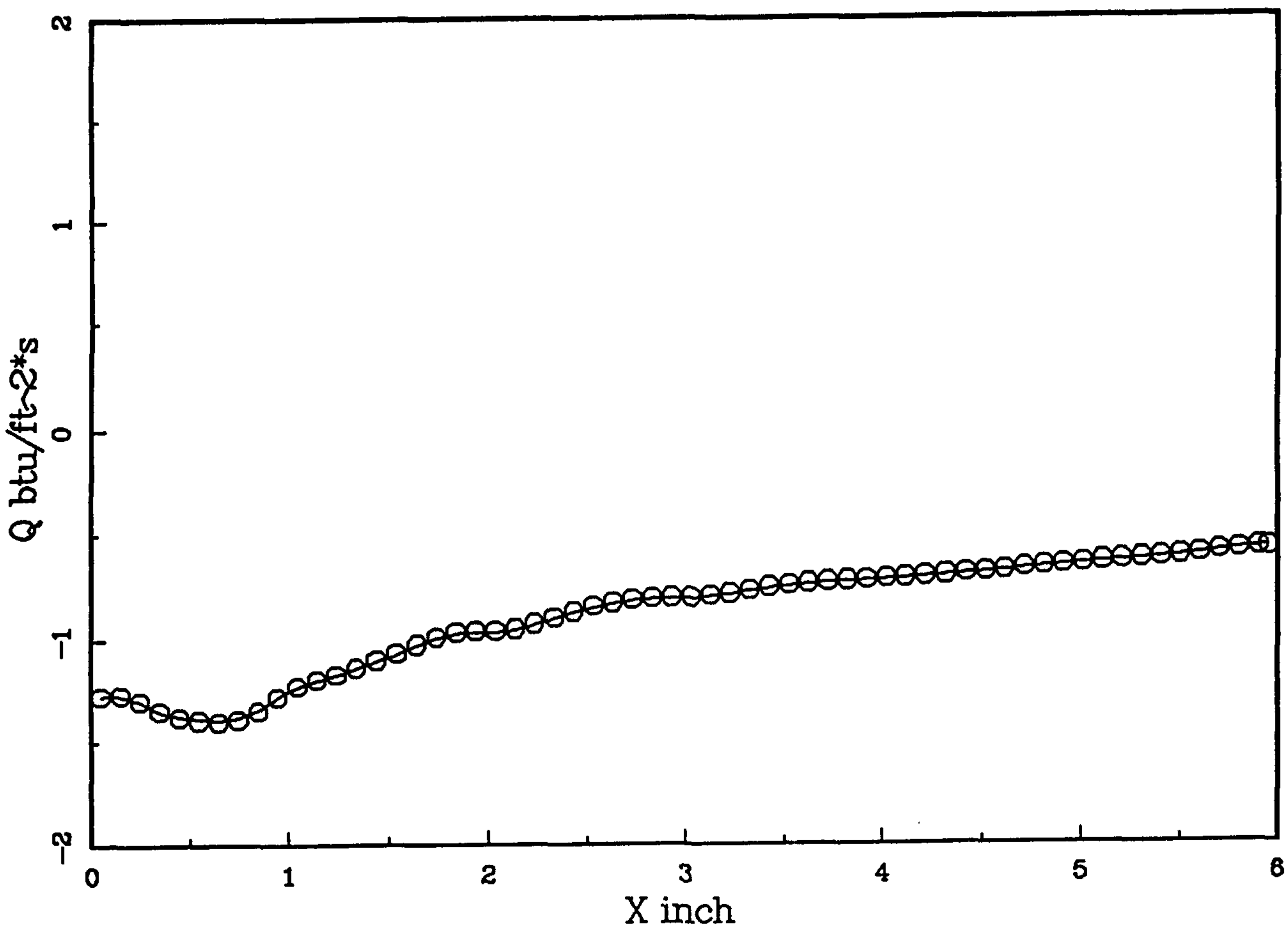

Figure 6-28

Comparisons between predicted quantities with experimental data show that the following conclusions can be drawn:

1. The GASP code has robust numerics and does a reasonable job capturing shocks and flow discontinuities.

2. The turbulence modeling now in GASP is inadequate to resolve flows with large adverse pressure gradients and separated regions.

3. The Baldwin-Lomax algebraic turbulence model now in GASP demonstrated grid dependence for predicting heat transfer. Improved turbulence modeling with a k-e model may negate the need for further refinement of the Baldwin-Lomax model.

Preliminary calculated results have been presented for the "D" nozzle and for the preliminary TARE model design.

6.8 REFERENCES

1. Baldwin, B.S. and Lomax, H., "Thin Layer Approximation and Algebraic Model for Separated Turbulent Flows", AIAA Paper No. 78-257, 1978.

2. Holden, M.S., "A Data Base of Experimental Studies of Shock Wave/Wall Jet Interaction In Hypersonic Flow", Calspan-University of Buffalo Research Technical Report, April 1990.

3. Jiang, Y., Chen, C.P. and Shang, H. M. "A New Pressure-Velocity Coupling Procedure for Inviscid and Viscous Flows at All Speeds," in Proc. 4th International Symposium on CFD, V.C. Davis, 1991.

4. Gordon, S. and McBride, B.J., CEC71 program, NASA Sp-273, 1971.

5. Hammond, G.P., "Turbulent Prandtl Number Within a Near-Wall Flow", AIAA J. 23, 1668, 1985.

6. Lordi, J.A., et. al., "Description of Nonequilibrium Effects on Simulation of Flows about Hypersonic Vehicles" AIAA paper 88 - 0476. Calspan Corporation, Buffalo, New York 14225, 1988.

Section 7
STRUCTURAL LOADING IN LENS FACILITY
Science and Technology Associates, Inc.

Studies of the Stress Levels and Motion of the LENS and 96" Shock Tunnel

7.1 Introduction

The stress/motion of the tunnel was initiated using two approaches:

- Numerical marching code
- Numerical solution to the wave equation

In general, for a rapidly applied load (i.e., an impact load) peak stresses of $\sigma + i\sigma$ will be reached where σ is the static live stress and i is a coefficient of impact. These stresses may be as much as 2X the static live stress and the strain is correspondingly large. However, where the body under impact is sufficiently massive, the maximum stress is equal to the static live stress. For the time constant of diaphragm rupture and energy involved, there will be no shock wave. The stress wave will be purely acoustic.

An analysis of the system for the first 3 msec of action after rupture was performed assuming that the Driver section was a massive rigid body. The 3 msec is approximately the time for the stresswave to reach to nozzle throat and coincidentally is about equal to the time for the expansion (sonic) wave to reach the west end of the Driver tube.

A brief look at the relative deformations of the Driver and Driven tubes showing the relative rigidity and confirming the rigid body assumption preceding, follows:

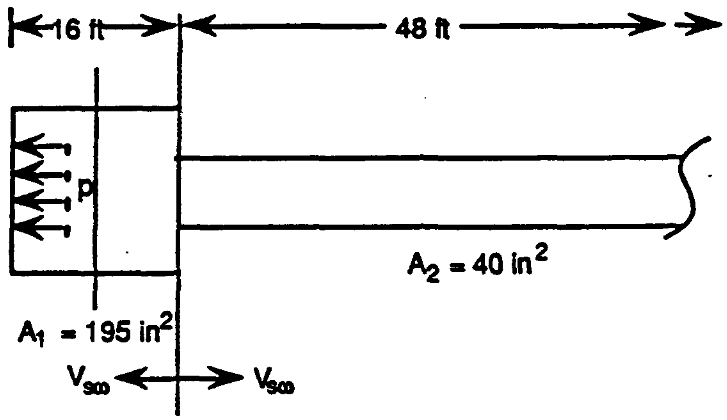

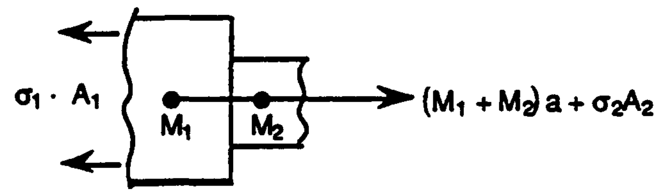

$$\frac{Fl_1}{A_1E} << \frac{Fl_2}{A_2E}$$

$$\frac{F}{E}\,\frac{16}{195} << \frac{F}{E}\frac{48}{40}$$

$$0.82\,\frac{F}{E} << 1.2\,\frac{F}{E}$$

Ratio = .06838

Deformation effects of the Driver are second order and can be neglected.

7.2 Stress Levels in Driven Tube

Taking the Driver as a rigid body and using the force on the west end as due to the entire internal area at peak pressure, the maximum possible movement in 0.003 seconds was calculated and shown to be 0.108 inches. The static live strain for the Driven tube would be 0.0008 and the deflection would consequently be 0.50 inches. Since the tube end can only move 0.108 inches, this indicates that the Driver section is so massive that very little stress and strain will be in the driven bar.

Using the basic equations as shown following the variation of stress with position in the bar was calculated for various masses of the Driver; 100 lbs, 1000 lbs, 5000 lbs, and 16000 lbs.

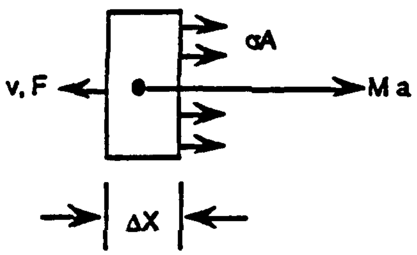

$F = \Sigma M_t\, a + \sigma A$

$\sigma = E\ s_s$

$\Delta s = S_s\, \Delta x = v_o t + \frac{1}{2} a\, t^2 = S_s t_{step}\, V_{sw}$

$v = v_o + at$

Step Size: $\Delta x = t_{step} \times V_{stresswave}$

$V_{stresswave} = 16{,}800$ ft/sec

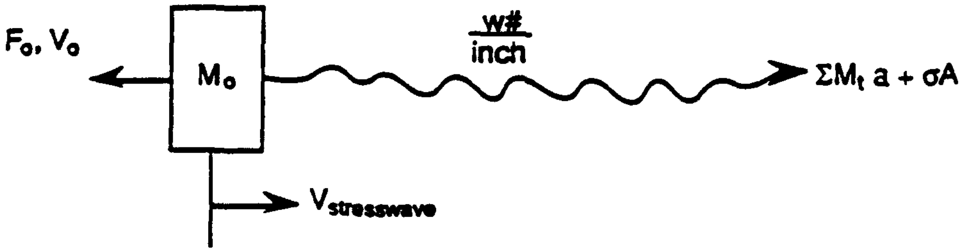

$$\Sigma M_t = M_o + \frac{w\#}{inch} \Sigma t\, V_{sw}$$

$$F = M\frac{dv}{dt} + V\frac{dm}{dt}$$

For an acoustic wave

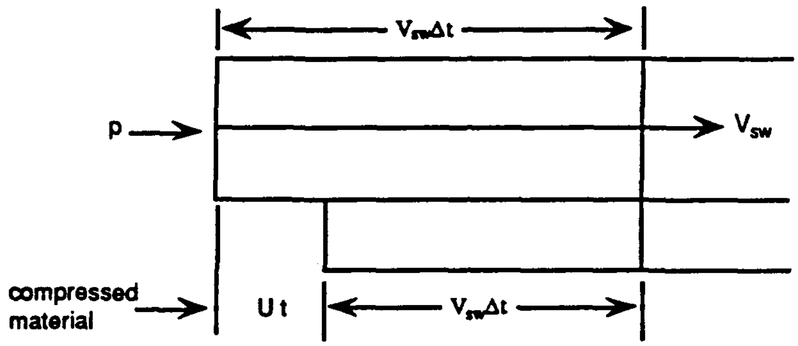

$$\frac{N_{s\omega}t - (V_{s\omega} - U)\,t}{V_{s\omega}t} = \frac{U}{V_{s\omega}}$$

From Hooks law

$$\frac{U}{V_{sw}} = \frac{P}{E}$$

momentum of deformed material = pt

$$p = \frac{\text{Force}}{\text{Unit Area}} \qquad t = \frac{\text{Time Increment}}{\text{Step}}$$

$$\frac{\rho}{g} = \frac{\text{Density}}{\text{Unit Area}} \qquad U = \text{Velocity of deformed material}$$

V_{sw} = Velocity of stress wave

$$\frac{\rho}{g} V_{sw} t \Delta U = pt$$

$$p\# = \frac{\rho}{g} V_{sw} \Delta U \qquad , \Delta U = at$$

$$p\# = \frac{\rho}{g} V_{sw} at \quad \text{due to } V\frac{dm}{dt}$$

Then $$\frac{\#}{\text{Unit Area}} \quad F = \left(M_o + \frac{\rho}{g} V_{sw} t\right) a + \sigma$$

$$\Sigma F = \left(\underbrace{M_o}_{\text{Driver};\ \Sigma M \text{ Previous steps}} + \frac{\rho}{g} A \underbrace{V_{sw} t}_{M_{step}}\right) M_{step} + \underbrace{\sigma A}_{\text{Stress at end of step}}$$

The bar position or slice was in ~ 1.0 ft increments. The figures 7-1 through 7-4, show that until the lowest mass (100 lbs), the stress right adjacent to the diaphragm doesn't build up to the static live stress. Further even in this case, the mass build up of the driven tube keeps the stress/strain near zero by the time 10 feet of mass is added.

7.3 Support of Optical System Design

Analytical support for the static and dynamic load effects was provided to Dr. J. Craig of PRI in Irvine, CA. Copies of analysis were sent to CUBRC.

Support in the model mounting system for LENS was provided to CUBRC. Axial and bending deflections of the model support system were calculated as well as vibration frequencies.

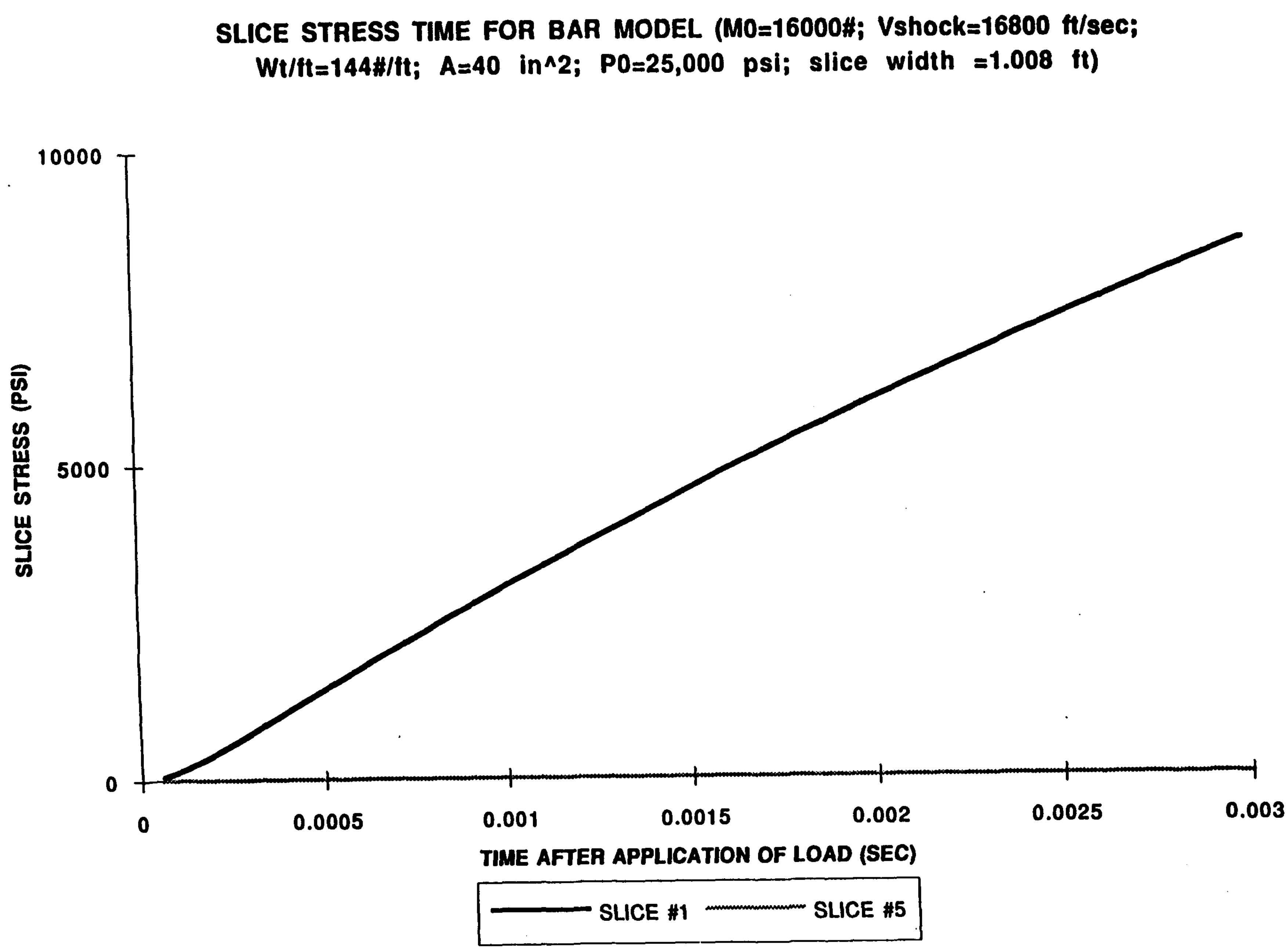
SLICE STRESS TIME FOR BAR MODEL (M0=16000#; Vshock=16800 ft/sec;
Wt/ft=144#/ft; A=40 in^2; P0=25,000 psi; slice width =1.008 ft)
SLICE STRESS (PSI)
10000
5000
0
0
0.0005
0.001
0.0015
0.002
0.0025
0.003
TIME AFTER APPLICATION OF LOAD (SEC)
SLICE #1
SLICE #5

Figure 7-1

SLICE STRESS TIME FOR BAR MODEL (M0=5000#; Vshock=16800 ft/sec; Wt/ft=144#/ft; A=40 in^2; P0=25,000 psi; slice width =1.008 ft)

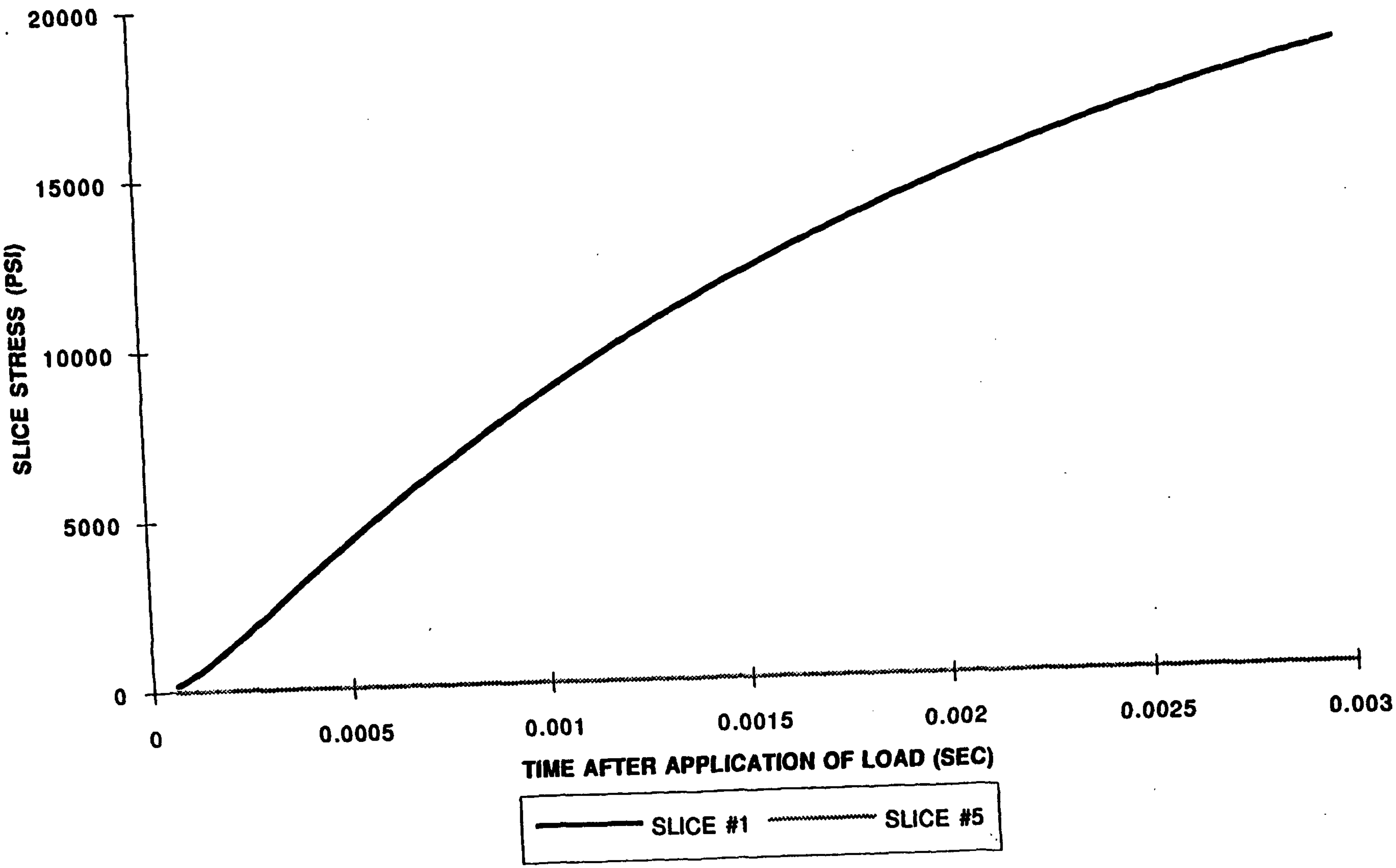

Figure 7-2

SLICE STRESS TIME FOR BAR MODEL (M0=1000#; Vshock=16800 ft/sec; Wt/ft=144#/ft; A=40 in^2; P0=25,000 psi; slice width =1.008 ft)

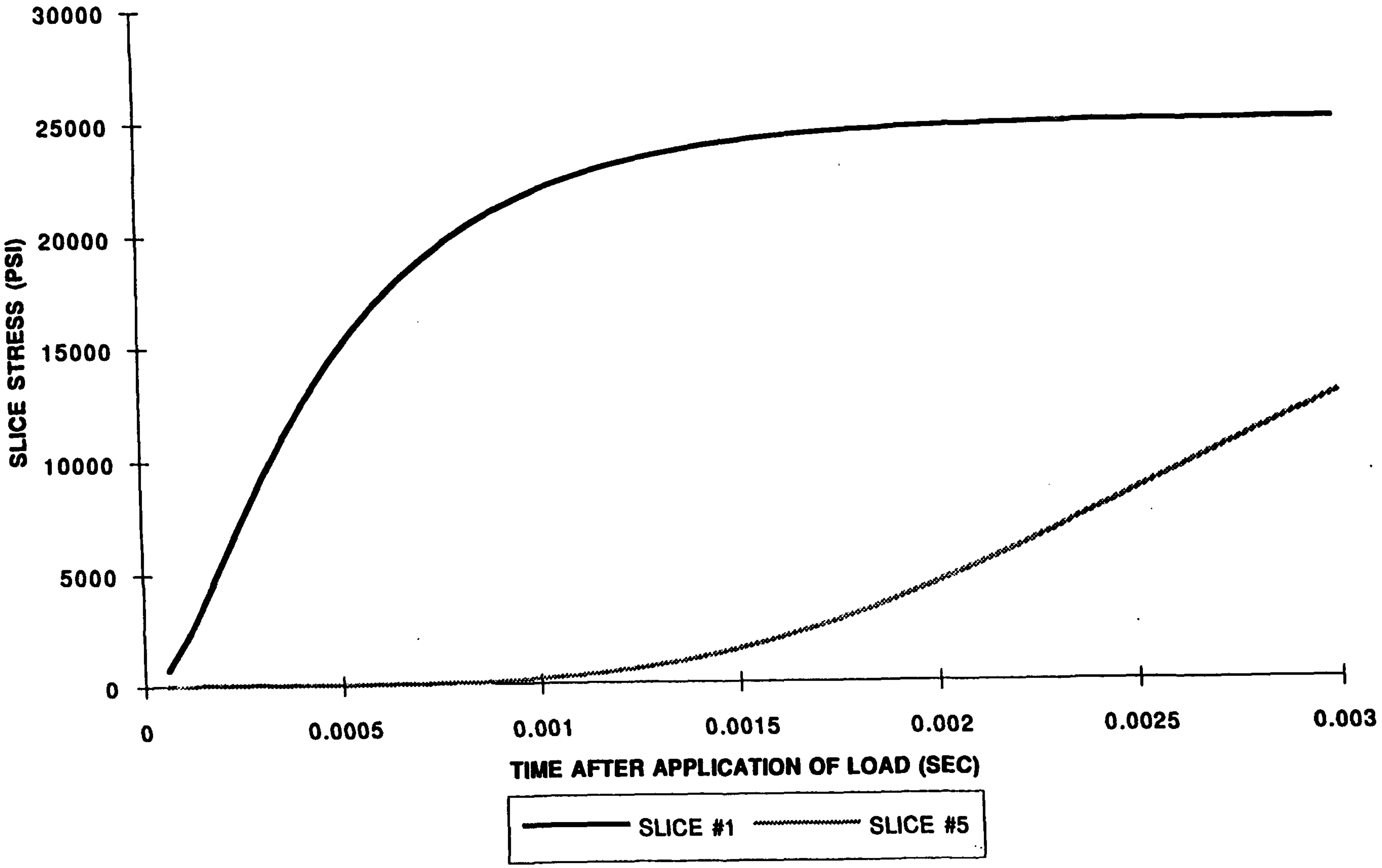

Figure 7-3

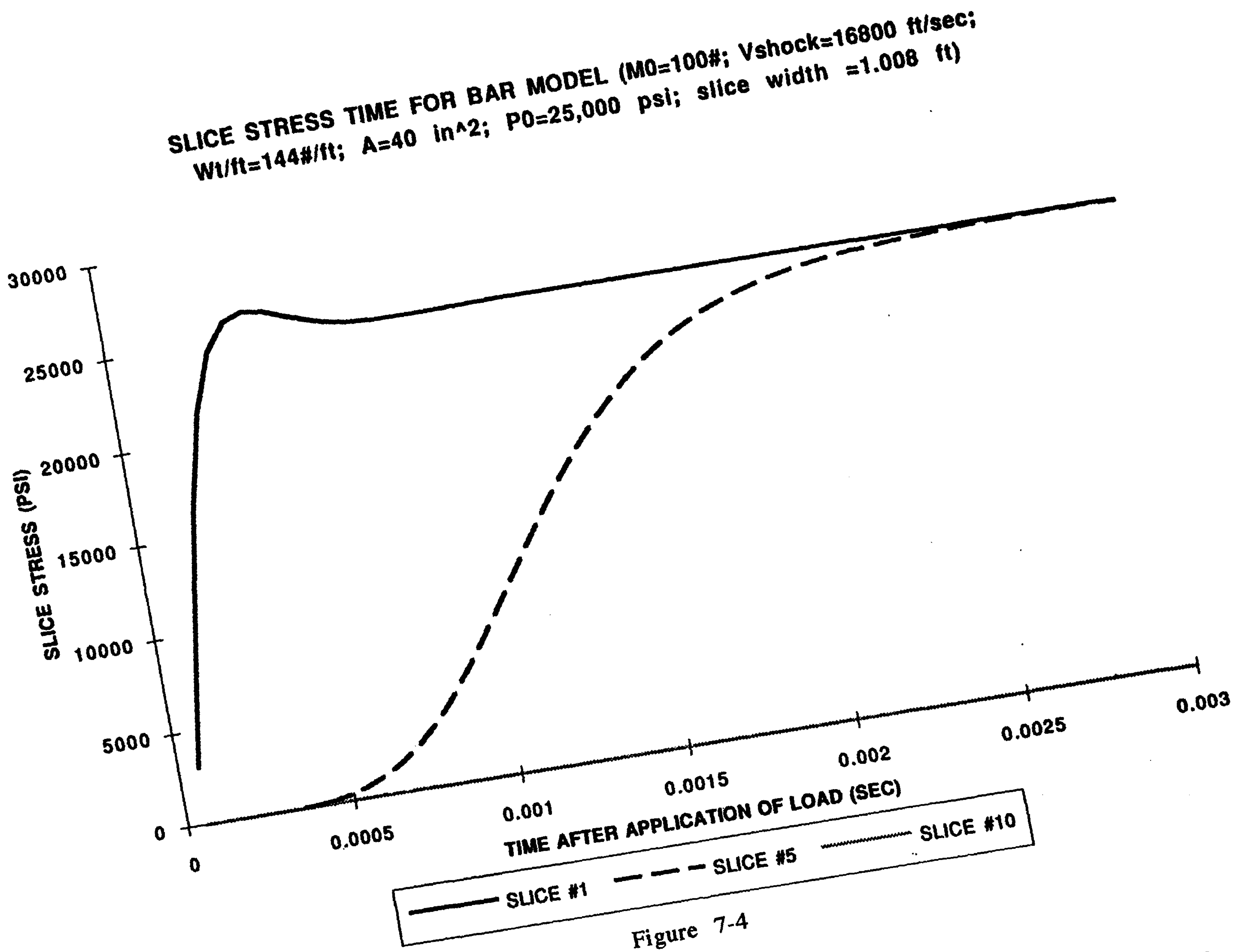
SLICE STRESS TIME FOR BAR MODEL (M0=100#; Vshock=16800 ft/sec;
Wt/ft=144#/ft; A=40 in^2; P0=25,000 psi; slice width =1.008 ft)
30000
25000
20000
15000
10000
5000
0
SLICE STRESS (PSI)
0
0.0005
0.001
0.0015
0.002
0.0025
0.003
TIME AFTER APPLICATION OF LOAD (SEC)
SLICE #1
SLICE #5
SLICE #10

Figure 7-4

Section 8
FLIGHT TEST SUPPORT
Sparta, Inc.

8.1 Introduction

The Aero Optic Evaluation Center (AOEC) is designed to provide accurate ground simulation and measurement of endo-atmospheric interceptor seekerhead Aero Optic phenomena. Key to providing this capability is the Large Energy National Shock Tunnel (LENS) facility. This shock tunnel can only provide partial simulation of these environments. There are, however, certain aspects of shock tunnel testing that require validation by actual flight measurements.

Two issues arise from the short (several milliseconds) test time. One is the uncertainty in results because there is insufficient time to produce natural heating of the model. Therefore, the coupled effects of combined pressure and heating are treated in an approximate manner. The other short test time question is whether or not the flow phenomena have time to establish. CFD calculations indicate that sufficient flow establishment time exists, but it must be remembered that these computer models themselves lack flight validation.

The final issue exists because of uncertainties in flowfield chemistry reaction rates. Those uncertainties indicate that the dissociated shocked test gas may not have sufficient time (nozzle length) to recombine into air prior to reaching the test model.

8.2 Flight Test Program

Objective and Approach

The objective of the SPARTA effort in support of the AOEC is to construct a high confidence flight test that will validate the LENS ground test results. The approach taken is to provide maximum duplication between ground and flight testing. This is achieved by selecting flight test environments that replicate ground test conditions; by flight testing the exact seekerhead configuration that is ground tested; and by using flight instrumentation in ground tests.

The critical test environments require achieving 14000 fps at 100 kft. Currently no interceptor booster system exists that can meet this requirement. The Army is developing such a system in support of the ENDO LEAP program, but the risk associated with that system not being available in the near term is high. Therefore, a flight test program based on existing sounding rocket technology was examined. It was found that a "piledriver" approach (launching near vertically, pitching over and firing down) could produce the required test condition using proven sounding rocket combinations. This launch approach permits reduction in several high risk areas of testing, but not without some degradation of desired measurements or experiments.

The Aero Optic measurements of interest that impact interceptor design/performance and require validation include: flowfield radiation, attenuation, blur, jitter, boresight error, boresight error slope, window and forebody thermal control performance. Table 1 shows a comparison between the new interceptor booster and existing sounding rocket flight test scenarios.

What is apparent from the table is that while the interceptor launch provides the best measurement scenario, the risk to mission success attributable to the undeveloped and unproven booster, shroud removal and target placement system forces the sounding rocket choice. The test and experiment scenario selected by SPARTA is based on that logic.

The specific experiments and test environment configured are:

Launch Vehicle and Trajectory

- Piledriver three stage sounding rocket. Two stages up, remove the shroud exoatmospherically, pitch over, gravity accelerate down, fire third stage down just prior to reentry and accelerate to 14000 fps.

Seekerhead

- ENDO LEAP tetracone, internally cooled forebody and nosetip, film cooled sapphire window.
- Optics boresighted at 20° corresponding to LENS primary look angle.

Experiment and Instrumentation

- Dedicated onboard radiometer for flowfield radiation.
- Ground based radar guided Deuterium-Fluoride laser illuminating the vehicle.
- Dedicated onboard radiometers for laser detection and attenuation measurement.
- Onboard focal plane array for blur measurement.

Test Vehicle

- Large bus containing avionics, beacons, telemetry, experiment support equipment and booster interface
- This vehicle (bus) capable of interfacing with ENDO LEAP and SDC BAA seekerhead concepts.

This experiment suite, seekerhead and test vehicle have been carried through conceptual design to prove test scenario feasibility. The report from the next phase will contain details of experiment sizing, instrument measurements specification, preliminary data processing and telemetry requirements and corresponding hardware selections, test range requirements, preliminary vehicle sizing and design layout and preliminary data processing and handling plan.

TABLE 1 CONFIDENCE IN EVENT OR MEASUREMENT

	LAUNCH SCENARIO	
	THIOKOL	PILEDRIVER
BOOSTER SYSTEM	LOW	HIGH
SHROUD REMOVAL	LOW	HIGH
TARGET PLACEMENT	LOW	HIGH
TARGET CHARACTER	HIGH	MED
A/O MEASUREMENTS		
•FLOWFIELD RADIATION	HIGH	MED
•ATTENUATION	HIGH	HIGH
•BLUE	HIGH	HIGH
•JITTER	HIGH	LOW
•BSE	MED	LOW
•BSE SLOPE	MED	LOW
THERMAL PERF. MEAS.		
•WINDOW	HIGH	HIGH
•FOREBODY	HIGH	HIGH